

1978

Effects of minor alloying additions on the strength and swelling behavior of an austenitic stainless steel

Gregory Raymond Gessel
Iowa State University

Follow this and additional works at: <https://lib.dr.iastate.edu/rtd>

 Part of the [Metallurgy Commons](#)

Recommended Citation

Gessel, Gregory Raymond, "Effects of minor alloying additions on the strength and swelling behavior of an austenitic stainless steel " (1978). *Retrospective Theses and Dissertations*. 6452.
<https://lib.dr.iastate.edu/rtd/6452>

This Dissertation is brought to you for free and open access by the Iowa State University Capstones, Theses and Dissertations at Iowa State University Digital Repository. It has been accepted for inclusion in Retrospective Theses and Dissertations by an authorized administrator of Iowa State University Digital Repository. For more information, please contact digirep@iastate.edu.

INFORMATION TO USERS

This material was produced from a microfilm copy of the original document. While the most advanced technological means to photograph and reproduce this document have been used, the quality is heavily dependent upon the quality of the original submitted.

The following explanation of techniques is provided to help you understand markings or patterns which may appear on this reproduction.

1. The sign or "target" for pages apparently lacking from the document photographed is "Missing Page(s)". If it was possible to obtain the missing page(s) or section, they are spliced into the film along with adjacent pages. This may have necessitated cutting thru an image and duplicating adjacent pages to insure you complete continuity.
2. When an image on the film is obliterated with a large round black mark, it is an indication that the photographer suspected that the copy may have moved during exposure and thus cause a blurred image. You will find a good image of the page in the adjacent frame.
3. When a map, drawing or chart, etc., was part of the material being photographed the photographer followed a definite method in "sectioning" the material. It is customary to begin photoing at the upper left hand corner of a large sheet and to continue photoing from left to right in equal sections with a small overlap. If necessary, sectioning is continued again – beginning below the first row and continuing on until complete.
4. The majority of users indicate that the textual content is of greatest value, however, a somewhat higher quality reproduction could be made from "photographs" if essential to the understanding of the dissertation. Silver prints of "photographs" may be ordered at additional charge by writing the Order Department, giving the catalog number, title, author and specific pages you wish reproduced.
5. PLEASE NOTE: Some pages may have indistinct print. Filmed as received.

University Microfilms International

300 North Zeeb Road
Ann Arbor, Michigan 48106 USA
St. John's Road, Tyler's Green
High Wycombe, Bucks, England HP10 8HR

7K13225

GESSEL, GREGORY RAYMOND
EFFECTS OF MINOR ALLOYING ADDITIONS ON THE
STRENGTH AND SWELLING BEHAVIOR OF AN
AUSTENITIC STAINLESS STEEL.

IOWA STATE UNIVERSITY, PH.D., 1973

University
Microfilms
International

300 N. ZEEB ROAD, ANN ARBOR, MI 48106

Effects of minor alloying additions on the strength and swelling
behavior of an austenitic stainless steel

by

Gregory Raymond Gessel

A Dissertation Submitted to the
Graduate Faculty in Partial Fulfillment of
The Requirements for the Degree of
DOCTOR OF PHILOSOPHY

Department: Chemical Engineering and Nuclear Engineering
Major: Nuclear Engineering

Approved:

Signature was redacted for privacy.

In Charge of Major Work

Signature was redacted for privacy.

For the Major Department

Signature was redacted for privacy.

For the Graduate College

Iowa State University
Ames, Iowa

1978

TABLE OF CONTENTS

	PAGE
ABSTRACT	ix
INTRODUCTION	1
VOID SWELLING	7
Introduction	7
Radiation Damage and Point Defect Generation	10
Void and Loop Nucleation	13
Growth Kinetics	22
Similitude of In-Reactor Behavior by Ion Bombardment	34
Control of Void Swelling through the Use of Metallurgical Variables	44
STRENGTHENING	52
Solid Solution Strengthening	52
Hardness	60
EXPERIMENTAL PROCEDURES	64
Specimen Preparation	64
Hardness Testing Equipment and Procedure	72
Ion Bombardment Procedure	75
RESULTS	83
Lattice Parameters	83
Microscopy	83
Modulus Measurements	94
Tensile Test Measurements	96
Hot Hardness Measurements	96
Swelling Measurements	132
DISCUSSION	148
Swelling Experiments	148
Hardness Experiments	175
CONCLUSIONS	186
REFERENCES	188
ACKNOWLEDGMENTS	200

LIST OF TABLES

TABLE	PAGE
1. Analyses of the Major Alloying Elements in Wt %	65
2. Average Impurity Levels [ppm (Wt.)]	66
3. Lattice Parameters of Selected Alloys	84
4. Modulus Measurements on Selected Alloys	95
5. Parameters for Void Growth Model	153
6. Fit Parameters for Swelling Data of Single Addition Alloys	163
7. H_0 and B Parameters for Fitting Hot Hardness Measurements .	180

LIST OF FIGURES

FIGURE	PAGE
1. Schematic representation of a displacement cascade	11
2. Defect aggregates (a) interstitial loop, (b) vacancy loop, (c) void	15
3. Void growth rate curve fitted to the data of Johnston et al.	29
4. Steady state vacancy concentration as a function of temperature	29
5. Steady state interstitial concentration as a function of temperature	30
6. Thermal equilibrium vacancy concentration as a function of temperature	30
7. Variation of swelling with Cr and Ni content for Ni ion irradiation	36
8. Variation of swelling with Cr and Ni content for neutron irradiation	37
9. Temperature dependence of swelling in nickel ion bombardment and neutron irradiated types 304 and 316 stainless steels	38
10. Displacement effectiveness for various energetic particles in nickel	40
11. Temperature dependence of swelling with and without minor additions	46
12. Effects of individual additions on the swelling of a base alloy	47
13. Schematic of dislocation segment and obstacle	52
14. Deformation map for nickel	59
15. Multiple specimen holder after ion bombardment	68
16. Back of multispecimen holder prior to ion bombardment	69

FIGURE	PAGE
17. ^{244}Cm -oxide source configuration for helium implantation . . .	71
18. Depth profile of preinjected He using the ^{244}Cm source . . .	73
19. Schematic drawing of hot hardness tester with specimen in place	74
20. Schematic of the ion bombardment chamber	76
21. Photograph of specimen heater and specimen holder assembly . . .	78
22. Detail of ion bombardment chamber	79
23. Detail section of ion bombardment chamber showing heater and thermocouple configuration	80
24. Typical profilometry trace of alloy after ion bombardment . . .	82
25. TEM micrograph of an Fe-7.6 Cr-21 Ni-1.4 Al-0.35 Nb alloy . . .	85
26. TEM micrograph of an Fe-7.3 Cr-20 Ni-4.0 Mo alloy	86
27. TEM micrograph of an Fe-7.4 Cr-22 Ni-0.69 Ti alloy	87
28. Optical metallograph of an Fe-7.5 Cr-20 Ni-Mo alloy	88
29. Optical metallograph of an Fe-7.5 Cr-20 N-W alloy	89
30. Optical metallograph of an Fe-7.5 Cr-20 Ni-Nb alloy	90
31. TEM micrograph of an Fe-8.5 Cr-21 Ni-3.9 Al alloy	92
32. TEM micrograph of an Fe-6.7 Cr-18 Ni-1.4 Nb alloy	93
33. Hardness and ultimate tensile strength as a function of temperature for an Fe-7.5 Cr-20 Ni alloy	97
34. Hot hardness data for an Fe-7.3 Cr-20 Ni-4.0 Mo alloy	98
35. Hot hardness data for an Fe-6.7 Cr-18 Ni-7.2 Mo alloy	99
36. Hot hardness data for an Fe-7.8 Cr-20 Ni-0.8 Al alloy	100
37. Hot hardness data for an Fe-7.4 Cr-21 Ni-2.2 Al alloy	101
38. Hot hardness data for an Fe-8.5 Cr-21 Ni-3.9 Al alloy	102

FIGURE	PAGE
39. Hot hardness data for an Fe-7.2 Cr-20 Ni-0.66 Nb alloy . . .	103
40. Hot hardness data for an Fe-7.1 Cr-19 Ni-0.88 Nb alloy . . .	104
41. Hot hardness data for an Fe-7.3 Cr-20 Ni-0.21 Ti alloy . . .	105
42. Hot hardness data for an Fe-7.7 Cr-21 Ni-0.39 Ti alloy . . .	106
43. Hot hardness data for an Fe-7.4 Cr-22 Ni-0.69 Ti alloy . . .	107
44. Hot hardness data for an Fe-6.9 Cr-20 Ni-0.43 Si alloy . . .	108
45. Hot hardness data for an Fe-7.4 Cr-19 Ni-0.86 Si alloy . . .	109
46. Hot hardness data for an Fe-6.7 Cr-19 Ni-1.80 Si alloy . . .	110
47. Hot hardness data for an Fe-7.7 Cr-21 Ni-2.3 W alloy	111
48. Hot hardness data for an Fe-8.0 Cr-21 Ni-5.5 W alloy	112
49. Hot hardness data for an Fe-7.0 Cr-20 Ni-8.9 W alloy	113
50. Hot hardness data for an Fe-7.5 Cr-19 Ni-0.53 Ti-0.43 Si alloy	114
51. Hot hardness data for an Fe-7.1 Cr-18 Ni-0.20 Ti-0.36 Si alloy	115
52. Hot hardness data for an Fe-7.0 Cr-19 Ni-0.37 Ti-0.77 Si alloy	116
53. Hot hardness data for an Fe-7.4 Cr-21 Ni-1.8 Mo-0.9 Al- 0.19 Ti-0.39 Si alloy	117
54. Hot hardness data for an Fe-7.0 Cr-20 Ni-3.8 Mo-0.76 Si alloy	118
55. Hot hardness data for an Fe-7.1 Cr-19 Ni-3.9 Mo-0.35 Ti alloy	119
56. Hot hardness data for an Fe-7.6 Cr-21 Ni-2.1 Al-1.7 Nb alloy	120
57. Hot hardness data for an Fe-8.1 Cr-26 Ni-1.7 Al-1.0 Nb alloy	121
58. Hot hardness data for an Fe-7.7 Cr-20 Ni-5.0 Mo-2.1 Al alloy	122

FIGURE	PAGE
59. Hot hardness data for an Fe-6.9 Cr-18 Ni-0.20 Ti-1.20 Si alloy	123
60. Hot hardness data for an Fe-8.0 Cr-21 Ni-1.4 Al-0.35 Ti alloy	124
61. Hot hardness data for an Fe-7.9 Cr-20 Ni-4.4 Mo-0.87 Nb alloy	125
62. Hot hardness data for an Fe-7.5 Cr-20 Ni alloy	126
63. Hot hardness data for an Fe-7.4 Cr-20 Ni-0.10 C alloy	127
64. Effect of alloying element on the hardness of an Fe-7.5 Cr-20 Ni ternary at 22°C	129
65. Effect of alloying element on the hardness of an Fe-7.5 Cr-20 Ni ternary at 400°C	130
66. Effect of alloying element on the hardness of an Fe-7.5 Cr-20 Ni ternary at 850°C	131
67. Step height versus temperature data for alloys containing molybdenum	133
68. Step height versus temperature data for alloys containing tungsten	134
69. Step height versus temperature data for alloys containing aluminum	135
70. Step height versus temperature data for alloys containing niobium	136
71. Step height versus temperature data for alloys containing titanium	137
72. Step height versus temperature data for alloys containing silicon	138
73. Step height versus temperature data for alloys containing carbon	139
74. Step height at the peak temperature versus solute concentration for all elements	142
75. Step height versus temperature for alloys containing double solute additions	144

FIGURE	PAGE
76. Step height versus temperature for alloys containing double solute additions	145
77. Step height versus temperature for alloys containing double solute additions	146
78. Void growth curves fitted to data for tungsten alloys	155
79. Void growth curves fitted to data for molybdenum alloys	156
80. Void growth curves fitted to data for niobium alloys	157
81. Void growth curves fitted to data for titanium alloys	158
82. Void growth curves fitted to data for silicon alloys	159
83. Void growth curve fitted to data for the 1.65 Al alloy	162
84. Phase diagram for the iron-molybdenum system	165
85. Phase diagram for the iron-titanium system	166
86. Phase diagram for the iron-nickel system	167
87. Phase diagram for the iron-tungsten system	168
88. Phase diagram for the iron-phosphorus system	169
89. Phase diagram for the iron-silicon system	170
90. Hot hardness data for an Fe-7.5 Cr-20 Ni-5.5 W alloy showing the empirical fit	176
91. Variation of the fit parameter ΔH with composition	181
92. Variation of the fit parameter Δb with composition	182
93. Calculated hot hardness and experimental data for an Fe-7.5 Cr-20 Ni-4.4 Mo-0.87 Nb alloy	183
94. Calculated hot hardness and experimental data for an Fe-7.5 Cr-20 Ni-3.6 Si-0.2 Ti alloy	185

ABSTRACT

A set of 32 alloys consisting of various additions of the elements Mo, W, Al, Ti, Nb, C and Si to an Fe-7.5 Cr-20 Ni alloy were made in order to investigate the effects of these solute additions on alloy swelling and strength. Both single and multiple additions were examined.

The influence of various solute elements on the swelling behavior in the range 500 to 730°C was investigated using 4 MeV Ni ion bombardment to a dose 170 dpa. It was found that on an atomic percent basis, the elements may be arranged in order of decreasing effectiveness in reducing peak temperature swelling as follows: Ti, C, Nb, Si, and Mo. Small amounts of aluminum enhance swelling. Additions of Si, Ti, or Nb truncate the high temperature swelling regime of the ternary alloy. Mo, W, and C do not have a strong effect on the temperature dependence of swelling. The results may be interpreted in terms of the effect of point defect trapping on void growth rates, and it is suggested that the changes in peak temperature are the result of small changes in the free vacancy formation energy. A method for treating certain multiple additions is proposed.

The effect of these alloying additions on short time high temperature strength properties was estimated using hot hardness measurements over the temperature range 22 to 850°C. On an atom percent basis Nb and Ti were most effective in conferring solid solution strengthening and Si the least effective. In the regime 22 to ~ 650°C, the hardness data was found to fit an equation of the form

$$H = H_0 + \frac{b}{T}$$

where H is the hardness, T is the temperature, and H_0 and b are constants for a given alloy. An empirical method was devised to estimate the hot hardness of alloys containing more than one solute addition.

INTRODUCTION

During the period 1950 to 1975 world energy consumption increased more than 300%. With this increase has come a growing reliance on oil and natural gas, 50% in 1960 to 70% in 1974. Unfortunately, there appears to be no relief in sight as more nations industrialize and the population increases. Although earth has finite resources and both oil and natural gas are relatively rare minerals, the world's economy continues to depend on an unprecedented rate of their use for sustenance.

In the U.S., which depends on oil and gas for more than 70% of its total energy, economical domestic reserves could be depleted by 2000. The whole question of energy supply appears shrouded with urgency. Some advocate "buying time" with stringent conservation practices, but these are not likely (to come in time) on an international scale. In any case, such measures would merely delay the ultimate crunch. Clearly, other sources must replace oil and natural gas as well as keep up with growth in demand. The amount of economic and social disruption involved will be a function of how quickly this transformation to other energy sources occurs. All conceivable sources must be considered; it is no longer our prerogative to discriminate irrationally against any given alternative. However, the options have to be ordered in priority, with those capable of the greatest contribution in least time heading the list. There will be no easy solutions. Those have passed and have in large measure contributed to the present dilemma. Each option will have great associated costs with the only flexibility being how they are paid.

Most nations, like the U.S., have recognized the nuclear option and placed it high on the list of alternatives. Nuclear energy in the form of light water reactor (LWR) technology relies on a resource, ^{235}U , that occurs in natural uranium with an abundance of 0.72%. Notwithstanding the tremendous energy release from fission the LWR is not a long-term option. To extend the fission contribution and utilize the remaining 99 plus percent uranium it is necessary to develop the fast breeder reactor (FBR) concept.

Liquid Metal Fast Breeder Reactors (LMFBR) have been in existence since 1951, but commercial utilization of this concept involves uncertain extrapolations of past and present operating experience. This uncertainty is not so much a question of safety but rather of economics. Economic feasibility dictates doubling times of 15 to 20 years, peak fuel burnups near 100-125 MWd/kg and operating temperatures in the range 350 to 700°C. To achieve this kind of performance the fuel subassemblies will be exposed to fast neutron fluences of $2-3 \times 10^{23}$ n/cm² ($E > 0.1$ MeV). In this temperature and fluence range significant amounts of radiation-induced deformation can result. At fast fluence exposures of 1.5×10^{23} the present reference cladding and structural alloy (20% cold worked 316 stainless steel) exhibits radiation-induced void swelling of 18% at the temperature of maximum swelling (1). In-reactor creep rates are a factor of 3 too high, and rupture stresses a factor of 3 too low to meet performance goals (2). Two courses of action seem possible. First, these limitations could be accepted and allowances made in core design to accommodate them. In principle this can be accomplished by increasing

both duct and cladding thickness to add strength and by allowing space for the expected dimensional changes. The price for this solution includes low peak burnups or low breeding ratios, both of which have associated higher energy costs. In fact such a solution is unacceptable because the resultant 40 year doubling time is impractically long. If the LMFBR is to make a contribution to energy supply, materials with improved properties must be developed.

Currently, the Experimental Breeder Reactor (EBR-II) is the only fast-neutron test facility available in the U.S. Reaching target fluences of 1×10^{23} n/cm² in EBR-II takes a minimum of 2-3 years. Yet this exposure equals only one year of full power operation in a commercial LMFBR. In the early 1980's the Fast Flux Test Facility will be available, and because of its higher fast neutron flux the exposure time required to provide the target fluence will be reduced from seven to one or two years. Between now and the time when the FFTF is available one needs to identify the crucial parameters affecting swelling, creep, and strength and learn to control these properties. To accomplish this, reactor irradiation studies must be supplemented by techniques that simulate some aspects of in-reactor behavior. One technique utilizes particles other than neutrons to produce radiation damage. For irradiation induced swelling studies in high nickel stainless steels, heavy ions like ⁵⁸Ni are particularly well-suited. Damage rates with ions (300 displacements per atom/hr) are significantly greater than would be achieved in a fast reactor (0.0035 dpa/hr). By using heavy ion techniques, one can accrue damage levels in a few hours normally

achieved only after years of irradiation in a fast reactor. There is no doubt that these methods can greatly advance the study of in-reactor behavior provided appropriate care is taken when analyzing the results. The two types of irradiation are most likely not equivalent; one must view them in light of the similitude they represent. One would like to determine the scaling laws that transform the ion irradiation into neutron irradiation. However, in the absence of such a relation, one can examine systematically the effects of parameter variations on the properties of a basic alloy using ion irradiation. Johnston et al. (3) has used this method to demonstrate the pronounced effect that composition can have on swelling. Composition appears to be the most potent variable at the metallurgist's disposal for controlling swelling.

The question naturally arises "what happens to other important properties while the composition is being varied to reduce swelling?". The answer requires simultaneous examination of alloys for other properties of interest in addition to swelling. Mechanical strength is certainly an important property. To carry out a systematic investigation of a large alloy set using conventional tensile testing techniques would be both costly and time consuming. Some attractive technique is needed to examine mechanical strength.

A correlation does exist between hot hardness and ultimate strength (4). Since the hot hardness technique involves simple specimen preparation and easily made measurements, it can be used to screen rapidly a large alloy set. However, in light of the uncertainty about what hardness is and the specific nature of its correlation with

ultimate tensile strength (UTS), this technique should be used to give only a relative ranking of alloy strength.

The realization that compositional variations can significantly affect alloy properties formed the basis for the present study. Ion bombardment and hot hardness techniques were used as vehicles to study such effects on irradiation induced swelling and mechanical strength. The strategy to be used is simple. First, one selects a base composition and then studies the effects of various alloying additions on both swelling and mechanical strength. These results can then be utilized to optimize the composition of the alloys for these properties.

The base composition Fe-7.5 Cr-20 Ni was chosen for this study. The decision to use 20% nickel was based on two separate factors. First is the observation that swelling decreases with increasing nickel content (3). Second is the realization that large nickel concentrations can adversely affect the breeding ratio. The low chromium content of Fe-7.5 Cr-20 Ni makes possible large substitutional additions while avoiding phase instability. By maintaining low carbon content (20 ppm) complicating carbide effects can be reduced or eliminated. To this base composition single and multiple additions of Si, Ti, Nb, W, Mo, and C are made. These alloys are then examined using ion bombardment and hot hardness techniques. The evaluation includes the combined effects of temperature and single compositional variations on the magnitude of swelling and mechanical strength of the pure ternary alloy. By using such an alloy set the relative effects of various additions can be compared directly. Rules for multiple addition can be postulated

from empirical relations established for single additions. These rules can then be checked with the experimental data obtained for multiple additions. Once the behavior of alloys with multiple additions can be predicted, various optimization schemes can be used to find the most suitable composition for a given application.

VOID SWELLING

Introduction

By 1966 a good deal of work had been conducted to examine the effects of neutron radiation on the properties of cladding materials. Radiation embrittlement appeared to be the major material limitation posed by fast reactor environments and a means of coping with it seemed at hand. During this period, Cawthorne and Fulton (5) reported results of Transmission Electron Microscopy (TEM) examination of 316 stainless steel that had been irradiated in the Dounreay Fast Reactor to fluences of 6×10^{22} n/cm² and at temperatures between 270 to 600°C. Their findings included an internal porosity consisting of a distribution of small (smallest resolvable, to 1100Å) essentially empty cavities. Subsequent observations showed that these so-called "voids" were generally associated with a decrease in density of the material (swelling). For reactor designers concerned with close tolerances, such dimensional changes were cause for great concern.

Since these initial findings, void swelling has been the subject of intensive investigation. Numerous reviews (6-8) and conferences (9-19) have addressed the subject. Olander (20) has recently reviewed many aspects of nuclear reactor fuel element behavior of which three chapters deal with radiation effects on cladding. The well-organized presentation in this volume provides an excellent introduction to the current literature.

The conditions under which void swelling occurs are well-known. Unfortunately, they correspond rather closely to proposed LMFBR operating conditions. For most metals, void swelling occurs in a temperature range 0.3 to 0.55 of the absolute melting temperature. For materials like stainless steel there is a threshold fast neutron fluence. The dependence of swelling on the fast neutron fluence has a threshold fluence ($\sim 10^{22}$ n/cm²) below which voids are not observed. The incubation period required to accrue this threshold fluence is sensitive to a number of material variables (temperature, alloy composition and microstructure). Ultimately, however, the threshold is reached and void swelling proceeds. Limited high fluence data are available and thus the precise functional dependence of swelling with fluence is not known. Several empirical fits (1) to existing data have been used to predict swelling at LMFBR fluences (3×10^{23} n/cm²). However, these data generally require substantial revision as more data at higher fluences are obtained. For reactor-irradiated stainless steel no upper bound for swelling has been observed. However, saturation has been observed in high energy ion bombardment (21) (effective neutron fluence $\sim 10^{24}$ n/cm²). Provided a connection exists between these two types of irradiation, one would predict saturation in swelling at neutron fluences of $\sim 10^{24}$ n/cm². But long before exposures of this magnitude are reached, swelling in stainless steel will have exceeded acceptable values.

The immediate result of fast neutron impingement on a crystalline solid is disorder. For each incident fast neutron a number of lattice atoms are displaced from their equilibrium sites resulting in a

population of interstitial atoms and corresponding vacancies.

Interstitials and vacancies can recombine and most point defects are lost through annihilation. Other possible aggregates include two-dimensional platelets (loops) consisting of either interstitials or vacancies. A loop has the effect of either adding or subtracting a plane of atoms from the lattice depending on whether it is interstitial or vacancy in character. Thus, interstitial loops result in volume expansion and vacancy loops give rise to volume contraction. If all point defects found their way to loops the net result would be little swelling. Vacancies can also agglomerate to form large three dimensional cavities (voids) which have no associated volume contraction. Migration of vacancies to voids allows volume expansion due to interstitials to go uncancelled, resulting in swelling.

With the realization that voids and interstitial loops are giving rise to void swelling, many questions ensue. What are the precursors of voids and interstitial loops and what energy constraints govern their formation? Once formed, do voids, for example, show the preference for vacancies that their growth would seem to dictate? How does the presence of other structures (precipitates, dislocations, etc.) affect the process? How can swelling be reduced or prevented?

Attempts to answer these and other related questions comprise what has come to be known as the physics of void swelling. There exist many theoretical explanations, some conflicting but most supported by only isolated observations. In the sections to follow, many of these explanations will be identified and discussed.

Radiation Damage and Point Defect Generation

Since swelling and voids are corresponding macroscopic and microscopic manifestations of point defect agglomeration, our attention first turns to the defects themselves and constraints governing their production. Interstitial and vacancy defects are a kind of measure of disorder present in a crystalline solid. For any temperature greater than absolute zero, their equilibrium concentrations distributions can be calculated using Maxwell-Boltzmann statistics. Irradiation by energetic particles brings additional energy to the lattice and results in further disorder. The concentration of point defects produced by radiation must be substantially greater than that due to thermal agitation in order to observe void swelling. Although cladding in a fast reactor will be subjected to radiations of various types, that due to neutrons is of primary concern. In principle, the creation of an interstitial-vacancy pair by a neutron-atom collision requires only that the neutron transfer at least an amount of energy of the order of 25-90 eV to the atom. The precise value of this threshold displacement energy (E_d) is a function of lattice type and crystallographic orientation. Collisions between neutrons and lattice atoms giving transferred energy $T > E_d$ can result in a primary knock-on atom (PKA) with considerable kinetic energy. The PKA then dissipates its energy through secondary collisions which produce additional displacements. The resulting collection of displacements (interstitial-vacancy pairs) produced by a single PKA is termed a displacement cascade. Figure 1 gives a schematic

ORNL-DWG 74-11518

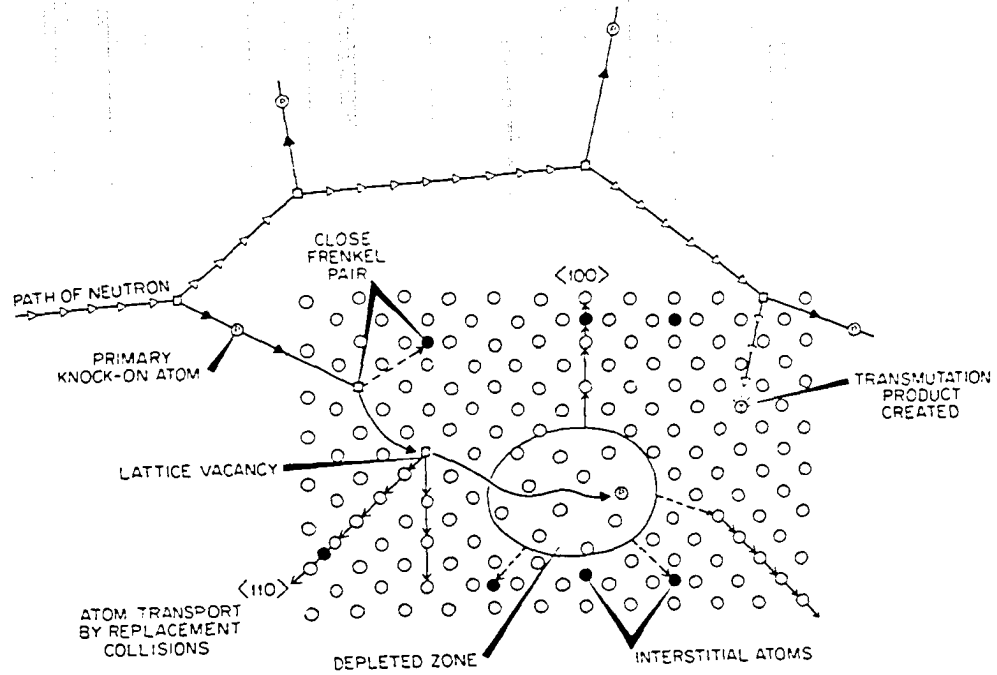


Figure 1. Schematic representation of a displacement cascade.

representation of a displacement cascade, and some particle interactions that constitute radiation damage. Also shown on this schematic is the presence of a vacancy-rich "depleted zone" produced in the vicinity of the PKA's final stopping place. Computer simulation has been exploited as a technique for understanding the effects of various collision processes on the displacement cascade structure (22) for various lattice structures. Field ion microscopy has been used to reveal the depleted zone of cascades (23). A single cascade process requires $\sim 10^{-13}$ sec. An annealing period (10^{-6} sec) ensues driven by the inherent thermodynamic instability of the collection of isolated point defects. During annealing, point defects jump about in an effort to lower the system's free energy. Options available include annihilation, clustering with like defects or entrapment at some structural feature (sink). Following this short trapping process most of the surviving defects exist as immobile clusters. Because of the random walk nature of annealing, it has been successfully simulated using computer assisted Monte Carlo techniques (24). Computer simulation incorporating constraints imposed by the particular lattice structure has been used to explain cascade details (25). There is a growing amount of evidence to indicate that many of the variables affecting void swelling show their influence as early as the cascade process (26). For example impurities may affect the way energy is transferred in various collision processes. The presence of an impurity atom of different mass or size could alter both focusing and channeling events. It will be recalled that in a focusing

event energy is transferred along a row of atoms while channeling refers to movement along open directions in the crystal lattice.

Transmutation reactions of the (n,p) and (n,α) type leading to hydrogen and helium production also play a key role in the swelling of stainless steels. Although the influence of hydrogen and helium on swelling will be discussed later, it suffices to say that gas atoms within the lattice can stabilize defect clusters. This is likely to be most pronounced with helium because of its very low solubility in stainless steels. Because (n,α) and (n,p) reactions are threshold reactions, gas production accompanies the presence of high energy neutrons. Gas generation is dependent on composition and neutron spectrum. Estimates have been made for gas production in stainless steels exposed to fast reactor neutron flux (27). These values generally fall in the range 0.1 to 1 ppm/dpa.

Void and Loop Nucleation

As previously explained, irradiation of metals by energetic particles results in vacancy and interstitial concentrations in excess of their thermal equilibrium values. Electron microscopy has confirmed the formation of defect clusters consisting solely of interstitials or vacancies in irradiated materials. Vacancies or interstitials can cluster to form voids, faulted loops, unfaulted loops, or stacking fault tetrahedra. Of concern to the present discussion are three dimensional vacancy aggregates (voids) and planar aggregates of either vacancies or interstitials (loops). These three types of structures are illustrated

schematically in Figure 2. Since the electron microscope has a practical limit of resolution for loops and voids of about 20 \AA , the very early stages of void formation are not accessible to direct observation. A 20 \AA diameter planar cluster (loop) will contain fewer defects than a three dimensional void of the same diameter. This fact coupled with the stronger image contrast for a loop (due to higher strains) accounts for the observation of loops long before voids were found during High Voltage Electron Microscope (HVEM) irradiations (28). Another important consequence of this void resolution limit is that conclusions about void embryo formation have been deduced from observations of resolvable voids. Implicit in such observations is the period of growth between the time an embryo is formed and the time it grows to the size which makes resolution possible. This comprises a basic difficulty in the study of void swelling phenomena. Despite this problem several conclusions about the void nucleation process have come to be widely accepted.

Gases are thought to stabilize three-dimensional vacancy clusters against collapse into planar loop aggregates. Insoluble gases such as helium seem to be most effective and are continuously produced in-reactor by various (n,α) reactions. Preinjection of helium results in an increase in the observed void density for both in-reactor (28) and ion bombardment (29) conditions. The effects of preinjected helium on swelling under ion bombardment show an initial increase, then a leveling off as more helium is added (30). All commercial stainless steels contain, by virtue of their processing, hydrogen, nitrogen, and oxygen.

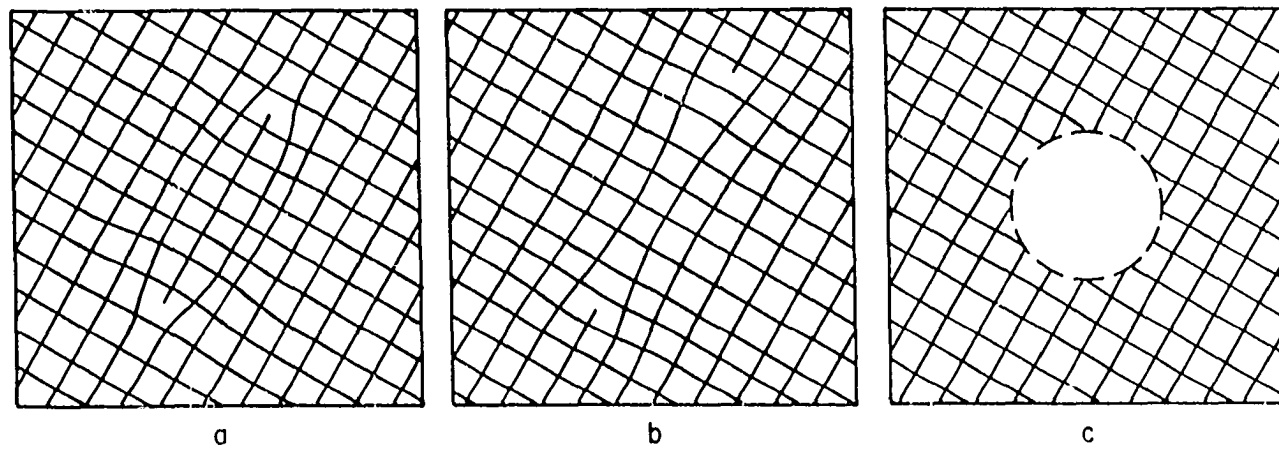


Figure 2. Defect aggregates (a) interstitial loop, (b) vacancy loop, (c) void.

The observation that large swellings are produced during ion bombardment in the absence of preinjection seems consistent with this fact. Some have postulated that the swelling incubation period (i.e., the fluence threshold 10^{22} n/cm²) is related to the time required to build up an appropriate concentration of helium (20).

Recognition that gases affect nucleation of voids should not preclude mechanistic considerations. At least two mechanistic approaches to nucleation have been suggested. Vacancy clusters could be viewed to form first (perhaps in cascades) and then become stabilized as gas atoms diffuse in. Alternatively, clustering could be facilitated by immobile gas atoms capturing mobile vacancies. For gases like helium that appear to be fairly immobile, the latter seems more feasible; however, for gases with greater diffusivities like hydrogen and nitrogen either option is possible.

The addition of various minor elements to stainless steels has been observed to have pronounced effects on the swellings observed after either neutron irradiation or ion bombardment. Some observations have shown that the addition of such impurities results in lower void densities at a given fluence (31). This observation is then interpreted as strong evidence for the inhibition of the void nucleation process by such impurities. Other observations show that alloying elements can result in an increase in void size but not void density (31). Calculations have shown that impurities acting as traps can reduce both nucleation and growth of voids (32). Again the question of the effect of impurities

is an open one, since the experimental observations most likely reflect both nucleation and growth effects.

Precipitates may also play an important role in void nucleation. It is common to observe voids associated with precipitates in irradiated stainless steels (28). Such observations do not indicate which formed first. The precipitate could be the result of impurity-vacancy binding. Here again it is difficult to develop an evolutionary history based solely on end point observations.

The formation of void embryos can be viewed qualitatively as analogous to crystallization from supersaturated solid solutions or condensation from vapor-laden gases. Despite the distinct difference resulting from the mutual annihilation of vacancies and interstitials, this early stage of void development has come to be known as nucleation. As in condensation, internal surfaces of a solid could act as sites for nucleation. This possibility has been considered by a number of authors under the name heterogenous nucleation (33); however, the approach has not been treated analytically. A framework for doing this may exist in classical work on nucleation of precipitates on precipitates, on grain boundaries, and on dislocations (34).

Point defects could also cluster as a result of random interactions. This homogeneous case eliminates the need for internal surfaces, and the case for voids has been treated by Katz and Wiedersich (35) and Russell (36) using adaptations of classical nucleation theory. The formation of a vacancy cluster does not insure its survival. Such clusters can shrink by either vacancy emission or interstitial capture. Thus the

term void embryo can be applied only to vacancy aggregates of some minimum size. Void nucleation theory as it stands is a phenomenological description of this process. It seeks to provide a quantitative framework for examining the influence of certain variables on the early phases of void formation. These basic concepts will be reviewed following recent discussions by Wiedersich and Katz (37) and Mansur and Wolfer (38).

Void nucleation theory describes the dynamics of vacancy clusters. Since a given cluster can either shrink out of existence or grow to become an observable void, one needs a way of characterizing its size. For vacancy clusters the number of vacancies (n) contained in the cluster provides a useful parameter. The growth of a given cluster requires vacancy absorption while shrinkage can occur by either vacancy emission or interstitial absorption. The dynamics of an assemblage of various size clusters can be described by a method similar to neutron slowing down theory (39).

The time rate of change of clusters containing n vacancies is expressed by simple flux balance in cluster size space. Doing this results in an equation of the form

$$\begin{aligned} \frac{\partial q(n)}{\partial t} = & [\beta_i(n+1) + \gamma_v(n+1)] q(n+1) - [\beta_v(n) + \beta_i(n) \\ & + \gamma_v(n)] q(n) + \beta_v(n-1) q(n-1) . \end{aligned} \quad (1)$$

where

$$\frac{\partial q(n)}{\partial t} = \text{time rate of change of vacancy clusters containing } n \text{ vacancies.}$$

$\beta_{v,i}(n)$ = capture rate of vacancies, interstitials by a vacancy cluster of size n .

$\gamma(n)$ = emission rate of vacancies from a vacancy cluster of size n .

To fully describe an assemblage of j different size clusters requires simultaneous solution of j coupled equations like (1). Such a problem demands numerical solution and can be expensive to solve. For purposes of solving for $q(n)$ it is useful to rewrite (1) in the following form:

$$\frac{\partial q(n)}{\partial t} = M(n-1) - M(n) \quad (2)$$

where

$$M(n) = \beta_v(n) q(n) - [\beta_i(n+1) + \gamma_v(n+1)] q(n+1) . \quad (3)$$

This process involves collecting all terms that involve flow between two adjacent cluster sizes. Such rearrangement makes the application of equilibrium constraints straightforward. Besides the direct solution to this transient problem, two steady state solutions are of interest. The steady state condition is imposed by setting $\partial q(n)/\partial t = 0$. One then generates a recursion relation between different q values by dictating the form by the equilibrium distribution. One such condition is that of constrained equilibrium (34) expressed in the condition

$$M(n-1) = M(n) = 0 . \quad (4)$$

This requires no net flux of clusters between different sizes.

It is reasoned that because the net flow is so small a first cut at the solution can be obtained by setting $\partial q(n)/\partial t = 0$. When (4) is applied to (3) a recursion relation of the following form results:

$$q^\circ(n) = \sum_{\ell=1}^{n-1} \frac{\beta_v(\ell) q^\circ(1)}{\beta_i(\ell+1) + \gamma_v(\ell+1)} \quad (5)$$

where

$q^\circ(n)$ = constrained distribution of vacancy clusters size n .

If one defines a free energy for formation of an n vacancy cluster as

$$\Delta G(n) = -kT \sum_{\ell=1}^{n-1} \ell n \frac{\beta_v(\ell)}{\beta_i(\ell+1) + \gamma_v(\ell+1)} \quad (6)$$

then (5) can be rewritten in the form

$$q^\circ(n) = q^\circ(1) \exp[-\Delta G(n)/kT] \quad (7)$$

The usefulness of the constrained equilibrium case is that it serves to define the free energy for formation of a vacancy cluster. It is worth noting that $q^\circ(1)$ is equivalent to the vacancy concentration. The $\beta_{i,v}(n)$ and $\gamma_v(n)$ terms in these equations are expressible in terms of the usual point defect parameters as

$$\beta_{i,v}(n) = (4\pi)^{2/3} (3\Omega n)^{1/3} Z_{i,v}^v D_{i,v} C_{i,v} \quad (8)$$

and

$$\gamma_v(n) = (4\pi)^{2/3} (3\Omega n)^{1/3} z_{i,v}^v(n) D_v C_v^e \exp\left[\left(\frac{2\sigma}{r(n)} - P\right) \Omega/kT\right] \quad (9)$$

where

$z_{i,v}^v(n)$ = capture efficiency of size n vacancy cluster for interstitials or vacancies,

$D_{i,v}$ = diffusion coefficient for free interstitials or vacancies,

$C_{i,v}$ = concentration of free interstitials or vacancies,

C_v^e = thermal equilibrium vacancy concentration,

Ω = atomic volume,

σ = specific surface energy of the cluster,

P = gas pressure within the cluster, and

$r(n)$ = radius of n vacancy cluster.

The $q^\circ(n)$ determined by the constrained equilibrium case can be used as a first iteration in the solution of the steady state nucleation rate

$$M = M(n) = M(n - 1) = \dots \quad (10)$$

As before, this condition together with (1) results in a recursion relation which can be expressed in terms of usual defect parameters as

$$M = \frac{(4\pi)^{2/3} (3\Omega)^{1/3} C_v^2 D_v}{\sum_{n=1}^{\infty} \frac{\exp[\Delta G(n)/kT]}{(n)^{1/3} z_{i,v}^v(n)}} \quad (11)$$

This approach provides a method for investigating the sensitivity of nucleation rate to various parameters. Although much of the discussion

in this section has centered around void nucleation, the same basic approach can and has been used to treat loop nucleation (35).

Traditionally void nucleation and growth have been treated separately. Recently, Wolfer et al. (40) have attempted to approach swelling theory from a more unified viewpoint. Their method builds upon the work of Katz and Wiedersich (35) and Russell (36) and some work on classical nucleation (34) but results in a Fokker-Planck type equation describing the evolution of the void or loop size distribution. This technique has been applied by the authors (40) to problems dealing with both swelling and irradiation creep.

The effects of helium gas on nucleation have been incorporated into the theory (37). Vacancy clusters are then characterized by both the number of vacancies and number of gas atoms. Solution of the nucleation problem becomes correspondingly more difficult. The general result of such calculations is that helium is found to lower the free energy for void nucleation.

Growth Kinetics

By considering the void as a three-dimensional vacancy precipitate, one can deduce the basic conditions for void swelling. The precipitation nature of this process requires a supersaturation of vacancies above the thermal equilibrium value. With increasing irradiation temperature the number of thermally created defects increases exponentially, diminishing the amount of vacancy supersaturation produced by irradiation. This implies an upper bound temperature for void formation. On the other

hand, fairly high temperatures are required since coalescence of vacancies dictates that they be mobile. Although vacancies are immobile at low temperatures, their mobility varies exponentially with temperature. Therefore, there exists a lower bound temperature for void swelling.

The formation of void nuclei represents still another important prerequisite for void swelling. Mere formation of void nuclei does not insure their continued growth. Simply stated, such growth requires that the net capture rate for vacancies must exceed that for interstitials. Net capture rate is used as a qualification since a vacancy can also acquire enough energy to escape or be "emitted" from the void. The emission rate will vary exponentially with void size and temperature and gas pressure. Even under conditions where defect emission is not important, one must understand why the vacancy flux to voids is greater than the interstitial flux.

The void may exhibit a direct preference for vacancies. Mansur and Wolfer (38) find this to be the case for coated voids, but their calculations indicate that small uncoated voids should prefer interstitials. Farrell et al. (41) have experimentally observed silicon-coated voids in neutron-irradiated aluminum. The system, exclusive of voids, may also exhibit a preference for a given defect. For example, interstitials are known to interact more strongly than vacancies with the strain field around dislocations (42,43). Norris (44) has experimentally measured the direct influence of local dislocations on void growth.

Unfortunately, reactor steels are more complex, containing many different point defect sinks. These can be classified into categories

based on their interaction with defects. Sinks can be of the neutral type exhibiting no net preference for either vacancies or interstitials. Evidence indicates that grain boundaries and incoherent precipitates (43) are neutral. The second classification is the sink exhibiting a preference for one type of defect. Dislocations are known to prefer interstitials while coated voids may be biased toward vacancies. Dislocations can be of the unfaulted loop, faulted loop or network type. Unfaulted and faulted loops differ in that the latter encloses a stacking fault. For austenitic stainless steels, faulted loops form first, then grow to a critical size at which unfaulting is energetically favored. Unfaulting is then followed by growth and movement of the resulting perfect loop. Dislocations are termed unsaturable sinks since, provided they are not pinned, they can absorb a vacancy or interstitial and climb. Recombination sites represent the third sink category. Here the sink merely traps a defect at its surface, making annihilation inevitable. Such sinks are saturable since they have a finite trapping surface or limited number of trapping sites. Coherent precipitates can act as recombination centers (45,46).

All this is very qualitative; fortunately an analytic framework has been developed for examining such questions. This framework utilizes chemical rate theory. Brailsford and Bullough (47) and Wiedersich (48) have extended the original work of Harkness and Li (49). Mansur (50) has given an assessment of the current status of the theory. Here we shall not dwell on algebraic detail but instead outline existing techniques.

The first step in growth calculations is to determine the concentrations of interstitials and vacancies in the system. This involves balancing the rate of production and removal of point defects which yields two equations.

$$\nabla \cdot \left(D_v \nabla C_v + \frac{D_v C_v}{kT} \nabla U_v \right) + G_v - RC_v C_i - \sum_j K_v^j C_v = \frac{\partial C_v}{\partial t} \quad (12)$$

$$\nabla \cdot \left(D_i \nabla C_i + \frac{D_i C_i}{kT} \nabla U_i \right) + G_i - RC_v C_i - \sum_j K_i^j C_i = \frac{\partial C_i}{\partial t} \quad (13)$$

where

v,i subscripts = vacancies and interstitials, respectively,

K^j = rate constants for losses at sinks,

C = point defect concentrations,

U = interaction energy at sinks,

G = generation rate of point defects,

R = recombination coefficient,

k = Boltzmann's constant,

T = absolute temperature,

t = time, and

D = diffusion coefficient.

Examination of the structure of these equations provides a clear indication as to the nature of this calculation. For example, the use of a single constant to describe losses of vacancies to a particular type of sink means sinks are treated as if homogeneously distributed.

This approach necessarily washes out details and treats any given sink as the average value. There is clear evidence that all sinks of a given type are not similar in all respects. Norris (44) has observed that voids in close proximity to dislocations grow more rapidly than isolated voids. Clearly, consideration is given only to single vacancies and interstitials.

Equations (12) and (13) can be solved for C_v and C_i . Generally this is facilitated by considering the system in a quasi-steady state allowing the time derivative to vanish. This simplification results from the capacity of point defect concentrations to change much more rapidly than does the sink microstructure. Void growth rate, for example, is a quantity of interest. If one considers the flux of point defects to the void, the void growth rate is obtained.

$$\frac{dr_v}{dt} = \frac{\Omega}{r_v} [z_v^v(r_v)D_v|C_v - C_v^e(r_v)| - z_i^v(r_v)D_iC_i] \quad (14)$$

where

r_v = void radius,

$C_v^e(r_v)$ = thermal equilibrium vacancy concentration at a void radius r_v ,

Ω = atomic volume,

$z_{v,i}^v(r_v)$ = capture efficiency for vacancies for interstitials at a void radius r_v .

It should be noted that

$$K = S(Z)D \quad (15)$$

where

S = sink strength.

Typical sink strengths are
for spherical sinks

$$S = 4\pi \int r Z(r) n(r) dr \quad (16)$$

where

$n(r) dr$ = number of sinks per unit volume of size r to $r + dr$

for cylindrical network dislocations

$$S = 2\pi L / \ln(R^n/r^n) \quad (17)$$

where

L = dislocation line density,

R^n = radius of outer boundary,

r^n = radius of inner boundary.

The same procedure is used for growth determination of interstitial loops or any type of microstructural feature. The values for C_v and C_i are obtained from the simultaneous solution of (12) and (13) and are then substituted into (14) or similar equation for another structure. The calculation loop is then closed by determining the new C_i and C_v values based on the sink changes. Obviously this method is one of numerical iteration. Analytical solutions are only obtained in the event that one allows certain processes to predominate.

Calculation of the void growth rate with temperature points provides a good example of the use of both the point defect balance equations

(12,13) and the void growth rate equation (14). The results of this type of calculation are shown in Figure 3. The first step in this process is to choose sufficient input parameters to define all terms in Equations (12) and (13) except the unknown defect concentrations C_v and C_i . These two quantities are then calculated by simultaneous solution of (12) and (13) and are shown in Figures 4(a) and 5(a) for the alloy of Figure 3. In addition, the thermal equilibrium vacancy concentration C_v^e is also calculated and appears in Figure 6(a). These three concentrations C_i , C_v , and C_v^e are then substituted into (14) to give the instantaneous growth rate of a void of size r . Reference to Figures 4(a), 5(a) and 6(a) demonstrates how the various defect concentrations interact to yield Figure 3. At low temperatures, the growth rate increases with increasing temperature because vacancy mobility is increasing. As the vacancy mobility increases, recombination becomes less likely and, therefore, losses to sinks increase. With less recombination, C_i necessarily increases as shown in Figure 5(a). At the same time the thermal equilibrium concentration C_v^e , Figure 6(a), is growing. The peak region of Figure 3 is reached as C_v^e approaches C_v . Beyond this peak, thermal emission of vacancies continues to reduce the growth rate as the temperature increases.

One of the purposes of this study is to investigate the effects of various solid solution impurity additions on the swelling of a given stainless steel. Many such impurities are known to exhibit interactions with point defects which can be characterized by various binding energies. Tabulations of such binding energies are available (51) and

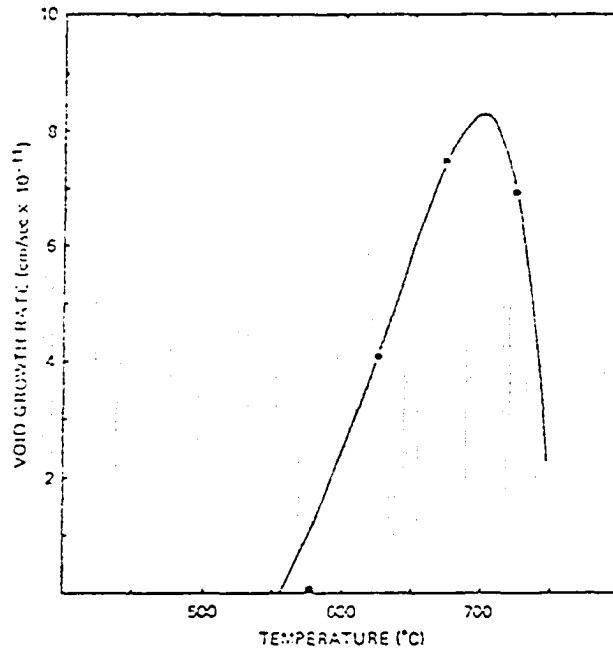


Figure 3. Void growth rate curve fitted to the data of Johnston et al. ((3) Fe-15 Cr-20 Ni alloy.)

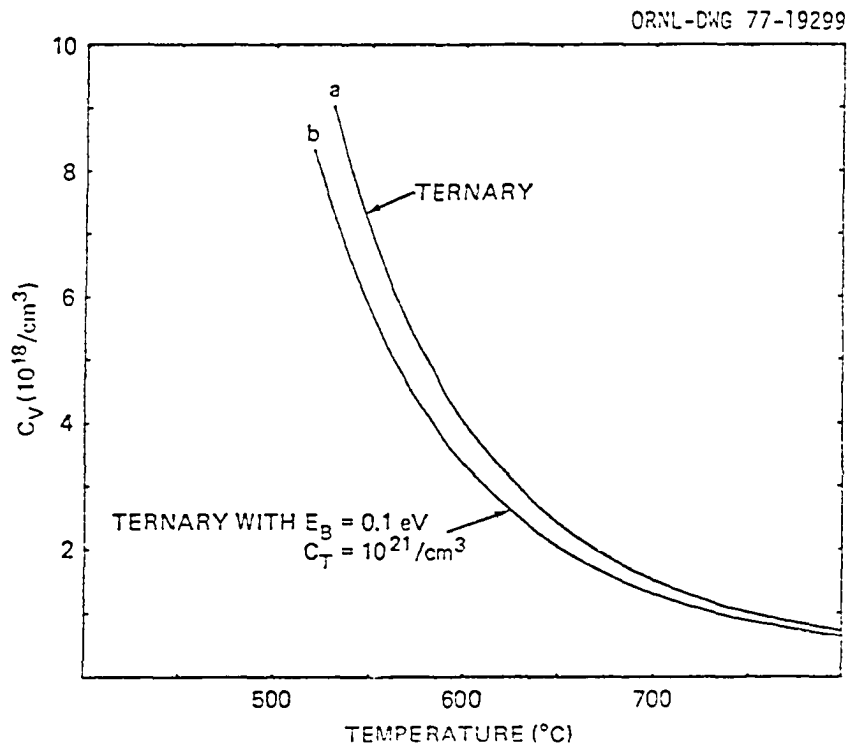


Figure 4. Steady state vacancy concentration as a function of temperature.

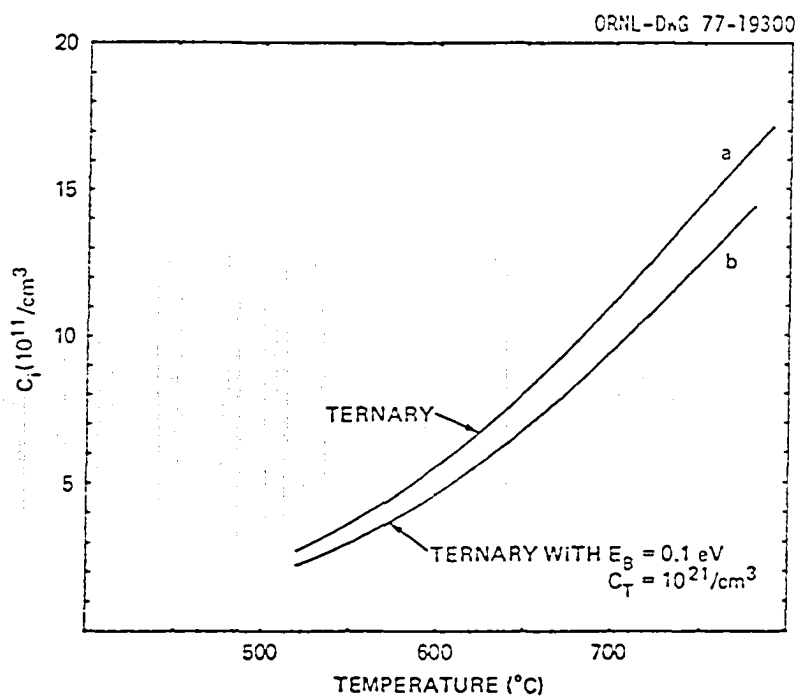


Figure 5. Steady state interstitial concentration as a function of temperature.

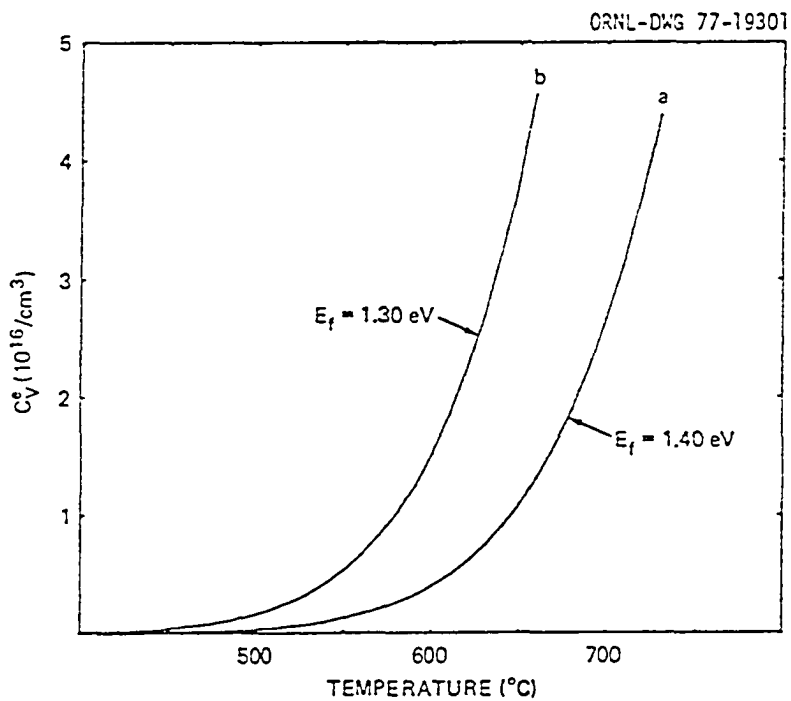


Figure 6. Thermal equilibrium vacancy concentration as a function of temperature.

refinement of measuring techniques continues to be an active area of research. In the realm of growth kinetics, such binding is termed trapping because it effectively removes free defects from solution. Mathematically these trapping effects can be introduced into the growth kinetics framework in a number of ways. Johnson and Lam (52), Smidt and Sprague (53) and Mansur et al. (32) have all treated this problem using slightly different approaches. Here the treatment considered by Mansur will be used to examine the effects of defect trapping on void growth rate. The new point defect balances become:

for free interstitials

$$G_i + C_i^T \tau_i^{-1} - R^F C_i^F C_V^F - R^{FT} C_i^F C_V^T - C_i^F v_i - \sum_j K_i^j C_i^F = 0 ; \quad (18)$$

for trapped interstitials

$$C_i^F v_i - C_i^T \tau_i^{-1} - R^{TF} C_i^T C_V^F = 0 ; \quad (19)$$

for trapped vacancies

$$C_V^F v_V - C_V^T \tau_V^{-1} - R^{FT} C_i^F C_V^T = 0 ; \quad (20)$$

for free vacancies

$$G_V + C_V^T \tau_V^{-1} - R^F C_i^F C_V^F - R^{TF} C_i^T C_V^F - C_V^F v_V - \sum_j K_V^j C_V^F = 0 , \quad (21)$$

where

G = point defect generation rate,

C^T = concentration of trapped defects,

C^F = concentration of free defects,

$R^F = 4\pi r_1(D_i + D_v)$ = recombination coefficient between free vacancies and free interstitials,

$R^{FT} = 4\pi r_2 D_i$ = recombination coefficient between trapped vacancies and free interstitials,

$R^{TF} = 4\pi r_3 D_v$ = recombination coefficient between free vacancies and trapped interstitials,

$\sum_j k_j^j C^F$ = losses of free defects to sinks (voids, dislocations, and grain boundaries),

$\tau = \tau_0 \exp(E_d/kT)$ = lifetime of the defect in the trapped state,

$E_d = E_m + E_b$ where E_m = defect migration energy and E_b - defect binding energy,

$\nu = 4\pi D r_3 C_t$ = defect trapping rate,

C_t = trap concentration,

D = diffusion coefficient of free defect.

One important result of such trapping considerations is to reduce the steady state defect concentration of the defect being trapped. In addition to this reduction is an enhanced recombination resulting from interaction of trapped defects with free ones. The case of vacancy trapping alone provides a good example of how trapping affects point defect concentrations. The necessary defect balances involve Equations (18), (19), and (20) with any terms involving C_1^T removed. The result of such considerations is to alter the steady-state free defect

concentrations C_v and C_i , while C_v^e is left unaltered. These effects for vacancy trapping can be seen by examining Figures 4 and 5, curves a and b, pages 29 and 30. The free vacancy concentration is reduced by the trapping. Since not all trapped vacancies recombine, the fractional reduction in C_i is not the same.

The equations given here present a very abbreviated version of growth calculations. Each individual term is a story in itself; some have been examined in detail. First is the matter of point defect generation rate (54,55). Capture efficiencies have been studied (56-58). The effectiveness of a given sink for point defect absorption could be viewed as limited by diffusion (59) or surface reaction rate (38). Fuel pin data (60) indicate an effect due to stress and this effect has been examined theoretically (61). Effects of gas (62,63) and free surfaces (64-66) have been examined. Free surface considerations are particularly important as they relate to ion produced damage. Effects of solute segregation have been treated (52,67-69). There is concern that solute additions found to reduce swelling may segregate losing their effectiveness at high neutron doses (68).

Reactor grade stainless steel presents a complex system. This system consists of various microstructural features which are forming, evolving, and interacting with one another as the irradiation progresses. Many of these component structures have been examined and simple descriptive expressions proposed. A number of interaction effects have also been parameterized. There have also been efforts to include these various microstructural descriptors together with the appropriate boundary

conditions, and to allow the microstructure to evolve numerically (70-72). These calculations require a number of materials parameter inputs (dislocation densities, etc.). Most often such information is not available and assumptions must be made. Predictions have been confined to restrictive cases. Calculations of growth kinetics can be useful in checking the accuracy of other aspects of radiation damage theory and in suggesting useful experiments.

Similitude of In-Reactor Behavior by Ion Bombardment

In the development of alloys for use in fast breeder reactors, one would like to use data generated under fast neutron irradiation conditions closely approximating a commercial LMFBR. The long duration of in-reactor experiments, facility limitations and reasonable time constraints will not permit this. In fact, mere confirmation of the acceptability of an alloy would take three years irradiation plus the time to prepare and then examine the irradiated samples. The need for similitude of neutron damage in the LMFBR environment is real.

Irradiation with high energy ions was first used to simulate high temperature neutron damage in 1969 by Nelson and Mazey (73). Since these initial experiments, a wide variety of ions and energies have been used. Voids have been observed in reactor steels subjected to ion irradiation. High energy ions are much more effective than neutrons in producing displacements. This fact, coupled with the beam intensities available using particle accelerators, greatly reduces the time required to reach a given displacement level. Ion bombardment can result in

displacement rates four orders of magnitude greater than in fast reactors. This time compression together with the ability to control closely the material environment makes the technique attractive. To be truly useful for reactor design purposes one needs to know that set of ion-irradiation parameters that will conservatively approximate the in-reactor case. An exact transformation may not be possible. Nevertheless, there appears to be qualitative agreement between ion and neutron irradiation results. Examples of this agreement include the increase in swelling incubation period produced by cold work (74,75), the enhancement and suppression of swelling by chromium (3) and nickel (3), respectively, in Fe-Cr-Ni alloys, the reduction in swelling produced by elements such as titanium and silicon in both simple and complex alloys (76), and the reduction in swelling which occurs in commercial alloys as the nickel content is increased (77). More specifically Johnston has compared the swellings of the same Fe-Ni-Cr ternary steels under neutron and nickel ion irradiation (78) as shown in Figures 7 and 8. The comparison is complicated by an apparent higher temperature for peak swelling for ion bombardment. Figure 9 illustrates this temperature shift for type 316 stainless steel. Such observations have prompted questions concerning the nature of the correlation (79). A recent workshop reviewed the status of ion simulation and its future role (80).

The national LMFBR alloy development program has embarked on a series of so-called Unified Simulation Program experiments designed to assess the equivalence of neutron and ion irradiation effects. A set of

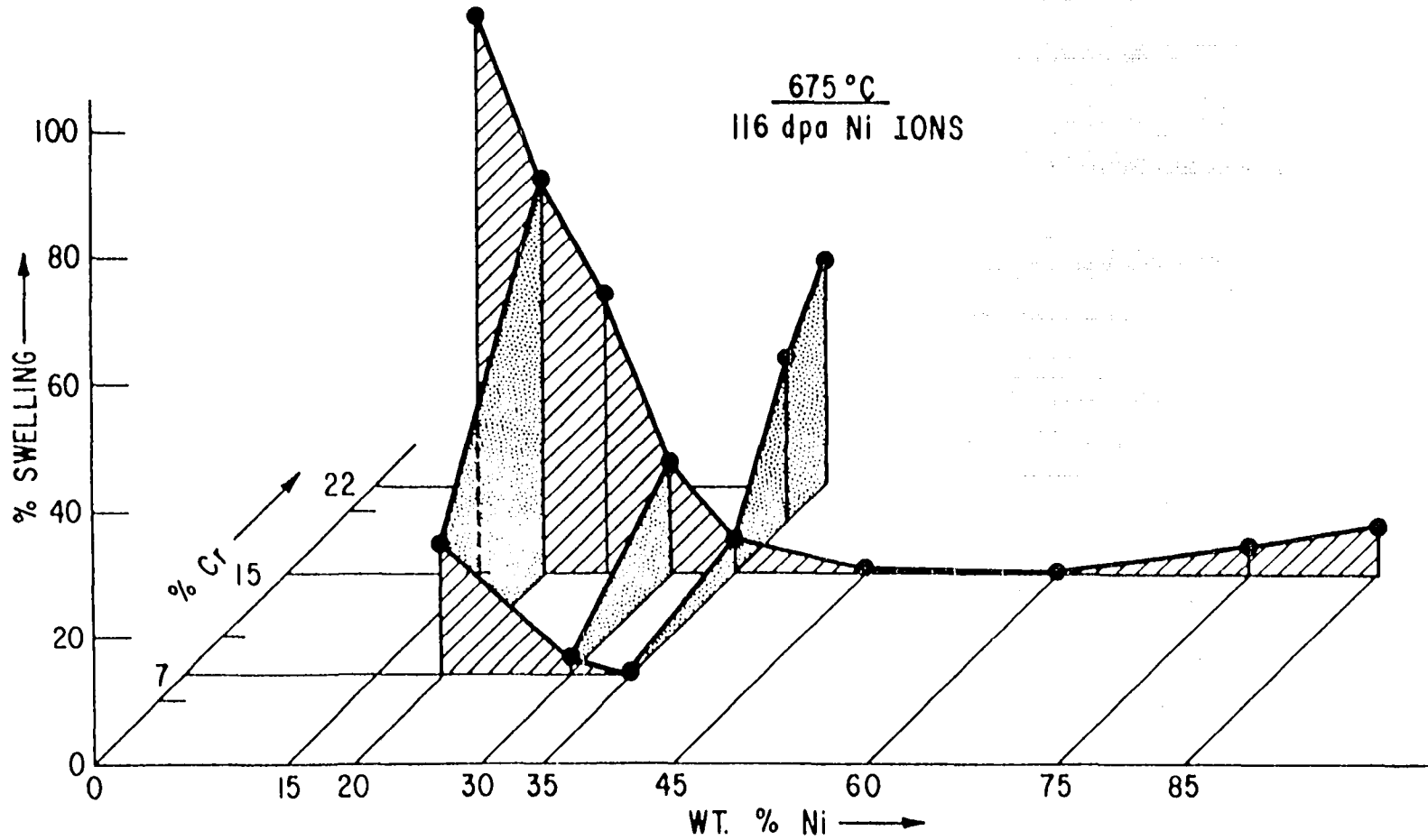


Figure 7. Variation of swelling with Cr and Ni content for Ni ion irradiation (3).

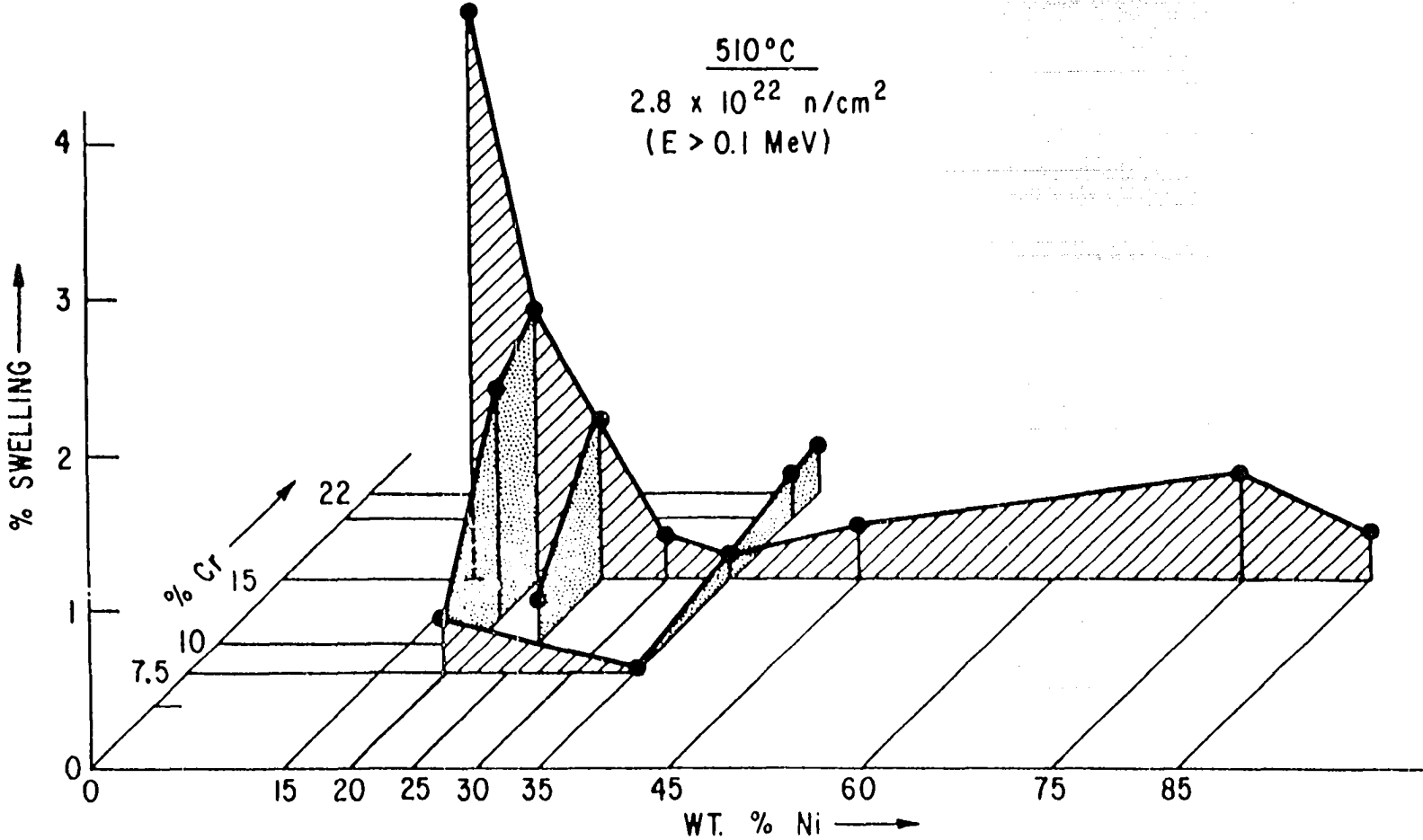


Figure 8. Variation of swelling with Cr and Ni content for neutron irradiation (3).

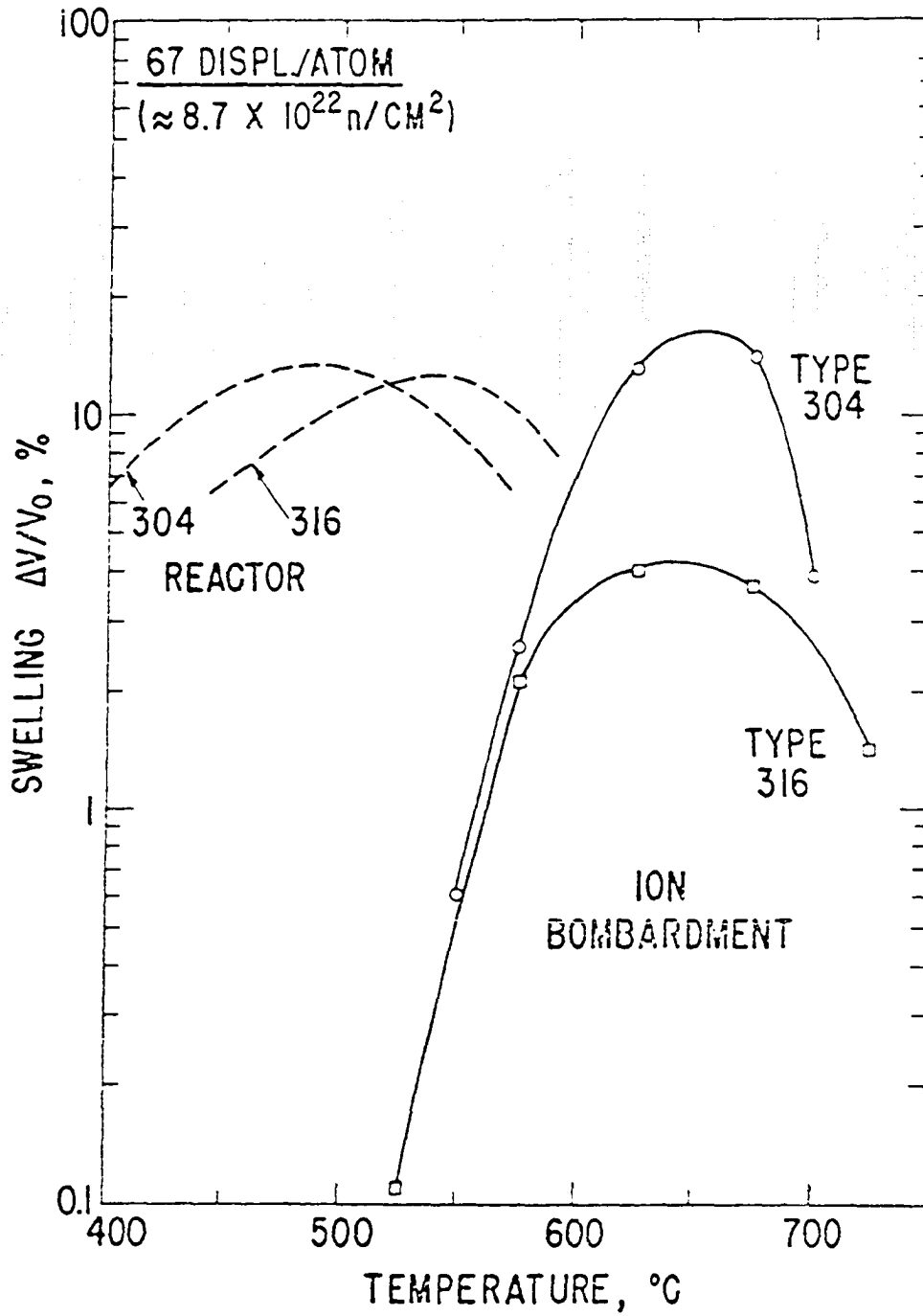


Figure 9. Temperature dependence of swelling in nickel ion bombardment and neutron irradiated types 304 and 316 stainless steels (3).

experiments seeks to compare the swelling and evolved microstructure in ion and neutron irradiated materials. If equivalence is not observed, the possibility of preconditioning to a desired microstructure in the reactor and then producing high dose behavior using ions will be examined. In the event of no equivalence, or perhaps more correctly an inability to recognize such, the conservative overestimate criterion could be exhibited. In this section some of the basic concepts and subtleties of ion bombardment effects and their similitude of neutron irradiation effects will be considered.

It should be noted that care has been exercised not to apply the term simulation in this section. That term refers to imitation and is inappropriate to the techniques being discussed. Since both irradiation time, irradiation temperature and damage rate are different for neutron and ion irradiation the engineering term similitude is more applicable.

A good point of embarkation is a discussion of the nature of displacement damage produced by various particles. Figure 10 shows the number of displacements per atom (dpa) as a function of depth from a free surface for various particles. Calculation of dpa involves determination of deposited energy; then, by assuming some displacement model this deposited energy is converted to displacements. The method is numerical and has been treated elsewhere (80,81). Examination of Figure 10 reveals obvious differences between neutron and ion damage. First is the spatial dependence. Neutrons create displacements uniformly throughout the material while ion damage is confined to a narrow band near the surface. This effect arises naturally from the basic differences in the way

Y-117804

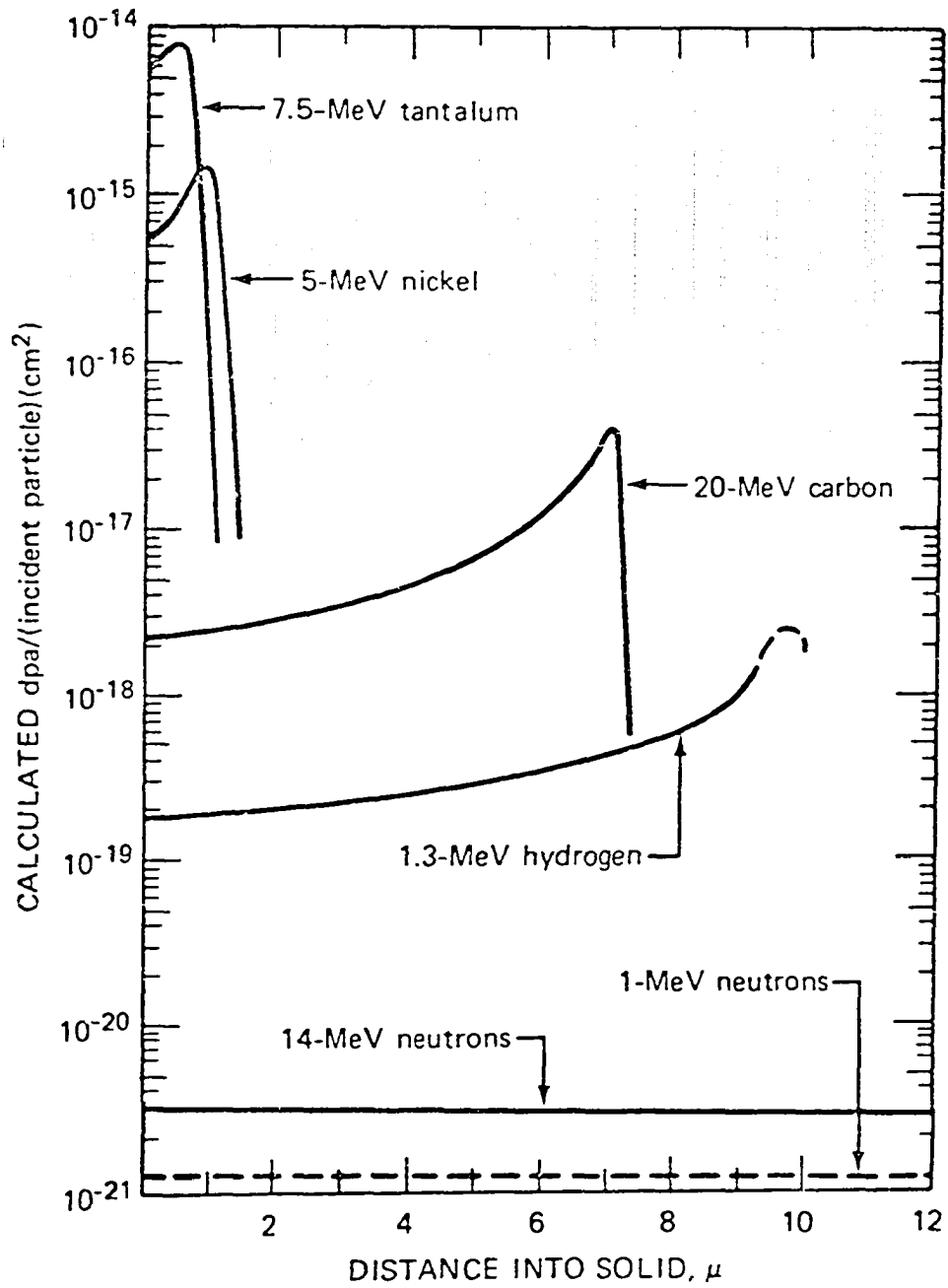


Figure 10. Displacement effectiveness for various energetic particles in nickel.

neutrons and heavy ions interact with matter. Neutrons by virtue of structure and lack of charge interact with the field of the nucleus over the complete energy range of interest to the LMFBR, i.e., the fission neutron energy distribution. Since cross sections for nuclear interaction are low for fission neutrons the mean free path of neutrons in most materials is long. Heavy ions (Ni, for example) consist of a nucleus together with nearly a full complement of electrons. In this case then, electronic interactions are the major interaction mode until the ion reaches a critical energy (≈ 100 keV for Ni). Below this critical energy, nuclear scattering predominates and a series of PKA's is produced within the last one-third of the primary particle range. This raises an important question concerning the possible spatial overlap of the cascades produced. The size of these cascades is unfortunately unknown. Arguments have been advanced (82) that for bombarding energies greater than ~ 100 keV the size of the cascades produced is always smaller than the mean free path between recoils. Nickel ion irradiations in steels will correspond to this boundary value. Thus, even if overlap of displacement cascades does not occur, their close proximity could result in a different short term annealing behavior. The net effect could be early formation of interstitial loops and suppression of free defects. It is important to realize that cascade calculations are presently inadequate, so much of this is hypothetical. Then, of course, it is not assured that such early clustering would change microscopically observable swelling.

Referring again to Figure 10 one can easily identify the second basic difference between neutron and heavy-ion irradiations. For the ions, a gradient in displacement density exists. Displacements can vary over the bombarding particle range by a factor of 4 for 5 MeV Ni ions and 70 for 20 MeV C ions. Such displacement gradients have been examined by Garner and Guthrie (83) and Johnston et al. (84). They conclude that this effect shifts the temperature dependence along the range. Both studies indicate that at low temperatures swelling will be confined to volumes near the surface and near the end of the particle range with no swelling expected in the peak damage range. Johnston (84) cites instances where such a swelling profile was observed.

Comparison of ion-bombardment and neutron-irradiation results is further complicated by the fact that the ion bombardment produces damage in close proximity to a free surface. As already mentioned swelling requires the development of a dislocation structure. Ion bombardment of annealed pure ternary alloys may result in low values of swelling due to dislocation escape to the surface. Since free surfaces or grain boundaries can act as sinks for point defects, there is the possibility that net flow to these sinks can result in compositional changes. With swelling so sensitive to composition, such effects give rise to anomalous swelling near the surface. By using Auger spectroscopy and TEM Johnston (84) has observed both excess swelling and compositional variations at depths of 500 nm from the bombardment surface. The conclusion to be reached here is that the bombarding particle must have

sufficient energy to produce peak damage at greater depths. For nickel ions this minimum energy is near 2 MeV.

As an energetic ion comes to rest within the bombarded solid the result is the implantation of an extra interstitial, and Brailsford and Mansur (85) have examined the effect of implanted interstitials on swelling during self-ion bombardment. Their void growth calculations show that deposited interstitials decrease swelling at all temperatures with the effect being most pronounced below the peak swelling temperature. The fractional swelling reduction calculated is 0.24 at 400°C and 0.03 at 600°C. This effect is important when comparing swelling vs. temperature profiles for ion and neutron irradiations. The neutron profile has a long low-temperature tail while the ion profile rises sharply at low temperature.

Another important difference between ion and neutron irradiations is the formation of transmutation products. Under neutron irradiation various (n,p) , (n,α) and (n,γ) reactions introduce chemically different species into the material undergoing irradiation. Helium, produced by (n,α) reactions with high energy neutrons, is important in nucleating voids. Ion irradiations do not produce such transmutation products which makes it necessary that they be injected prior to or during the bombardment. Whether either of these methods is equivalent to the neutron irradiation remains an open question.

While a wide variety of ions has been used for neutron damage, the use of some ions is questionable on intuitive grounds. The use of H^+ , He, O, N or other gases is highly suspect since one may, in fact, be

injecting nucleation or trapping sites. Injection of carbon ions may induce carbide precipitation that would not otherwise occur. As a precautionary measure, until this problem has been examined in detail, ions should be considered only if they correspond to an element which comprises a large portion of the chemical makeup of the alloy.

As these remarks indicate, the exact nature of the relationship between neutron and ion irradiations is unknown. However, there is much qualitative agreement to recommend ion bombardment as a similitude of in-reactor behavior. This technique can be exploited to maximum advantage by keeping as many variables controlled as possible. Ion irradiation seems particularly well-suited for studying the effects of systematic variations of metallurgical variables on materials behavior in radiation environments.

Control of Void Swelling Through the Use of Metallurgical Variables

Since the discovery of void swelling by Cawthorne and Fulton in 1967, experiments have identified several metallurgical variables that suppress void swelling. In this section these variables will be presented along with possible reasons for their effectiveness. The discussion will be confined to Fe-Cr-Ni alloys.

Perhaps the most significant variable is major alloy composition. Johnston et al. (86) examined a series of Fe-Cr-Ni alloys using 5 MeV Ni ions and found that large differences in swelling resulted from changes in Ni and Cr contents. These results are summarized in Figure 7, page 36.

Care should be taken when interpreting these results since they apply to a single temperature, and it is known that changes in alloy composition can cause changes in the temperature dependence of swelling as shown in Figure 11. More properly, one should plot % swelling at the peak swelling temperature vs. composition. Once this is done nickel and chromium content are still found to have pronounced effects on the magnitude of swelling. Recent data (84) for low neutron fluences (2×10^{22} n/cm²) have confirmed these general trends.

Void swelling in stainless steels has also been found to be sensitive to minor impurities. The addition of titanium (87) and niobium (88) to austenitic steel results in less swelling. Bloom and Stiegler (87) added 0.2 wt. % Ti to type 304L and observed a fourfold decrease in swelling. Leitnaker et al. (89) examined both commercial type 316 and a special high purity steel (HPS) heat containing low C, N, Si, S, and Mn. Their data show enhanced swelling in the HPS alloy at low neutron fluences (2×10^{22} n/cm²). The additions Si, P, Mn, Mo, Co, and C to type 316 have been observed by Bates (90) to result in swelling suppression at low neutron fluences. Bloom et al. (76) have added Si, Ti, V, W, Zr, and Cu to type 316 creating an alloy (LS1) that resists swelling at high nickel ion bombardment doses (600 dpa, E. Kenik, ORNL 1977). Johnston et al. (86) has used 5 MeV Ni ions to examine the effects of impurities on the swelling of a pure ternary alloy (Figure 12). Zr, Ti, Nb, and Si were found to be potent swelling suppressants. Aluminum, molybdenum, carbon, boron, and phosphorus additions resulted in alloys with greater swelling than the ternary alloy. In addition to effecting

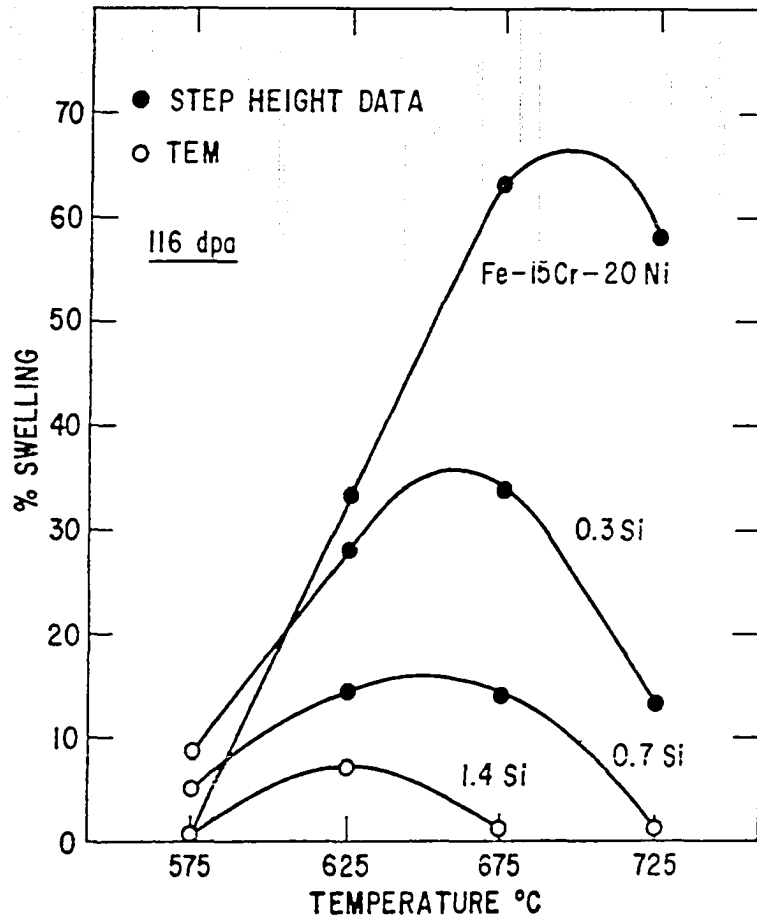


Figure 11. Temperature dependence of swelling with and without minor additions (86).

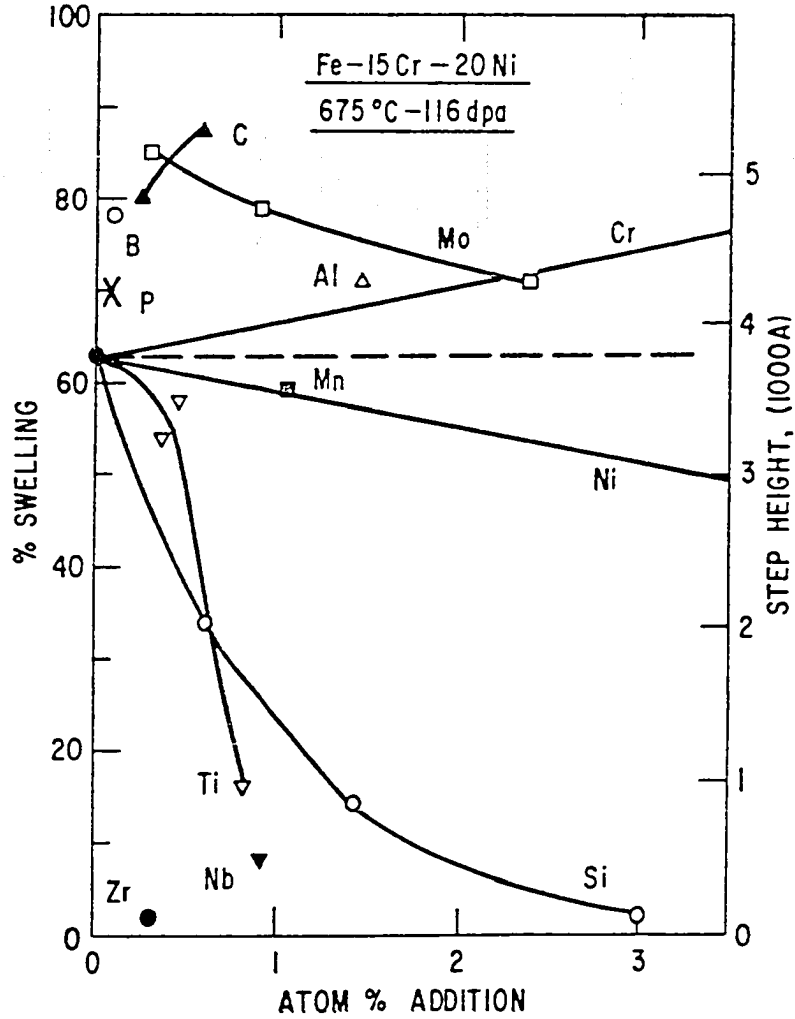


Figure 12. Effects of individual additions on the swelling of a base alloy. (Note step height refers to measurements made by surface profilometry (86).)

a change in the magnitude of swelling at a given temperature, the minor additions were found to change the temperature dependence of swelling. Johnston found that the swelling of an alloy created by adding impurities to a pure ternary could be predicted using the expression:

$$\Delta V (C_1 + C_2 + \dots) = \Delta V(0) \exp \left(- \sum_i \alpha_i C_i \right) \quad (22)$$

where

$\Delta V(0)$ = swelling of ternary alloy,

C_i = concentration of impurity i ,

α_i = empirically determined constant for impurity i , and

$\Delta V(C_1 + C_2 + \dots)$ = swelling of composite alloy.

When silicon and titanium were added, the resulting swelling was found to be lower than predicted by Equation (22). This has been considered as evidence for an interaction which Johnston has termed a synergism. However, the only combined addition studied was silicon plus titanium. Examination of other combinations might reveal a simple inability of Equation (22) to calculate correctly the swelling for multiple impurity alloys. It should be noted that all data indicating swelling suppression by impurities in austenitic steels are the result of either ion bombardment or low fluence neutron irradiation. Questions have been raised about the persistence of this effect to higher fluences (68). It has been suggested (68) that such impurities will segregate at higher neutron fluences resulting in enhanced swelling.

Even if impurity induced swelling suppression does not persist out to higher fluences, its occurrence at low neutron fluence needs to be

explained. To suppress swelling, impurities must alter kinetics so that recombination is enhanced and/or clustering of like defects is inhibited. There are many ways this can occur. Interactions among impurity atoms, self-interstitials and/or vacancies can alter the thermal equilibrium concentrations of defects. This would have the effect of shifting the temperature dependence of void swelling. Basic interactions between point defects and impurities can result in changes in the formation and migration energies for defects which can affect both the magnitude and temperature dependence of swelling.

The introduction of impurities could interfere with the dislocation climb process. Mechanisms by which this could occur include a reduction in defect absorption resulting from jog poisoning or an inhibition of the free movement of jogs. Such interaction could also result in loops and voids being coated with the impurity. E. Kenik (Oak Ridge National Laboratory, private communication 1977) has observed silicon coated loops in modified type 316 after irradiation with 4 MeV Ni ions. He further compared the 1% Si modified type 316 with unmodified type 316 upon irradiation up to displacement levels of 600 dpa. The loops in the silicon modified alloy remained faulted, preventing dislocation network development. In addition to the absence of voids, a number of fine precipitates were observed. Chemical analysis showed that the faulted loops are coated with silicon. One might reason that some impurities can alter the stacking fault energy so as to inhibit unfauling of the loops. Farrell et al. (41) has also observed silicon coated voids in neutron irradiated aluminum. Interaction between impurities

and point defects could result in changes in their mobilities and result in enhanced recombination. With dislocation climb impeded, the system's bias for interstitials would be greatly reduced. Indeed, many explanations are possible, and each impurity may influence swelling kinetics or void nucleation differently. Although some impurities appear to be potent swelling suppressors, the reasons why are at present not understood.

Aside from compositional changes, void swelling has been found sensitive to various structural variables. Cold work is one such variable. The reasoning is that a high dislocation density acts as the dominant sink for vacancies and interstitials. Experimental results for neutron irradiated type 316 show that this can be a large effect at fluences as high as 1.3×10^{23} n/cm². Such effects are, of course, limited in temperature range since above 650°C cold work in type 316 readily undergoes recovery. Optimum amount of cold work appears to be in the range 20-30%.

The presence of coherent precipitates can make an alloy resistant to swelling. Carpenter and Ogle (45) have observed such effects for neutron irradiated aluminum-copper alloys. By processing the alloys to produce certain metastable precipitate particles a highly swelling resistant alloy was produced. The amount of swelling suppression was a function of precipitate size distribution and type. These authors explain such suppression in terms of the coherent precipitate mechanism discussed by Bullough and Perrin (46). This mechanism involves trapping at point defects and enhanced recombination.

Other factors are known to influence swelling in stainless steels. Prior heat treating has its effect (91). Aged materials often swell more than annealed ones. This fact is not surprising since aging is expected to change the alloy composition. Grain size can be important provided it is kept below 1 μm (92). For such small grain sizes grain boundaries can become the dominant sink for point defects.

STRENGTHENING

Solid Solution Strengthening

The strength of a metal is related to the critical stress required to produce plastic deformation. Plastic deformation, however, is a macroscopic observable resulting from microscopic dislocation motion. Obstacles that dislocations must either glide through or climb or bow around such as impurities, precipitates, voids, and other dislocations give rise to a higher strength or flow stress. Each type of obstacle can be quantitatively characterized by its dispersion and its interaction with glide dislocations. In this section some of the basic concepts related to strengthening by solid solution alloying will briefly be considered. Several comprehensive reviews (93-95) exist.

To illustrate the concepts involved consider a lone obstacle in the slip plane of a single dislocation. The situation is shown schematically in Figure 13 where a dislocation segment AB and obstacle O are shown.

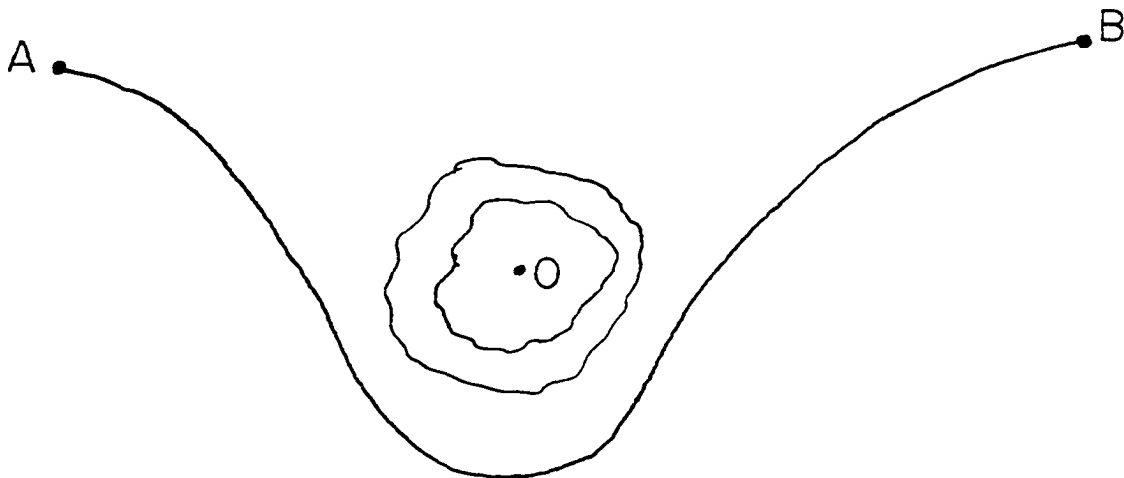


Figure 13. Schematic of dislocation segment and obstacle.

The equilibrium shape of segment AB represented by ϕ' represents a balance between an externally applied force F_e and a spatially dependent force F_o . This can be represented mathematically by

$$\int_A^B \frac{F_o(\ell)}{E_\ell} b d\ell - \int_A^B \frac{F_e b}{E_\ell} d\ell = \phi' \quad (23)$$

where ℓ is a parameter along AB and E_ℓ is the dislocation line energy. This expression simply states that the shape a dislocation assumes is a difference between two integrated curvatures. The first term represents the integrated dislocation curvature resulting from the force field of the obstacle [$F_o(\ell)$] while the second represents that caused by an externally applied force (F_e). The ϕ' angle can be considered as a measure of the strength of different obstacles for a given applied force. The expression given here is applicable in the most general case; solid solution impurities can be treated as a limiting case. As an approximation, one considers the impurity to be a point obstacle whose presence can be represented by a spherically symmetric force field. The total force in the normal direction (F_{tot}) must be balanced in magnitude by the normal components of line energy from AC and CB. The inherent symmetry makes these two components equal. This gives

$$F_{tot} = 2E_\ell \cos\left(\frac{\pi - \phi'}{2}\right) . \quad (24)$$

One can similarly define a critical force F_{crit} and critical orientation

ϕ'_{crit} at which the dislocation overcomes the obstacle. For $\phi'_{\text{crit}} < \pi$ the dislocations can shear through 0 while for $\phi'_{\text{crit}} \geq \pi$ the dislocation closes on itself moving ahead but leaving a loop around the obstacle. This latter Orowan process places an upper limit on F_{tot} for strengthening since no additional strengthening is gained for $F_{\text{tot}} > F_{\text{crit}}$. In other words, once the obstacle is strong enough to require slip by the Orowan mechanism no additional gain in alloy strength results from increased obstacle strength. The treatment afforded by Equation (2) has been extended by incorporating explicitly the functional dependence of E_2 and F_{tot} (95,96).

The foregoing treatment represents a phenomenological approach to solid solution strengthening. One might naturally inquire as to the physical origin of such obstacle strengths. Both elastic and electrostatic interactions have been considered. Substitutional impurities can produce either a lattice dilatation or contraction resulting in elastic stresses. The nature of this effect was first examined by Mott and Nabarro (97) and has been subjected to increasingly more detailed treatments (98). A "misfitting" atom will experience an interaction with a dislocation characterized by some binding energy. For example, an atom producing an increase in lattice parameter will be attracted to regions under dilatation. A number of authors have attempted (with varying degrees of success) to fit experimental solid solution strengthening data to this "size" effect. The parameter generally used is

$$\epsilon_a = \frac{da/a}{dC} \quad (25)$$

where a is the lattice parameter and C the solute concentration.

Impurities can also produce local changes in elastic constants giving rise to another type of elastic interaction (99-102). Depending upon whether the region is "harder" or "softer" than the bulk, a dislocation will experience a repulsive or attractive force from the obstacle. This so-called modulus effect is generally regarded to be much smaller in magnitude than the corresponding size interaction. A dimensionless parameter used to describe this effect is

$$\epsilon_m = \frac{dm/m}{dC} \quad (26)$$

where m represents either the shear modulus (G) or Young's modulus (E). Attempts have been made to fit experimental strengthening data using both E and G . Fleischer (103) has argued that while neither ϵ_G nor ϵ_a can singly fit the experimental data, reasonable agreement can be obtained using

$$\frac{d\tau}{dC} \propto |\epsilon_G - \alpha\epsilon_a| \quad (27)$$

where τ is the flow stress and α is a constant. Saxl (104) has pointed out a number of specific errors in the Fleischer treatment that alter the allowable α values. The electrostatic interaction is only mentioned here because it is expected to be most important in ionic crystals.

At this point, all the remarks have been confined to individual obstacle strengths. Clearly the spatial distribution of obstacles should have some bearing on strengthening. One useful way to characterize a given array is with an effective obstacle spacing (ℓ_{eff}). One expects intuitively that the strength should vary inversely with ℓ_{eff} . In any case, the macroscopic flow stress (τ) will be given by

$$\tau = \frac{Gb}{\ell_{\text{eff}}} f(F_{\text{tot}}) . \quad (28)$$

The problem of calculating ℓ_{eff} for a random array of point obstacles is necessarily a statistical one and has been examined by several authors. Pinning of flux lines in superconductors provides a good analogy to solid solution strengthening. Labusch (105) has used this analogy to refine the statistical theory of solution hardening. More recently Nabarro (98) has utilized a much more intuitive framework developed by Lowell for pinning centers in superconductors. Since ℓ_{eff} is not an easy parameter to measure one would like to have its value as a function of measurable quantities. Concentration of solute is one such quantity. As the solute concentration (C) increases one expects the spacing between obstacles to decrease. Realizing that some clustering of solute atoms is possible the general case can be represented by

$$\tau \propto c^n . \quad (29)$$

The previously mentioned treatments represent different limiting cases and result in different n values. Labusch (105) calculates $n = 2/3$

while Friedel (106), and Mott and Nabarro (97) give the value 1/2. This difference in n value results from the former treatment allowing for statistical clustering of solute. Actually above $c = 10^{-3}$ it is probably unlikely that solute atoms can be considered as dispersed singly throughout the matrix.

A real alloy is likely to contain several solid solution impurities giving rise to a distribution of obstacle strengths. Naturally the question arises as to how these different contributions should be combined to give the composite flow stress. One might simply reason

$$\tau_{\text{tot}} = \sum_i \tau_i \cdot \quad (30)$$

Koppenaar and Kuhlmann-Wilsdorf (107) have successfully applied a relation of the form

$$\tau_{\text{tot}}^2 = \sum_i \tau_i^2 \cdot \quad (31)$$

Other possibilities include

$$\tau_{\text{total}} = \sum_i \tau_i f_i \quad (32)$$

where f_i represents the fraction of obstacles of type i . All methods seem plagued with difficulties when the situation to be analyzed contains many weak obstacles in the presence of a few very strong ones.

Another important aspect of strengthening is its temperature dependence. This dependence most likely results from the temperature sensitivity of elastic constants and the onset, with increasing

temperature, of alternative deformation mechanisms. Flow stress is generally found to decrease with increasing temperature. The decrease in modulus with increasing temperature certainly contributes to this fall off in flow stress. In steels like 316 and 304 vacancies become mobile at temperatures between 550 and 600°C. Above that temperature range one would expect the onset of deformation processes that involve a flux of vacancy to dislocations. The most likely candidate in austenitic steels is dislocation climb. A detailed description of dislocation climb can be found in any text on dislocations. Basically the process involves motion of the dislocation out of its slip plane by the absorption or loss of vacancies (or interstitials). Calculations for climb around an obstacle of given shape have been performed (95). While the exact formulation depends on geometry, the strain rate $\dot{\epsilon}$ can generally be represented by

$$\dot{\epsilon} \propto CD_v \quad (33)$$

where C gives the concentration of vacancies near the dislocation and D_v is their associated diffusion coefficient. Although the interdependence of stress, strain rate, temperature, and deformation mechanism is complex, Ashby (108) has devised a graphical method for representing them simultaneously. Figure 14 is an example of a so-called deformation map for nickel. Regions of predominance for various mechanisms are indicated. Construction of such diagrams begins with constitutive equations of the form $\dot{\epsilon} = f(\sigma, T)$ for each deformation mechanism. These various equations are equated to establish boundaries

PLEASE NOTE:

Print on some pages is small
and indistinct. Filmed in the
best possible way.

UNIVERSITY MICROFILMS.

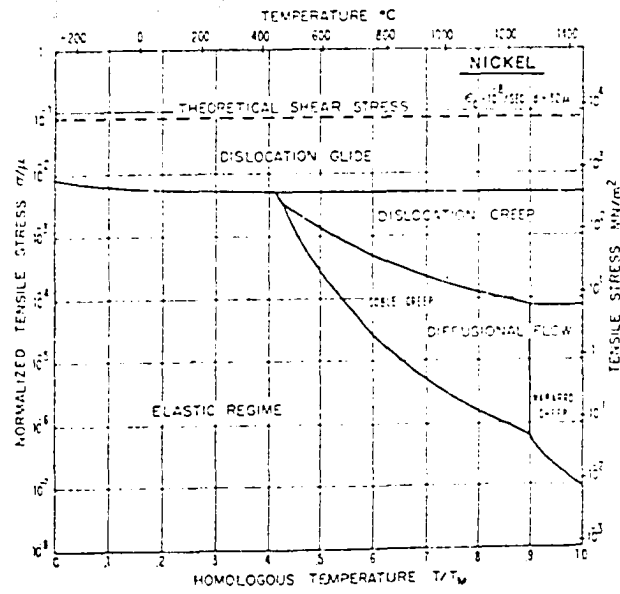


Figure 14. Deformation map for nickel (108).

where different mechanisms produce equal contributions to the total strain rate. The real usefulness of this approach is that it provides a good catalogue of deformation mechanisms.

Hardness

The hardness of a material is defined as its resistance to local indentation. In practice, hardness is determined by releasing a load onto a material surface using a hard punch of specified geometry. Although a number of shapes are available, the one of interest here is the Vickers indenter. This configuration consists of a square pyramid with 136° between faces; and it has the advantage that the resulting impression is geometrically similar regardless of its size. After indentation, the applied load is divided by the surface area of the impression. This calculated quantity is called the diamond pyramid hardness number (DPH). The salient features of the hardness test are ease of specimen preparation and simplicity of measurement. Unfortunately, the physical understanding of hardness has not advanced to a point where it can be used as a quantitative tool in the study of deformation mechanisms. Several correlations have been developed between hardness and other mechanical properties which allow hardness measurements to guide alloy development and to determine heat treatment effects, etc. In principle, since the indentation process involves plastic deformation, one expects some relation between the DPH and flow stress (Y). This relationship has been represented as a proportionality between hardness (H) and (Y) through a so-called constraint factor

(C) (109). In the most general case, it is expected that this relationship would be nonlinear with (C) being a function of strain hardening. Attempts have been made to calculate the functional form of (C) for various indenter shapes (109). One such recent calculation performed by Shaw and DeSalvo (110) used elastic and plastic solutions under a blunt indenter to calculate a value for C of 3.0. This value is expected to vary for real indenters which only approximate this blunt condition.

From the applications standpoint, the temperature dependence of hardness is more useful than a single value at some given temperature. Comprehensive reviews concerning the temperature dependence of hardness do exist (111,112). Most of the work, to date, has involved the empirical fitting of experimentally determined hot hardness values; there are as many equations as data sets. However, these expressions generally fall into the three categories defined by the following expressions:

$$\text{Log } H = A + BT \quad (34)$$

and

$$H = A + BT \quad (35)$$

and

$$H = A + BT^n . \quad (36)$$

Unfortunately, this purely empirical data analysis technique precludes understanding based on physical processes. Equations of the above types are generally not applicable over a wide temperature range. This

difficulty in fitting the data is usually ascribed to a change in deformation mechanism and is best seen by examining a typical hot hardness curve. Figure 54 represents a typical hardness vs. temperature profile in the sense that its shape is observed in most steels. Many metals show a change in slope near $0.5 T_m$.

Much of the interest in hardness stems from a desire to use it as an indication of other mechanical properties. There have been a number of such correlations. Yield stress has been correlated with hardness and nomographs exist for determining one from the other (113). Various correlations exist between creep rate and hardness (114-116). Experimental work at elevated temperatures has resulted in a hardness vs. ultimate tensile strength (UTS) correlation over a large temperature range (4,117). More recently Moteff et al. (4) have observed for type 304L steel that the UTS and hardness have very similar temperature dependences. This was expressed in a correlation of the form

$$H = 3 \left(\frac{n}{0.217} \right)^{-n} \sigma \quad (37)$$

where

H = hardness,

σ = ultimate tensile strength,

n = strain hardening coefficient.

This expression is originally due to Tabor (118) and is basically empirical in nature. This empirical correlation approach does not insure that there is a physical relationship between hardness and any of

these properties. Some early work examined the region beneath the hardness indentation and found evidence of dynamic recrystallization. Some more recent work using microscopic examinations appear to have shed some additional light on the physical processes involved in the hardness test (119). In any case, most of the evidence tends to support the contentions that the hardness test is very complex.

Perhaps most noteworthy is the marked similarity between the temperature dependence of hardness and UTS for the stainless steels. In this vein it may be possible to use hardness as a relative indication of how strong a given steel is likely to be.

EXPERIMENTAL PROCEDURES

Specimen Preparation

The base alloy Fe-7.5 Cr-20 Ni and seven master alloys, each containing one of the major alloying elements, W, Mo, Al, Ti, Si or Nb, were melted by International Nickel Corporation and fabricated into one-half inch bar stock. These alloys were then arc melted under helium in various proportions to produce the set of alloys shown in Table 1. Compositions are given in Wt% in Table 1. Besides the major components, other elements were present as impurities in each alloy, as shown in Table 2. The alloys were reduced to sheet stock 0.060-inch thick by hot rolling. Optical metallography was performed on each element series to detect any precipitation from solid solution.

Hardness specimen preparation

Hardness specimens one-inch square were cut from the 0.060-inch thick sheet and drilled to produce a 1/8-inch diameter hole for accommodating a thermocouple. These were annealed for 15 minutes at 1050°C in vacuum, and then polished using 0.5 μm diamond abrasive polishing compound.

Ion bombardment specimens

Tabs of the 0.060-inch thick sheet were annealed 30 minutes at 1150°C in vacuum then cold rolled to a thickness 0.023 inch. A final anneal was conducted in vacuum for 15 minutes at 1050°C. One-inch squares were sheared from this 0.023-inch thick sheet and then slit into

Table 1. Analyses of the Major Alloying Elements in Wt %

Alloy	Fe	Cr	Ni	Mo	W	Al	Ti	Si	Nb	C
M1	Bal	7.4	20.0	2.1						
M2		7.3	20.0	4.0						
M3		6.7	18.0	7.2						
W1		7.7	21.0		2.3					
W2		8.0	21.0		5.5					
W3		7.0	20.0		8.9					
A1		7.8	20.0			0.8				
A2		7.4	21.0			2.2				
A3		8.5	21.0			3.9				
T1		7.3	20.0				0.21			
T2		7.7	21.0				0.39			
T3		7.4	22.0				0.69			
S1		6.9	20.0					0.43		
S2		7.4	19.0					0.86		
S3		6.7	19.0					1.80		
N1		7.2	20.0						0.66	
N2		7.1	19.0						0.88	
N3		6.7	18.0						1.40	
MS1		7.0	20.0	3.8				0.76		
MA1		7.7	20.0	5.0		2.1				
MT1		7.1	19.0	3.9			0.35			
MN1		7.9	20.0	4.4					0.87	
AT1		8.0	21.0			1.4	0.35			
AN1		7.6	21.0			2.1			1.7	
TS1		7.1	18.0				0.20	0.36		
TS2		7.5	19.0				0.53	0.43		
TS3		7.0	19.0				0.37	0.77		
TS4		6.9	18.0				0.20	1.20		
C1		7.4	20.0							.10
MAST		7.4	21.0	1.8		0.9	0.19	0.39		

Table 2. Average Impurity Levels [ppm (Wt.)]

<100	Al	80	Si
5	B	5	Ti
30	Co	10	V
50	Cu	30	W
30	Mn	10	Zr
30	Mo	10	H
20	Nb	30	O
20	P	30	N
15	S	100	C

strips 0.124 ± 0.005 -inch wide. From these strips samples approximately 0.170 inches long were cut with a Buehler low speed diamond wheel.

Each sample was reduced to a thickness of 19 mils by grinding equally on both sides with 600 grit silicon carbide paper, engraved for identification, separated with tantalum sheets, encapsulated in helium and annealed for 15 minutes at 1050°C . A single sample of each alloy together with standards of 316 stainless steel were loaded into each slotted cylinder, Figure 15. A total of 19 samples, with their cut surfaces extending, were accommodated in a single cylindrical holder. A set screw in one side of the cylinder held the stack of chips in place while grinding on 600 grit silicon carbide paper to produce two flat surfaces. A minimum thickness of 5 mils was removed from each side. The stack of chips was then laser welded to the holder on one side to prevent movement as can be seen in Figure 16. Welded holders were mounted in polishing blocks with 3 to 4 mils extended and then polished flush using 600 grit silicon carbide paper. The purpose of removing 8 to 10 mils of material was to insure that the subsequent ion bombardment be done on surfaces that had not been exposed directly to the furnace environment. Surface preparation was done on a Syntron vibratory polishing machine using a succession of abrasives $1 \mu\text{m}$ Al_2O_3 removing 2-3 mils, $0.3 \mu\text{m}$ Al_2O_3 removing more than 2 mils, and $0.5 \mu\text{m}$ diamond removing $0.4 \mu\text{m}$. In order to prevent a kind of corrosion manifesting itself as grain relief, ethylene glycol was used as the medium for the final diamond polish; for the Al_2O_3 polishing steps distilled water was found to be adequate. Ethylene glycol tends to

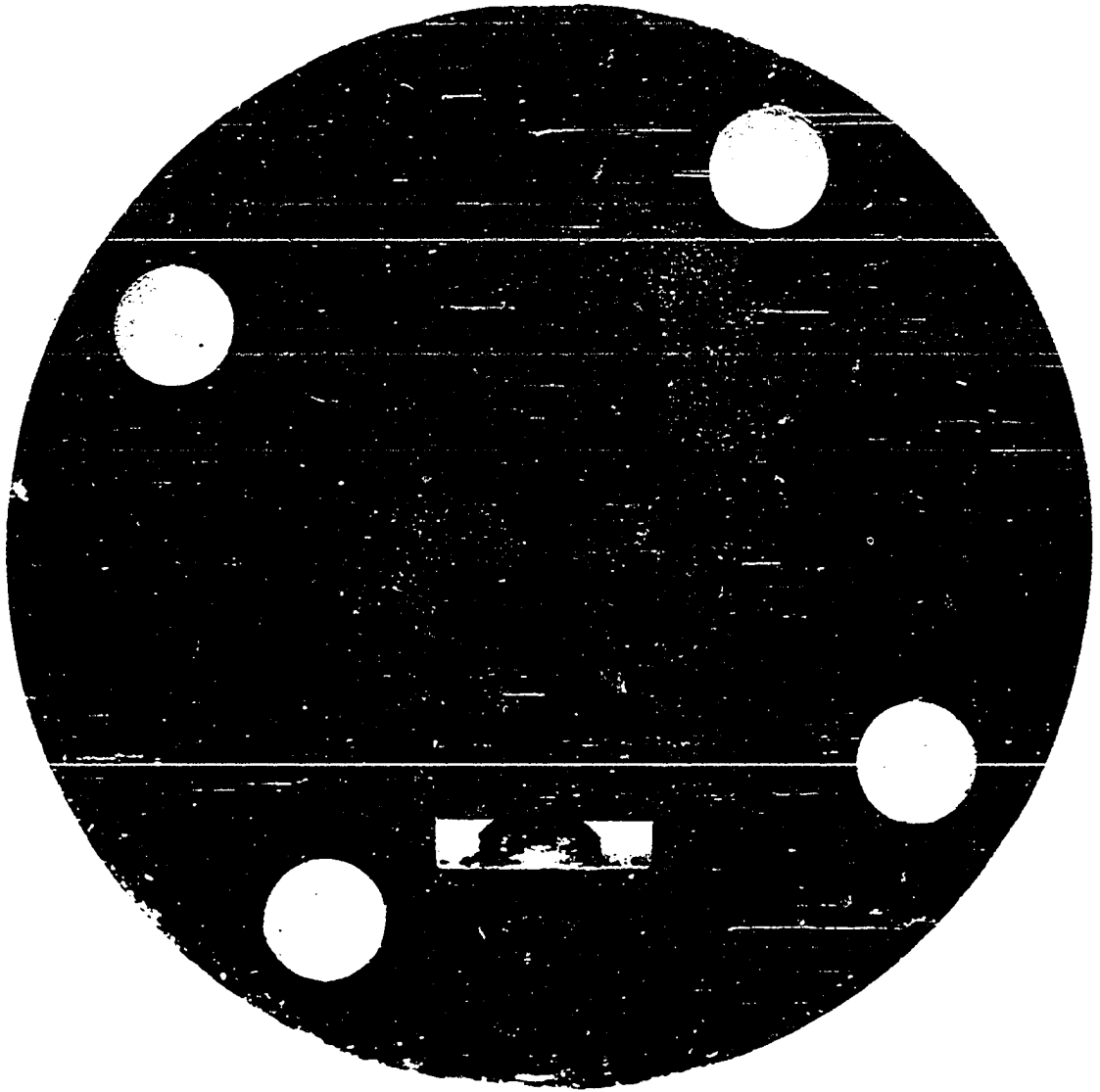


Figure 15. Multiple specimen holder after ion bombardment.
(Dark band is the region that was covered
by mask during ion irradiation.)

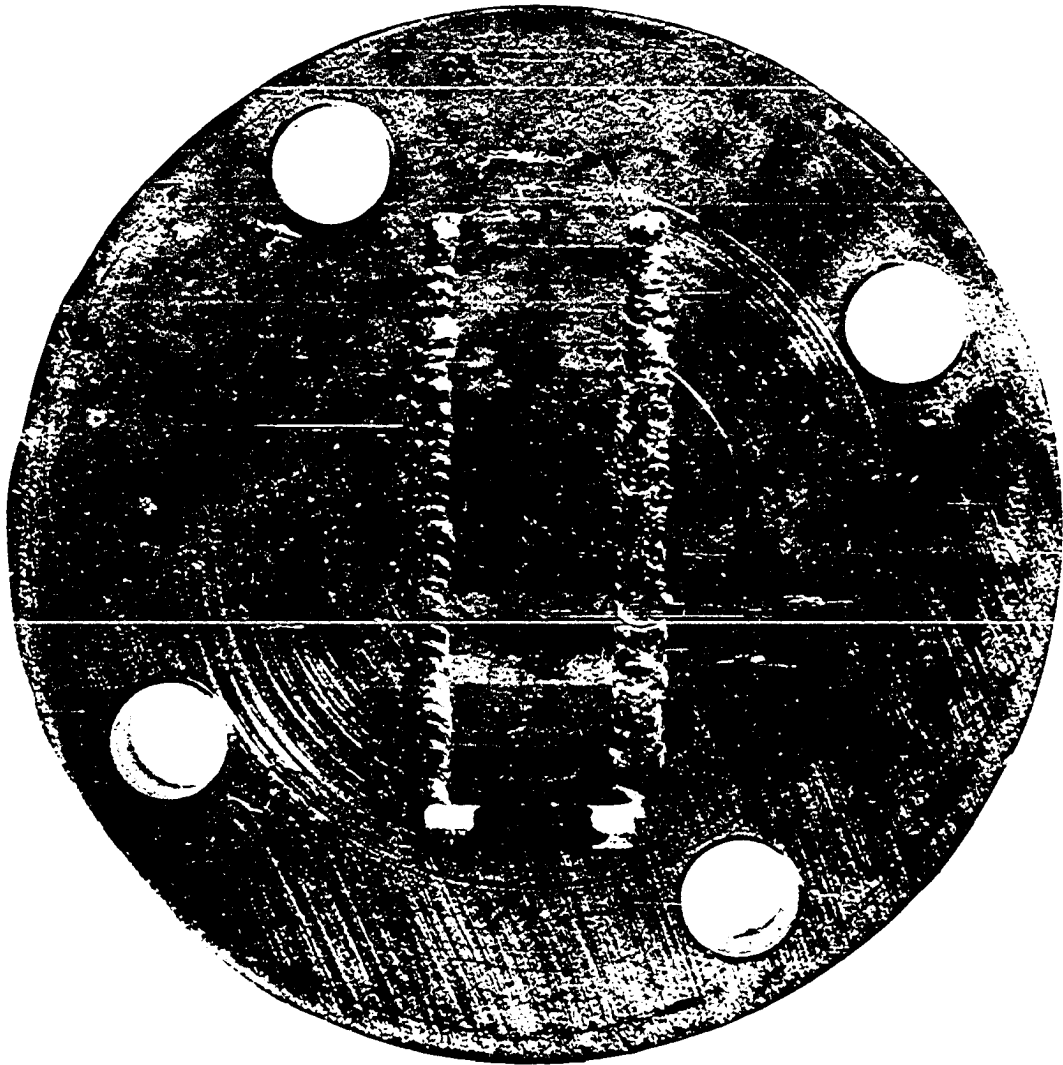


Figure 16. Back of multispecimen holder prior to ion bombardment.
(Both the set screw and laser welds are shown.)

hydrolyze upon exposure to the atmosphere resulting in corrosion thus severely limiting bowl life. Following an ultrasonic cleaning in C_2H_5OH each holder was examined at a magnification of 500X for surface smoothness using a Nomarski interference microscope. Surfaces found to be acceptable by this procedure were examined using a Sloan profilometer and found to be smooth to within 25 \AA . It is worth noting that ultrasonic cleaning in pure H_2O produced a pitting over the surface on a scale of approximately 200 \AA for exposures as short as 10 minutes.

Once an acceptable surface was obtained, it was implanted with He atoms using an arrangement shown in Figure 17. The source consisted of a thin, uniform layer of ^{244}Cm -oxide evaporated on a stainless steel disk. A spacer ring elevated the specimen target from the source preventing scratching of the polished surface. To prevent surface contamination of the target cylinders, they were mounted in rectangular holders and covered with 2 \mu m Al foil. The covering step was conducted in a glove box backfilled with argon and involved gluing the foil with epoxy. Experience has shown that H_2O in the presence of α -radiation from the ^{244}Cm source will produce a rusty looking corrosion layer on both the cylinder and chips. With the foil in place, the target was transferred to another glove box and exposed to the ^{244}Cm source as shown in Figure 17 for a period of 72 hours. The distribution of the implanted helium produced by this technique has been calculated based on the range of the 5.8 MeV α particles emitted (120), and verified by experimental α - α scattering techniques (121). The distribution was

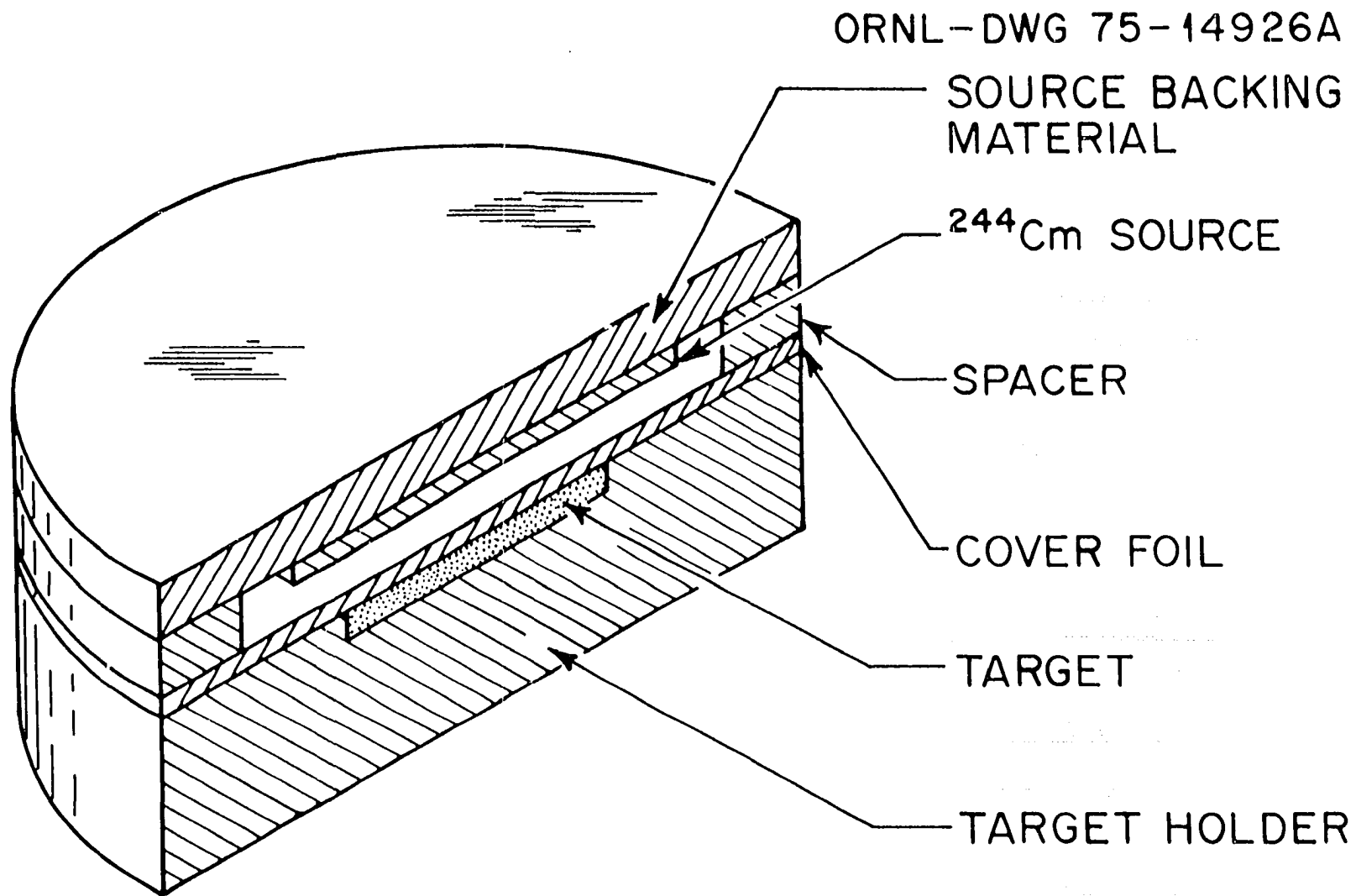


Figure 17. ^{244}Cm -oxide source configuration for helium implantation (120).

found to be uniform in the first 4-5 μm range at 5 appm then decreased linearly to zero at 10 μm . These results are shown graphically in Figure 18.

Hardness Testing Equipment and Procedure

Figure 19 shows the hot hardness tester and specimen in the testing configuration. In order to eliminate moisture, the apparatus was kept under a 10^{-6} torr vacuum when not in use.

To conduct the hardness test, a polished disk was placed on the Inconel anvil. A tantalum wedge was placed in a hole at the disk center forcing the specimen thermocouple to make good contact with the specimen. With the disk in place the muffle furnace was raised into position, radiation shields were replaced, the bell jar was lowered and the entire system was pumped to 10^{-6} torr. An indentation was made by raising the specimen using the coarse and fine adjustments until contact was achieved with the sapphire Vickers indenter. By continuing to raise the anvil assembly the load, consisting of indenter and any added weights, was released onto the disk surface. After a prescribed time, as determined by a stopwatch, this load was removed by reversing the process. The instant of load release was identified using a simple electric circuit and ammeter connecting the indenter and its support. Once the indenter was free of its support the circuit was opened.

The indentation process was conducted manually. To examine the effect of load hold time on the observed hardness value, hold times were varied from 10 sec to 30 sec on some 304L stainless steel. The results

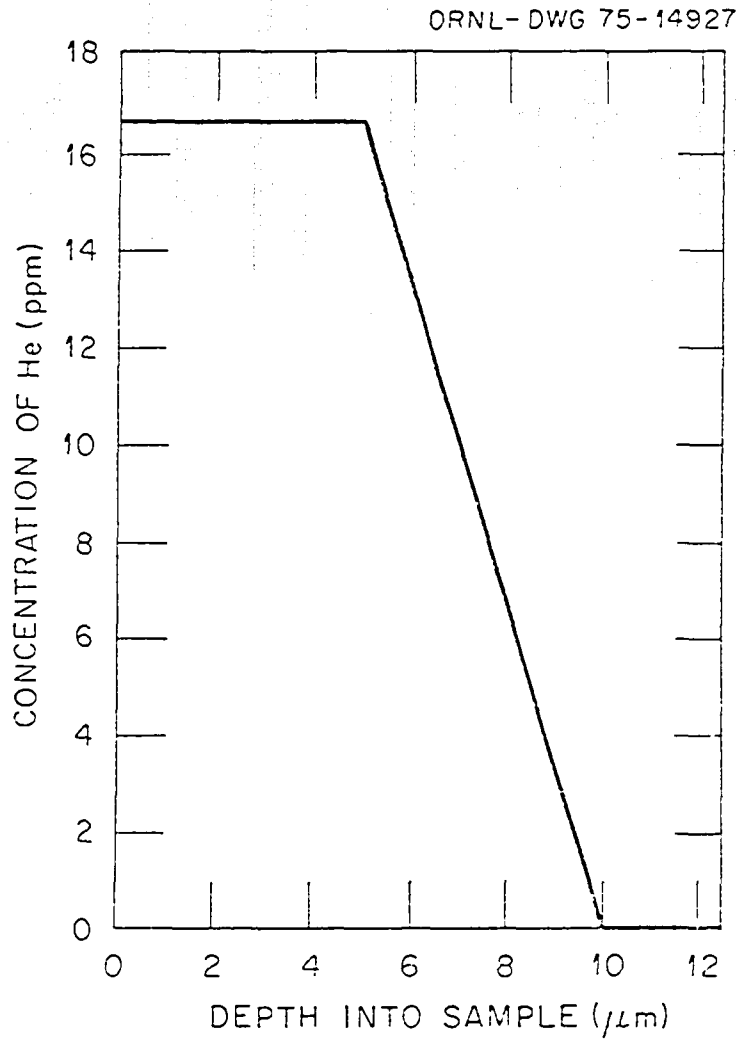


Figure 18. Depth profile of preinjected He using the ^{244}Cm source (120).

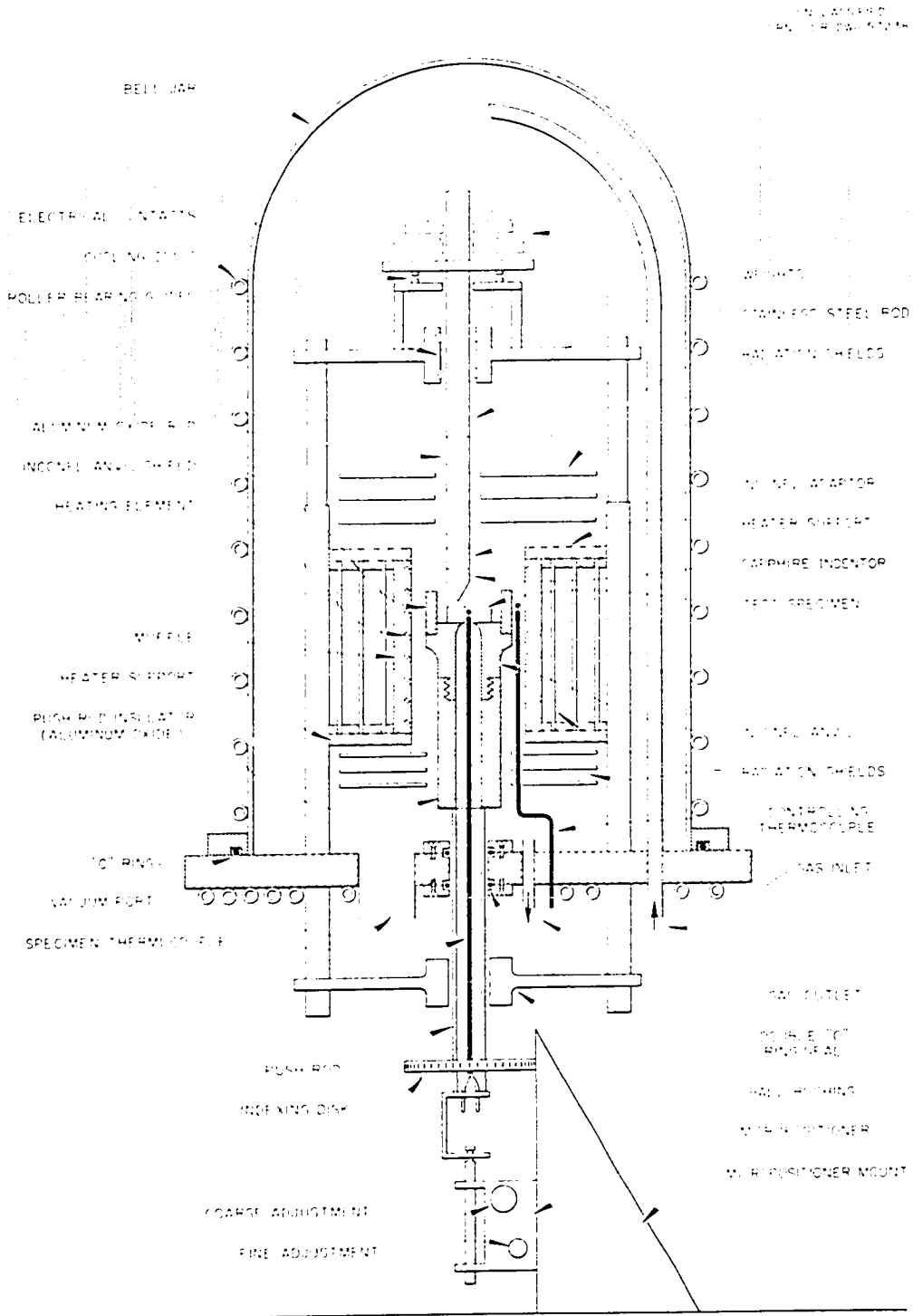


Figure 19. Schematic drawing of hot hardness tester with specimen in place.

showed that for an indentation time of 20 sec and variations 5 sec either side, the observed hardness varied by one dph number or less.

Specimen temperature was monitored by a thermocouple equipped with a multirange potentiometer. Furnace temperature was set by using a previously calibrated variac, and measured with a thermocouple and potentiometer. A load of 1985.76 grams and indentation time of 20 seconds were used for all hot hardness tests. Both diagonals for each impression were measured using a Kentron microhardness tester and averaged. Since a damaged indenter can drastically affect hardness determination, each indentation must be established as a good one. This is accomplished by focusing deep into the impression and looking for any irregularities in the surface. Once established as a good number, the average diagonal was then used to calculate indentation surface area and hence diamond pyramid hardness number. Hot hardness was examined between 22°C and 850°C at 50°C increments for each alloy.

Ion Bombardment Procedure

Specimens found to have acceptable surface quality following the helium implantation were subjected to ion irradiation. Ion irradiation utilized the 6 MV ORNL electrostatic accelerator to produce a 4 MeV $^{58}\text{Ni}^{+2}$ beam with a flux of about 6×10^{12} ion cm^{-2} sec^{-1} . Details of the accelerator have been presented elsewhere (122).

Figure 20 is a schematic drawing of the specimen chamber of the ORNL facility. This diagram shows the basic configuration of the specimen wand, specimen heater, specimen thermocouples, guard heaters and

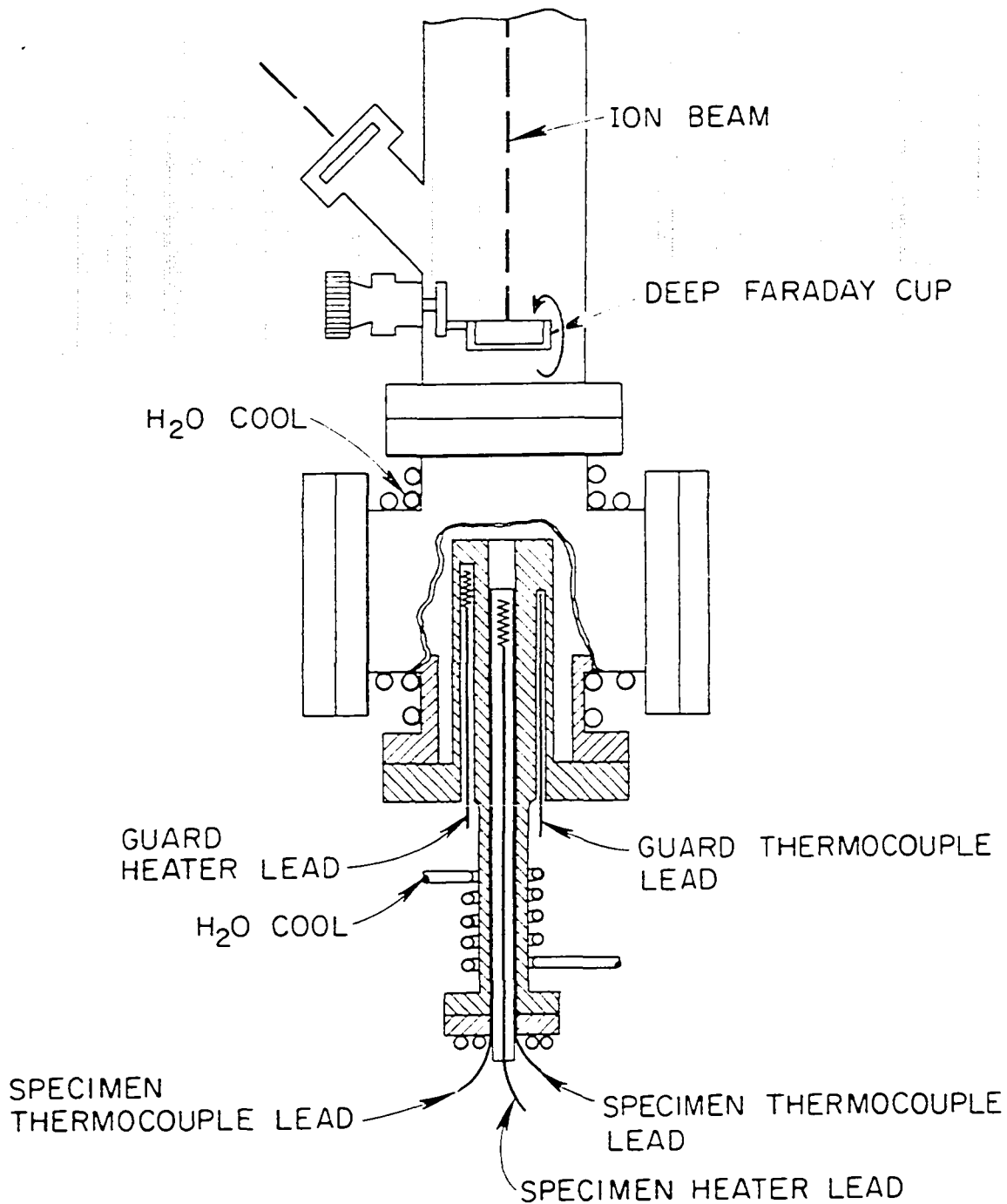


Figure 20. Schematic of the ion bombardment chamber.

guard thermocouples. The specimen wand is a cylinder onto which the individual specimen holders (Figure 15, page 68) are affixed with screws. The specimen heater assembly consists of a small resistance and eight peripheral thermocouples mounted on the end of a cylinder which is inserted into the specimen wand. The specimen heater and wand are shown in Figure 21 and a more detailed drawing of their configuration in the chamber is provided by Figure 22. Figure 23, a detail section of the specimen chamber near the end of the specimen heater, shows the configuration of various heaters and measuring thermocouples. In addition to the heating provided by the guard and specimen heaters, the ion beam produces a net energy flux to the specimen and must be determined. Since the 4 Mev Ni ion range in these steels is the order of 1 μm , beam heating is localized at the surface. To determine this effect, six thermocouples were spot welded to the beam-exposed surface and temperatures measured as a function of beam current and heater settings. An empirical fit to these data was used to determine beam heating for given bombardment conditions. During an actual irradiation, specimen temperature was monitored with six thermocouples pressed against the back of the specimen holder as shown in Figures 22 and 23. During all bombardments, the chamber was kept under a vacuum of 10^{-7} to 10^{-8} torr.

Both the damage level and beam heating calculations require that one accurately monitor the beam current. To accomplish this, a pair of perpendicular vanes sweep the beam at a prescribed frequency (11 Hz) intercepting about 3% of the total flux. The signal from the vanes after

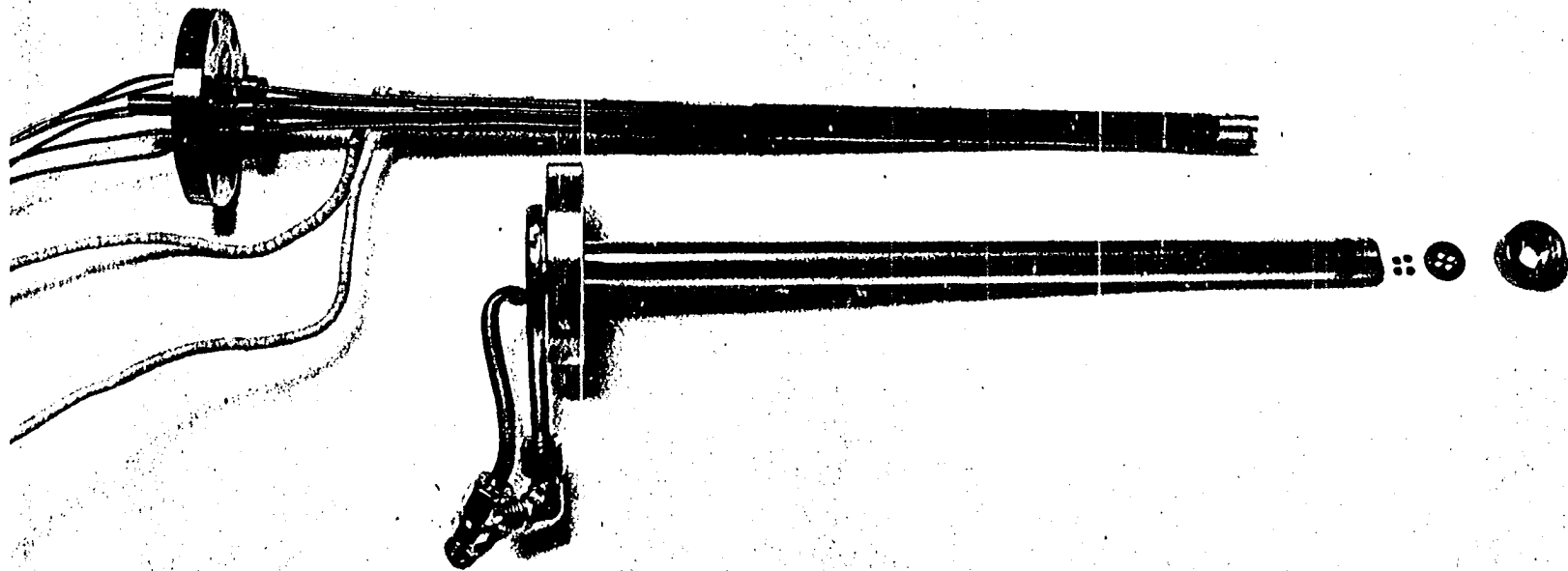


Figure 21. Photograph of specimen heater and specimen holder assembly.

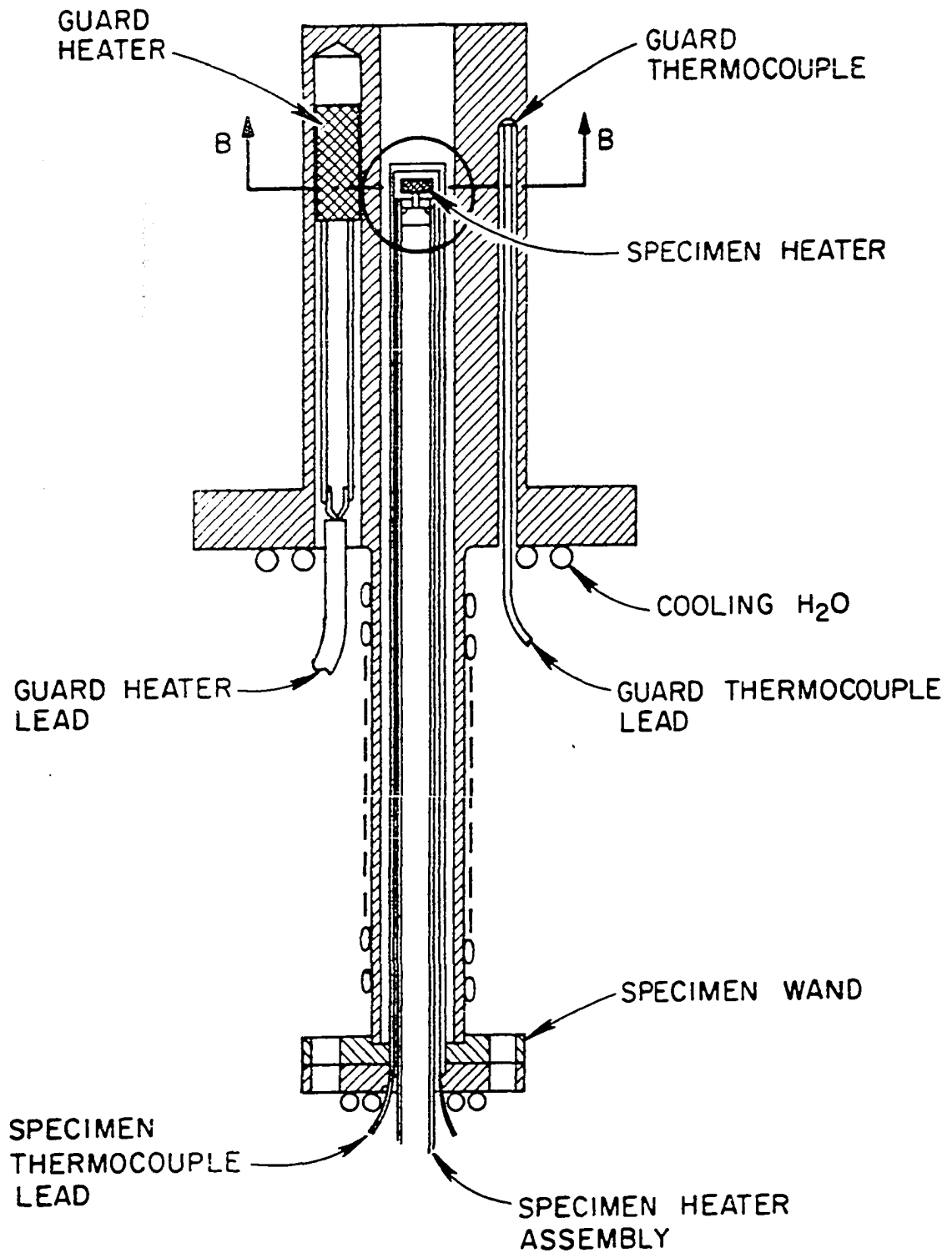


Figure 22. Detail of ion bombardment chamber.

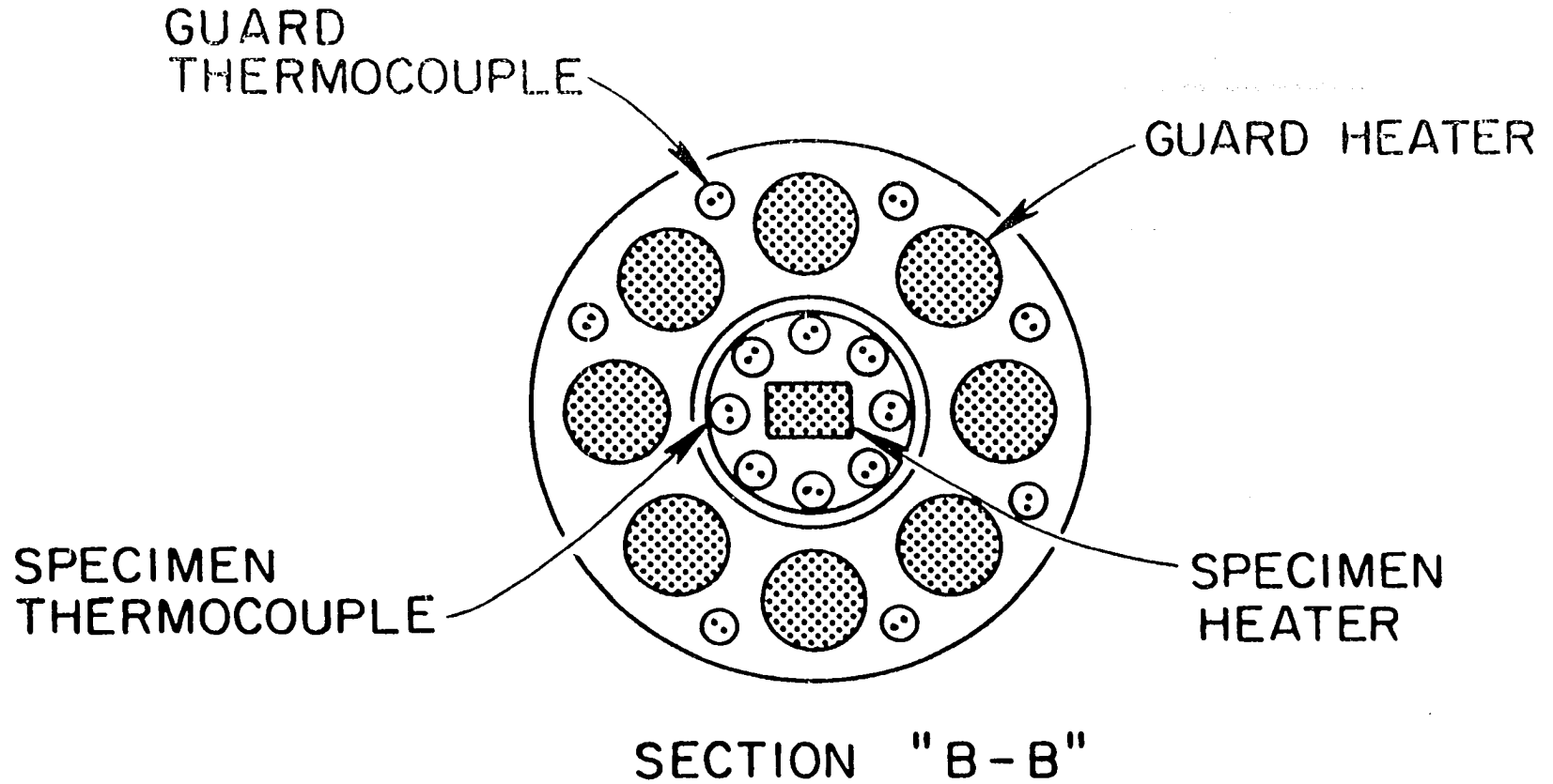


Figure 23. Detail section of ion bombardment chamber showing heater and thermocouple configuration.

suitable electronic processing was used to monitor and maintain beam uniformity. As an additional beam calibration, the deep Faraday cup shown in Figure 20 was periodically inserted into the beam. Beam area at the specimen was about 1 cm^2 .

Each specimen is fitted with a mask (strip 20 mils wide) to shadow a portion of the specimen from the ion beam. Since these regions shadowed from the beam do not swell, this masking procedure produces two steps. Figure 15, page 68, shows a holder in the postirradiation condition with the masked region clearly visible. The magnitude of the discontinuity between masked and unmasked regions has been correlated with volume changes due to swelling (123). Following ion irradiation all specimens in each holder were examined using a Sloan profilometer. Figure 24 shows a typical trace across the swelling step region. Five scans traversing the length of each specimen produced ten step heights. These values were averaged to yield a single step height value for each alloy at a given set of irradiation conditions. As an additional check on spatial uniformity of the beam, step height values for the various 316 standards were compared. It is imperative to this technique that all specimens be exposed to the same radiation dose or a suitable correction applied.

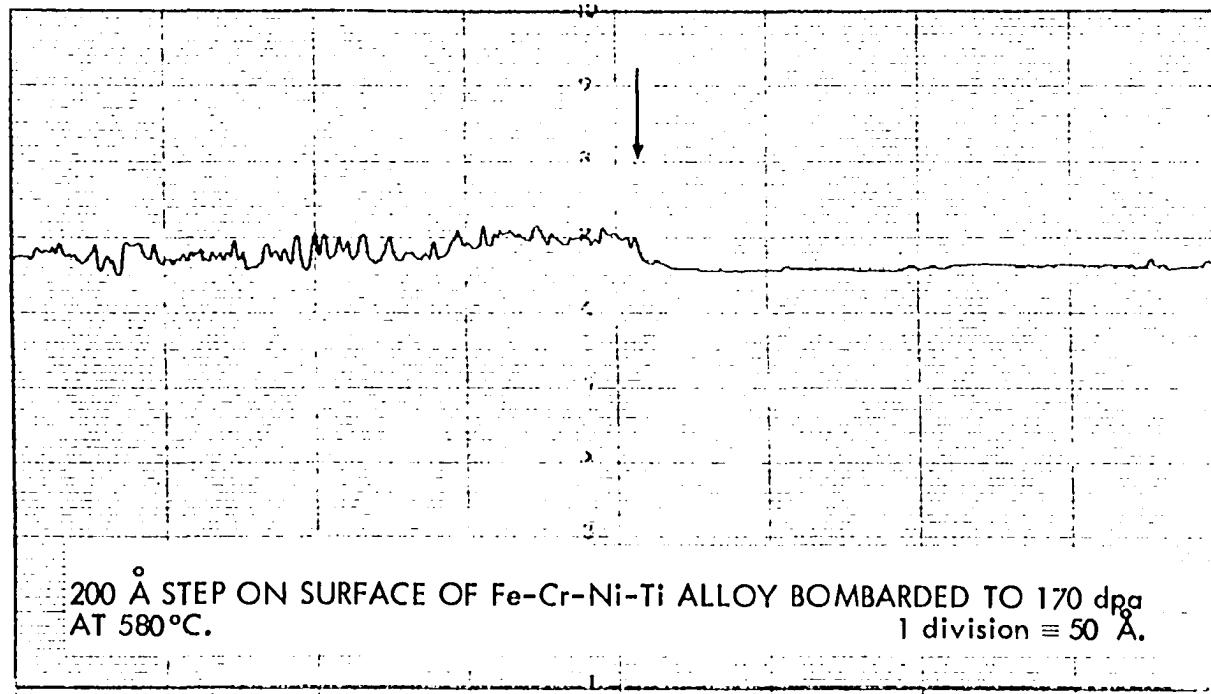


Figure 24. Typical profilometry trace of alloy after ion bombardment.

RESULTS

Lattice Parameters

In order to characterize the alloys more fully, lattice parameter measurements were made. These results are presented in Table 3. Additions of Ti, Nb, Mo, and W were found to dilate the lattice while additions of silicon resulted in a slight contraction. Aluminum additions produced more complex behavior. The addition of 1.6 at. % Al and 4.5 at. % Al resulted in formation of two phases in the alloys.

Microscopy

Optical microscopy and TEM examinations were carried out on all alloys in the solution treated condition since it was recognized that in each case, the highest impurity concentration added probably approached the limits of solid solubility. Nearly complete solution was achieved in 29 of the 32 alloys; there were less than two or three particles 0.2-0.5 μm diameter in each grain. Figures 25, 26 and 27 are TEM micrographs representative of most of the alloys. However, in the alloys containing 4.34 atom % Mo, 2.90 atom % W and 0.85 atom % Nb, solution was not completely achieved by the normal fabrication procedure and so the final annealing temperature was raised to 1250°C. This greatly reduced the number of undissolved globular particles within the grains but some precipitation occurred at the grain boundaries during cooling to room temperature as can be seen from the optical metallographs (Figures 28, 29, 30). Thus, in these three alloys, the quoted atomic



Figure 25. TEM micrograph of an Fe-7.6 Cr-21 Ni-1.4 Al-0.35 Nb alloy. (25,000X; 1050°C/15 min and 630°C/5 hr.)



Figure 26. TEM micrograph of an Fe-7.3 Cr-20 Ni-4.0 Mo alloy.
(50,000X; 1050°C/15 min and 630°C/5 hr.)

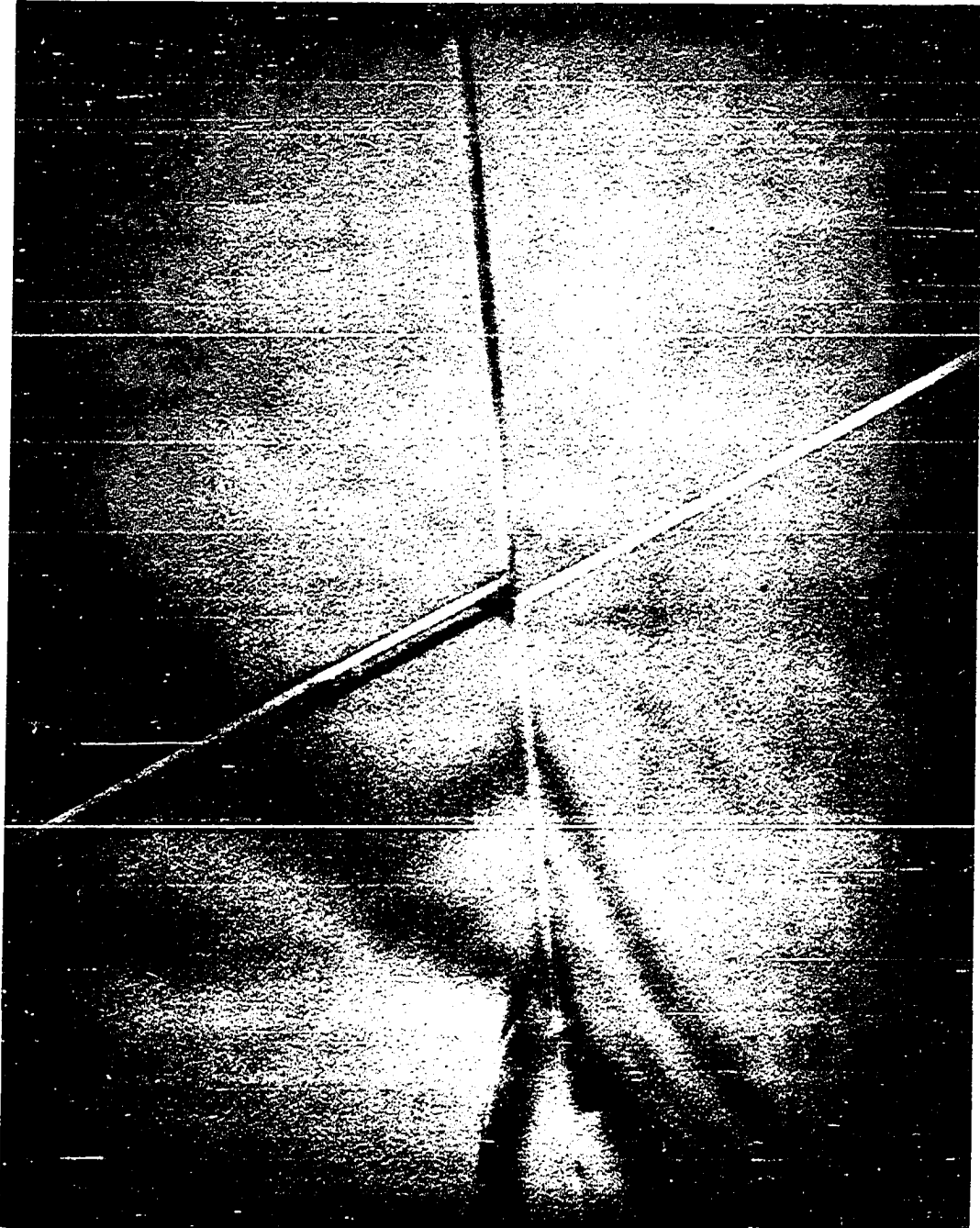


Figure 27. TEM micrograph of an Fe-7.4 Cr-22 Ni-0.69 Ti alloy.
(50,000X; 1050°C/15 min and 630°C/5 hr.)

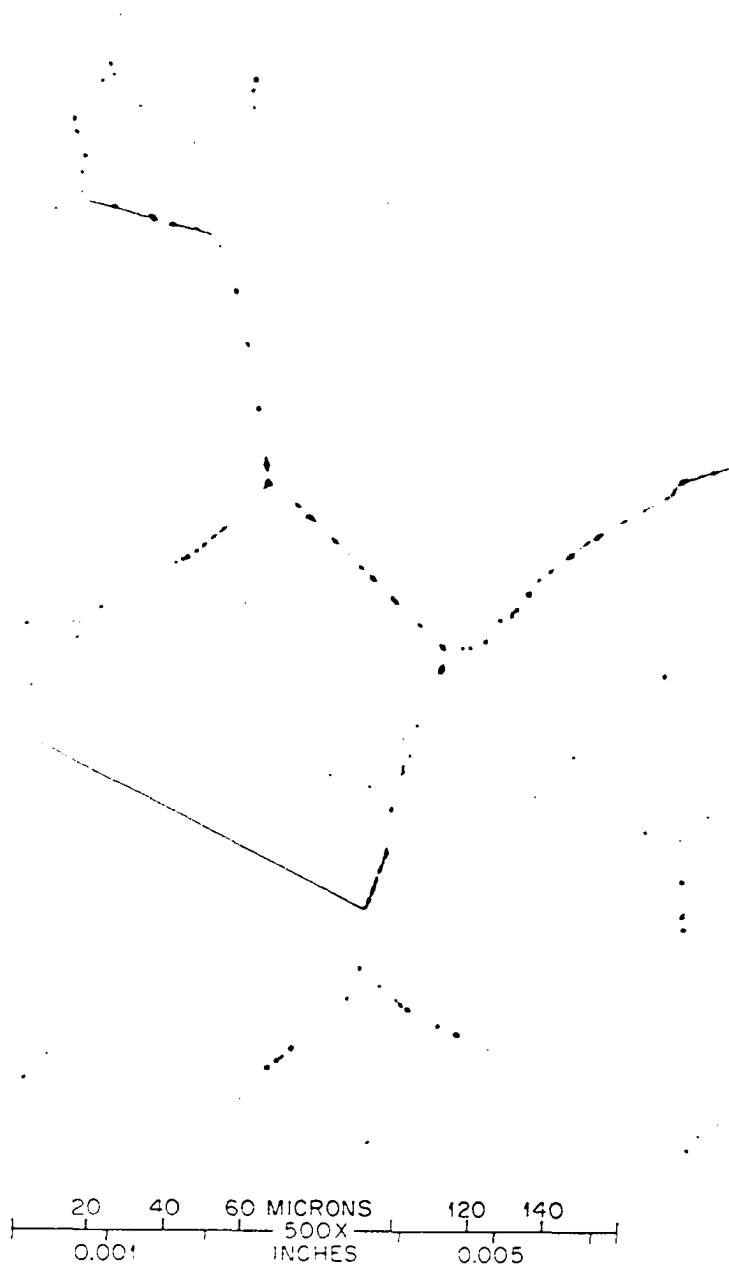


Figure 28. Optical metallograph of an Fe-7.5 Cr-20 Ni-Mo alloy.
(500X; 1250°C/30 min.)

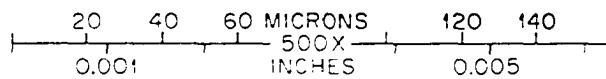


Figure 29. Optical metallograph of an Fe-7.5 Cr-20 Ni-W alloy.
(500X; 1250°C/30 min.)

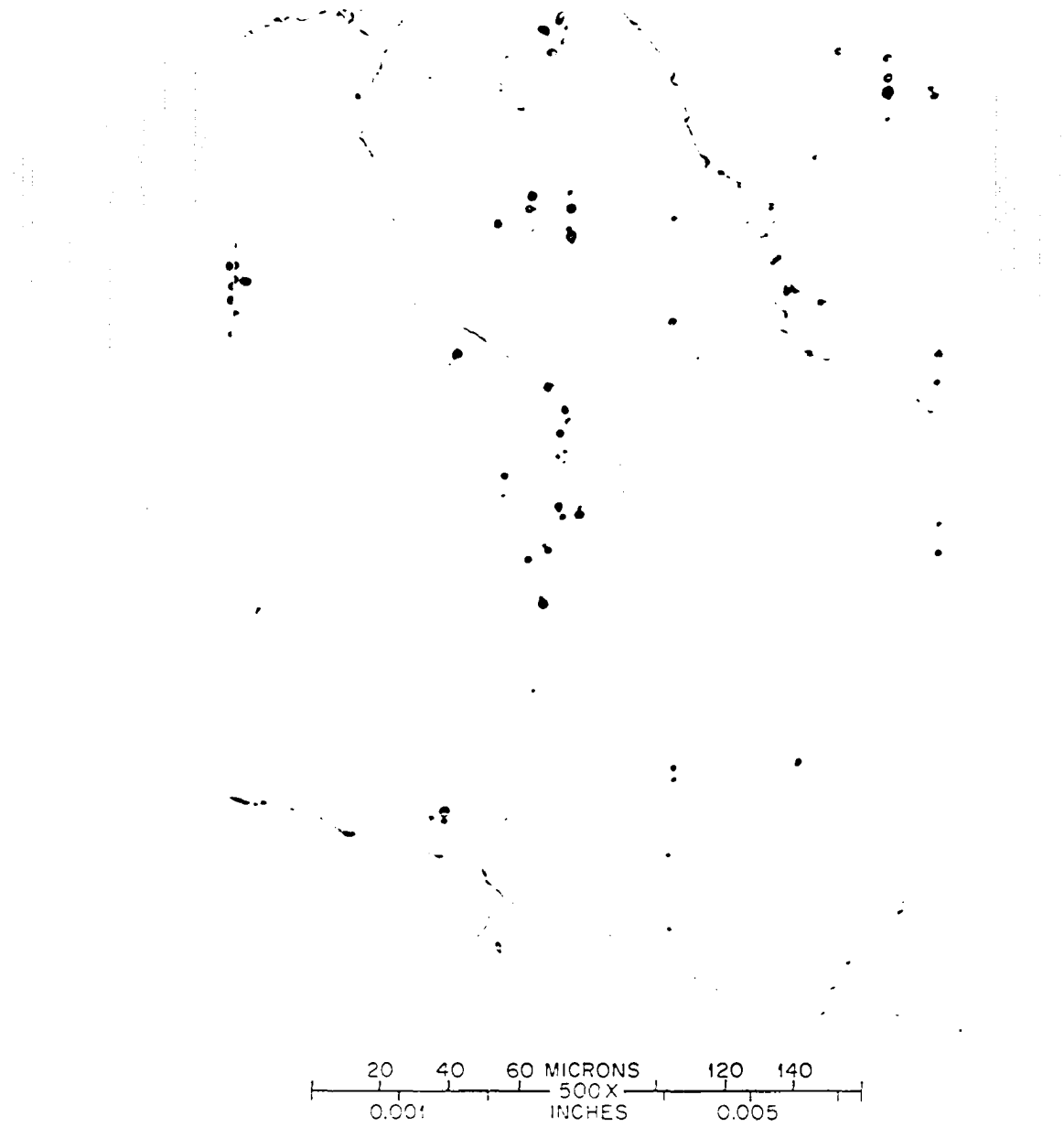


Figure 30. Optical metallograph of an Fe-7.5 Cr-20 Ni-Nb alloy.
(500X; 1250°C/30 min.)

concentrations overestimate the amount of solute in solid solution.

Extensive information pertaining to precipitation during ion bombardment was not obtained since the specimen geometry precludes the use of TEM for postirradiation examination. An assessment of alloy stability was made, however, by examining specimens which had been aged at 630°C for five hours to simulate the thermal history during ion bombardment. Evidence of significant precipitation was observed in only two alloys: A3 and N5, Table 1, page 65. The alloy containing 7.81 atom % Al exhibited $\sim 10^{17}$ particles/cm² after aging as shown in Figure 31. The average particle diameter determined from the width of strain contrast images was $\sim 60 \text{ \AA}$. Diffraction patterns showed that the precipitate had an L1₂ crystal structure indicating that it was probably a γ' phase. Aging 100 hours at 630°C resulted in an apparent phase transformation which left the specimen magnetic. This observation appears to be consistent with the Fe-Al phase diagram. The 0.85 atom % Nb alloy also showed considerable lattice strains in bright field images (Figure 32), and evidence of diffuse scattering around matrix spots in the electron diffraction pattern. Although precipitate reflections could not be detected, the alloy appeared in a clustered condition. It is likely that precipitation occurred in the A3 and N5 alloys during ion bombardment. It is possible that the irradiation environment may cause phase changes in other alloys that are not observed upon thermal aging. Recently E. Lee (Oak Ridge National Laboratory, private communication 1977) has used TEM to examine the M1 alloy after ion



Figure 31. TEM micrograph of an Fe-8.5 Cr-21 Ni-3.9 Al alloy.
(140,000X; 1050°C/15 min and 630°C/5 hr.)



Figure 32. TEM micrograph of an Fe-6.7 Cr-18 Ni-1.4 Nb alloy.
(140,000X; 1050°C/15 min and 630°C/5 hr.)

bombardment to 140 dpa. He found no evidence of precipitation or solute segregation.

Modulus Measurements

Modulus measurements were performed by measuring the propagation of an acoustic disturbance through a cylinder fitted with transducers. The method involves experimental determination of density (ρ), longitudinal acoustic velocity (V_L) and shear acoustic velocity (V_S). The shear modulus (G) and Young's modulus (E) are then computed using

$$G = \rho V_S^2 \quad (38)$$

$$E = G \frac{3\rho V_L^2 - 4G}{\rho V_L^2 - G} \quad (39)$$

Because of the dimensional requirements of this technique, modulus determinations were made only on the master alloys and some refabricated Al alloys. These results are summarized in Table 4. At the concentrations examined, Si, W, and Al increased the moduli while Ti, Mo, Nb, and C reduced their values from those of the pure ternary. These data should not be used as a measure of the effects of various solute additions on the modulus of the ternary alloy. The reasons for this are at least twofold. First, each data point was obtained at the extremity of solute addition where solubility was likely to have been exceeded. Secondly, the effect of different textures was not taken into account. Texture is likely to vary with alloying and can have a strong influence on the modulus results.

Table 4. Modulus Measurements on Selected Alloys

Alloy	Shear Modulus (G) (dynes/cm ² × 10 ¹¹)	Young's Modulus (E) (dynes/cm ² × 10 ¹²)
Ternary	7.36	1.89
M3	7.28	1.82
W3	7.56	1.91
A1	6.51	1.69
A2	5.83	1.45
A3	7.46	1.91
T3	7.35	1.87
S3	7.71	1.94
N3	7.02	1.79
C1	5.97	1.56
AT1	5.97	1.47
AN1	6.63	1.59
MA1	5.77	1.38

Tensile Test Measurements

Tensile tests over the temperature range 22 to 800°C for the base composition (Fe-7.5 Cr-20 Ni) were conducted. Sheet specimens 0.040-in. thick were pulled using an Instron testing machine at a constant cross-head speed of 0.01-in./min. Helium gas flowed past the specimens to reduce oxidation. Figure 33 displays ultimate tensile strength and hot hardness vs. temperature for the ternary alloy. These data agree well with the observations of Moteff et al. (4) that hot hardness and ultimate tensile strength are correlated and have similar temperature dependences.

Hot Hardness Measurements

With the hot hardness-hot tensile correlation established for the ternary (Fe-7.5 Cr-20 Ni) alloy, hot hardness tests were performed on all 31 alloys. Figures 34 through 63 present the hot hardness data for all alloys of the set. In each case diamond pyramid hardness number is plotted as a function of temperature over the range 22 to 850°C. All solute additions were found to result in increased alloy hardness. In the temperature region below 500°C all alloys show the same temperature dependence with increasing solute additions; a simple shifting of the level on the hot hardness curve represents a different strain rate. As was shown in the section on solid solution strengthening, the strain rate due to climb is directly proportional to the vacancy diffusion coefficient D_v . Since D_v depends on the mobility of the vacancy, so the

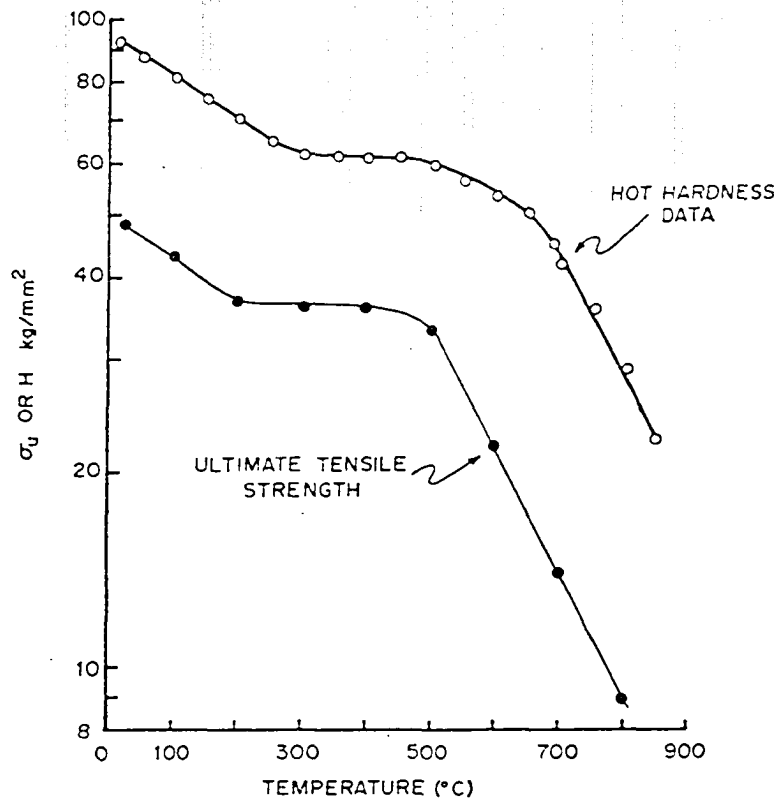


Figure 33. Hardness and ultimate tensile strength as a function of temperature for an Fe-7.5 Cr-20 Ni alloy.

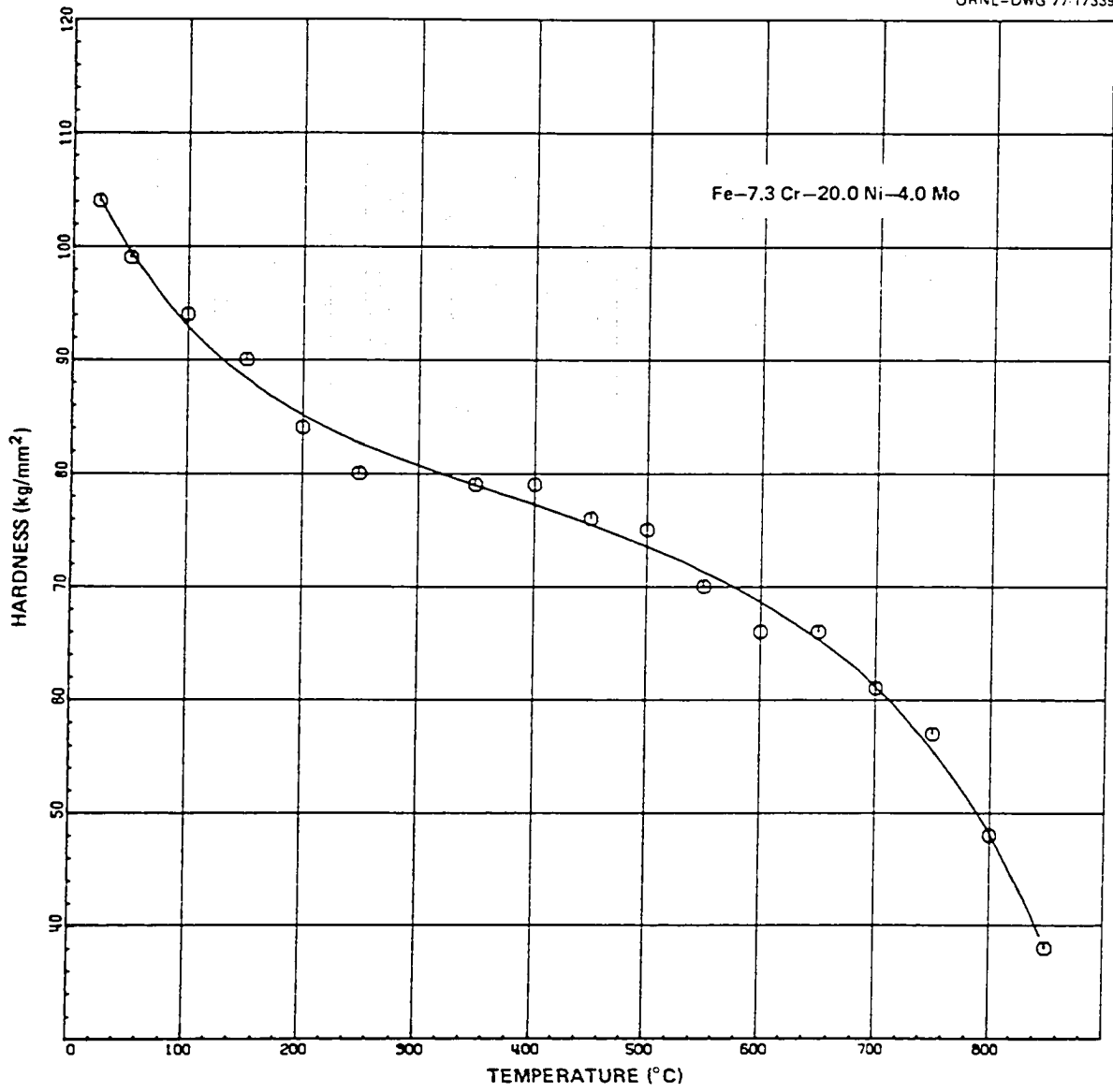


Figure 34. Hot hardness data for an Fe-7.3 Cr-20 Ni-4.0 Mo alloy.

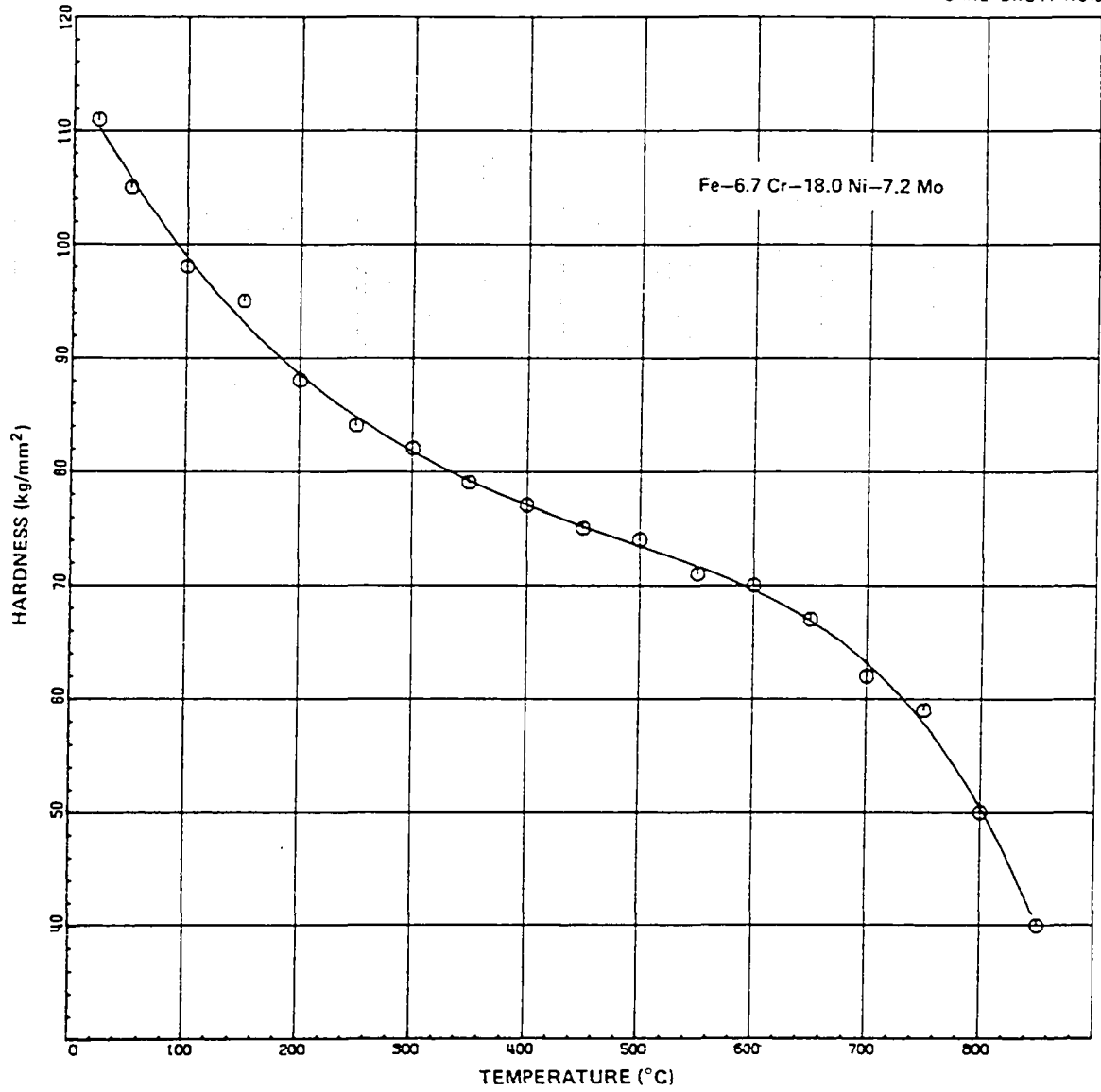


Figure 35. Hot hardness data for an Fe-6.7 Cr-18 Ni-7.2 Mo alloy.

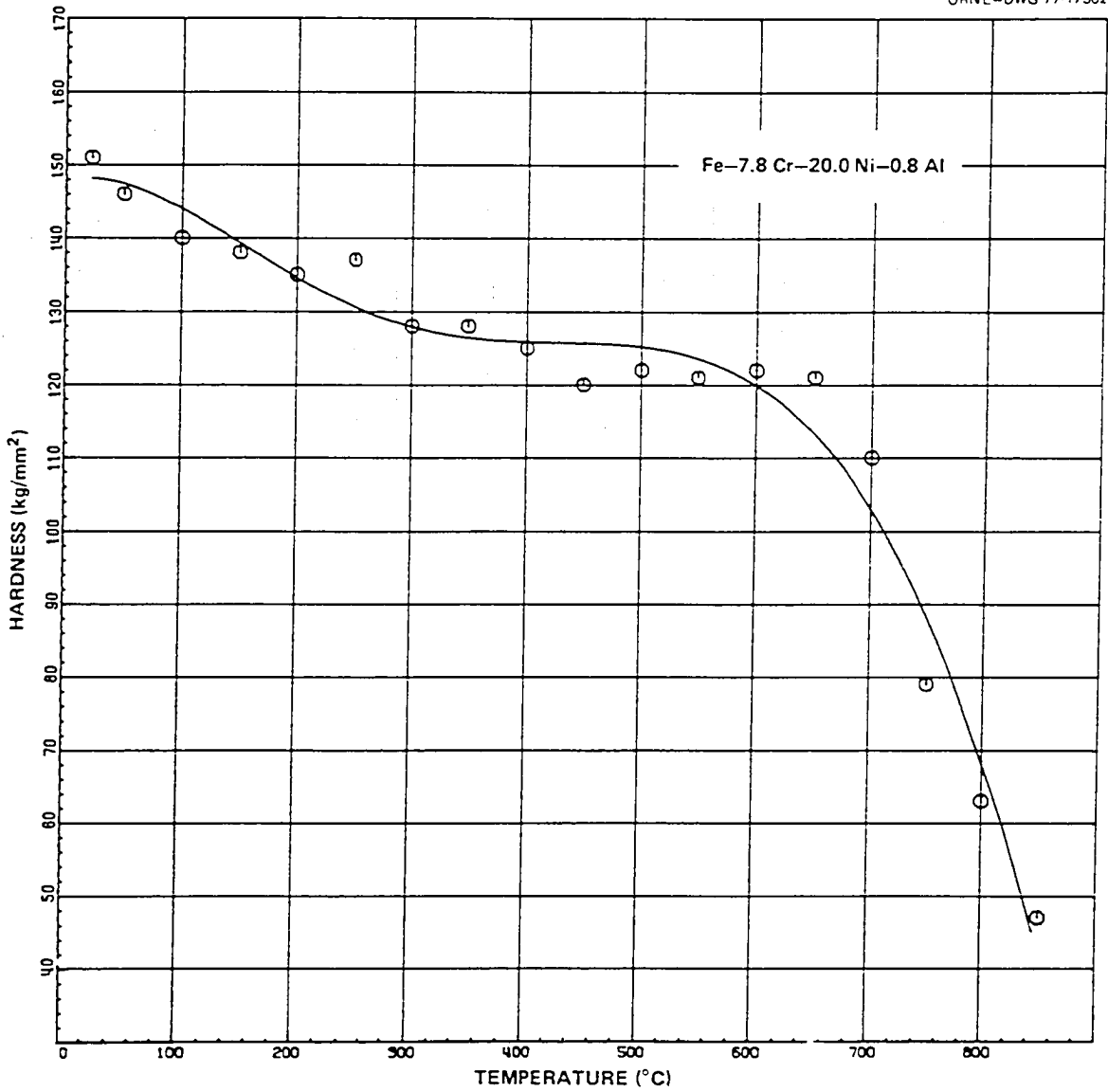


Figure 36. Hot hardness data for an Fe-7.8 Cr-20 Ni-0.8 Al alloy.

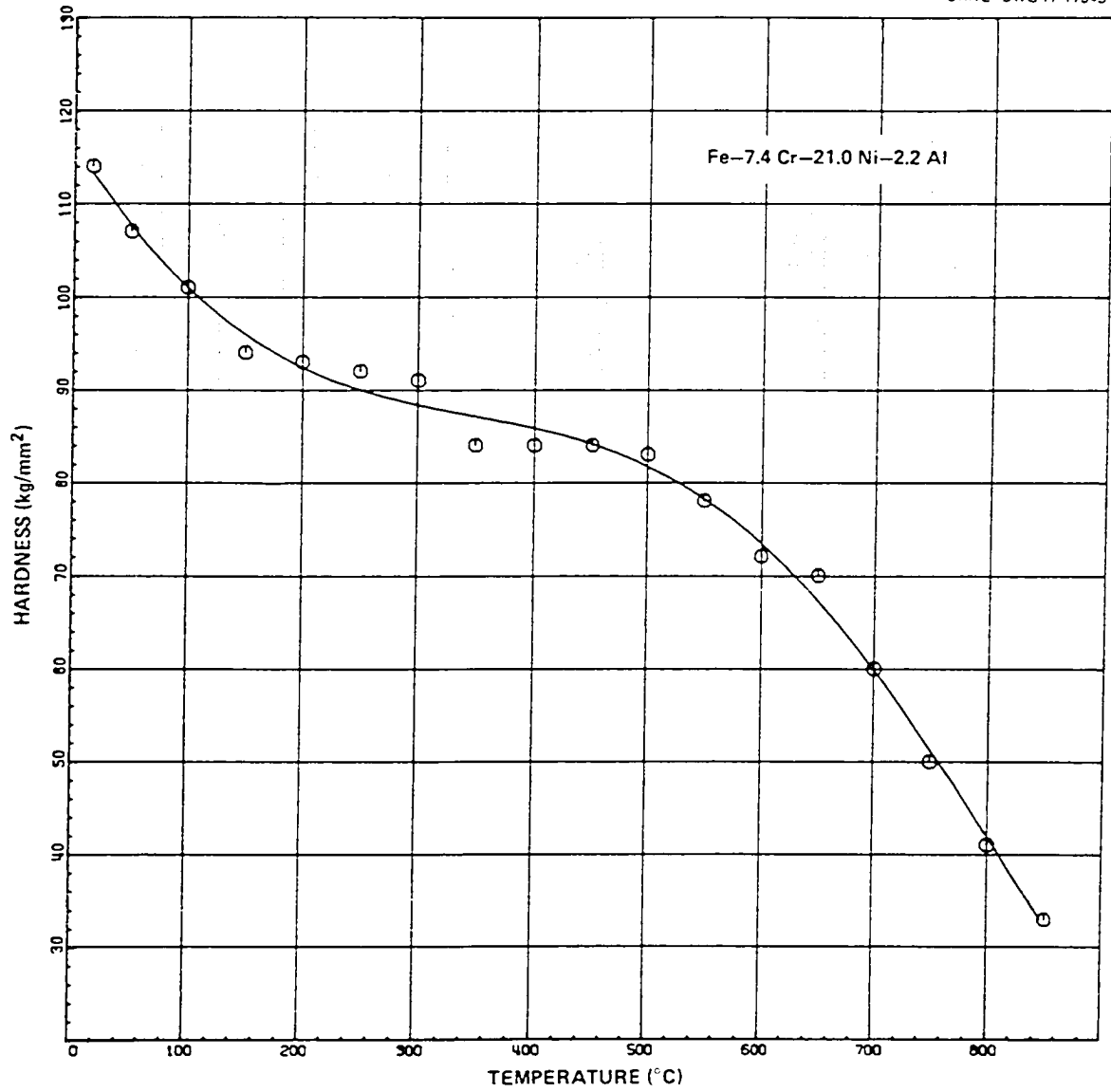


Figure 37. Hot hardness data for an Fe-7.4 Cr-21 Ni-2.2 Al alloy.

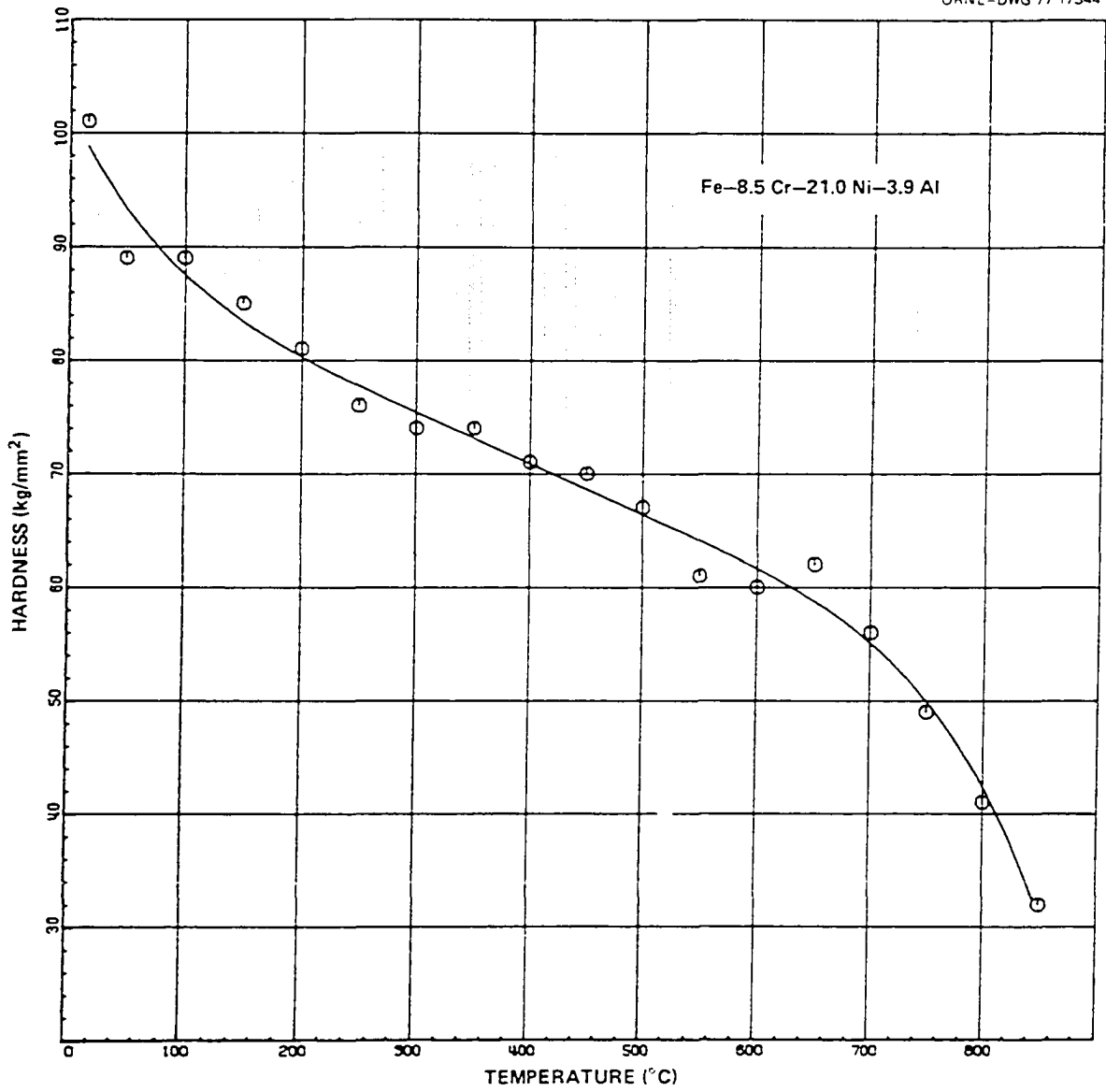


Figure 38. Hot hardness data for an Fe-8.5 Cr-21 Ni-3.9 Al alloy.

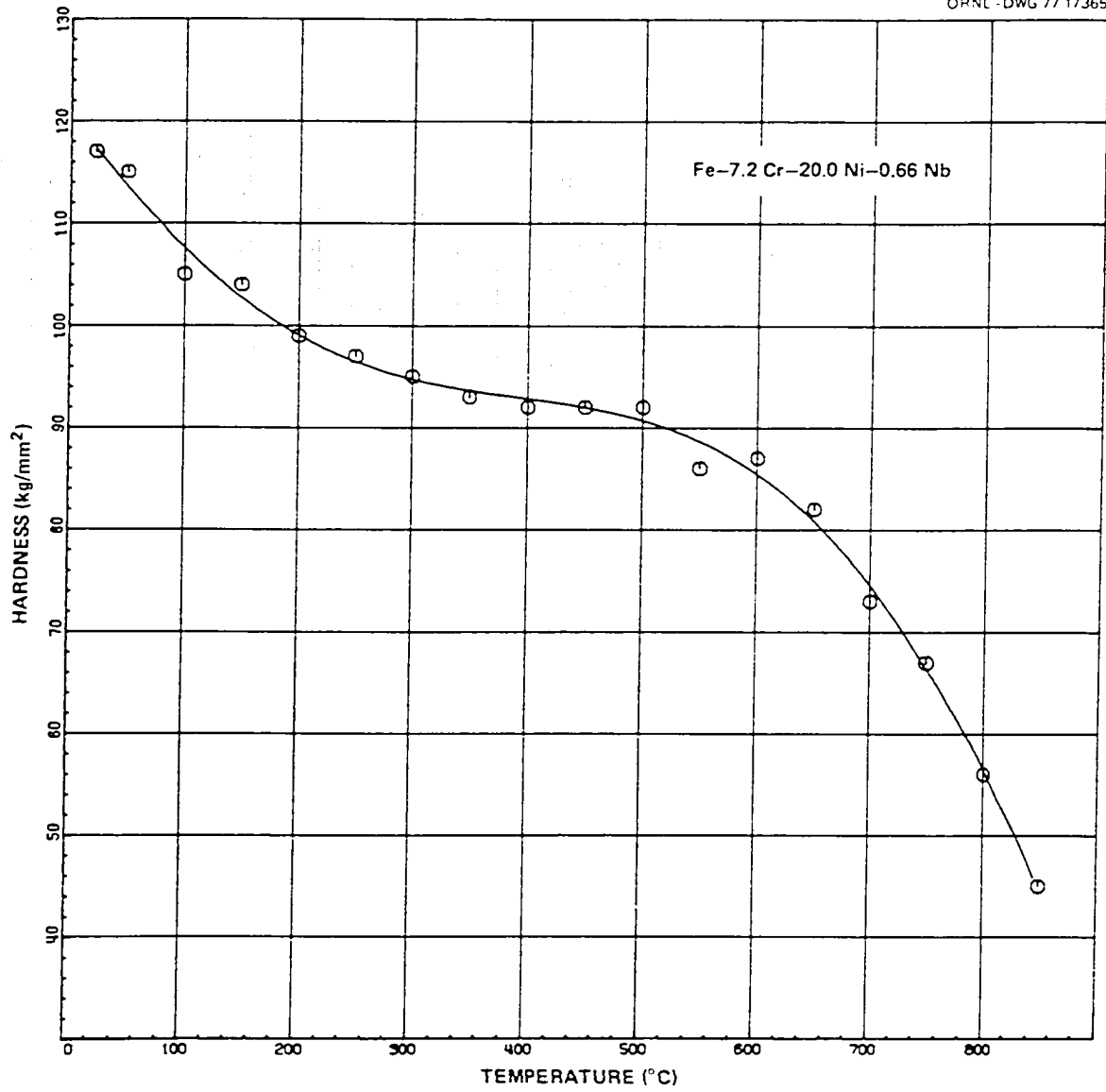


Figure 39. Hot hardness data for an Fe-7.2 Cr-20 Ni-0.66 Nb alloy.

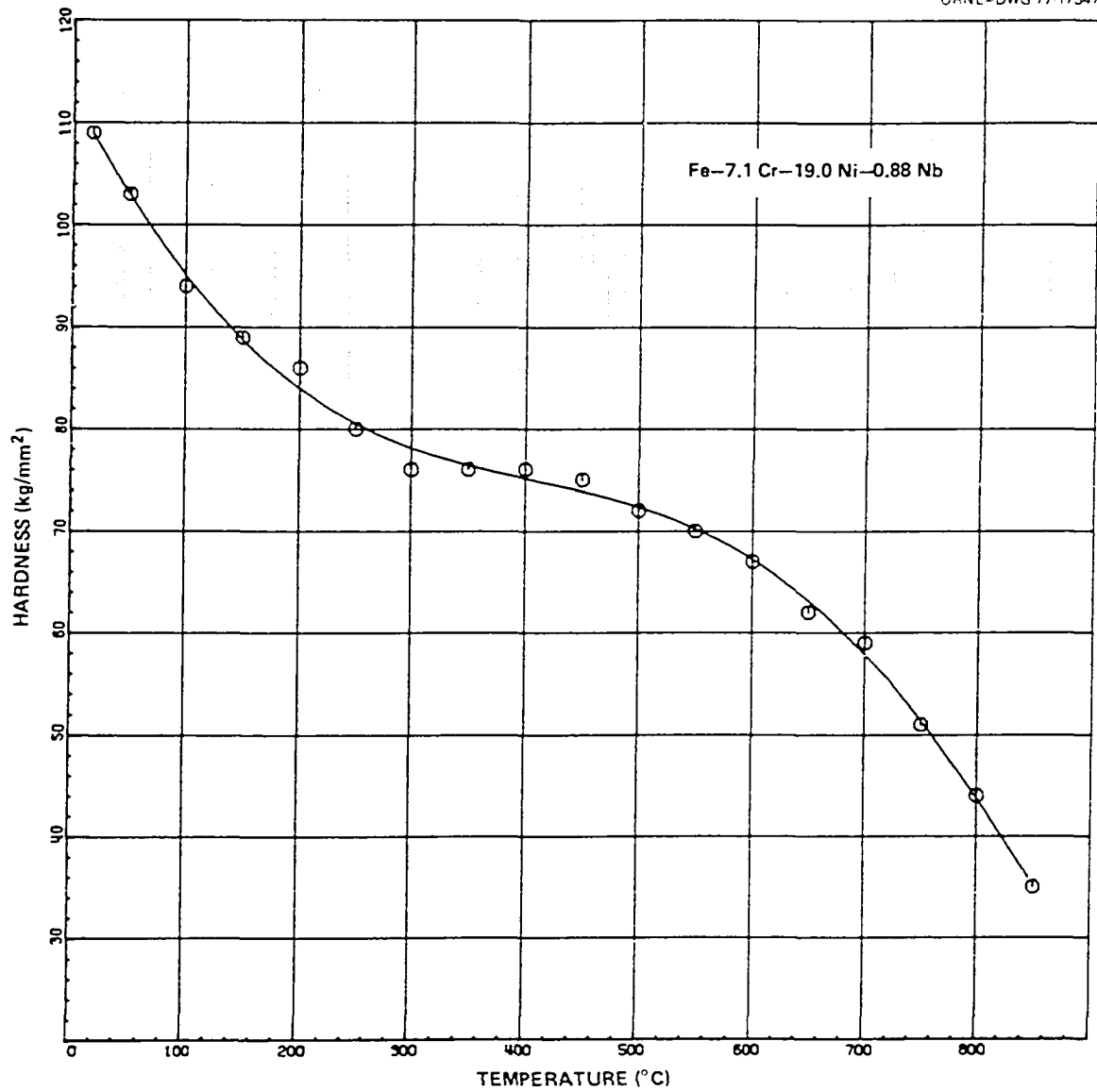


Figure 40. Hot hardness data for an Fe-7.1 Cr-19 Ni-0.88 Nb alloy.

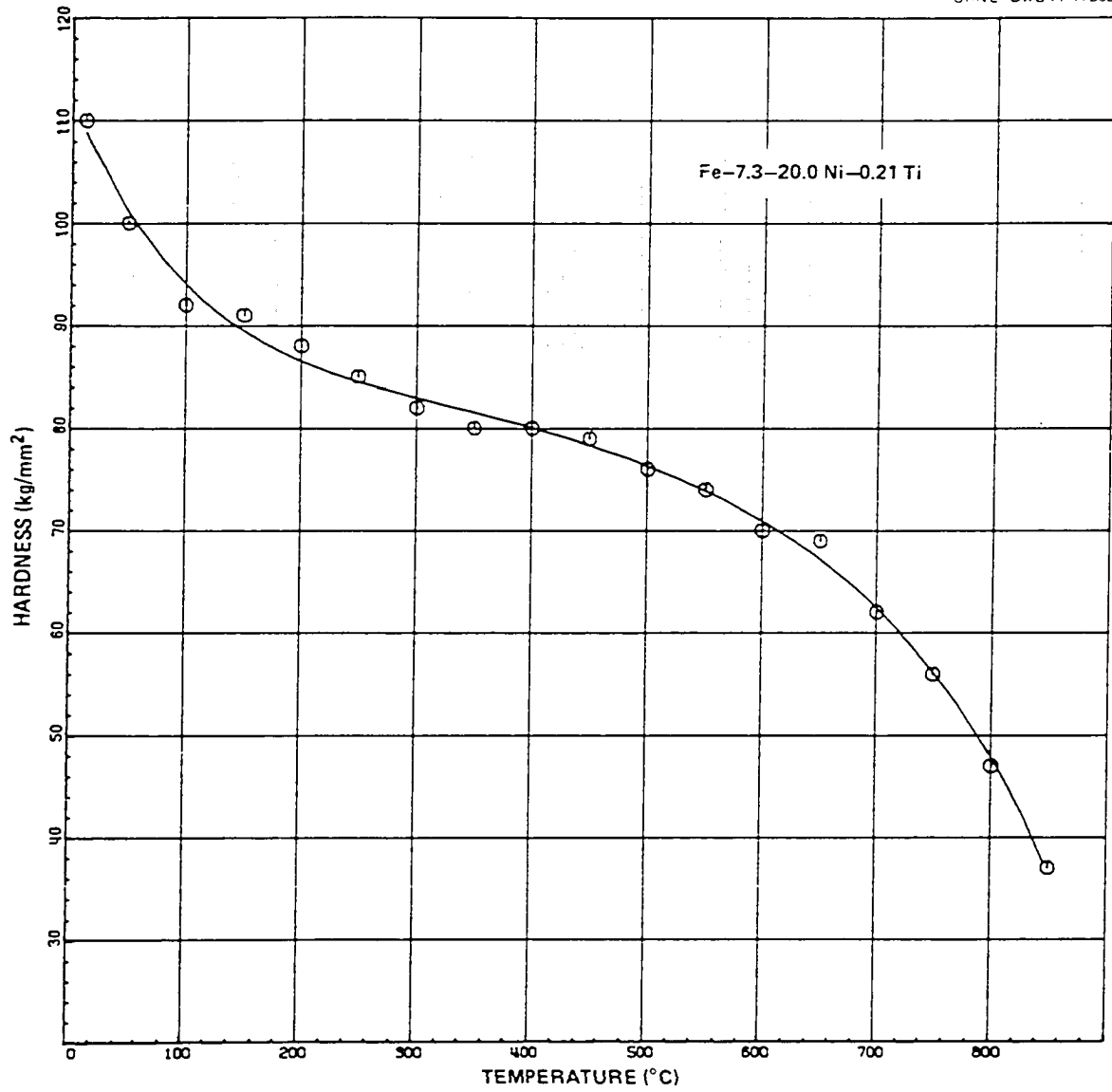


Figure 41. Hot hardness data for an Fe-7.3 Cr-20 Ni-0.21 Ti alloy.

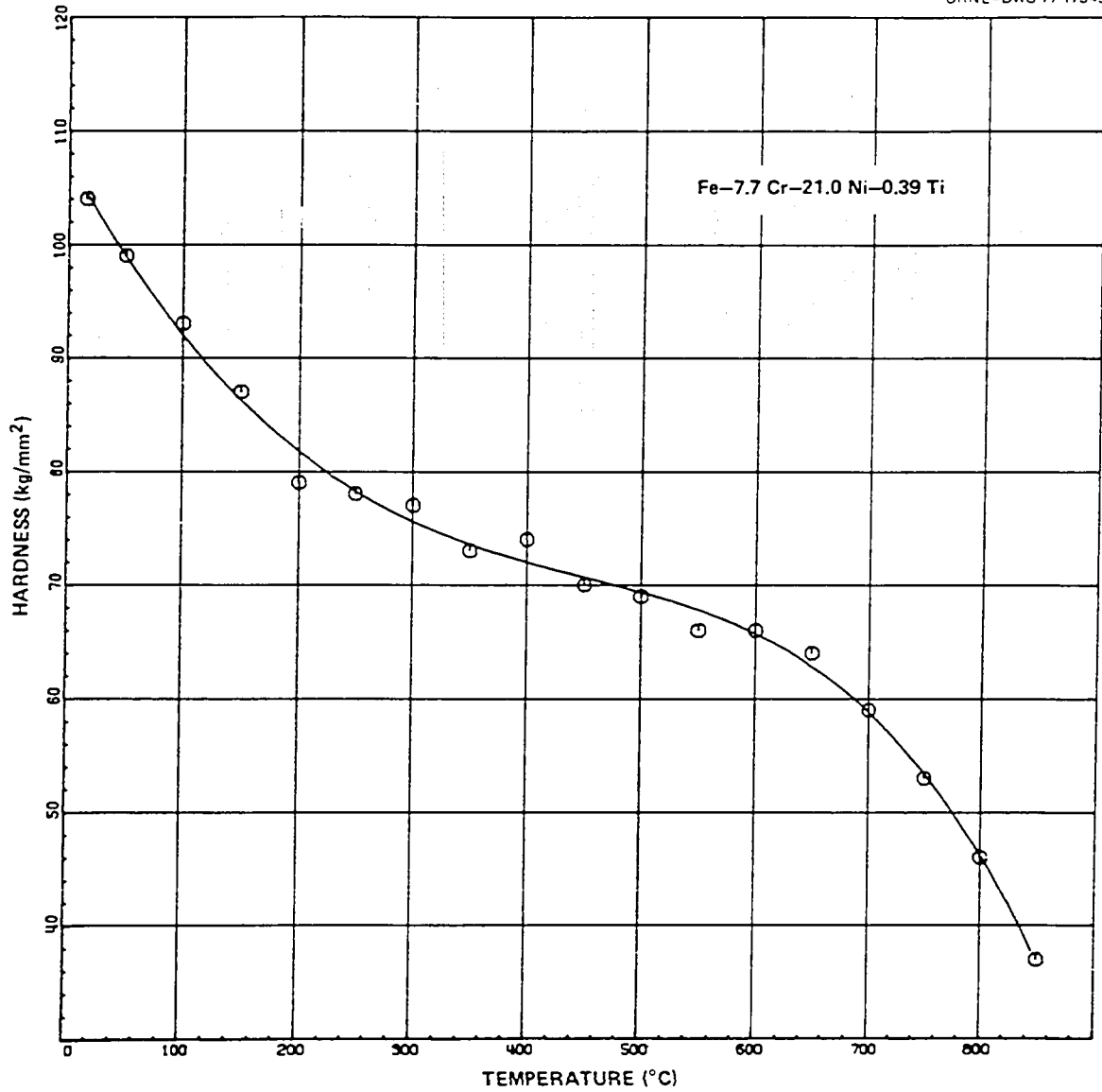


Figure 42. Hot hardness data for an Fe-7.7 Cr-21 Ni-0.39 Ti alloy.

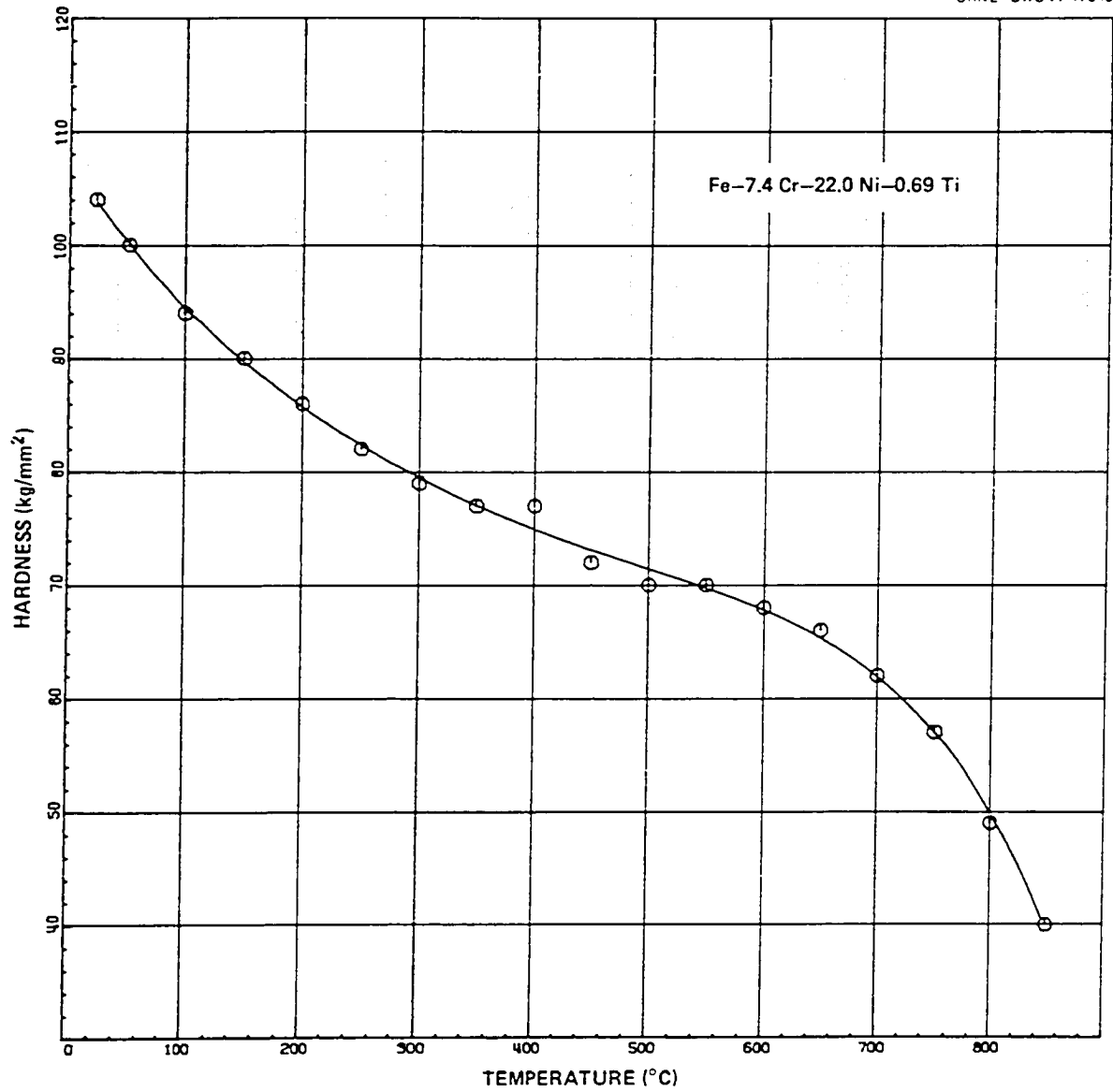


Figure 43. Hot hardness data for an Fe-7.4 Cr-22 Ni-0.69 Ti alloy.

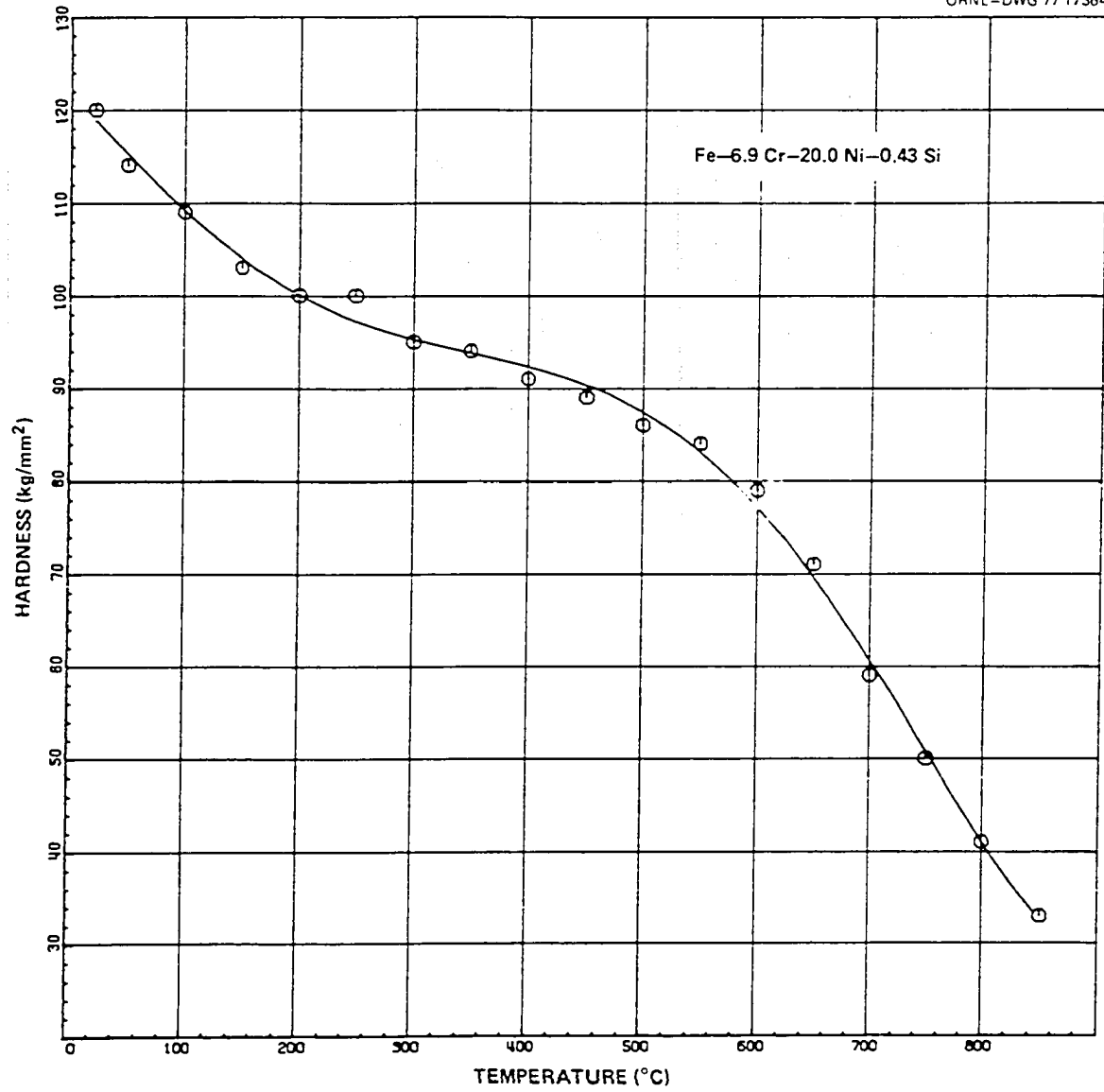


Figure 44. Hot hardness data for an Fe-6.9 Cr-20 Ni-0.43 Si alloy.

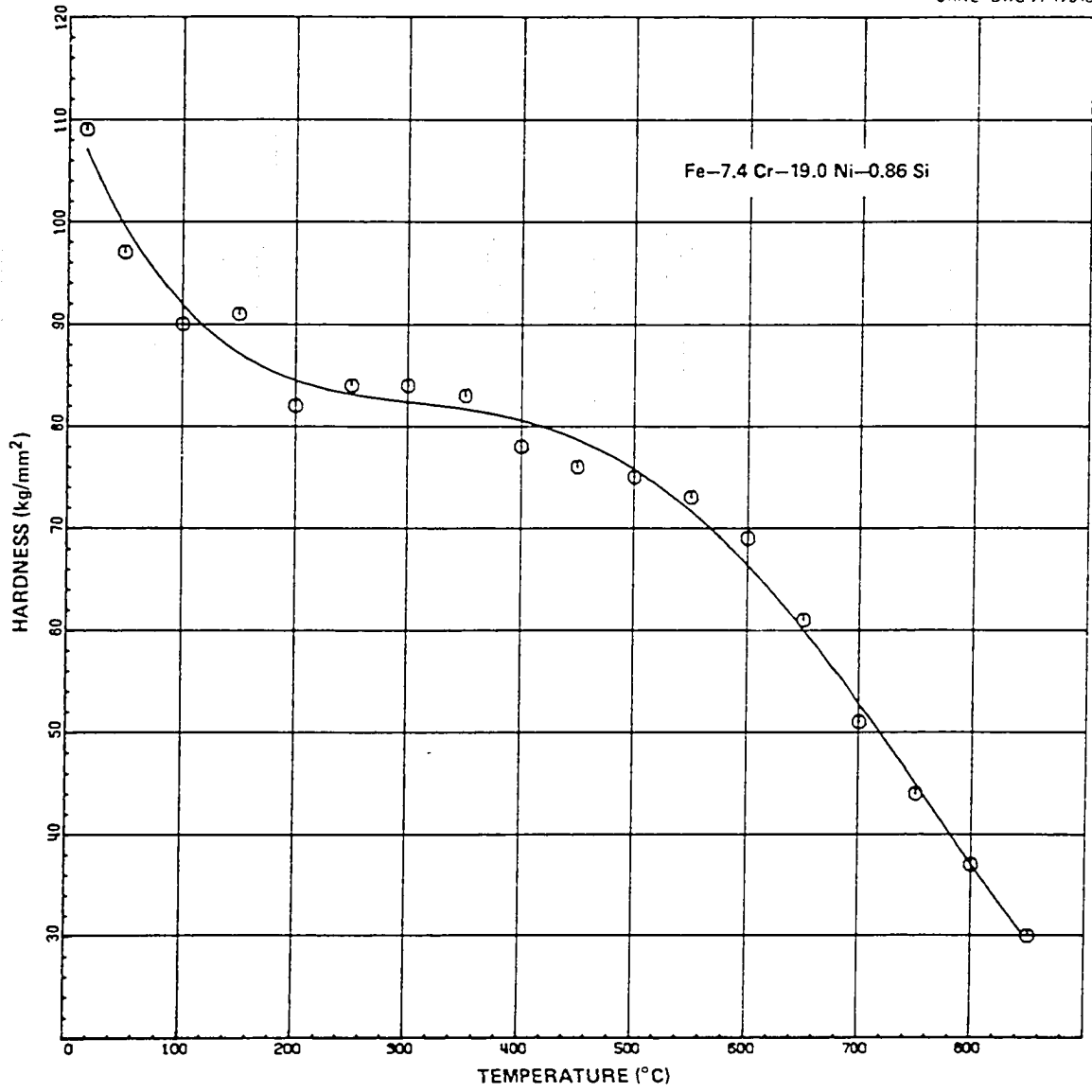


Figure 45. Hot hardness data for an Fe-7.4 Cr-19 Ni-0.86 Si alloy.

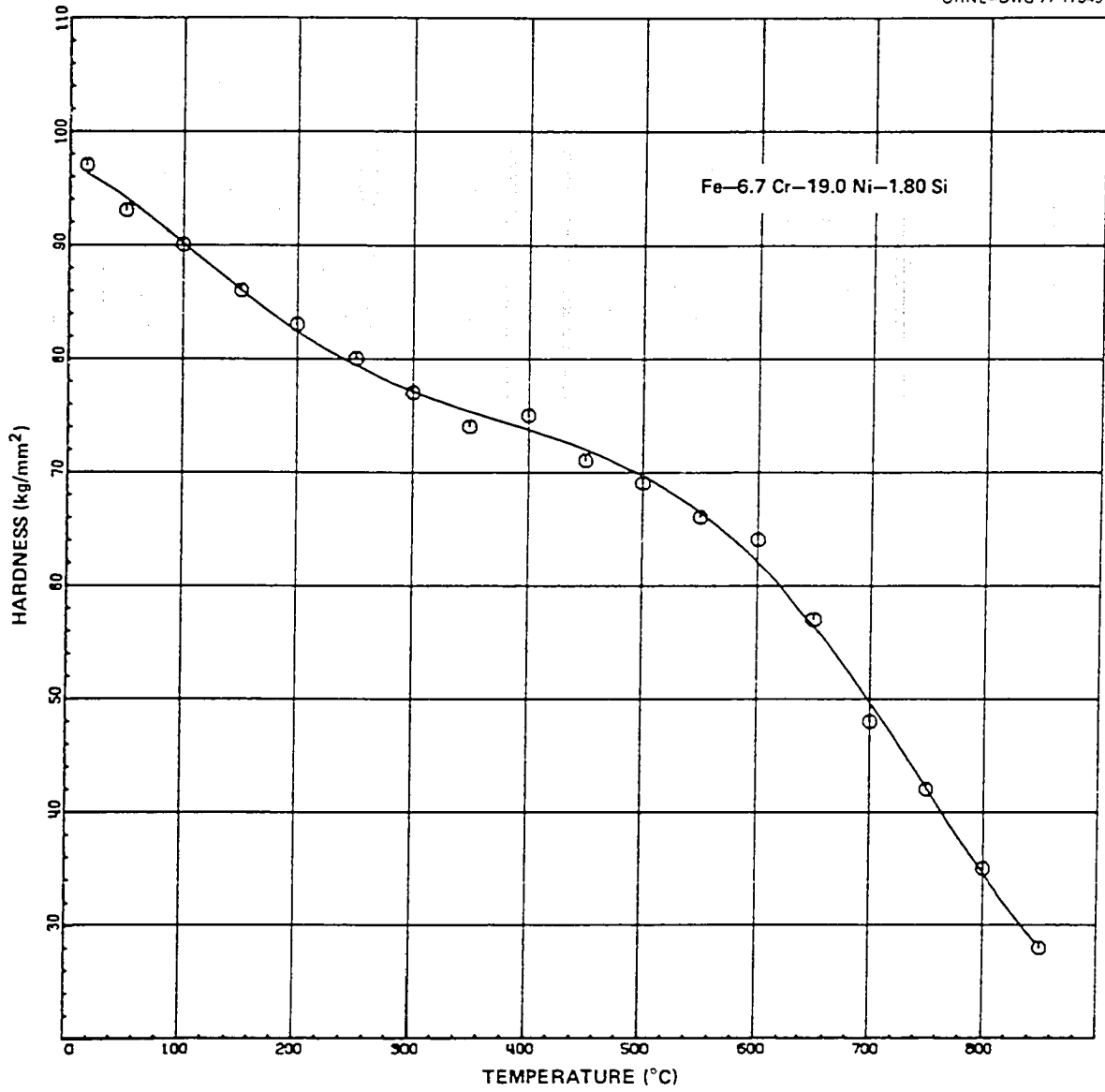


Figure 46. Hot hardness data for an Fe-6.7 Cr-19 Ni-1.80 Si alloy.

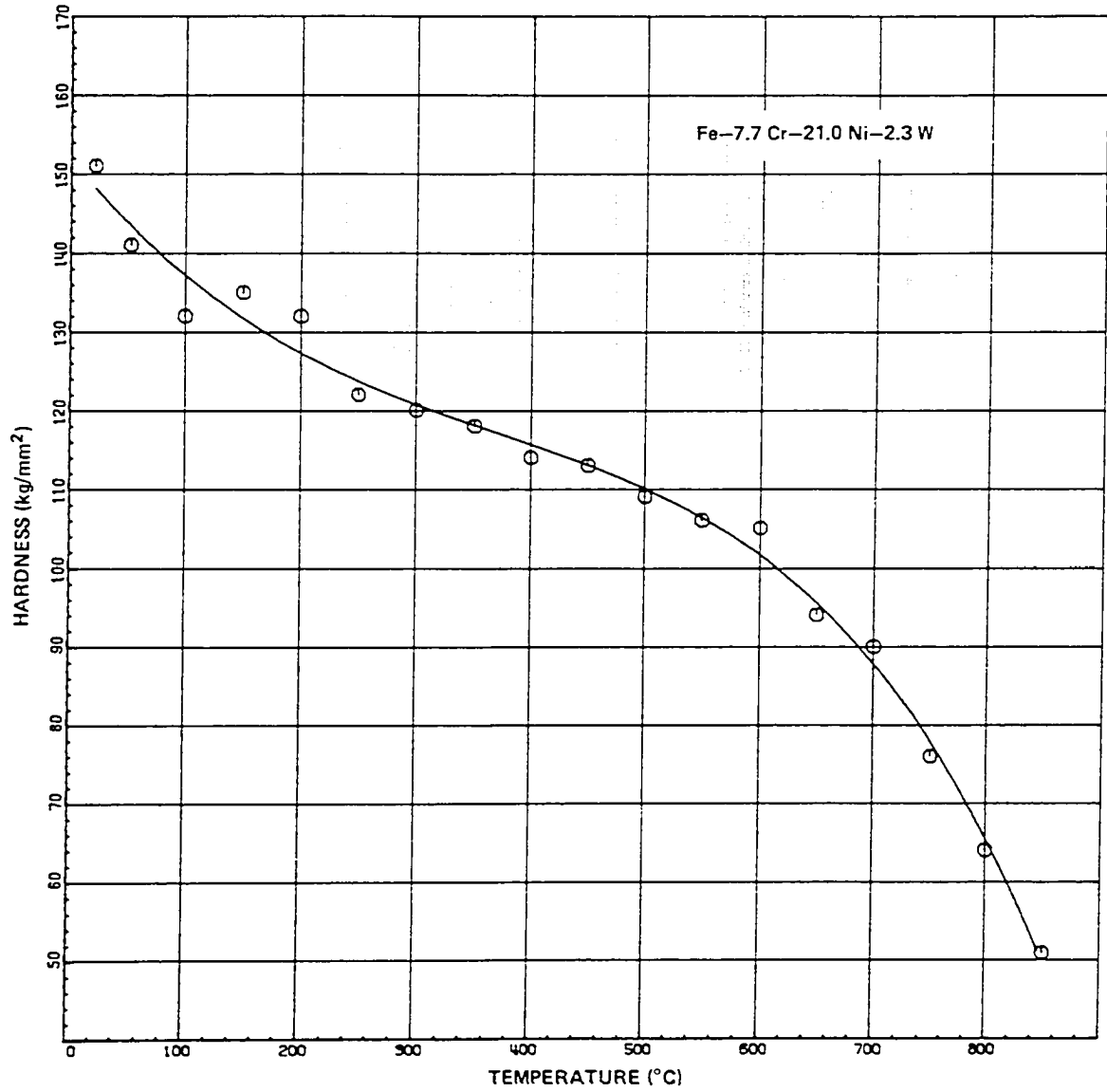


Figure 47. Hot hardness data for an Fe-7.7 Cr-21 Ni-2.3 W alloy.

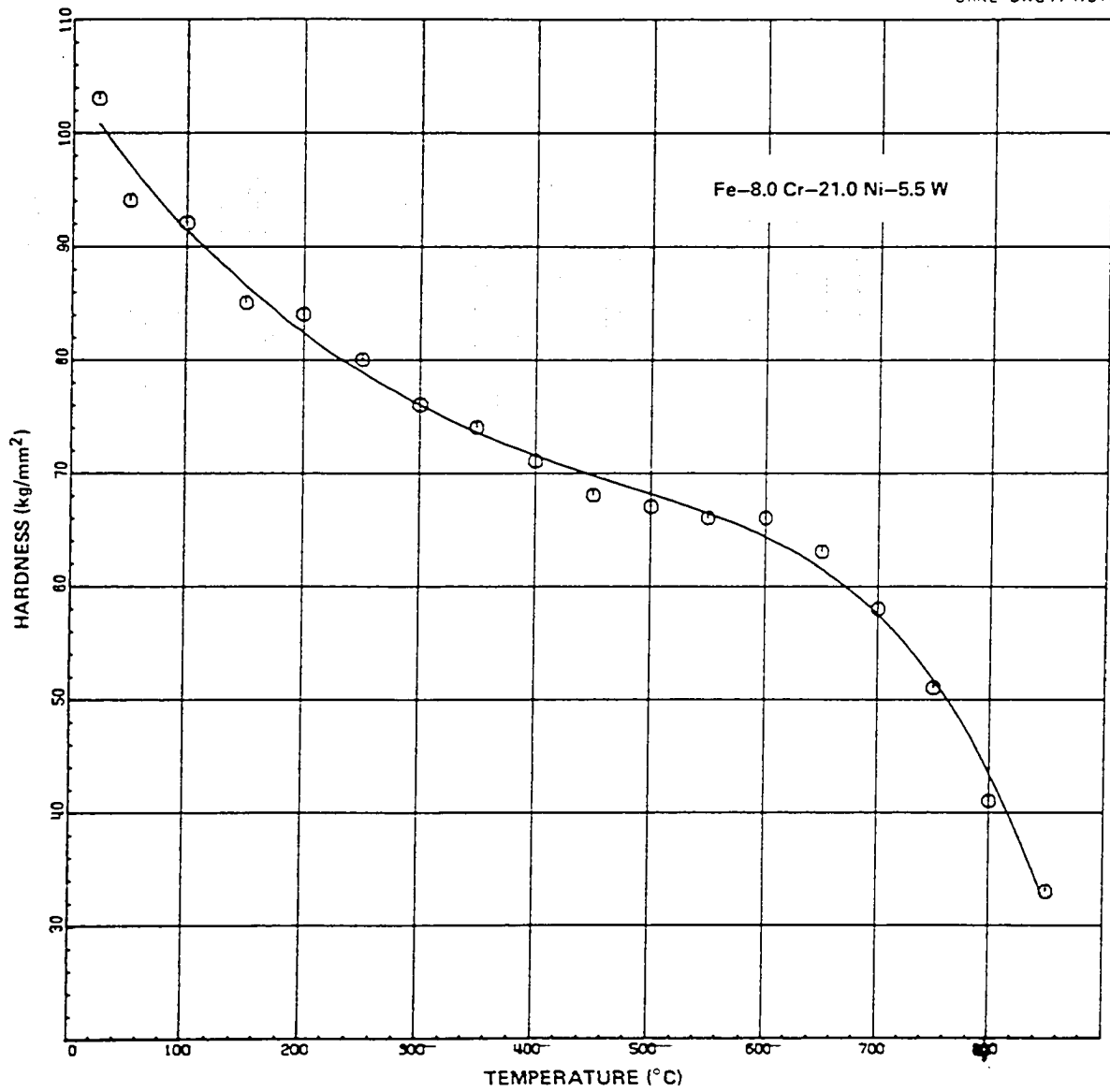


Figure 48. Hot hardness data for an Fe-8.0 Cr-21 Ni-5.5 W alloy.

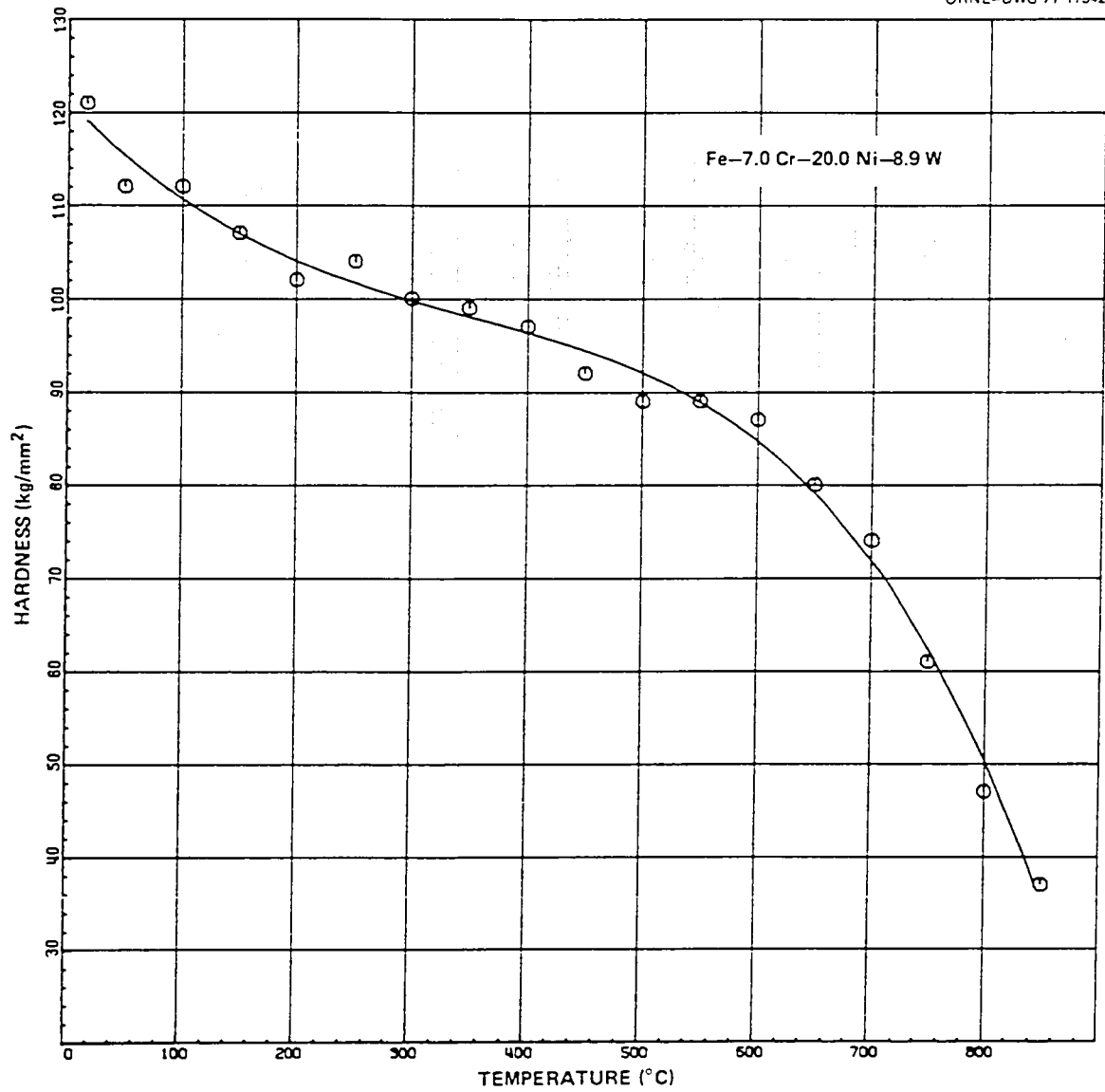


Figure 49. Hot hardness data for an Fe-7.0 Cr-20 Ni-8.9 W alloy.

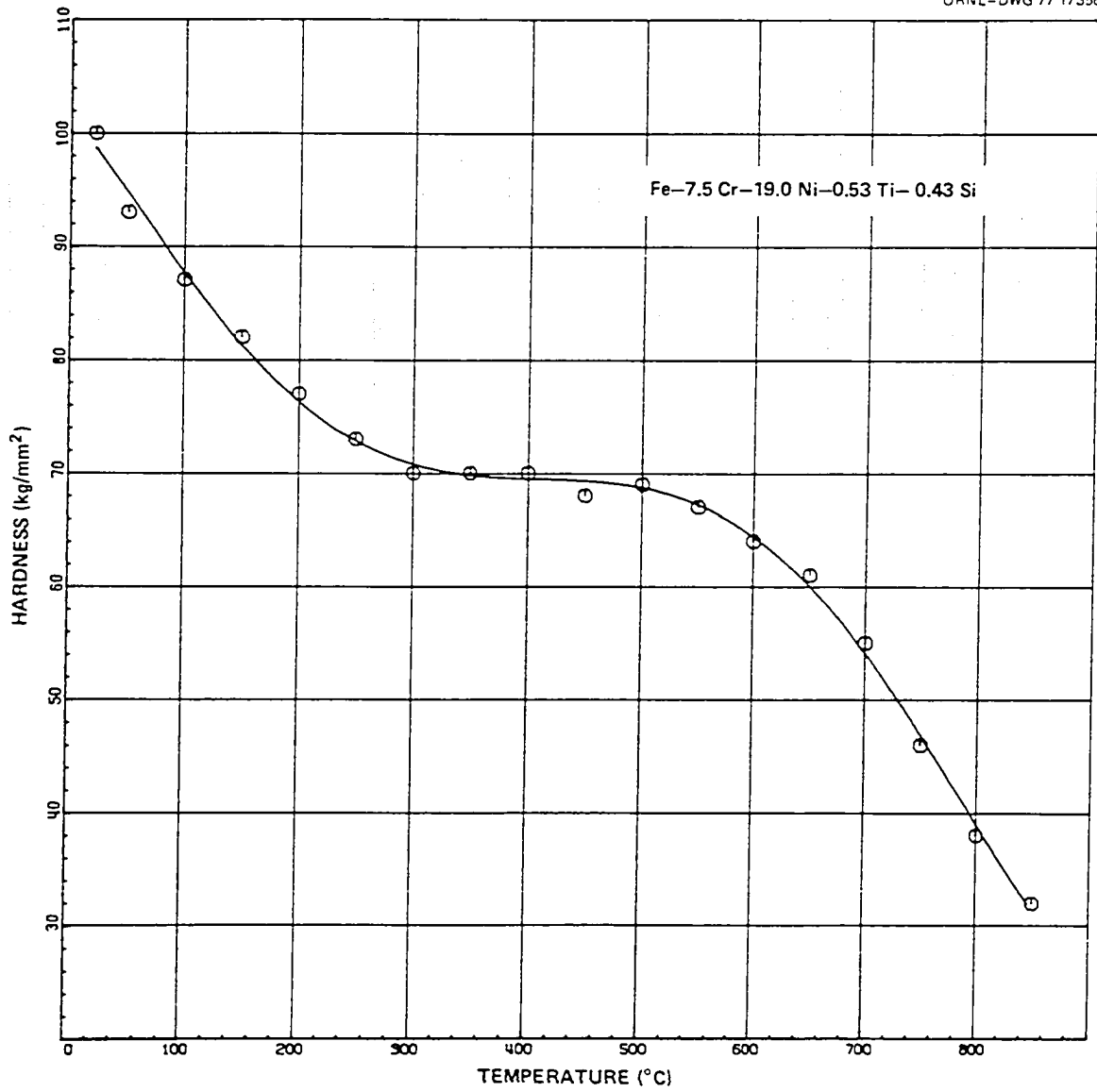


Figure 50. Hot hardness data for an Fe-7.5 Cr-19 Ni-0.53 Ti-0.43 Si alloy.

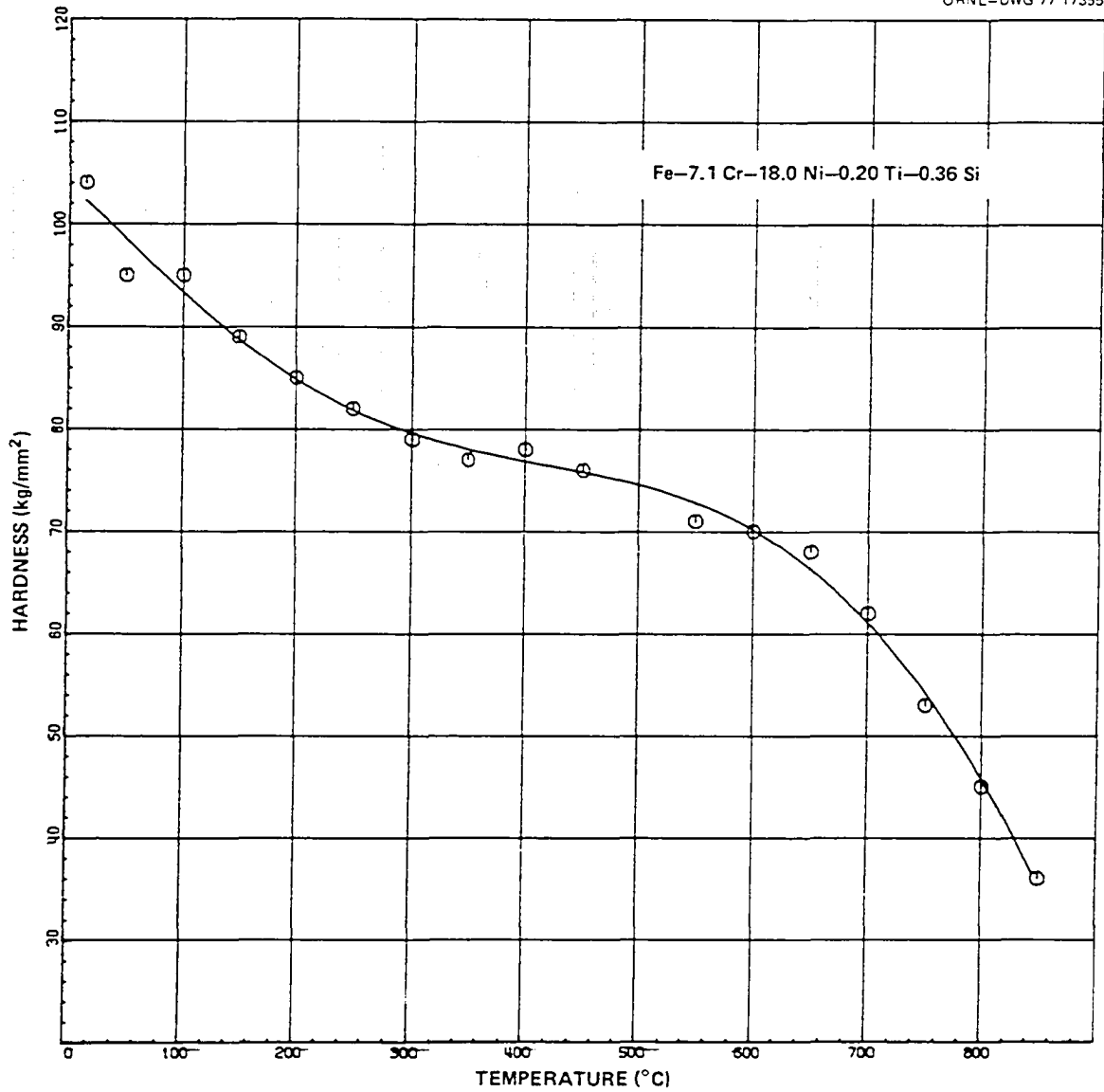


Figure 51. Hot hardness data for an Fe-7.1 Cr-18 Ni-0.20 Ti-0.36 Si alloy.

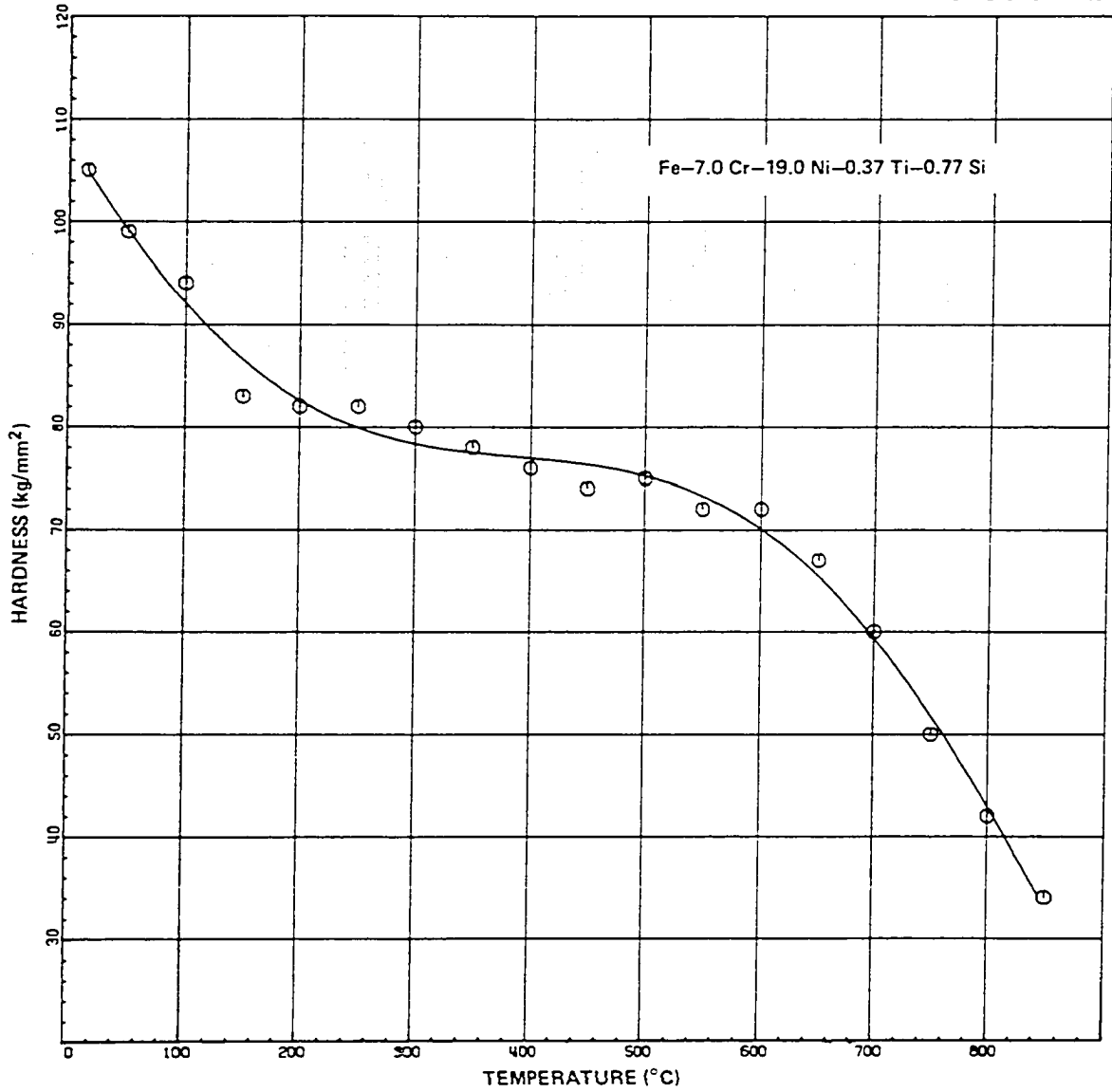


Figure 52. Hot hardness data for an Fe-7.0 Cr-19 Ni-0.37 Ti-0.77 Si alloy.

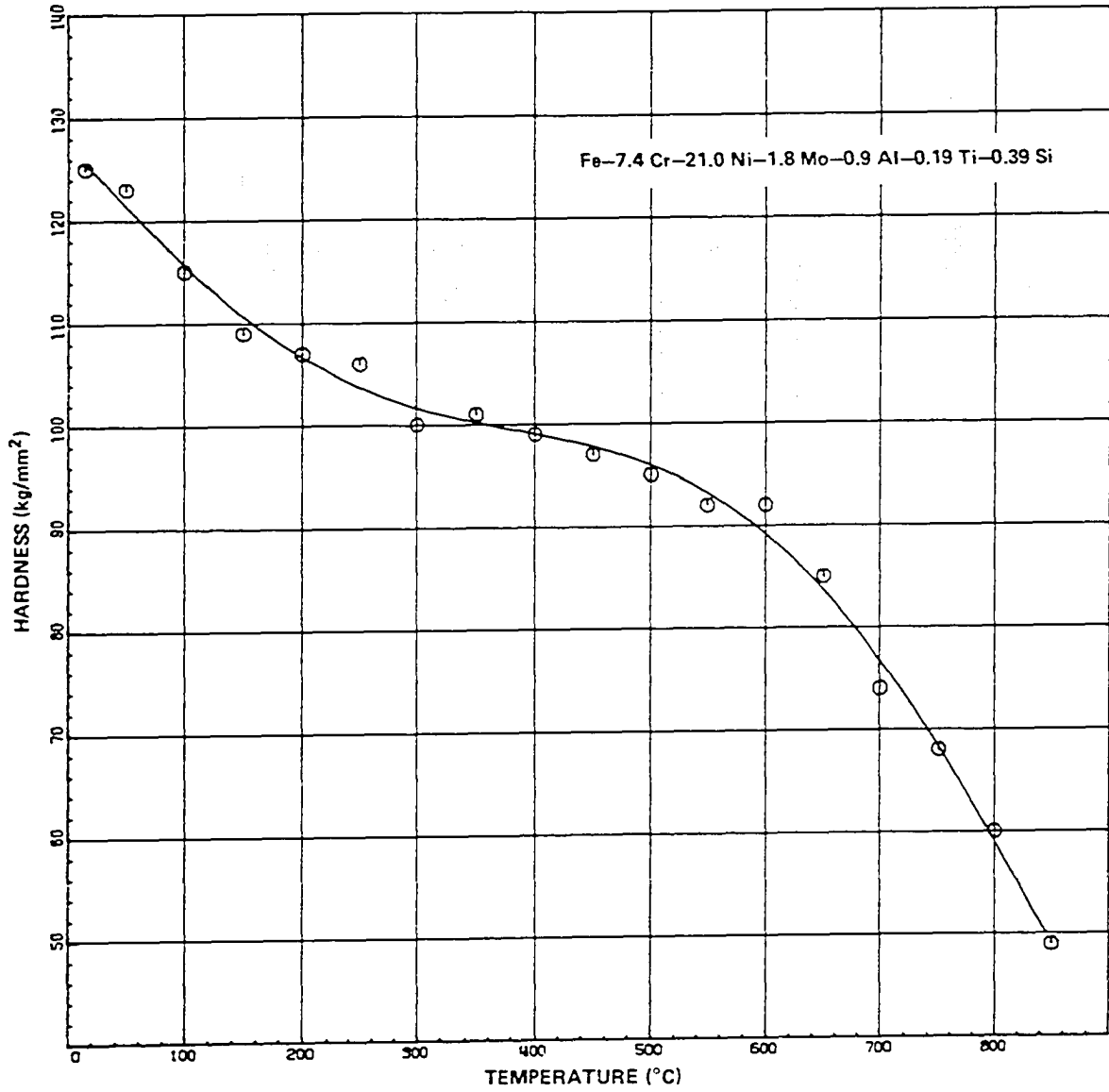


Figure 53. Hot hardness data for an Fe-7.4 Cr-21 Ni-1.8 Mo-0.9 Al-0.19 Ti-0.39 Si alloy.

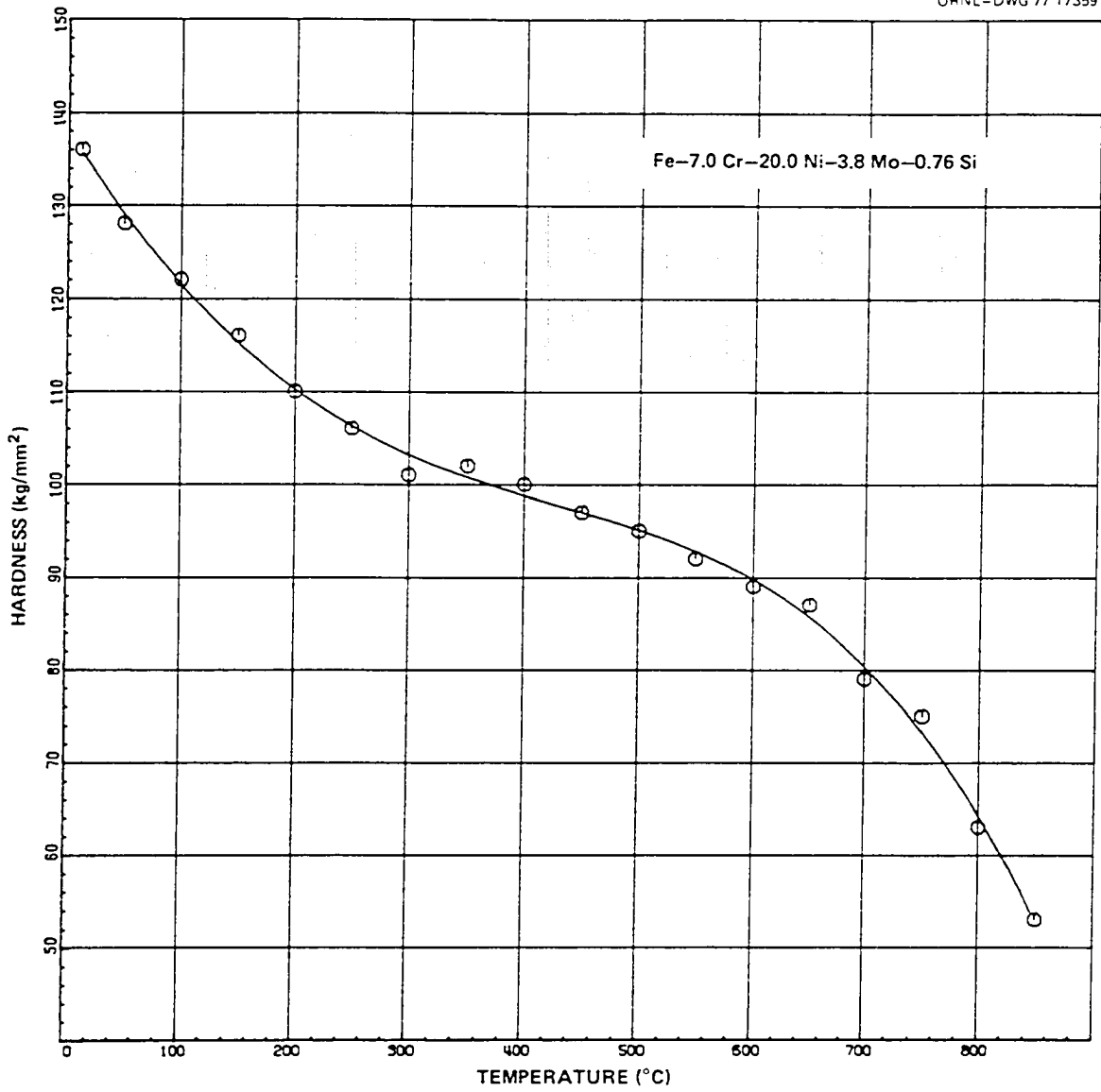


Figure 54. Hot hardness data for an Fe-7.0 Cr-20 Ni-3.8 Mo-0.76 Si alloy.

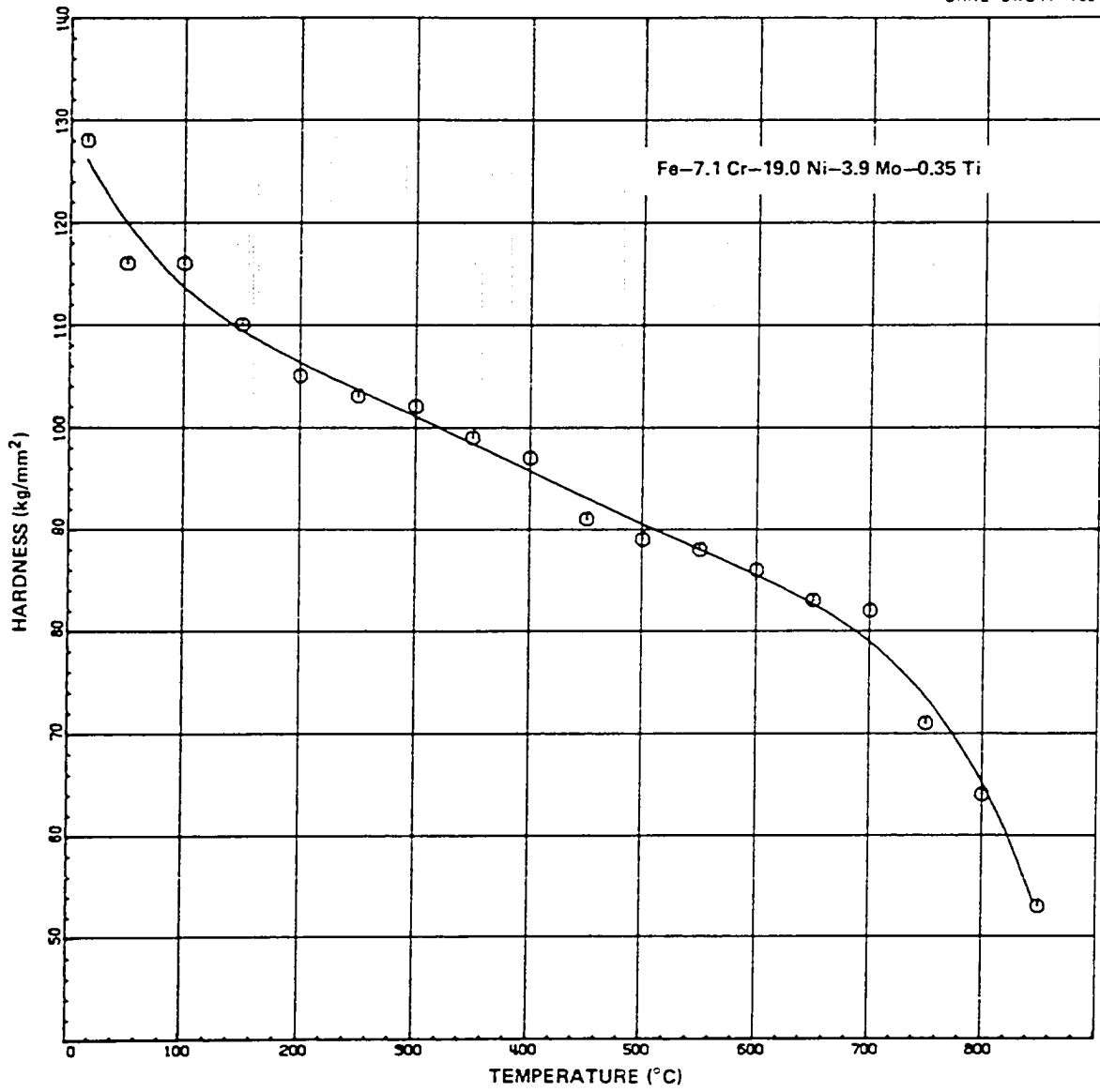


Figure 55. Hot hardness data for an Fe-7.1 Cr-19 Ni-3.9 Mo-0.35 Ti alloy.

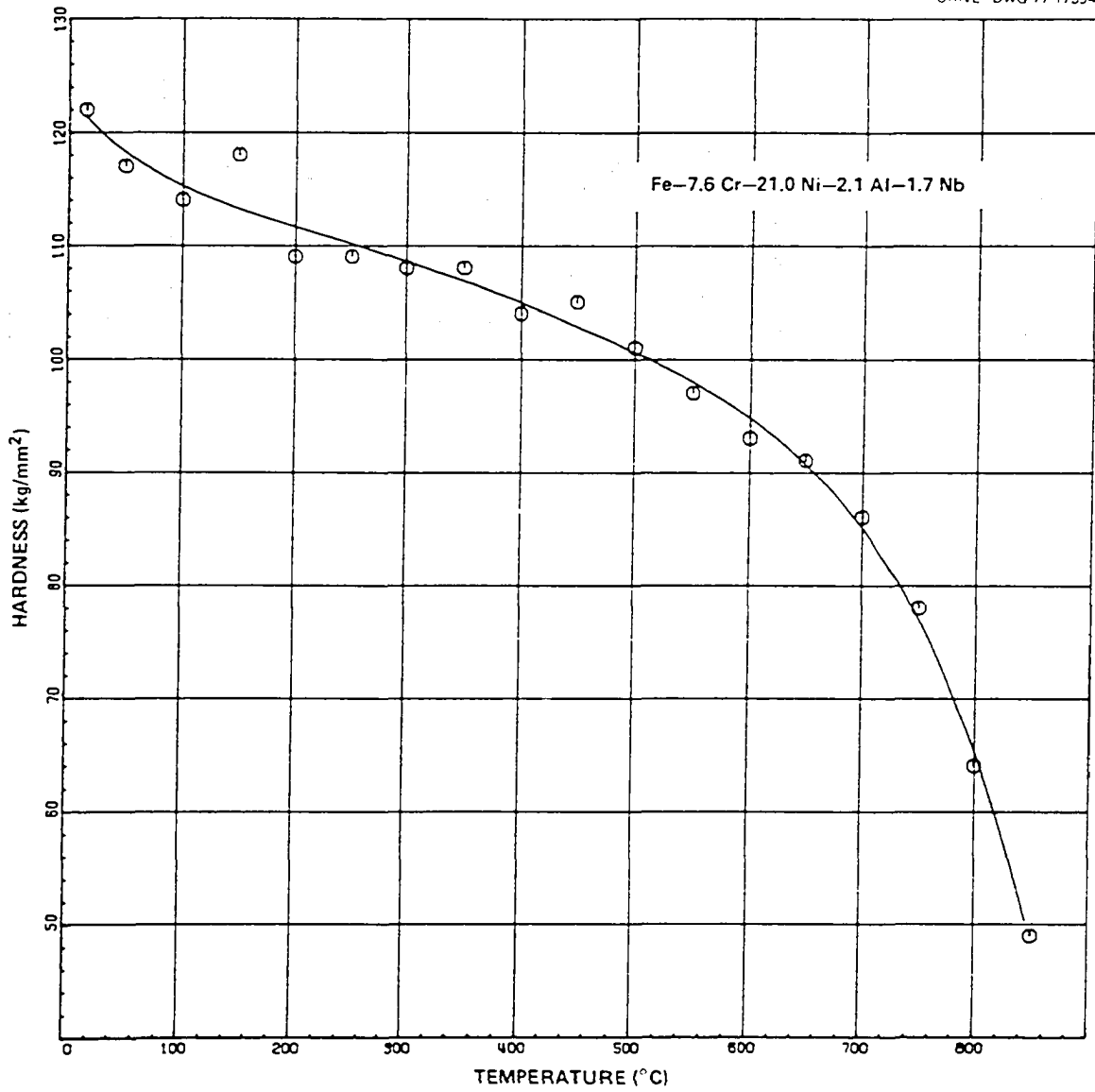


Figure 56. Hot hardness data for an Fe-7.6 Cr-21 Ni-2.1 Al-1.7 Nb alloy.

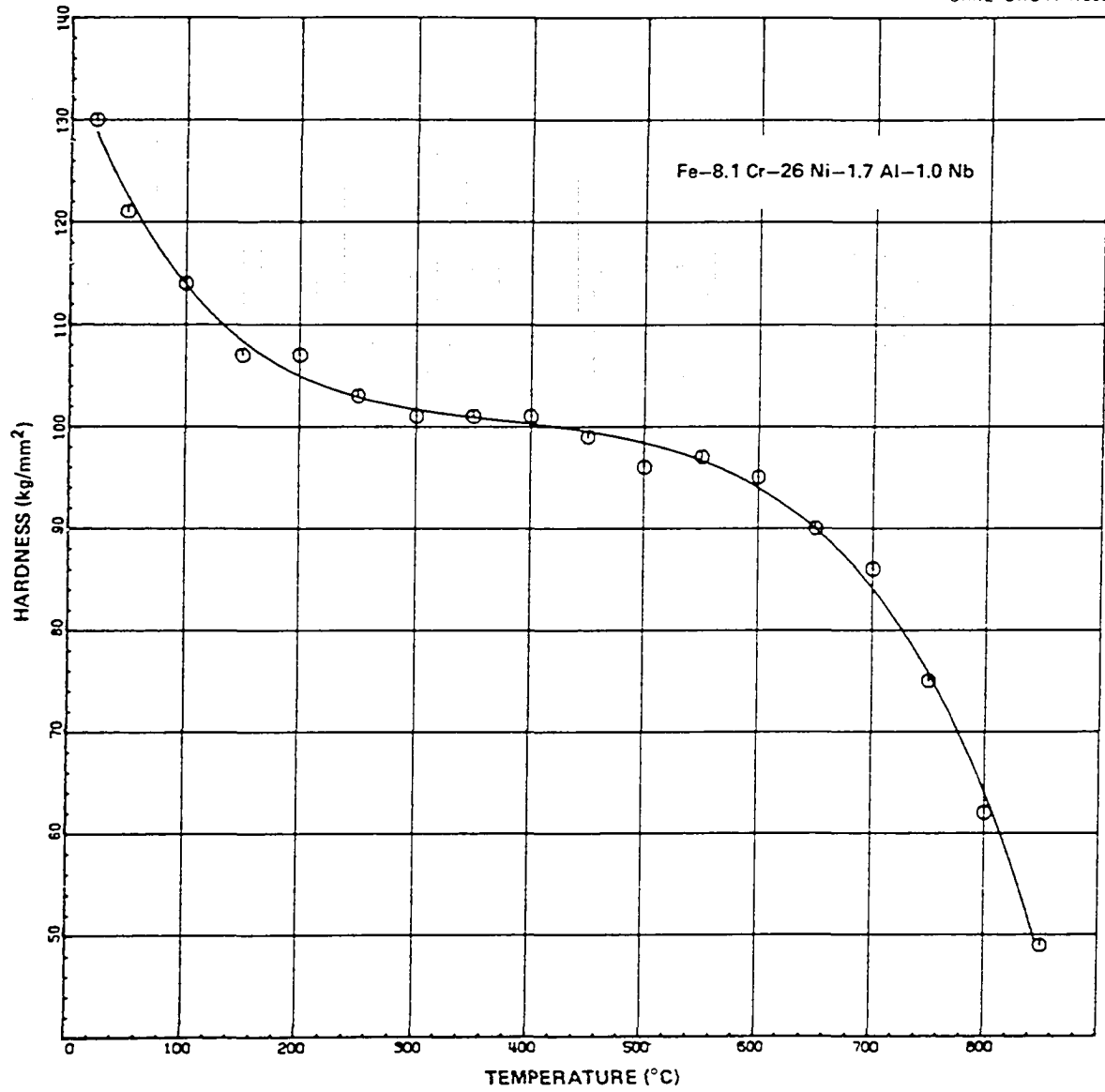


Figure 57. Hot hardness data for an Fe-8.1 Cr-26 Ni-1.7 Al-1.0 Nb alloy.

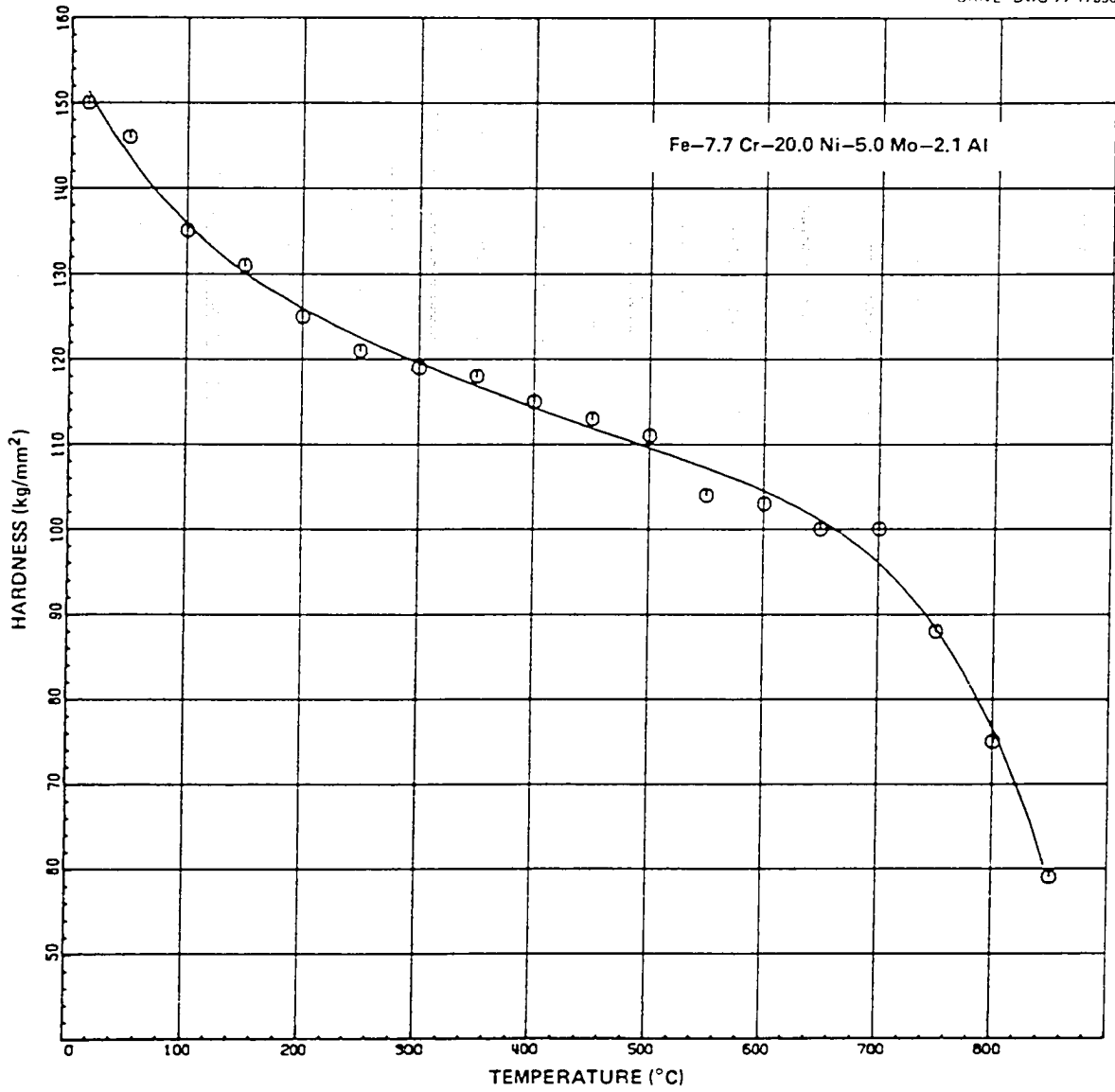


Figure 58. Hot hardness data for an Fe-7.7 Cr-20 Ni-5.0 Mo-2.1 Al alloy.

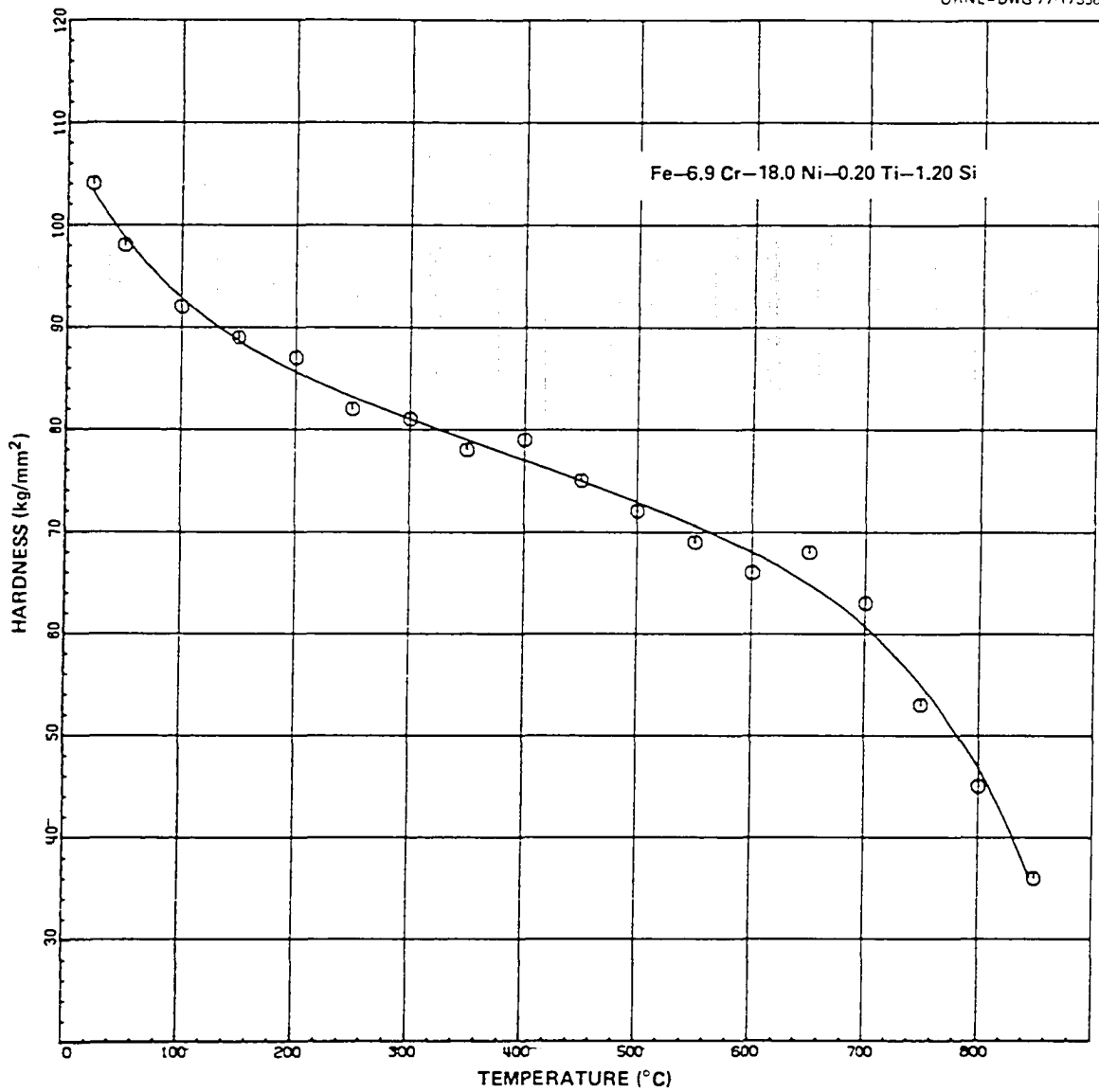


Figure 59. Hot hardness data for an Fe-6.9 Cr-18 Ni-0.20 Ti-1.20 Si alloy.

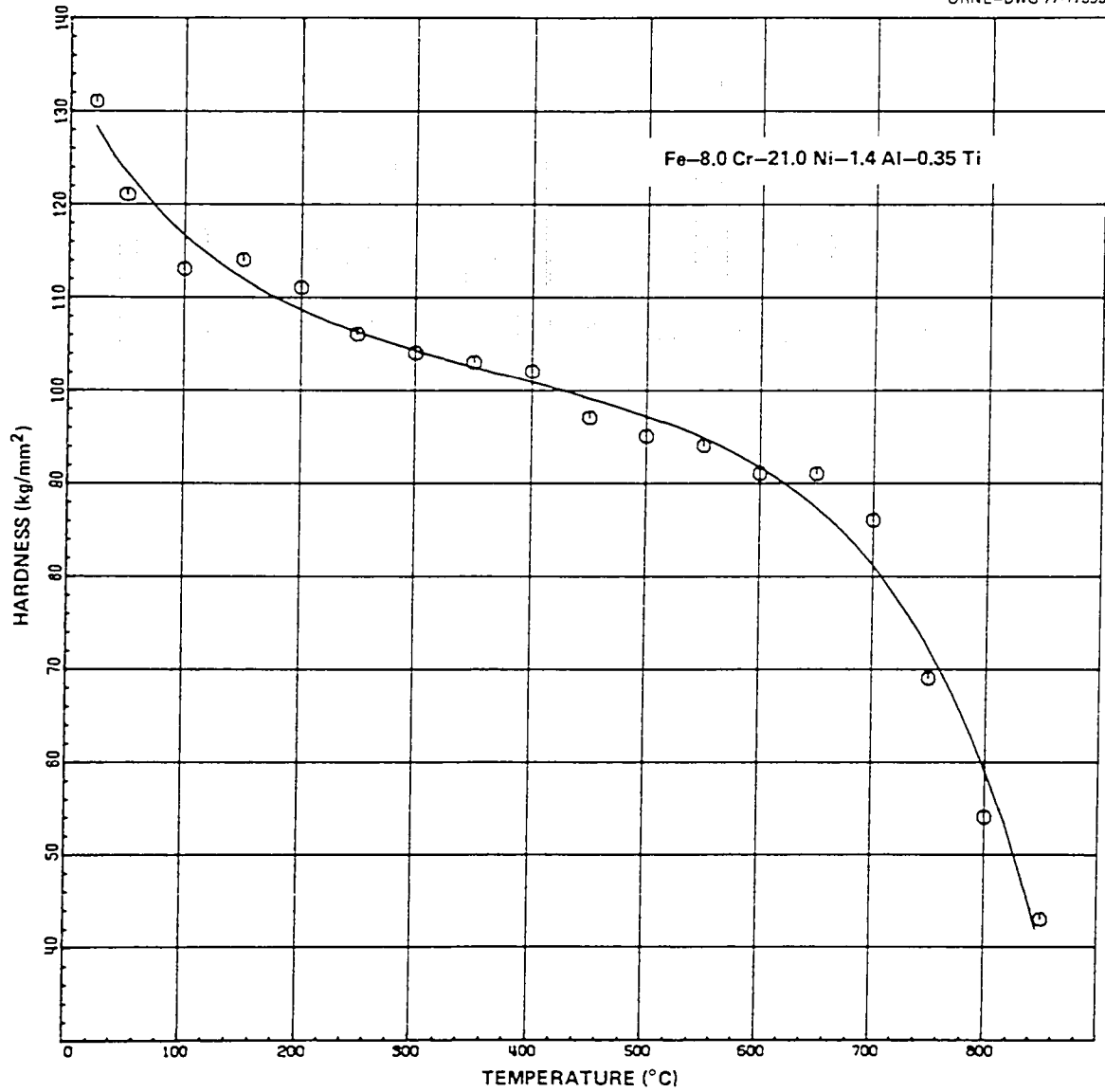


Figure 60. Hot hardness data for an Fe-8.0 Cr-21 Ni-1.4 Al-0.35 Ti alloy.

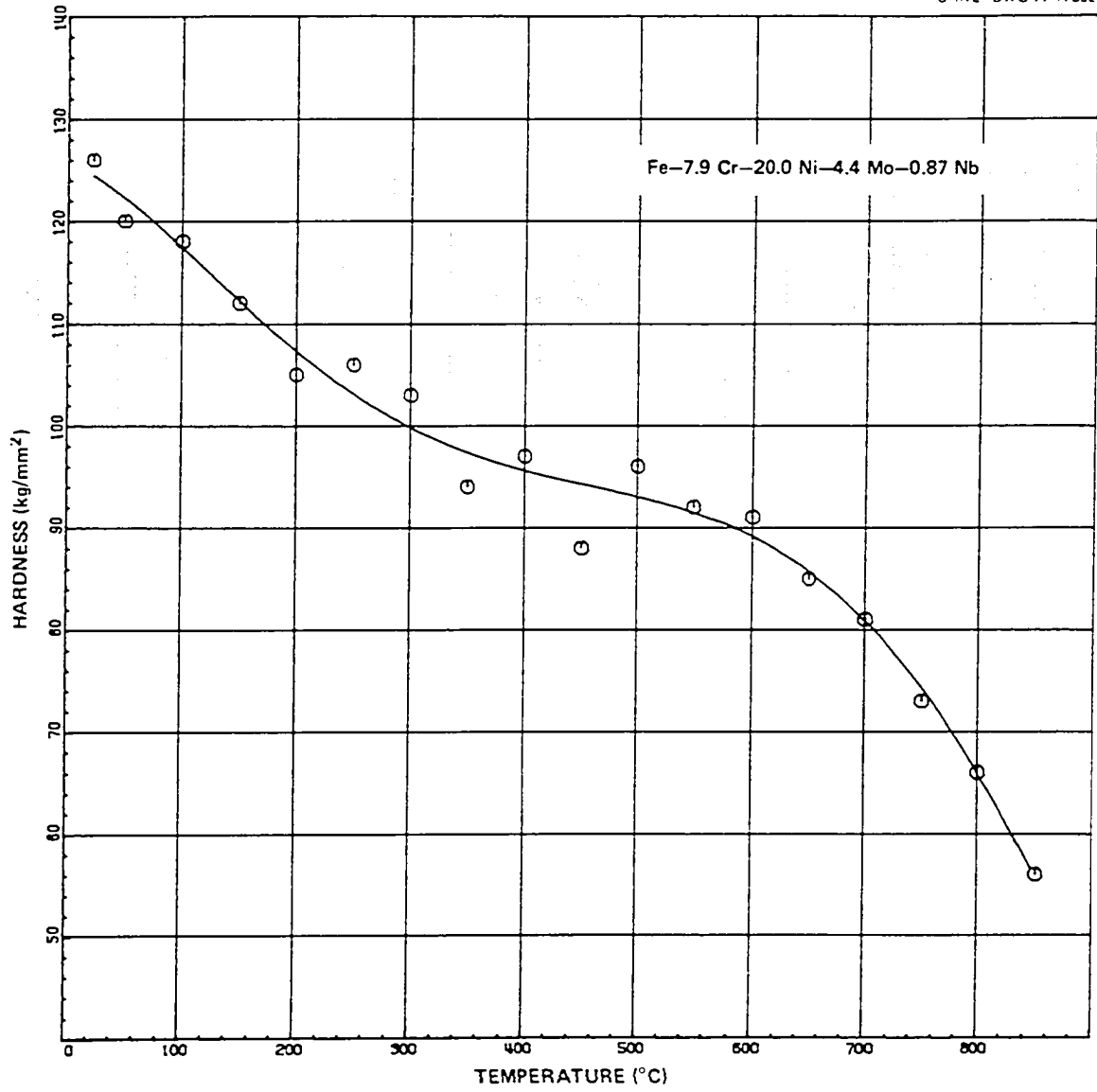


Figure 61. Hot hardness data for an Fe-7.9 Cr-20 Ni-4.4 Mo-0.87 Nb alloy.

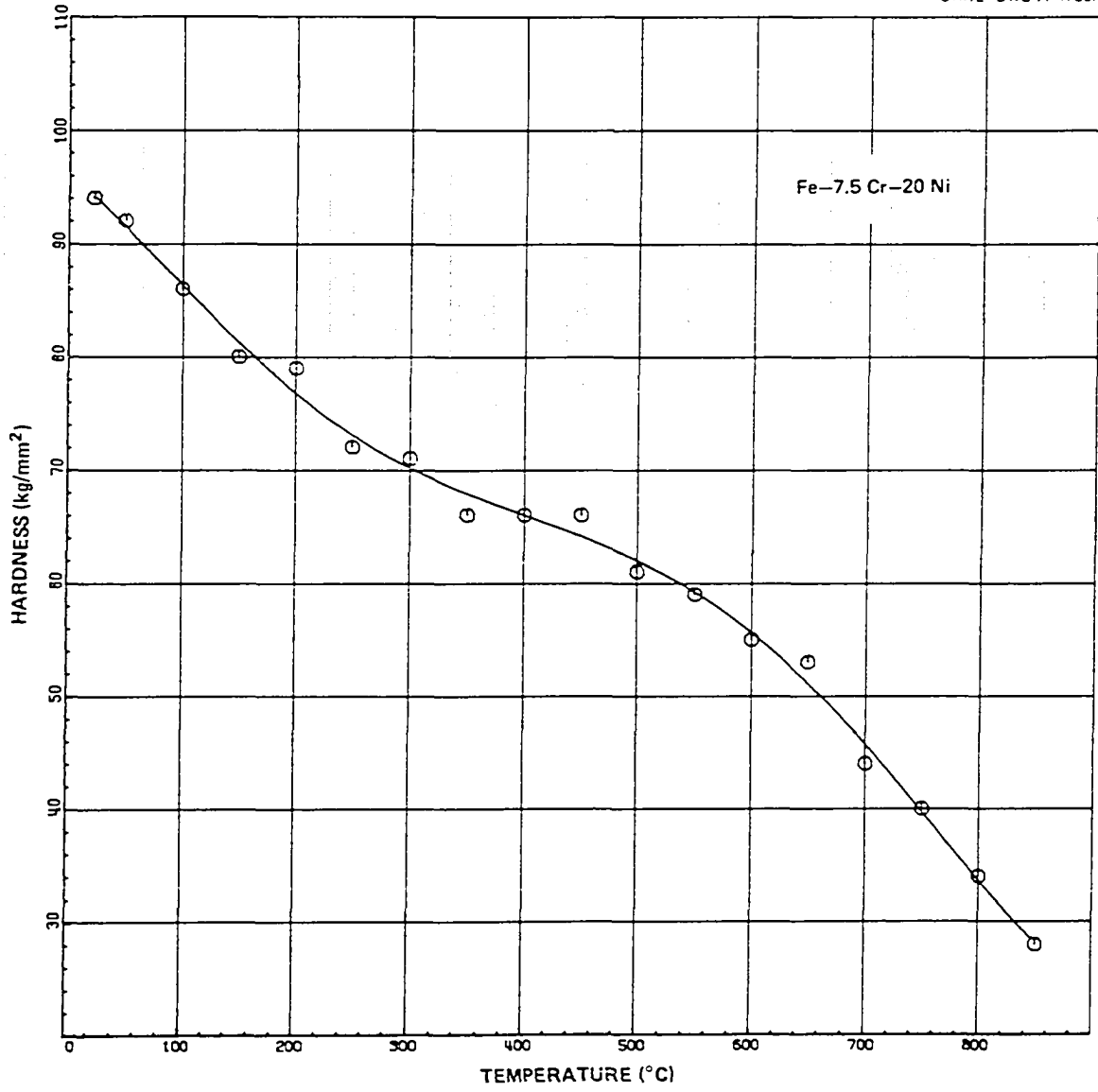


Figure 62. Hot hardness data for an Fe-7.5 Cr-20 Ni alloy.

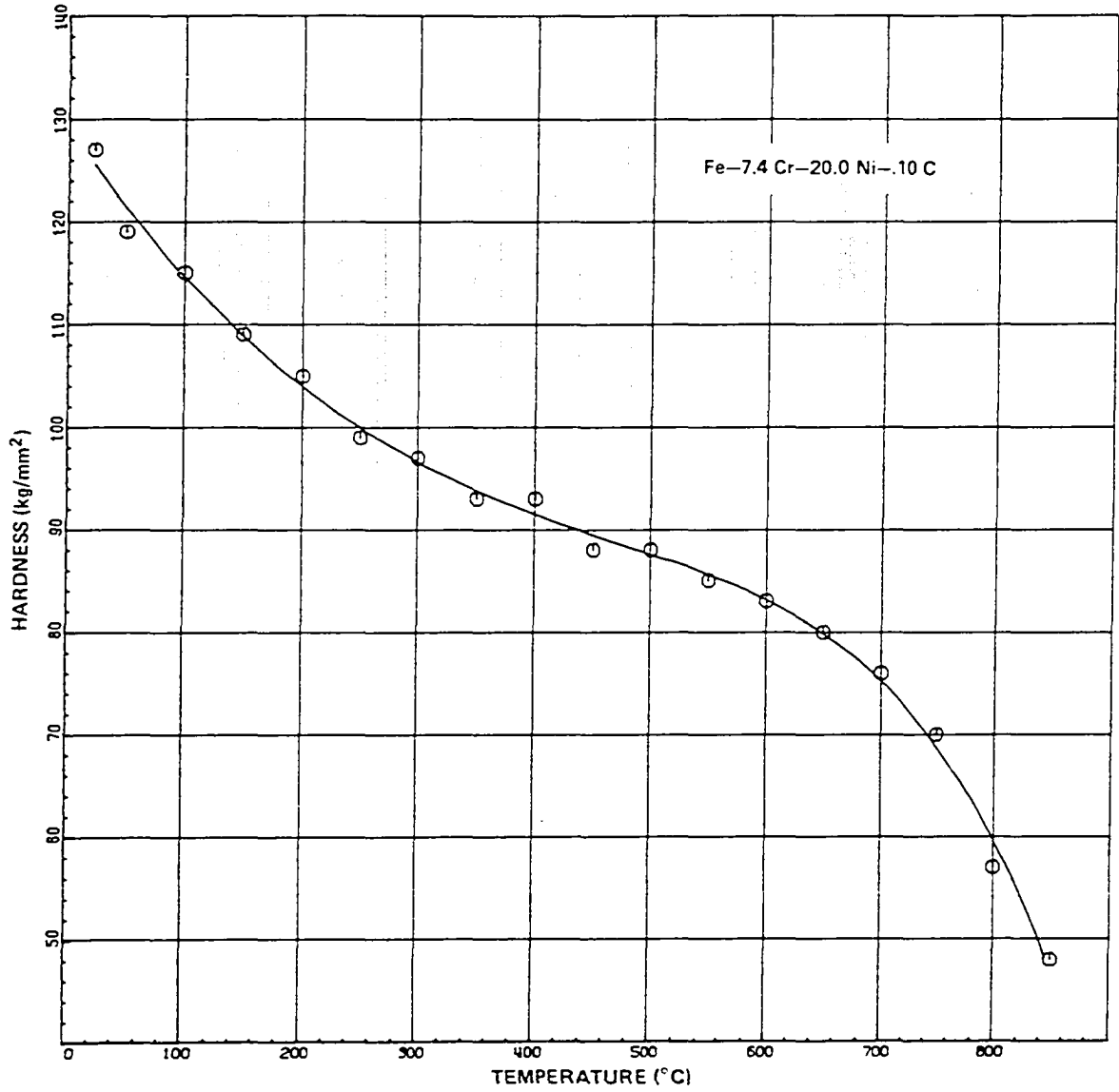


Figure 63. Hot hardness data for an Fe-7.4 Cr-20 Ni-0.10 C alloy.

increased vacancy mobility beyond 600°C could possibly explain the increased strain rate there. At temperatures below 600°C the hardness also decreases with increasing temperature but at a much less rapid rate. This decrease is probably due to a decrease in the modulus with temperature. Such decreases in modulus with temperature have been observed in other stainless steels of similar composition.

Examination of Figures 34-63 shows that each addition affects the shape of the hardness curve. All additions do result in an increase in hardness over that of the base alloy. However, on an atom percent basis each element produces a different amount of hardening. This is clearly shown in Figures 64-66 which give hardness as a function of atom % addition of the different elements. There is some variation in the way the elements are ranked at different temperatures. This most likely results from experimental scatter. At most temperatures the elements in decreasing order of effectiveness are Nb, Ti, Mo, W, Al and Si. The question naturally arises as to what factors influencing alloy hardening gives rise to the observed relative effectiveness. Reference to Table 3, page 84, gives some indication. The lattice parameter changes and observed swellings rank in the same fashion. While the observed changes in lattice parameter alone do not account for the hardness increases, they are a measure of the lattice dilatation resulting from a given addition. As previously mentioned, this lattice dilatation has associated strains which impede dislocation motion.

Another effect of alloying on the hardness of the ternary alloy is to alter the shape of the hardness curve in the temperature region

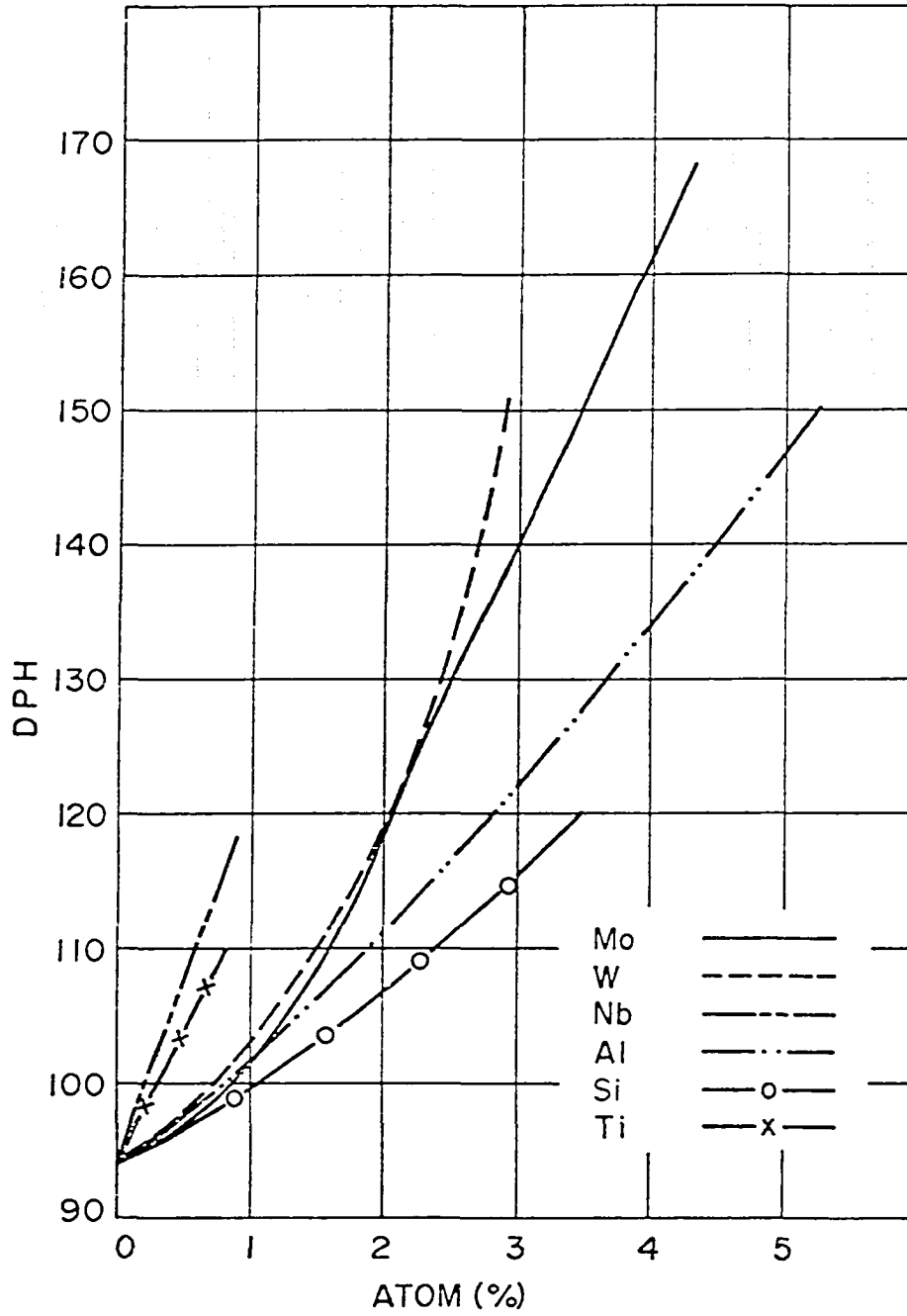
Y-136150
ORNL-DWG 76-2525

Figure 64. Effect of alloying element on the hardness of an Fe-7.5 Cr-20 Ni ternary at 22°C.

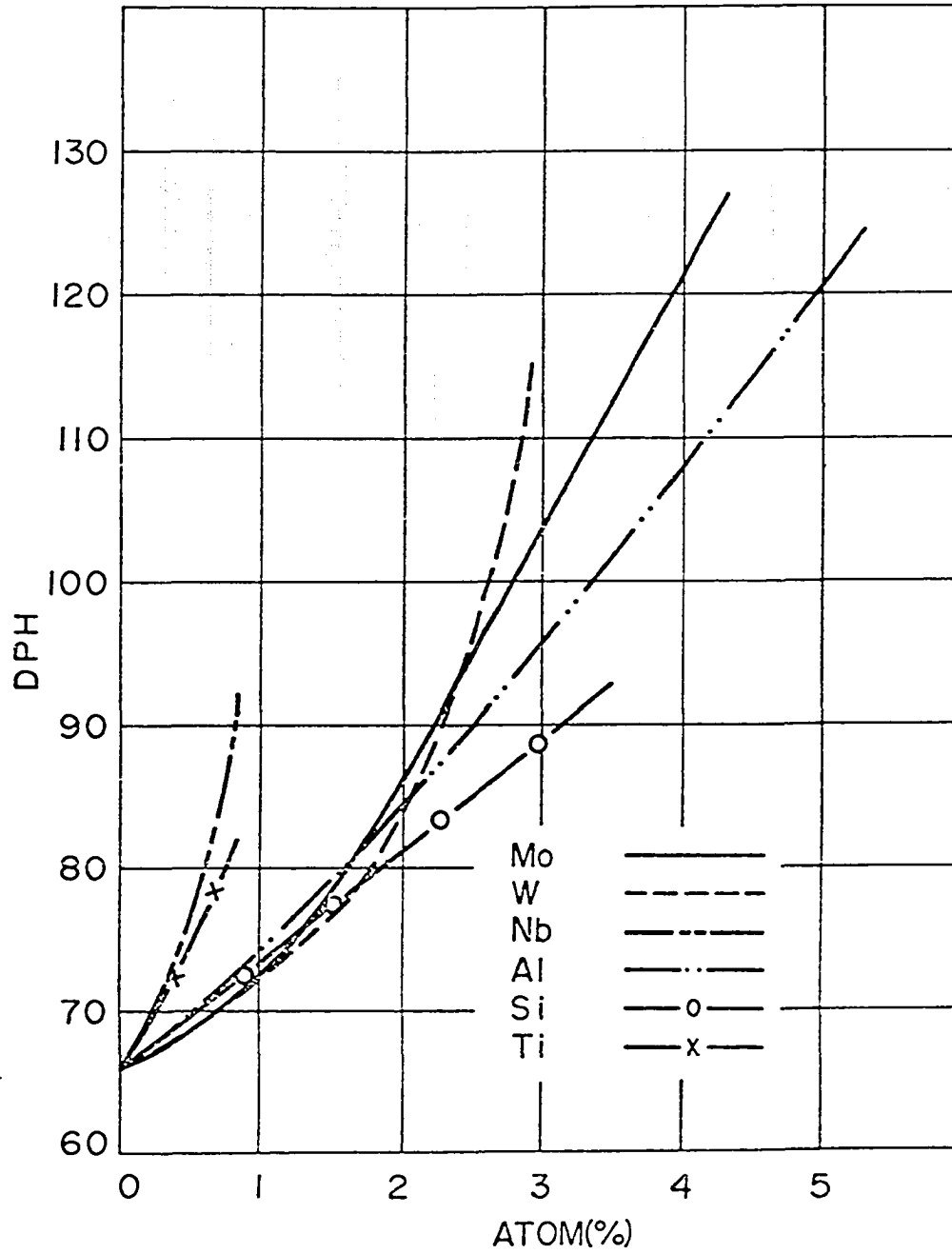


Figure 65. Effect of alloying element on the hardness of an Fe-7.5 Cr-20 Ni ternary at 400°C.

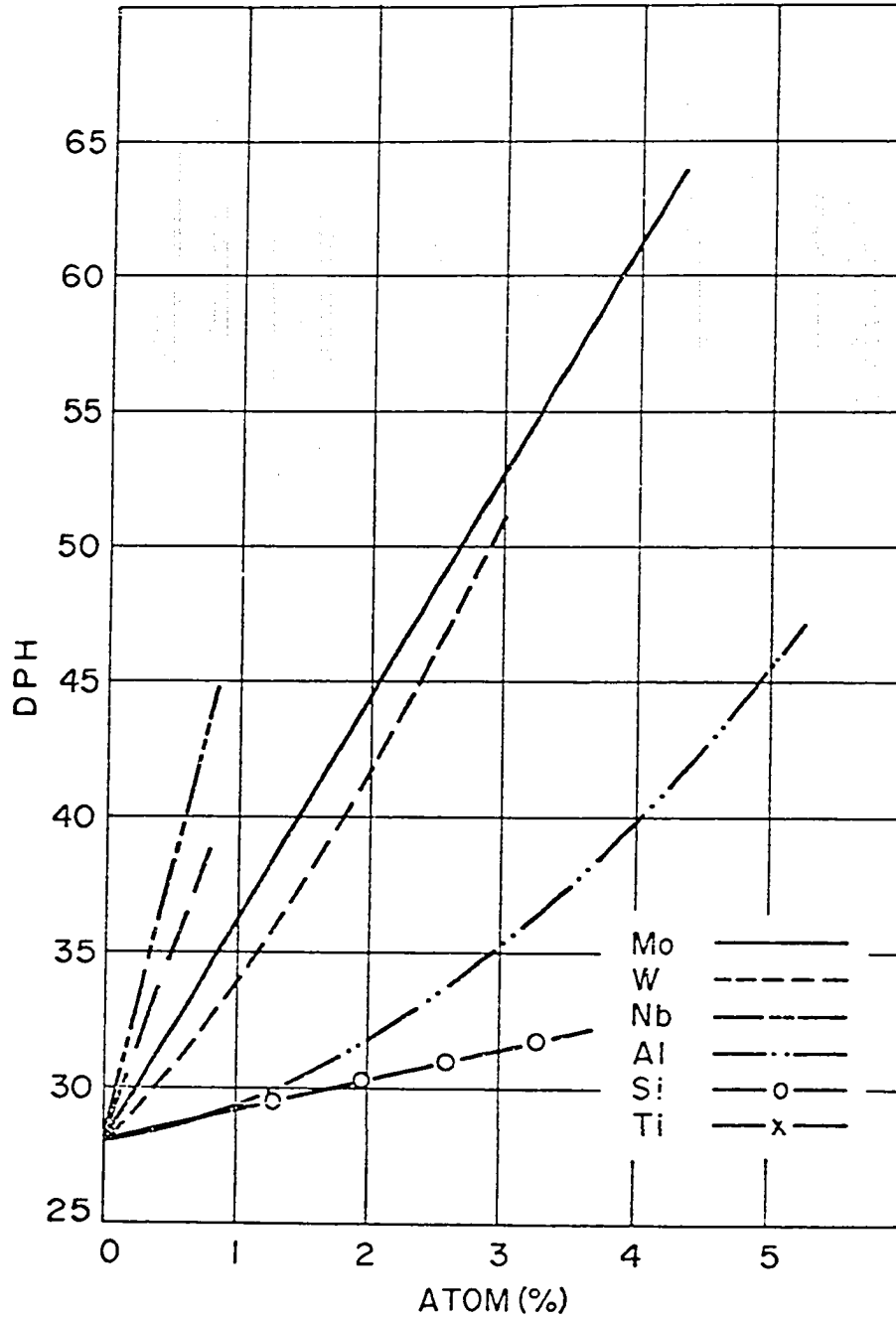
Y-136152
ORNL-DWG 76-2527

Figure 66. Effect of alloying element on the hardness of an Fe-7.5 Cr-20 Ni ternary at 850°C.

below 600°C. At higher temperatures (500-850°C), Ti, Mo, W, and Nb additions show a temperature dependence similar to that for the ternary alloy while for Al and Si additions the hardness decreases more rapidly with increasing temperature. As Figures 64, 65 and 66 clearly show, some elements are considerably more effective in producing strengtheners.

Swelling Measurements

Single additions

Step height versus temperature data for the alloys containing single solute additions are presented in Figures 67-73. Continuous curves have been hand drawn through each set of points. An estimate of the swelling in the peak damage region was obtained from the empirical relationship, 1% peak swelling $\equiv 60 \text{ \AA}$ step height, determined by Johnston et al. (3). It should be noted that step height values of $\sim 100 \text{ \AA}$ represent the lower limit of detection of swelling. Additions of molybdenum or tungsten produced similar effects. Both elements suppressed swelling without any marked influence on the peak swelling temperature, as shown in Figures 67 and 68. The magnitude of peak swelling decreased with increasing solute concentration except that in the case of 4.34 Mo alloy, swelling was slightly greater than in the other two molybdenum alloys. Only one addition of carbon was investigated, Figure 73. Swelling was reduced over the entire temperature range without a noticeable change in peak swelling temperature range. Alloys containing Si, Ti, or Nb behaved in a significantly different manner. For a given atomic percent

below 600°C. At higher temperatures (500-850°C), Ti, Mo, W, and Nb additions show a temperature dependence similar to that for the ternary alloy while for Al and Si additions the hardness decreases more rapidly with increasing temperature. As Figures 64, 65 and 66 clearly show, some elements are considerably more effective in producing strengtheners.

Swelling Measurements

Single additions

Step height versus temperature data for the alloys containing single solute additions are presented in Figures 67-73. Continuous curves have been hand drawn through each set of points. An estimate of the swelling in the peak damage region was obtained from the empirical relationship, 1% peak swelling $\equiv 60 \text{ \AA}$ step height, determined by Johnston et al. (3). It should be noted that step height values of $\sim 100 \text{ \AA}$ represent the lower limit of detection of swelling. Additions of molybdenum or tungsten produced similar effects. Both elements suppressed swelling without any marked influence on the peak swelling temperature, as shown in Figures 67 and 68. The magnitude of peak swelling decreased with increasing solute concentration except that in the case of 4.34 Mo alloy, swelling was slightly greater than in the other two molybdenum alloys. Only one addition of carbon was investigated, Figure 73. Swelling was reduced over the entire temperature range without a noticeable change in peak swelling temperature range. Alloys containing Si, Ti, or Nb behaved in a significantly different manner. For a given atomic percent

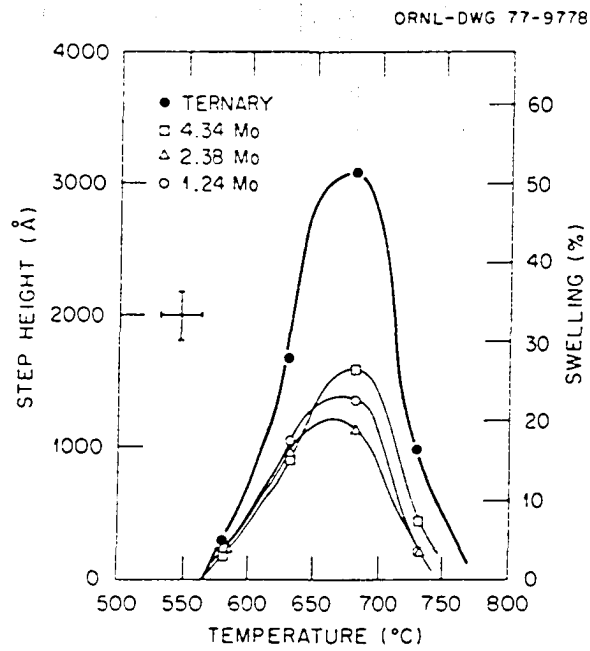


Figure 67. Step height versus temperature data for alloys containing molybdenum.

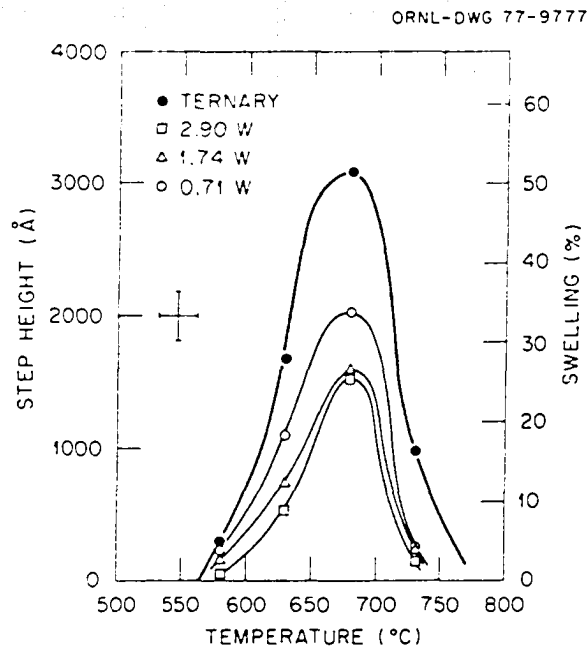


Figure 68. Step height versus temperature data for alloys containing tungsten.

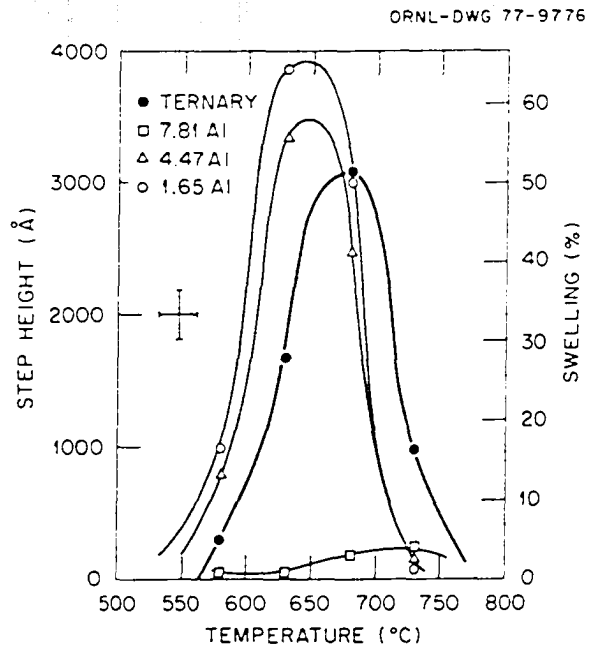


Figure 69. Step height versus temperature data for alloys containing aluminum.

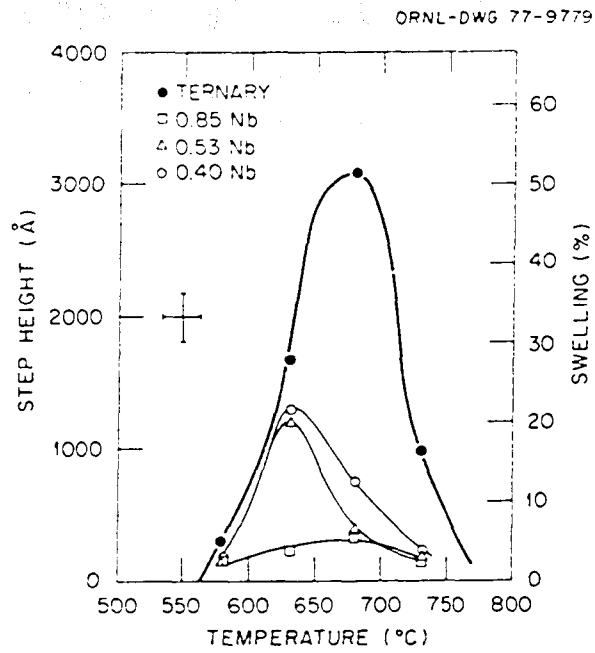


Figure 70. Step height versus temperature data for alloys containing niobium.

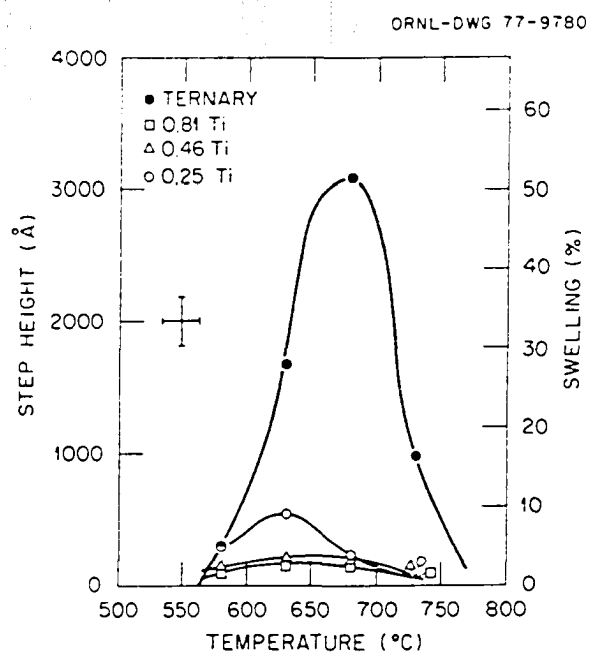


Figure 71. Step height versus temperature data for alloys containing titanium.

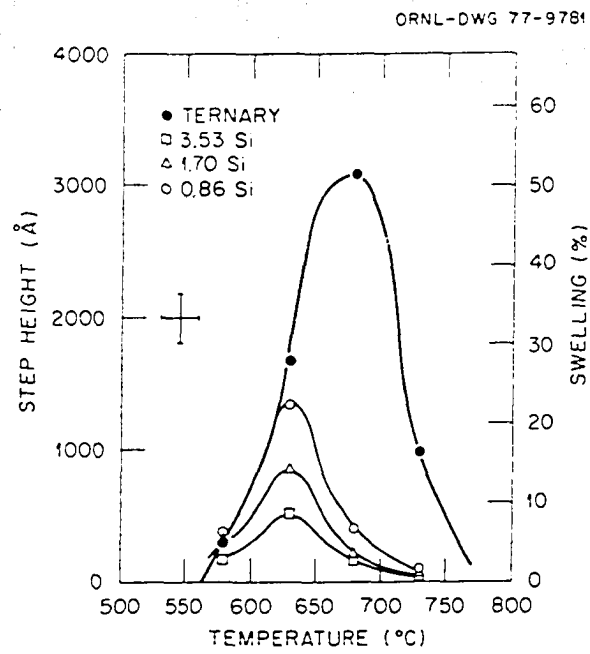


Figure 72. Step height versus temperature data for alloys containing silicon.

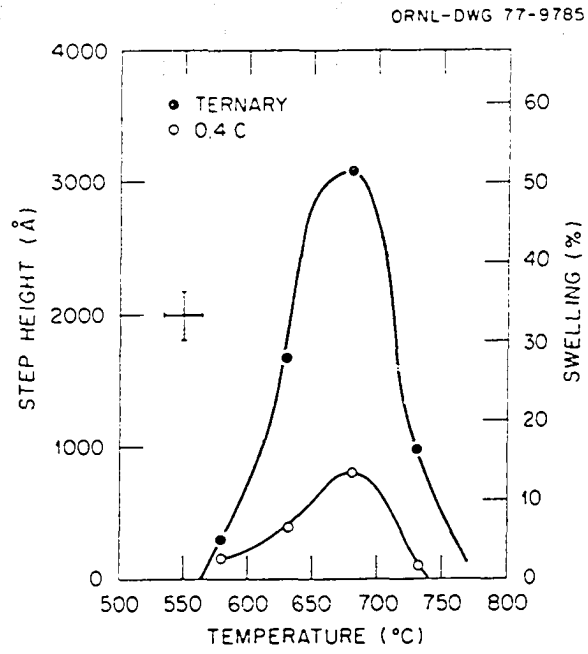


Figure 73. Step height versus temperature data for alloys containing carbon.

addition, swelling was reduced more effectively than in the case of molybdenum or tungsten alloys, and in addition, the peak swelling temperature was reduced by about 60°C. Titanium was the most effective element, Figure 71, and the addition of only 0.46 at % reduced swelling to the limits of detectability at all temperatures. Niobium also strongly reduced high temperature swelling, Figure 70. The addition of 0.85 at. % Nb depressed the swelling curve to below the 5% level, although, as pointed out previously, there is a strong possibility that precipitation of a fine coherent phase occurred in this alloy during bombardment. The behavior of aluminum, Figure 69, is of considerable interest since it is a component of many γ' strengthened stainless steels and nickel alloys. The addition of 1.65 at. % Al produced a significant increase in swelling accompanied by a decrease in peak swelling temperature. When the aluminum concentration was increased to 4.47 at. %, peak swelling decreased slightly but was still greater than in the ternary alloy. However, a further increase to 7.81 at. % eliminated swelling at all temperatures. Thermal aging studies revealed the formation of a finely dispersed γ' at the peak temperature in this alloy. It is suggested that as the aluminum is added to the ternary alloy a finely dispersed phase is eventually formed which inhibits swelling and overrides the swelling enhancement due to the aluminum in solution.

Since the temperature dependence of swelling varies with solute addition, any comparison of the relative effectiveness of each element will vary with the temperature selected. For example, from Figure 69,

aluminum may be considered to enhance swelling at 600°C, have no effect at 675°C and to suppress swelling at 700°C. We have therefore chosen to compare the effectiveness of each element at the peak swelling temperature for each alloy. Figure 74 shows peak temperature swelling plotted against atomic concentration for each solute. Of the elements studied, titanium is the most effective in suppressing swelling followed in order by C, Nb, Si, Mo, W, and Al. In most cases, although swelling is reduced rapidly by the initial addition, the effect eventually begins to saturate.

These results are in general agreement with those obtained by Johnston et al. working with an Fe-15 Cr-20 Ni base alloy (84). However, molybdenum and carbon provide two notable exceptions. Johnston et al. found that an initial addition of ~ 0.4 at. % of molybdenum increased the swelling of the base alloy at 675°C. With increased levels of molybdenum, swelling subsequently decreased, but always remained higher than in the ternary alloy. In the present work, molybdenum additions from 1.24 to 4.34 at. % reduced swelling at all temperatures with swelling tending to increase slightly at the highest concentration. It has been demonstrated that the techniques used in the two laboratories produce the same results with the same alloys and it is concluded that the behavior of molybdenum is related to the difference in chromium content between the two alloys. With regard to the effect of carbon, Johnston et al. found that additions of 0.3 and 0.6 at. % successively increased swelling at 675°C. In our work it was found that an addition of 0.4 at. % carbon decreased swelling over the entire temperature range. Thus the influence of carbon

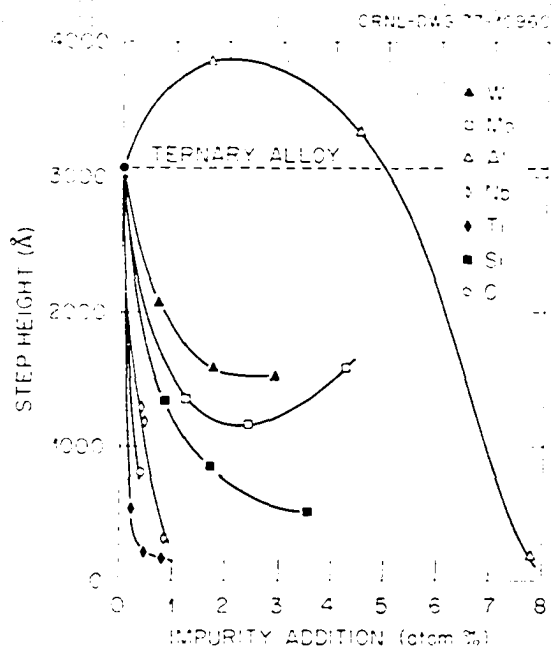


Figure 74. Step height at the peak temperature versus solute concentration for all elements.

and molybdenum on swelling appears to be strongly dependent upon the chromium content of the host alloy.

Double additions

The data for four silicon and titanium alloys are shown in Figure 75. Two aspects of these data are particularly noteworthy. First, all four alloys show very little swelling. A step of 150-200 Å is expected to result from nickel ion injection alone. This consideration places all these measurements at the limit of detectability. Second, despite their large dissimilarity in composition all four alloys show step heights that are identical within experimental error. Likewise, the step height appears to have little or no temperature sensitivity. In Figure 76 data are shown for alloys containing molybdenum with further additions of Nb, Ti, and Si. Again the alloys containing (Mo + Ti) and (Mo + Si) show essentially no swelling over the whole temperature range examined. The 2.63 Mo + 0.56 Nb alloy does, however, exhibit measurable swelling. The temperature dependence of this composite alloy does not appear to differ greatly from that observed for the 0.53 Nb single addition. The magnitude of swelling is, however, lower than what is observed for either the 0.53 Nb alloy or 2.38 Mo alloy. Experimental data for three alloys containing aluminum together with additions of Ti, Mo, and Nb are contained in Figure 77. In both the (Al + Ti) and (Al + Mo) alloys the swelling is less than what one sees for the single aluminum additions yet greater than what is observed with either titanium or molybdenum added singly. Aluminum and niobium single

ORNL-DWG 77-9786

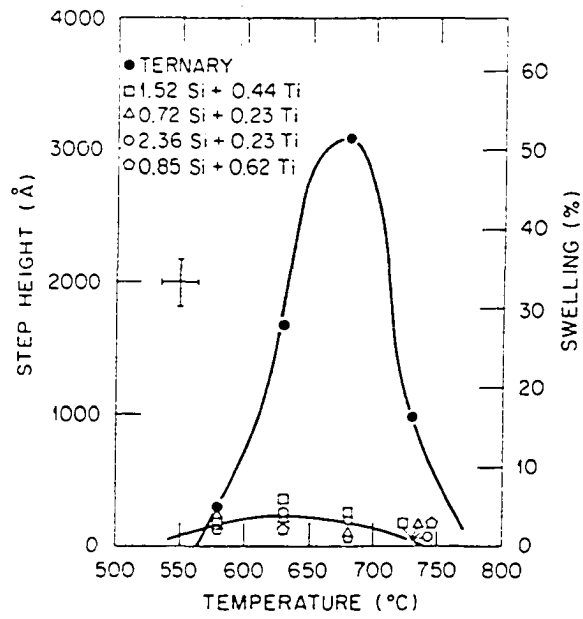


Figure 75. Step height versus temperature for alloys containing double solute additions.

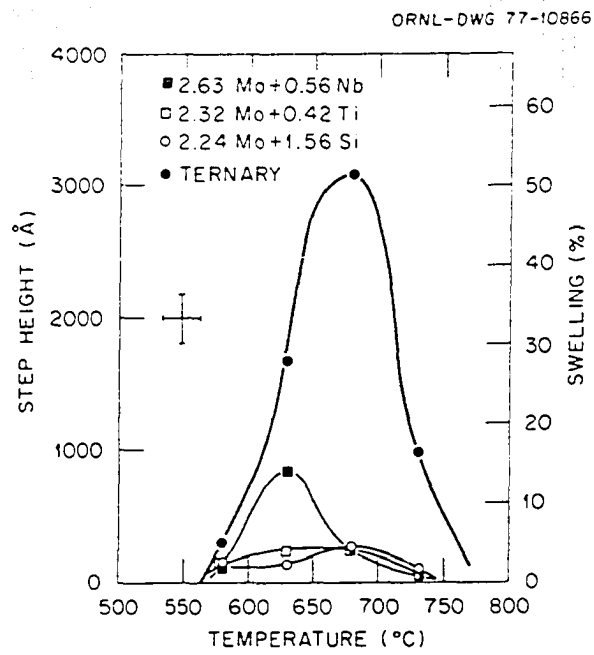


Figure 76. Step height versus temperature for alloys containing double solute additions.

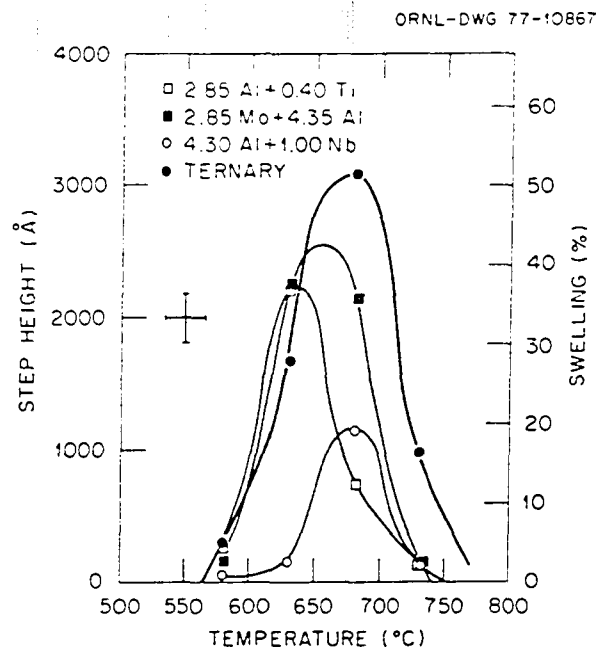


Figure 77. Step height versus temperature for alloys containing double solute additions.

addition produce peak swelling at temperatures of 600-630°C, but in this temperature range swelling appears to be a minimum for the Al + Nb alloy.

DISCUSSION

This section should be regarded as an attempt to extract from that data set some physical understanding of the role that composition plays in both void swelling and strengthening. Because swelling and strengthening have been investigated using very different techniques, each will be considered by itself. Wherever possible, results and interpretations from one data set will be viewed for consistency with the other. Care will be exercised to prevent the analysis from escaping bounds imposed by the nature of the experiments. Aside from a physical understanding one desires some guidance for improving the properties of technologically important alloys. Where possible, suggestions as to how this can be accomplished are presented. Lastly, the data analysis invoked here is not presented as an explanation but rather a reasonable interpretation. It is hoped that such ideas will open new avenues of thought and result in future increased understanding.

Swelling Experiments

General considerations

Before embarking on a discussion of the swelling results it is worthwhile to review some important aspects of the experiments together with the limitations they impose. All irradiations were performed with 4 MeV nickel ions, and no speculations concerning in-reactor behavior will be made. Since swellings were determined by surface profilometry, one expects zero swelling alloys to exhibit a 150-200 Å step due to net

nickel implantation. Care must be taken not to assign too much importance to step heights at this level. TEM was conducted on the alloys in both annealed and aged conditions, and most alloys were found to be free of precipitates prior to irradiation. However, no post-irradiation microscopy was performed. This lack of microstructural information means the effects of temperature and composition on dislocation density, loop density, void density, etc. cannot be treated. Without void densities, questions concerning the role of composition on nucleation cannot legitimately be addressed. There are good reasons to believe that nucleation effects play a small role in these experiments. Preinjection with helium insures that sites for the nucleation of voids exist at the beginning of bombardment. This is likely to make swelling less nucleation limited. More importantly, the large swellings exhibited by most alloys insure behavior well within the void growth regime.

Analysis framework for swelling results

In view of the previously stated considerations these results will be treated in terms of solid solution effects on void growth kinetics. Within this framework, one is forced to consider how much solute additions can interact with point defects so as to produce alterations in void growth. First, there is a body of evidence to suggest that such additions can alter vacancy formation (E_V^f) and migration (E_V^m) energies (124,125,126). Unfortunately, the meaning of such quantities, let alone methods for determining them in multicomponent alloys, is not understood.

For example, one can alloy two pure metals, A and B, each with different E_v^f values. What is the E_v^f value of any resultant AB alloy? How does its magnitude depend on the relative amounts of A and B present? Second, solutes can also interact with point defects by exhibiting binding or trapping. Such binding can be characterized by binding energies between vacancies and or interstitials and the solute atom. The effect of defect trapping on void growth was considered in detail in a previous section. Here we write down the general case for different types of vacancy and interstitial traps (types m and n , respectively). The basic conservation equations are:

For free vacancies

$$G_v + \sum_m C_{vm}^T \tau_m^{-1} - C_v^F \sum_m v_m - R^{TF} C_v^F \sum_n C_{in}^T - R^F C_i^F C_v - C_v^F \sum_j K_v^j = 0, \quad (40)$$

For trapped vacancies type m

$$C_{vm}^F - C_{vm}^T \tau_m^{-1} - R^{FT} C_i^F C_{vm}^T = 0, \quad (41)$$

For trapped interstitials type n

$$C_{in}^F - C_{in}^T \tau_n^{-1} - R^{TF} C_v^F C_{in}^T = 0, \quad (42)$$

For free interstitials

$$G_i + \sum_n C_{in}^T \tau_n^{-1} - C_i^F \sum_n v_n - R^{FT} C_i^F \sum_m C_{vm}^T - R^F C_i^F C_v - C_v^F \sum_j K_v^j = 0, \quad (43)$$

where

$G_{v,i}$ = rate of generation of vacancies and interstitials by all processes (irradiation, implantation, thermal processes),

$C_{v,i}^F$ = concentration of free vacancies and interstitials,

$C_{vm,in}^T$ = concentration of trapped vacancies mth type and trapped interstitials nth type,

$v_{m,n}$ = trapping rate for vacancies at mth type trap and interstitials at nth type trap,

$\tau_{m,n}^{-1}$ = lifetime in trapped state for vacancies mth type and interstitials nth type,

$R^F = 4\pi r_g (D_i + D_v)$ - recombination coefficient between free vacancies and free interstitials,

$R^{TF} = 4\pi r_3 D_v$ - recombination coefficient between trapped vacancies and free interstitials,

$R^{FT} = 4\pi r_3 D_i$ - recombination coefficient between trapped interstitials and free vacancies, and

$\sum_j K_{v,i}^j C_{v,i}^F$ = losses of free vacancies and free interstitials to sinks such as voids, dislocations, grain boundaries.

In the section on growth kinetics the effects of defect trapping were considered in detail. The case presented here is a generalization to include many different types of vacancy and interstitial traps simultaneously. Expressions given previously for trapping rate, lifetime, etc., are consistent with the appropriate subscript changes. The strategy of solution is the same. First one solves for the steady

state free defect concentrations C_v^F and C_i^F . These concentrations are then substituted into the void growth rate equation (14).

Single additions

To investigate the experimental data using the growth rate calculation, a set of physically reasonable parameters was chosen to generate a void growth rate curve (C_v vs. T) which fitted the shape of the experimentally determined swelling-temperature data for the ternary alloy. The parameters used are listed in Table 5. The next step involves producing growth rate curves to match the swelling versus temperature data for various single additions. Several methods for doing this are possible. To illustrate the one chosen here consider the alloys A1, A2, and A3 produced from the ternary by additions of X, Y, Z atom % of element A. The first step in this procedure is to fix all parameters to generate the behavior of alloy A1. With the experimental data grid being at 50°C temperature increments, judgement about the quality of agreement between fit and data is necessarily subjective. Once the agreement is deemed adequate, curves for alloys A2 and A3 are generated using the same fixed parameters but setting concentrations of A at Y and Z atom percents, respectively. It is possible that some of the fixed parameters may be functions of composition. However, inclusion of such dependence on composition is not justified at this time because of a lack of information. A limiting case is presented here. Certainly the fits will be no worse if additional parameters are also allowed to vary with composition.

Table 5. Parameters for Void Growth Model

Point defect generation rate	$G_{i,v} = 6.4 \times 10^{20}$ defects/cm ³ /sec
Void surface energy	$\gamma = 1200$ ergs/cm ²
Dislocation density	$\rho = 5 \times 10^{10}$ cm/cm ³
Vacancy migration energy	$E_v^m = 1.38$ eV
Interstitial migration energy	$E_i^m = 0.15$ eV
Vacancy formation energy	$E_v^f = 1.40$ eV
Void radius	$r = 100 \text{ \AA}$

Vacancy and interstitial trappings were introduced separately and the binding energies determined to give a fit to the experimental swelling-temperature data. As mentioned previously, the swelling rate is sensitive to the extent of defect trapping, but the temperature dependence of the rate is only slightly influenced. Examination of the experimental data for Si, Ti, and Nb additions indicates that the apparent shift in peak swelling temperature is brought about by a suppression of high-temperature swelling rather than by a translation of the entire swelling curve. This observation suggests that in these alloys the thermally created vacancy concentration overrides the irradiation-produced supersaturation at a lower temperature than in the case of the ternary alloy, thus truncating the high-temperature swelling regime. This situation which could result from a change in vacancy formation energy was discussed in the section on growth kinetics.

Accordingly, the data for the alloy containing the lowest concentration of a given element was fitted with a void growth rate curve by allowing either vacancy or interstitial binding and also by allowing small changes in vacancy formation energy. Growth rate curves for alloys containing higher additions of the same element were then calculated by changing only the solute concentration to agree with chemical analysis.

The results of this analysis are shown in Figures 78-82 with the experimental data superimposed. The banded regions of the theoretical curves reflect the $\pm 10\%$ uncertainty in the determination of solute concentration by chemical analysis. With the parameters listed in Table 5 and no trapping a reasonable fit was obtained to the data for

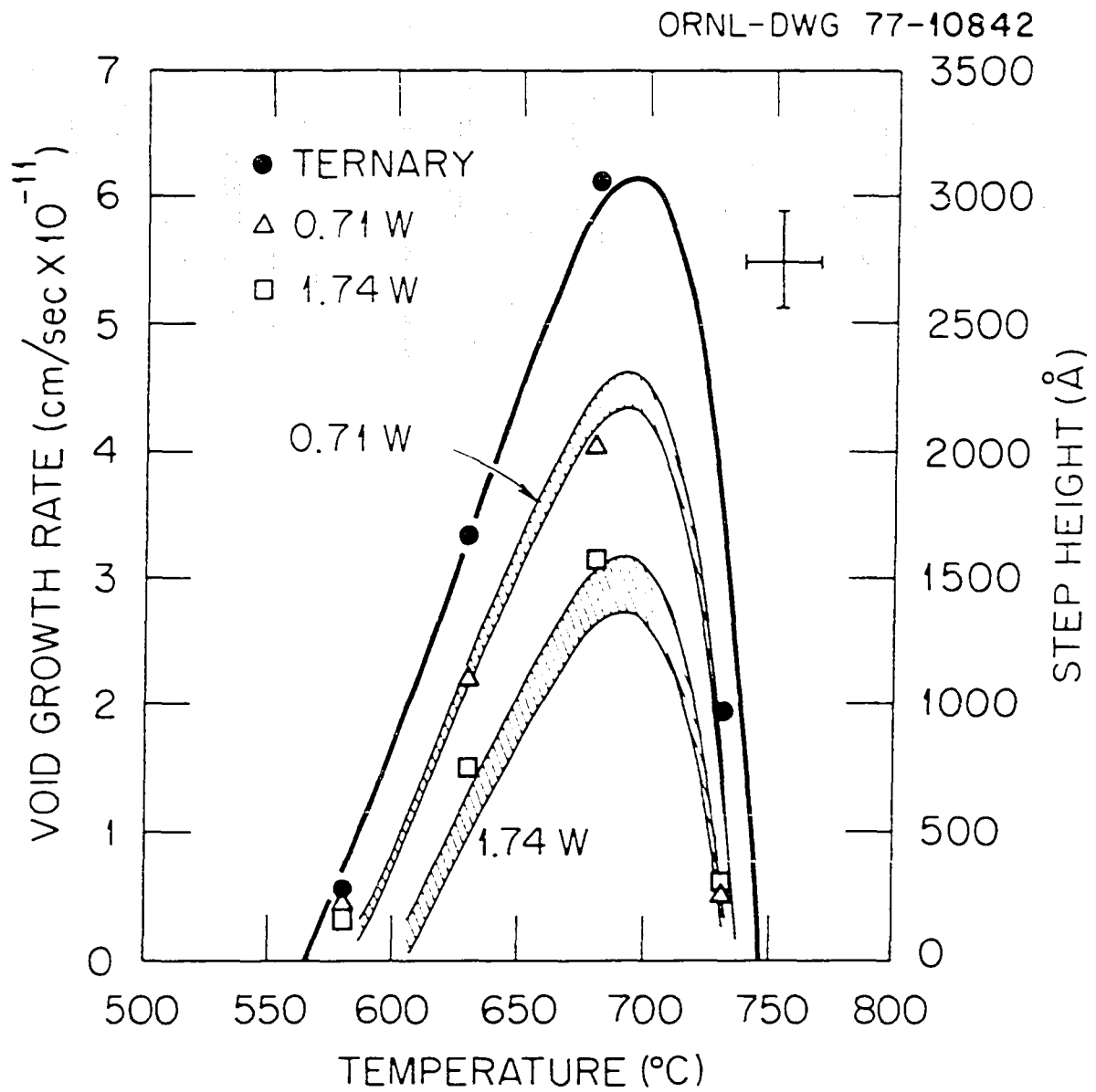


Figure 78. Void growth curves fitted to data for tungsten alloys.

$$(E_V^B = 0.14 \text{ eV}; E_V^f = 1.40 \text{ eV.})$$

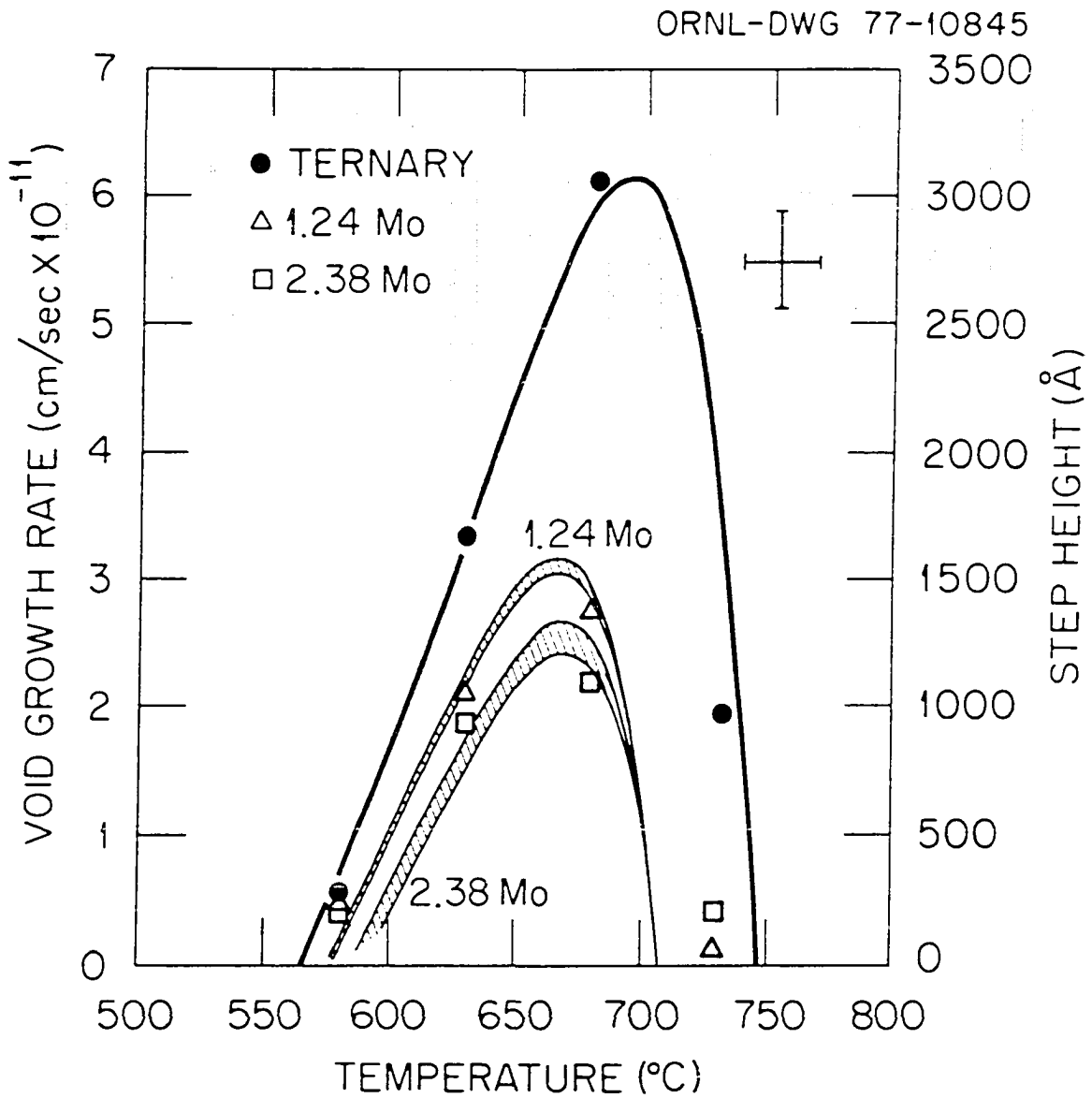


Figure 79. Void growth curves fitted to data for molybdenum alloys.

$$(E_V^B = 0.05 \text{ eV}; E_V^F = 1.33 \text{ eV.})$$

ORNL-DWG 77-10844

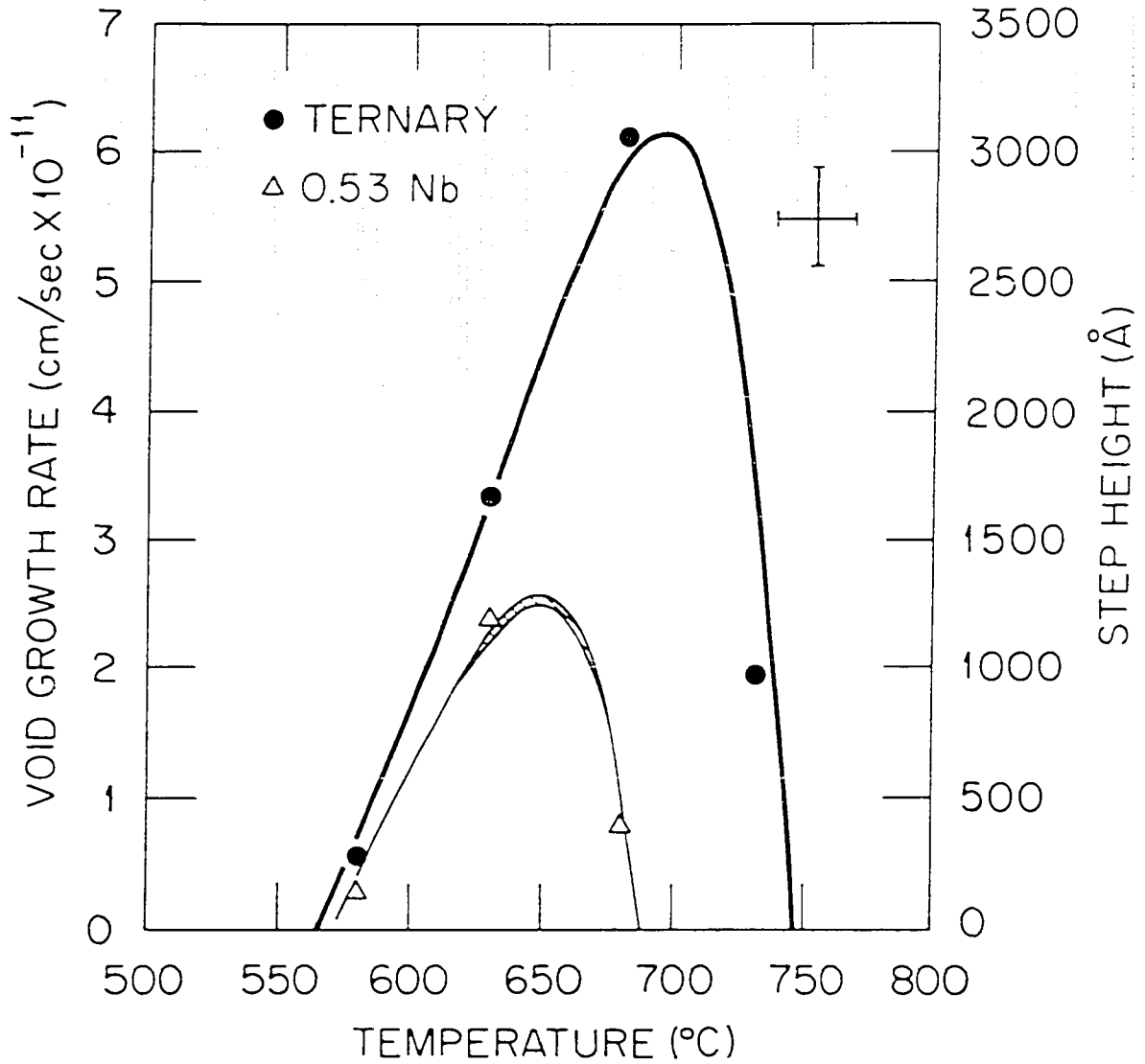


Figure 80. Void growth curves fitted to data for niobium alloys.

($E_V^B = 0.04$ eV; $E_V^f = 1.30$ eV.)

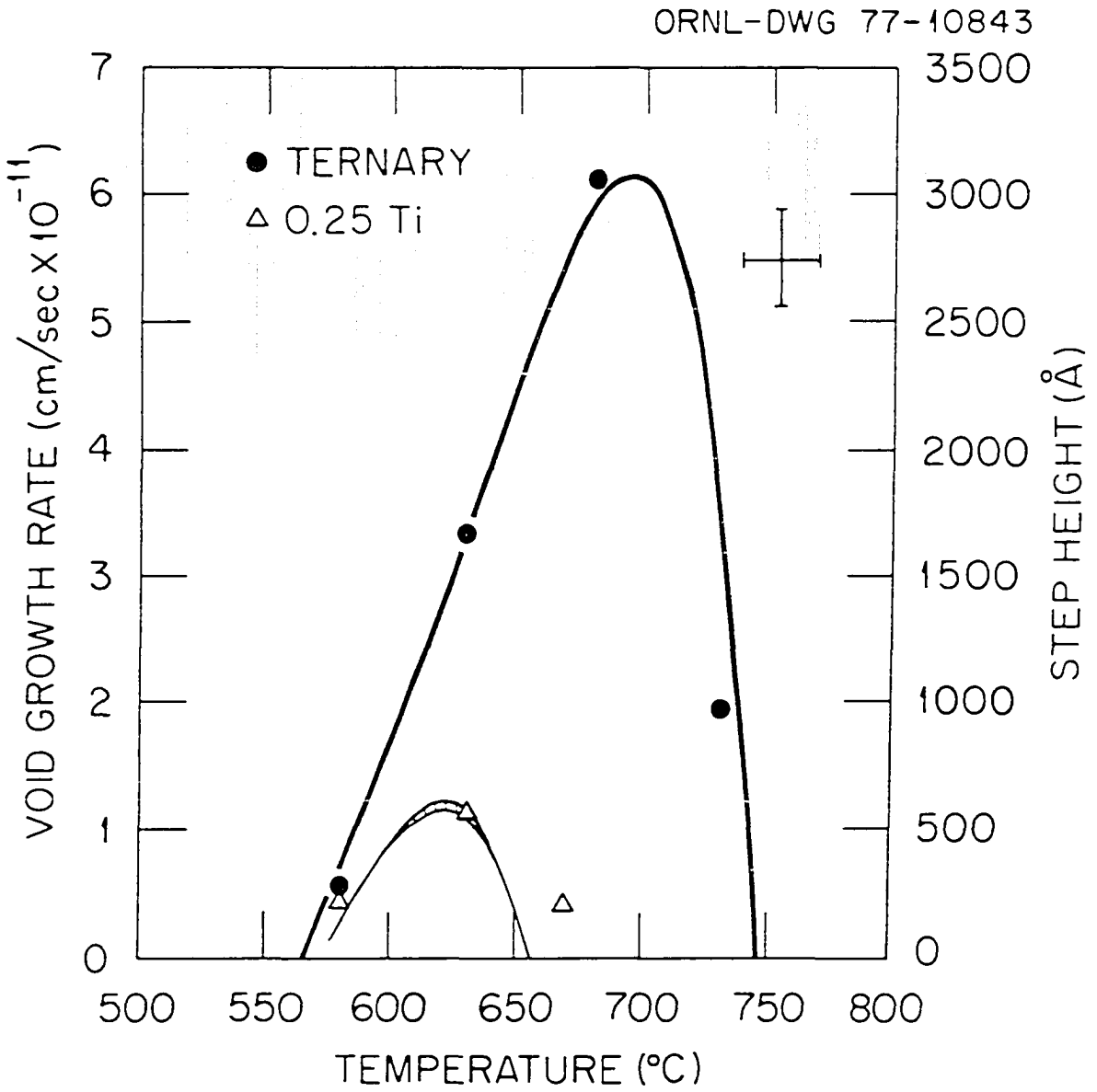


Figure 81. Void growth curves fitted to data for titanium alloys.

$$(E_V^B = 0.10 \text{ eV}; E_V^f = 1.25 \text{ eV.})$$

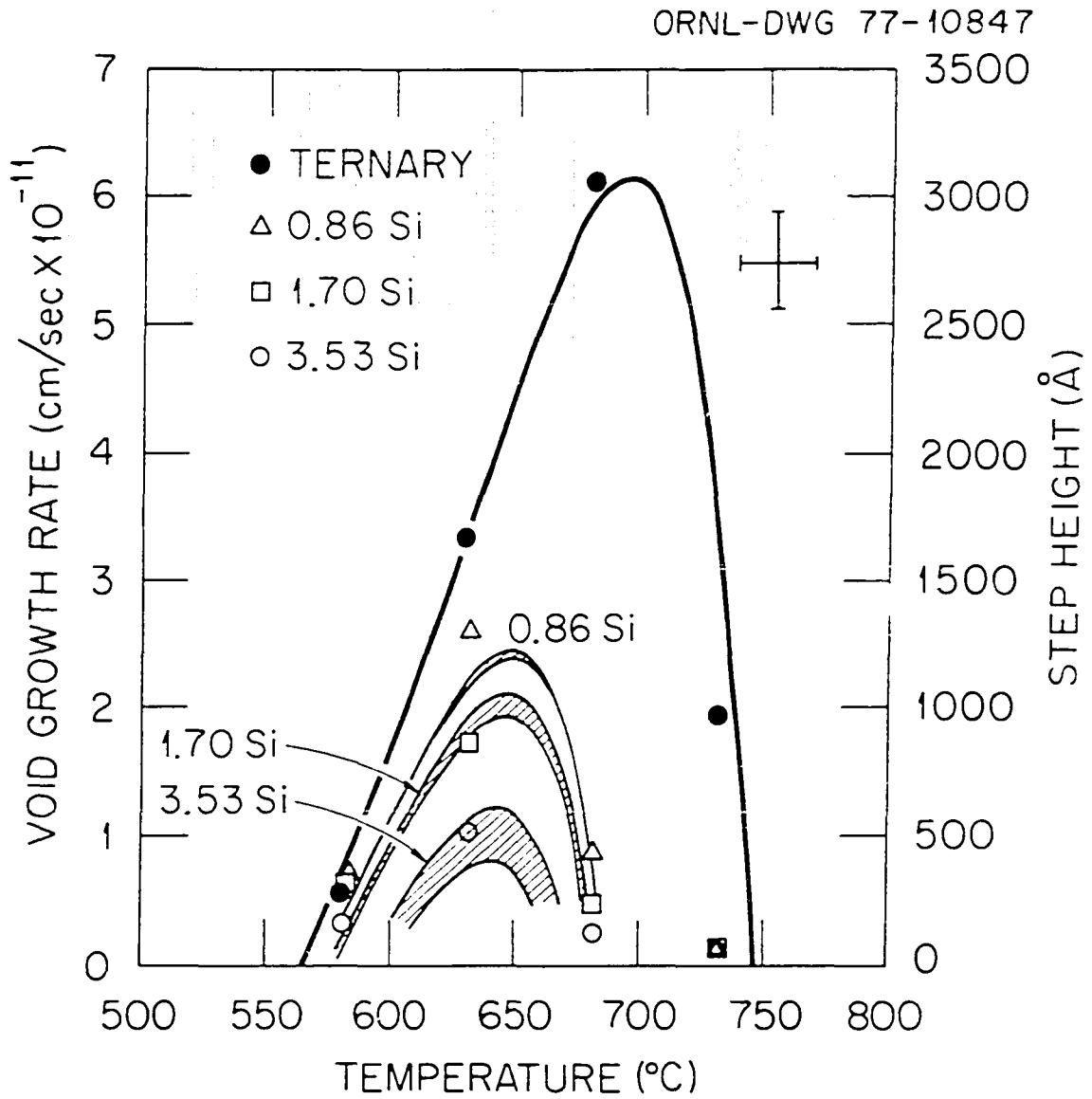


Figure 82. Void growth curves fitted to data for silicon alloys.

$$(E_i^B = 1.20 \text{ eV}; E_v^f = 1.30 \text{ eV.})$$

the ternary alloy. Although the hand drawn curves in Figures 67 through 73, pages 133-139, show the ternary peak at approximately 675°C, the location of this peak is obviously a matter of subjective judgement when the temperature increments are large. The computed curve shows the peak to be at 690°C and is probably a better representation of the data since it is based on a physical model rather than on arbitrary judgement.

For the 0.71 W alloy (Figure 78, page 155), the best fit was obtained by considering vacancy trapping with $E_V^B = 0.14$ eV. A reasonable fit to the 1.74 W data was generated by increasing the solute concentration to 1.74 at. % and keeping all other parameters fixed. For the 1.24 Mo alloy (Figure 79, page 156) vacancy trapping also produced a better fit with $E_V^B = 0.05$ eV. In addition to allowing vacancy trapping, the vacancy formation energy was lowered by 0.07 eV. Using these parameters and a solute concentration of 2.38 at. % curves representing the 2.38 Mo alloy were computed. In the niobium case (Figure 80, page 157), the concentrations of niobium in the first two alloys were too close together to justify a separate treatment while swelling in the third alloy was effectively zero. This means that only the lowest solute concentration could be considered, which makes the partitioning of binding energy and formation energy changes nonunique. A similar situation exists with the titanium alloys. Since two of the alloys exhibited very little swelling, only the lowest titanium concentration is considered (Figure 81, page 158). For the 0.53 % Nb alloy and the 0.25 % Ti alloy vacancy trapping with E_V^B values of 0.04 eV and 0.1 eV, respectively, combined with values of $E_V^f = 1.30$ eV and $E_V^f = 1.25$ eV, respectively, gave reasonable

approximations to the data. The silicon alloys provided the only instance in which interstitial trapping appeared to fit the data better than did vacancy trapping. For the 0.86 % Si alloy (Figure 82, page 159) values of $E_i^B = 1.20$ eV and $E_V^F = 1.30$ eV were chosen. To generate curves for the other two silicon alloys the solute concentrations were set at the appropriate values. The 1.65 % Al alloy presents another class of behavior. Examination of the experimental data for the two lowest aluminum additions indicates that the apparent shift in peak swelling temperature is brought about by an enhancement of the low temperature swelling. This observation suggests that at a given temperature vacancies have greater mobility in these aluminum alloys than in the ternary. This situation could result from a decrease in the vacancy migration energy (E_V^m) by 0.06 eV and is shown in Figure 83. Although the computed curve does not match the data points particularly well the general trend is certainly in the correct direction. No attempt was made to fit the data for this or the other two aluminum alloys because of the likelihood of precipitation effects.

The fit parameters used to obtain the growth rate curves are given in Table 6. Undue weight should not be placed on the precise numerical values of formation and binding energies used to fit the growth rate curves to the swelling data. For example, the formation energy might have been treated as a variable continuous in solute concentration. There is some logic in doing this, but in the absence of specific knowledge about such a relationship there is no rationale for including it. The important point is, that using this approach the effects of

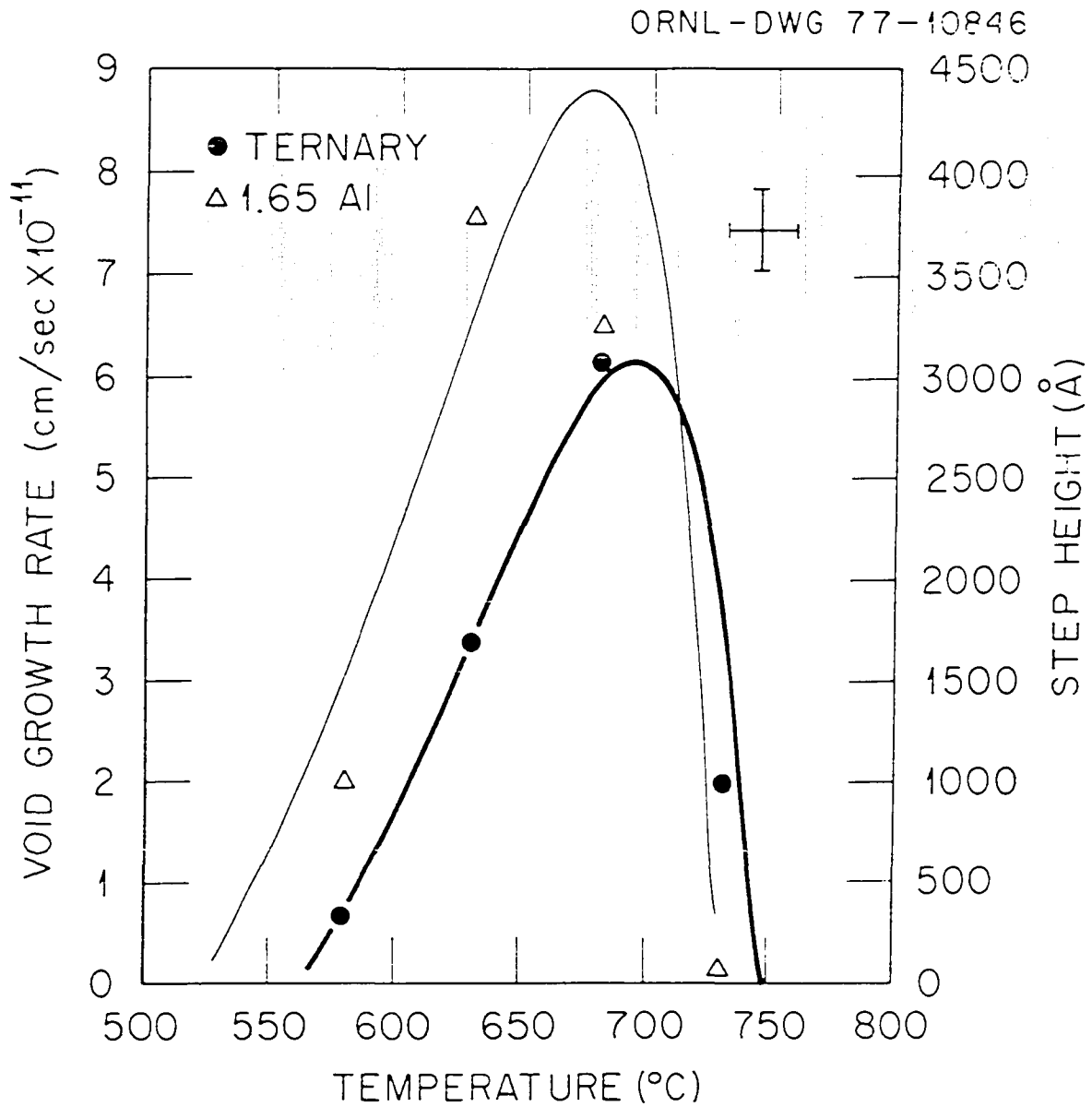


Figure 83. Void growth curve fitted to data for the 1.65 Al alloy.
 ($E_V^M = 1.32$ eV; $E_V^f = 1.40$ eV.)

Table 6. Fit Parameters for Swelling Data of Single Addition Alloys

Alloying Element	Vacancy Formation Energy (eV) E_v^f	Vacancy Migration Energy (eV) E_v^m	Vacancy-Impurity Binding Energy (eV) E_v^B	Interstitial-Impurity Binding Energy (eV) E_i^B
Ternary	1.40	1.38	0	0
Tungsten	1.40	1.38	0.14	0
Molybdenum	1.33	1.38	0.05	0
Niobium	1.30	1.38	0.04	0
Titanium	1.25	1.38	0.10	0
Silicon	1.30	1.38	0	1.20
Aluminum ^a	1.40	1.32	0	0

^aThese values for aluminum do not represent a fit to the data but instead indicate a trend.

various solute elements on the temperature dependence of swelling can be accounted for by considering small changes in vacancy formation energies coupled with vacancy or interstitial trapping. Two questions logically follow from the analysis. First, does one expect such decreases in formation energy upon adding solute? Second, are there likely to be solute-defect interactions characterized by binding energies of the sizes required here?

Since E_i^B , E_v^B , or E_v^f values are not available for these alloys neither question can be answered with certainty. There are some indications that the changes proposed here are indeed physically reasonable. For example, there exist correlations between melting temperature (T_m) and formation energy (E_v^f) (125,126). Such relationships are strictly empirical, but, if one thinks of both vacancy creation and melting in terms of thermally sensitive reduction of bond-strength, some intuitive basis appears for the correlation. Since iron is a major constituent in all these alloys, one might consider the effects of the various impurities on the melting temperature of iron. On the basis of E_v^f values generated by this work, the decrease of T_m with increasing solute concentration, in order of increasing sensitivity, should be Mo, Si, Nb, and Ti. Little or no effect is expected for tungsten. The binary phase diagrams, Figures 84 through 89, seem to support this concept. Such considerations would lead one to expect rhenium additions to increase formation energy resulting in greater swelling than for the ternary. Similarly, phosphorous should act as a swelling suppressant. There is evidence in type 316 stainless steel that the addition of phosphorous does reduce void-swelling

Fe-Mo Iron-Molybdenum

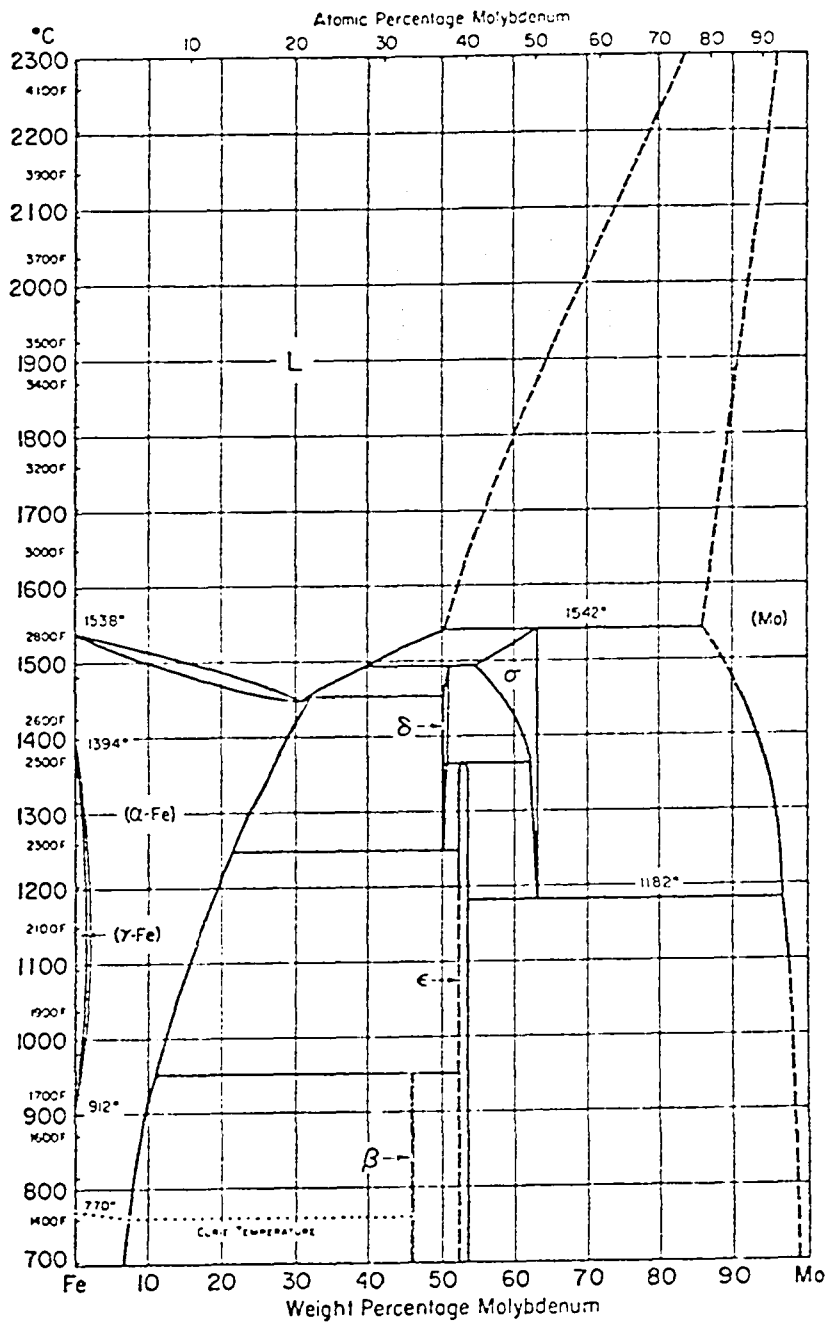


Figure 84. Phase diagram for the iron-molybdenum system (127).

Fe-Ti Iron-Titanium

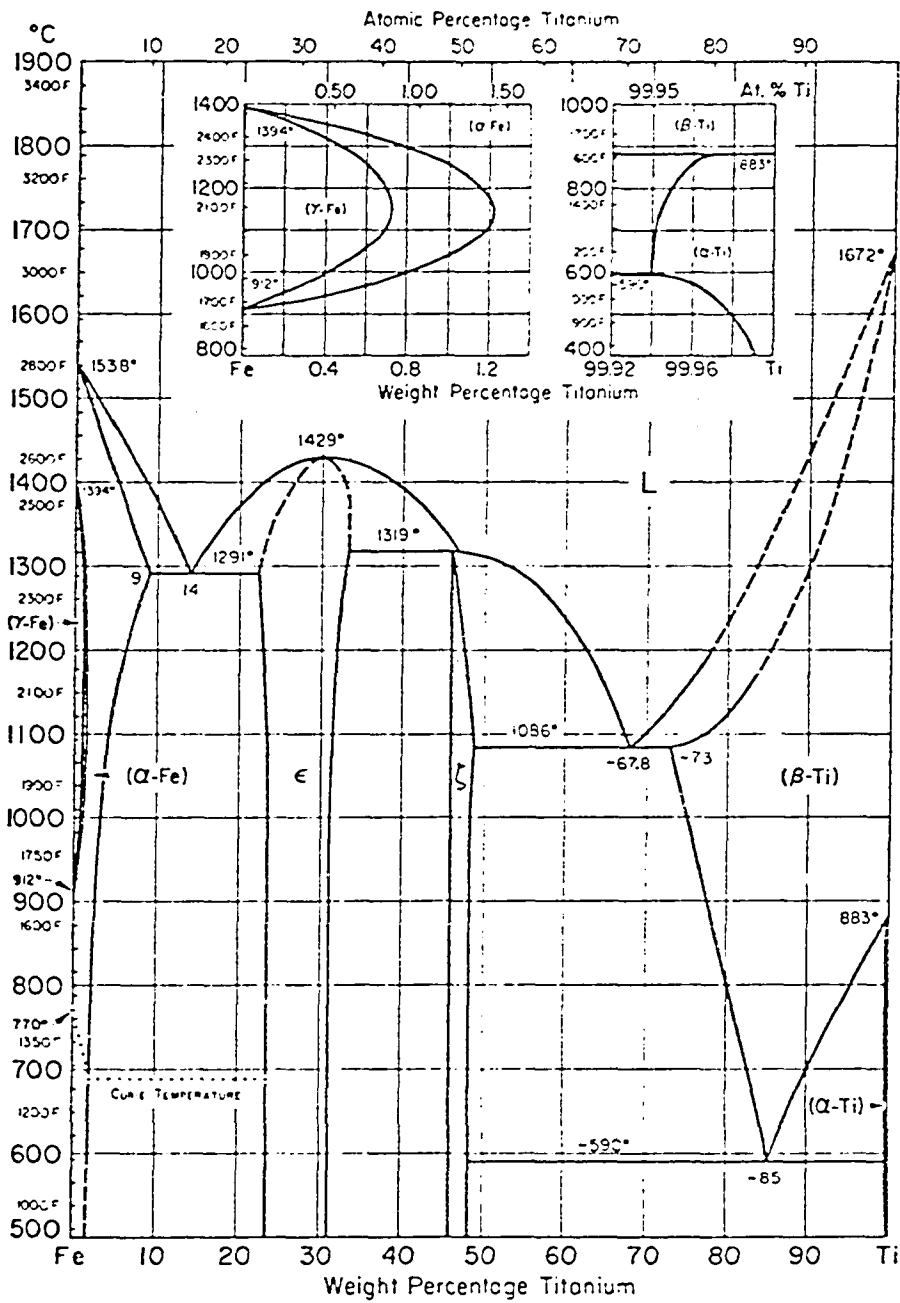


Figure 85. Phase diagram for the iron-titanium system (127).

Fe-Ni Iron-Nickel

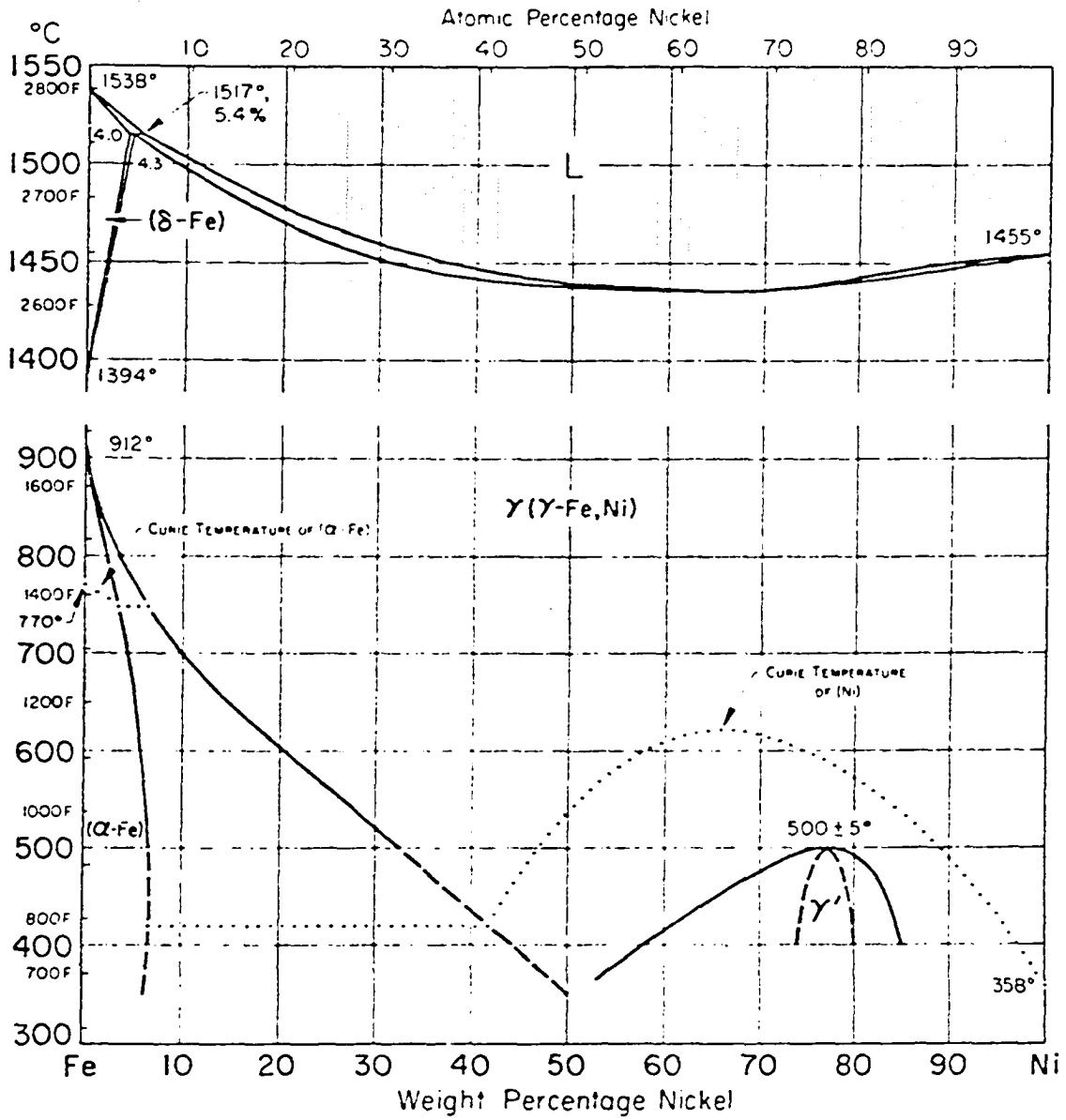


Figure 86. Phase diagram for the iron-nickel system (127).

Fe-W Iron-Tungsten

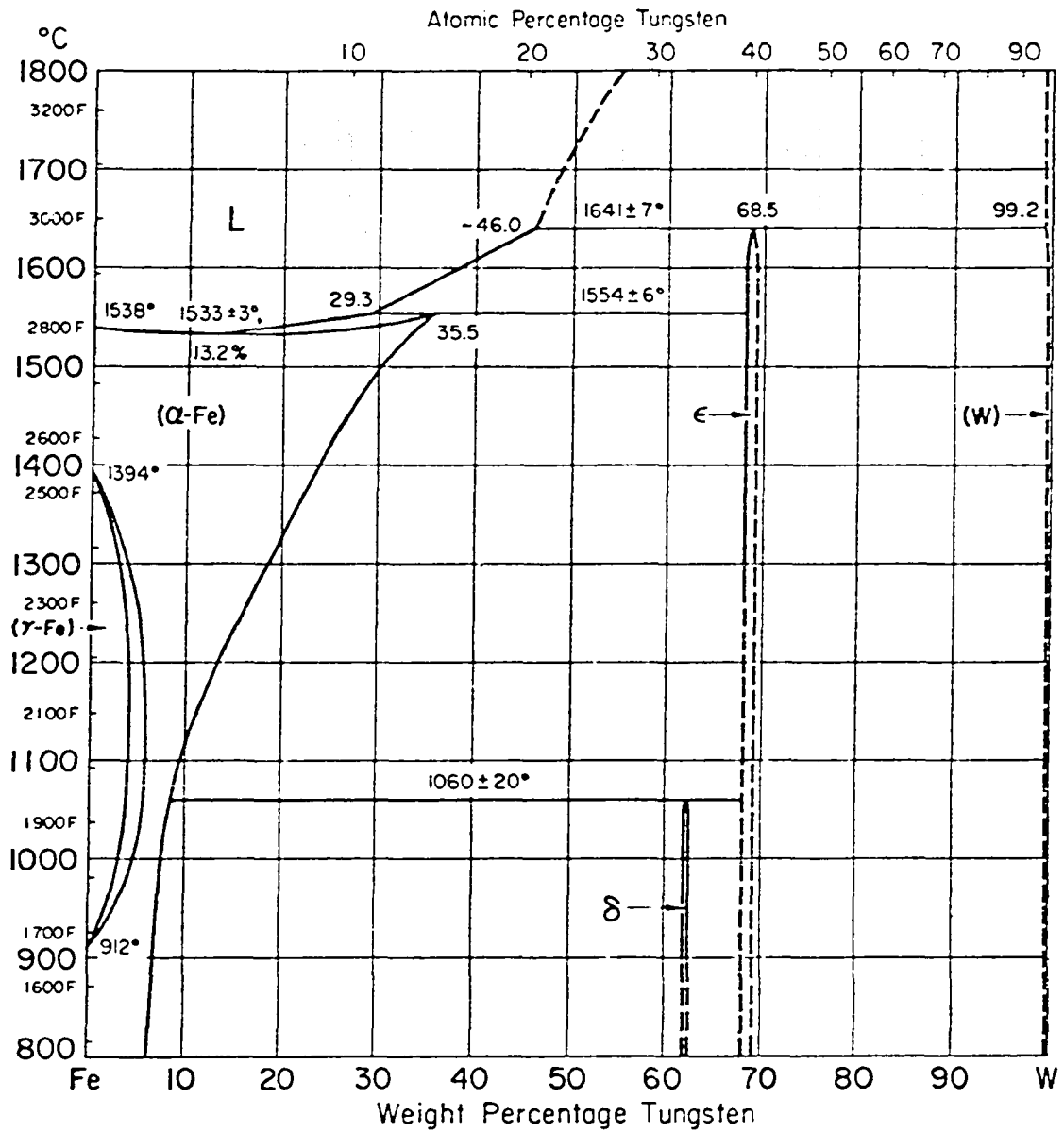


Figure 87. Phase diagram for the iron-tungsten system (127).

Fe-P Iron-Phosphorus

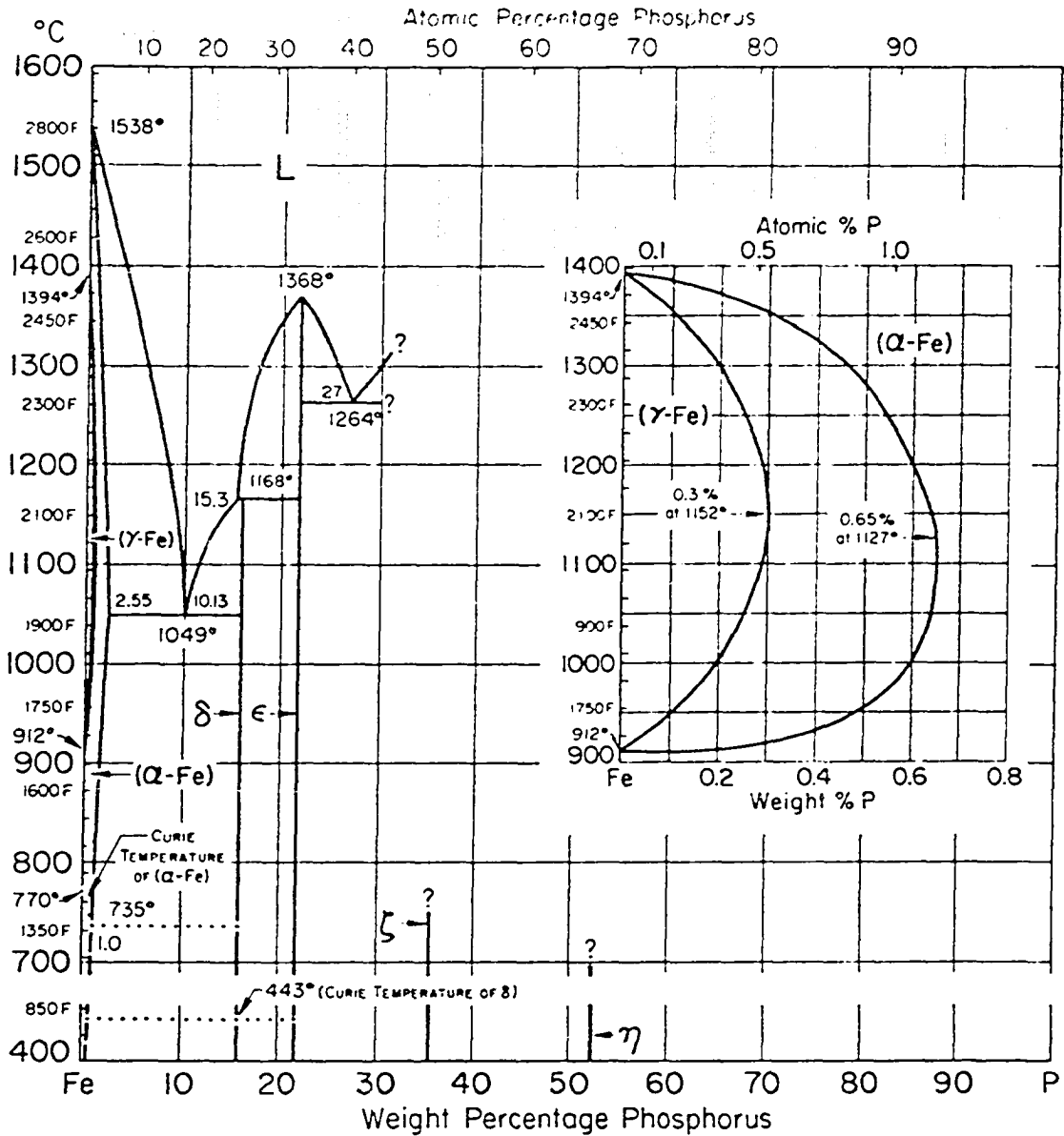


Figure 88. Phase diagram for the iron-phosphorus system (127).

Fe-Si Iron-Silicon

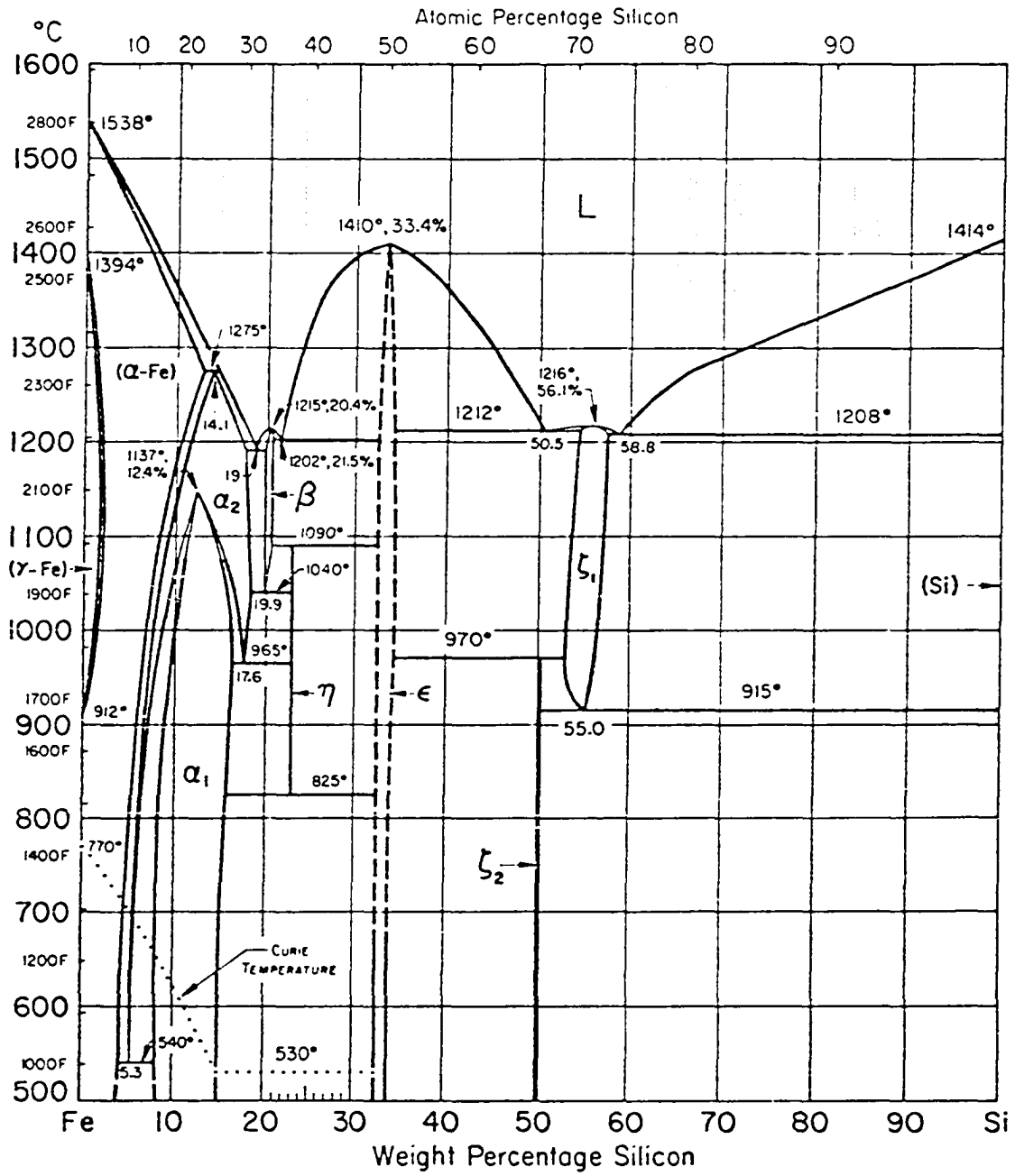


Figure 89. Phase diagram for the iron-silicon system (127).

(90). This is, of course, speculative but does indeed suggest some interesting experiments. The very exciting possibility that band theory could shed some light on how formation energies change with alloying is probably years away. With regard to solute-defect binding there exists a wealth of data on other systems which yield a spectrum of values. Measured binding energies for impurities with vacancies range from less than 0.1 eV to 2 eV (126). Thus, binding energies required here are definitely at the conservative end of this spectrum.

Double additions

The apparent success in treating single addition alloys naturally prompts one to attempt a description of the double additions within the same framework. Since most commercial alloys have several constituents, this inquiry can be motivated on practical grounds as well.

The double additions chosen for this study do place serious limitations on the kind of analysis that can be performed. As previously stated, alloys containing (Si + Ti), (Mo + Ti) and (Mo + Si) showed essentially zero swelling. In these cases too much solute was added and complete analysis is not possible. An important question regarding the minimum amount of solute required to achieve zero swelling requires another test matrix. Another problem arises due to an inability to fit correctly the aluminum single additions. Without a scheme for treating these alloys, those double additions involving aluminum cannot be examined meaningfully. In the case of single additions each was found to produce a certain swelling versus temperature profile. In many of

those cases the temperature grid was too large to define the exact shape of the profile. When two elements having different temperature dependent swellings are added simultaneously the details as a function of temperature become more important. The present study used 50°C increments; however, indications are that the temperature dependencies need to be mapped much more finely.

Analysis framework

When considering multiple addition it would seem most natural to ask whether various constituents act independently or interact. However, if each constituent is considered to interact with defects, strictly independent action is not likely. For example, consider one constituent which enhances vacancy mobility and another that traps vacancies. Clearly, the behavior of each of these two species is interrelated. This point can be further illustrated by considering the effects of adding two different elements that act as vacancy traps but have their own characteristic trapping parameters. One added piece of information at our disposal is the nature in which each element acts when added singly to some alloy. The naive analyst would propose simply to add the effects of each element acting singly to obtain the composite behavior. Actually this approach represents the worst approximation as can be easily seen from point defect balances. It will be recalled that the effect of defect traps is to reduce free point defect concentrations; however, the extent of trapping also depends on the concentration of free defects in the system. Thus when solutes A and B are added

simultaneously their trapping becomes coupled through the free defect concentrations. Thus to do each new addition correctly it is necessary to include its presence in the basic defect balance equations and then do the growth rate calculation again. In the case of many types of interstitial and vacancy traps, C_i and C_v can be separated easily to give a single equation in either C_i or C_v . For example, one can consider m different types of vacancy traps. The point defect balances can be obtained from (40), (41), and (43) by neglecting all terms containing n . These can be solved using trivial algebra to yield a single equation in C_i .

$$\begin{aligned}
 R \sum_j K_i^j \prod_{L=1}^m (R^{FT} \tau_L C_i + 1) C_i^2 - [R(G_i - G_v) - \sum_j K_i^j K_v^j] \prod_{L=1}^m (R^{FT} \tau_L C_i + 1) \\
 - G_i \sum_j K_v^j (R^{FT} \tau_L C_i + 1) - [G_i - G_v - \sum_j K_i^j] R^{FT} \sum_{\substack{k=1 \\ L \neq k}}^m \tau_k v_k \prod_{L=1}^m (R^{FT} \tau_L C_i + 1) = 0.
 \end{aligned} \tag{44}$$

This can be rewritten using permutations if one defines

$$P(\tau_1 \dots \tau_m, 0) = 1$$

then

$$\begin{aligned}
 R \sum_j K_i^j \sum_{L=0}^n P(\tau_1 \dots \tau_n, L) (R^{FT})^L C_i^{L+2} - [R(G_i - G_v) - \sum_j K_i^j K_v^j] \sum_{L=0}^n \\
 P(\tau_1 \dots \tau_n, L) (R^{FT})^L C_i^{L+1} - G_i \sum_j K_v^j \sum_{L=0}^n P(\tau_1 \dots \tau_n, L) (R^{FT})^L C_i^L
 \end{aligned}$$

$$- [G_i - G_v - \sum_j K_i^j] \sum_k \tau_k v_k \sum_{\substack{L=0 \\ L \neq k}}^n P(\tau_1 \dots \tau_n, L) (R^{FT})^L C_i^{L-1} = 0 \quad (45)$$

τ_k not included

For m vacancy traps one then has to solve an equation in C_i^{m+2} . With this value of C_i , C_v can be obtained from the original balances and the growth rate calculated as usual. The inherent symmetry of the defect balances in v and i makes it possible to generate the solution for n different types of interstitial traps by a simple subscript interchange and exchange of R^{TF} for R^{FT} . When both interstitial and vacancy trappings are considered simultaneously, the equations are coupled from the outset and must be solved numerically.

One problem thwarts the application of this scheme to the double additions used in this study. It will be recalled that in addition to trapping, a change in vacancy formation energy was invoked to fit the single additions. In the absence of some idea how formation energy changes with composition, this effect cannot be correctly taken into account in alloys containing multiple additions. In light of the sensitivity of swelling to the vacancy formation energy assumptions about its compositional dependence are not justified. Ideally the model should be reformulated making vacancy formation energy a parameter continuous in solute concentration. The correct treatment of these double additions must await illumination of the nature of that functional dependence.

Hardness Experiments

In a previous section the basic concept of hardness was treated briefly. While there have been extensive measurements of hardness, the understanding of this phenomenon is very limited. The results of hot hardness tests on the alloy set considered in this study has also been presented. These data should give some indication as to how hardness varies with composition. Considering the many correlations between hardness and other properties one should, in principle, get some qualitative estimate of their sensitivity to composition. Treatment of this type of data to estimate effects on correlated properties necessarily must be qualitative so long as hardness is only qualitatively understood. The correlated property of interest here is the ultimate tensile strength (UTS). More important than a numerical correlation is the observation that both hot hardness and UTS have very similar temperature dependencies. Thus, the hardness results can be used as an indication of the relative importance of various elements in strengthening a Fe-20 Ni-7.5 Cr steel.

Before examining the effects of various additions, it is worthwhile to first consider the hardness versus temperature curve of the Fe-20 Ni-7.5 Cr-5.5 W shown in Figure 90. The shape is similar to that which is generally observed in 300 series stainless steels (4). It consists first of a region of negative slope and concave upward curvature. This region extends to about 600°C where the curvature turns downward. The inflection point near 500°C could be an indication of a change in

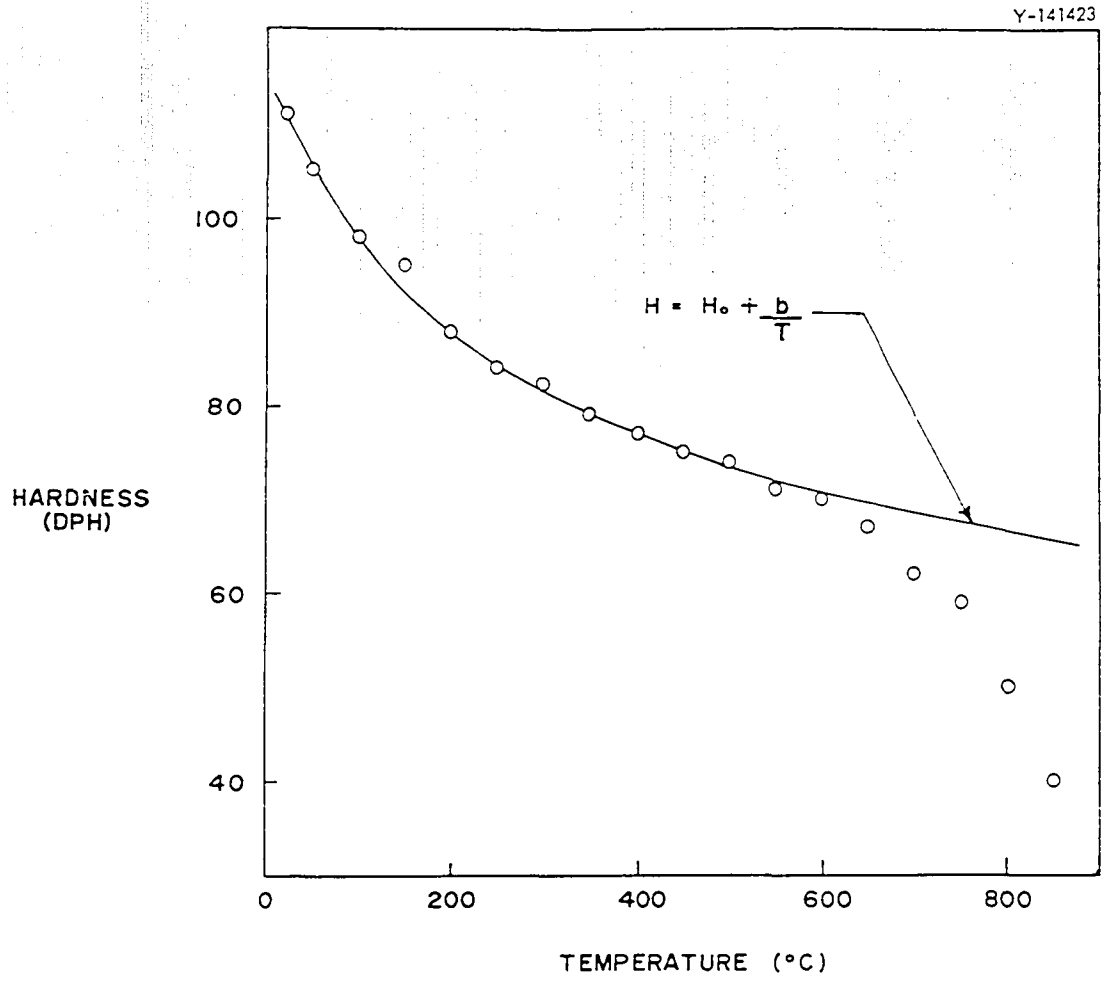


Figure 90. Hot hardness data for an Fe-7.5 Cr-20 Ni-5.5 W alloy showing the empirical fit.

deformation mechanism. It is known, that in such steels, vacancies become mobile at temperatures in this vicinity. The increased mobility of vacancies would then result in an increasing dislocation climb contribution to the deformation rate. The term deformation rate is important since the hardness tests performed in this study involved holding a fixed load on the specimen for a fixed time. As the temperature is increased, the impression size increases. Thus, each point each addition raises the curve to a higher hardness level without significantly altering the temperature dependence. This is what one expects if the increase in alloy addition simply increases the barrier density. However, there appears to be a limit to the sensitivity of hardness to composition changes. This can be seen in Figures 39-42, pages 103-106, for the two lowest additions of both Nb and Ti. For the two lowest Nb alloys the compositions differ by about 0.1 atom % while for the Ti alloys the difference is 0.2 atom %; nevertheless the hardness curves overlap. For the W, Mo, Al and Si alloys, where the composition separations are greater, the hardness curves are clearly separated.

The region above 600°C seems to be affected quite differently. In this region subsequent alloying additions produce a much steeper temperature dependence. The slope of this dependence is greater for the Al and Si alloys although all additions produce slopes greater than the ternary Fe-7.5 Cr-20 Ni alloy. In the swelling data analysis, it was found that one possible interpretation involved the change in vacancy formation energy upon alloying. This change would have the effect of increasing the vacancy concentration and as seen from Equation 33, would

increase the strain rate due to climb. This explanation is questionable since no formation energy change was invoked to explain W alloy swelling behavior, yet such additions produce an increased slope in hardness above 600°C. Actually the observed changes in slope are most pronounced for alloys likely to be outside the solubility limits. The possibility exists that for these alloys at the higher temperatures the decrease in hardness was accelerated by removal of material from solution.

In light of the apparent similarity in behavior of the UTS and hot hardness, the measurements made on this set could be compared on a relative basis. While the hardness and UTS values would not be identical, one could expect their relative trends to be similar. In this way, the hardness results could be used to estimate the relative effectiveness of various additions as strengthening agents. There are many possible ways to extract this kind of information. First, one could pick the temperature of interest and plot hardness vs. composition. To facilitate this type of analysis and alleviate some problems resulting from data scatter, an attempt was made to fit empirically the hardness data for each alloy. The region between 22°C and 600°C was chosen to demonstrate one possible approach. Of the expressions usually found to fit hot hardness data one of the form:

$$H = H_0 + bT^n \quad (46)$$

with $n = -1$ most closely described this set of measurements. Figure 90 displays the fit for a Fe-7.5 Cr-20 Ni-5.5 W alloy. The associated

constants H_0 and b describing each alloy are shown in Table 7. While this fitting procedure has no physical basis, it serves as a catalogue of all hardness values between 22°C and 600°C. No attempt was made to extend the fitting into the region above 600°C. The degree of hardening is then defined in terms of an athermal ΔH and a thermally sensitive Δb , each referenced from the H_0 and b values of the pure ternary. Expressed mathematically this takes the following form:

$$\Delta H = H_0 \text{ (addition)} - H_0 \text{ (ternary)} \quad (47)$$

$$\Delta b = b \text{ (addition)} - b \text{ (ternary)} . \quad (48)$$

In Figures 91 and 92, ΔH and Δb are plotted as a function of atom percent addition of various elements. These figures may be used to estimate the hardness of multicomponent alloys. For alloys containing two additions there are two values of ΔH and Δb which combined in some way. This data set indicates that for alloying elements having similar electronegativities and size factors, the resultant alloy behavior may be estimated by summing ΔH and Δb . For example the hot hardness data for an Fe-7.5 Cr-20 Ni-4.4 Mo-0.87 Nb alloy is shown in Figure 93. The continuous line is an expression of the form Equation (46) with the terms H and b calculated from the data shown in Figures 91 and 92 using the relationships:

$$\Delta H_{\text{tot}} = \Delta H_{\text{Mo}} + \Delta H_{\text{Nb}} \quad (49)$$

$$\Delta b = \Delta b_{\text{Mo}} + \Delta b_{\text{Nb}} . \quad (50)$$

Table 7. H_0 and B Parameters for Fitting Hot Hardness Measurements

Alloy	H_0	b
M1	53.9	16.2
M2	64.5	18.4
W1	48.1	15.9
W2	50.6	17.8
W3	89.7	17.5
A1	62.9	14.5
A2	78.5	12.0
A3	105.5	13.5
T1	46.7	16.8
T2	50.4	14.0
T3	87.8	14.1
S1	55.3	12.5
S2	58.1	13.4
S3	69.7	14.6
N1	48.1	17.6
N2	52.7	15.3
N3	70.5	13.6
MS1	70.3	19.1
MT1	73.1	15.4
MN1	69.9	17.0
AT1	79.2	14.2
AN1	93.7	8.1
TS1	44.2	16.0
TS2	57.5	13.4
TS3	57.3	13.2
TS4	53.2	14.7
C1	58.0	14.3
Mast	77.2	14.2
Ternary	43.8	15.3

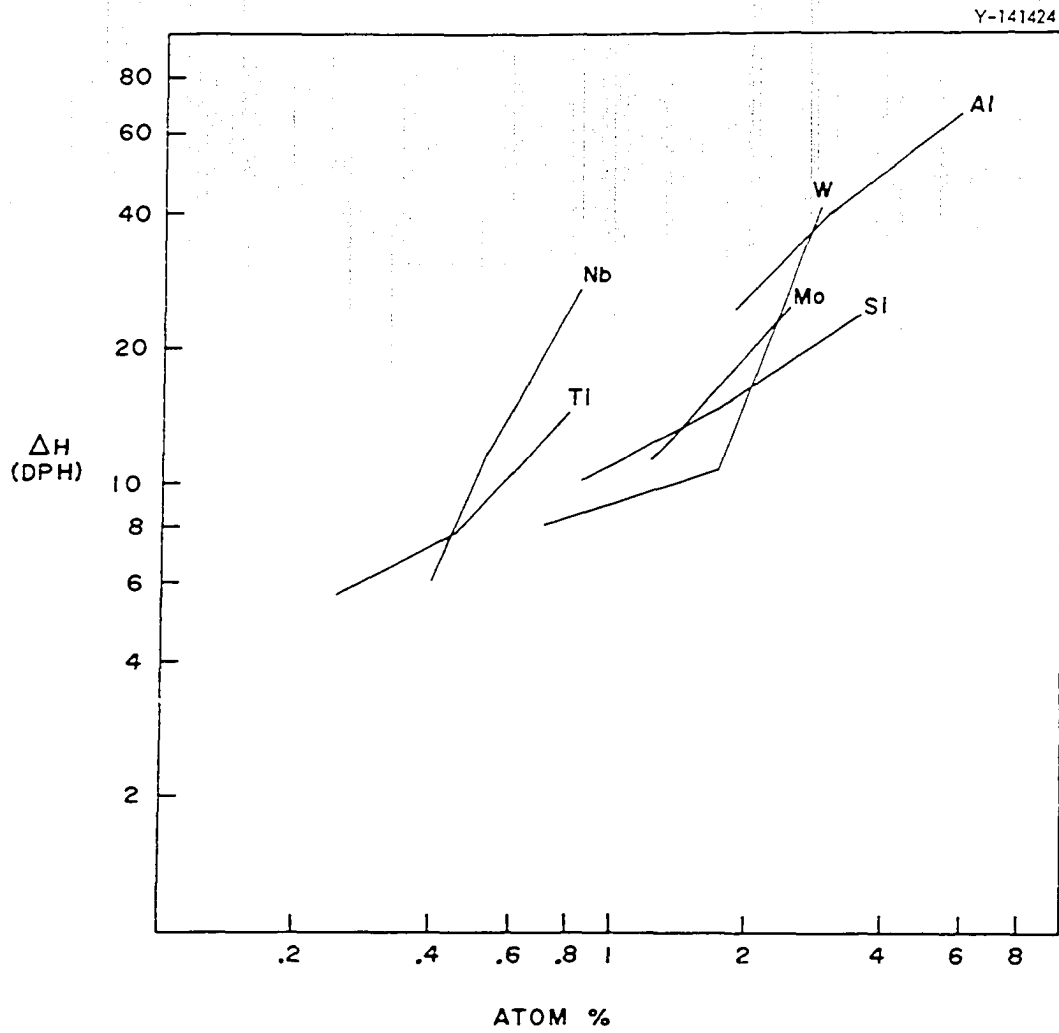


Figure 91. Variation of the fit parameter ΔH with composition.

Y-141417

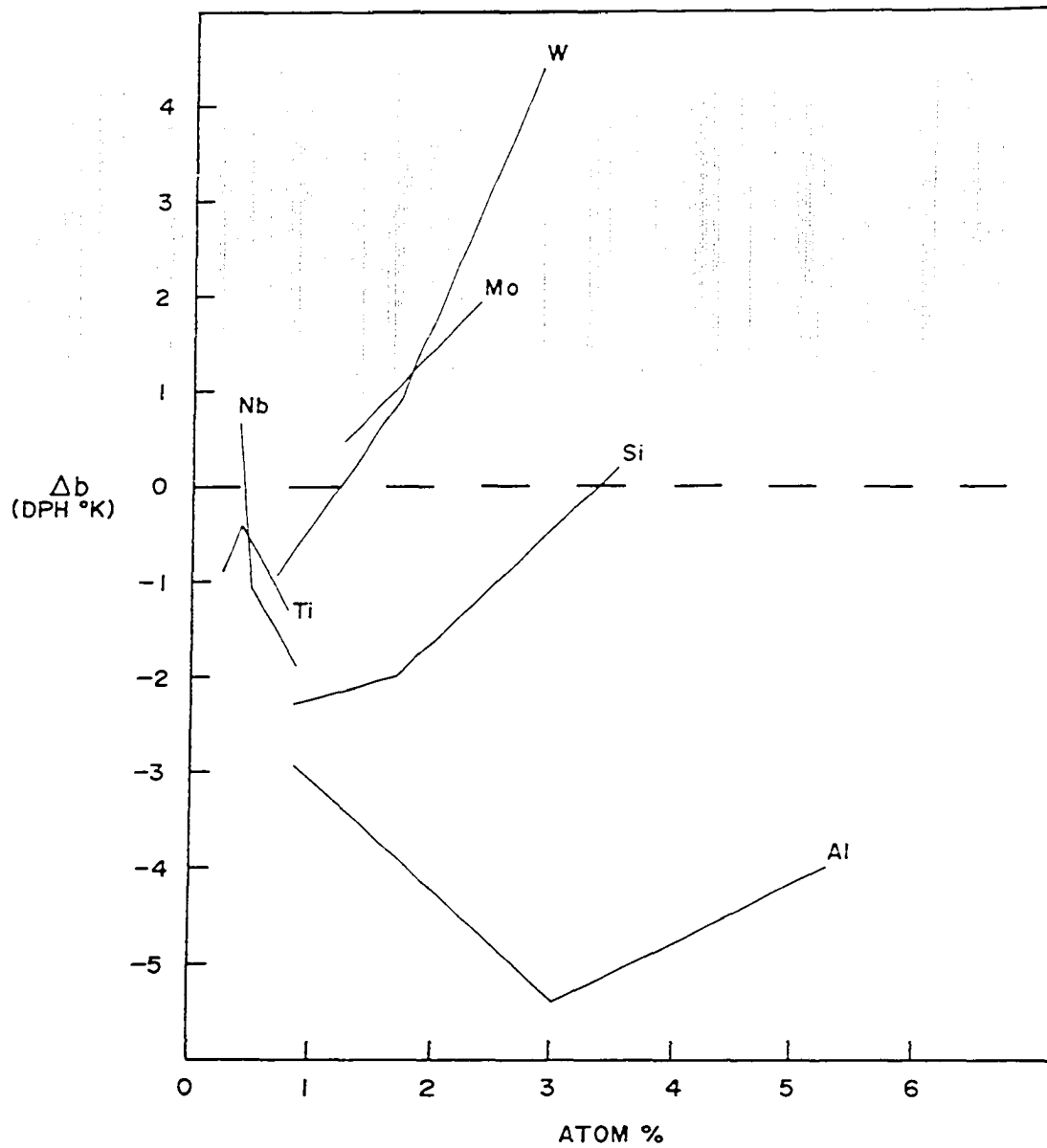


Figure 92. Variation of the fit parameter Δb with composition.

Y-141418

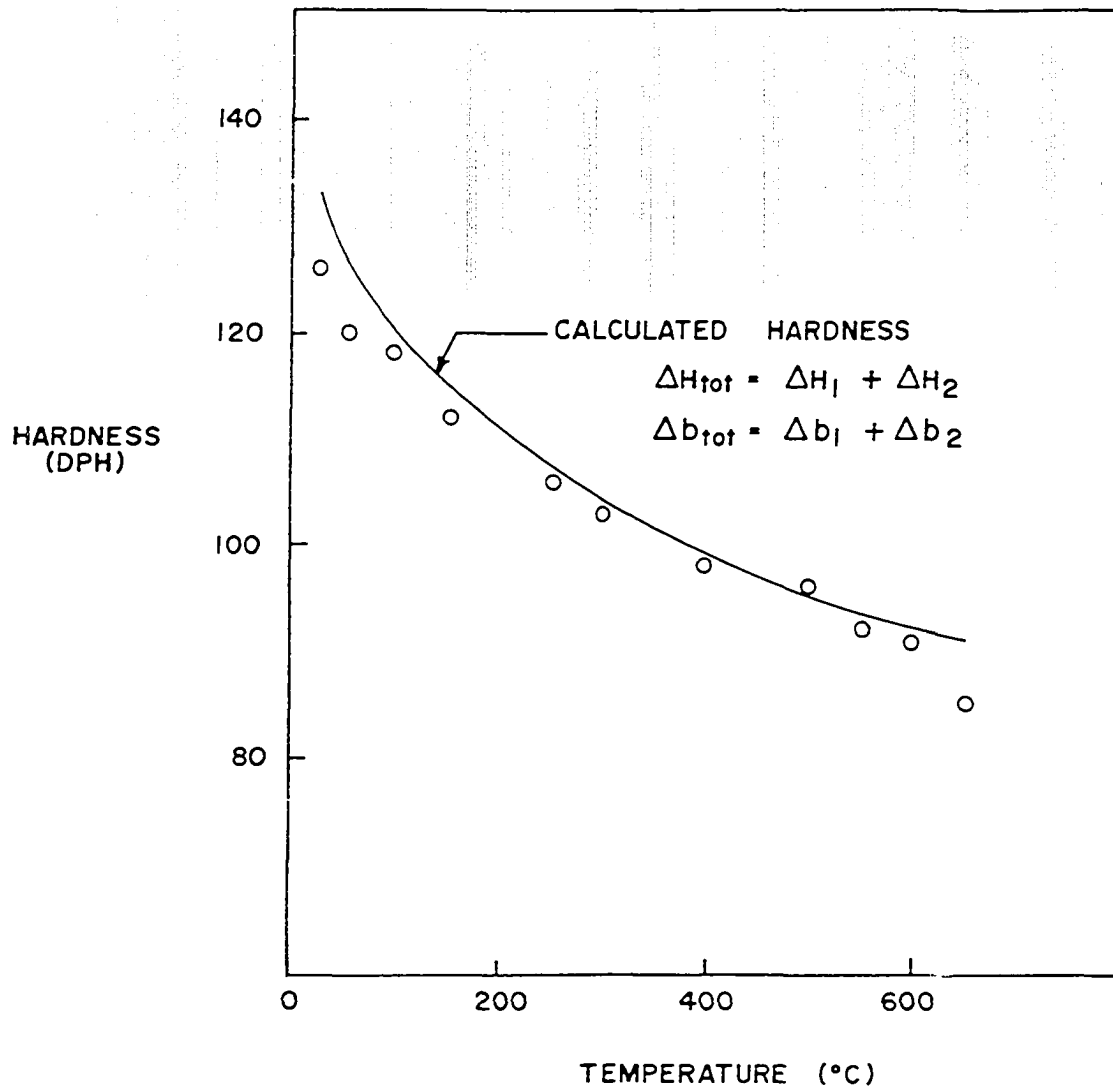


Figure 93. Calculated hot hardness and experimental data for an Fe-7.5 Cr-20 Ni-4.4 Mo-0.87 Nb alloy.

This procedure gives an estimate, and great care should be exercised when one of the addition levels is outside the limits of addition explored using the single additions. For additions, where two elements with substantially different size factors or electronegativities are involved, e.g., silicon and titanium, the simple addition method gives a very poor fit. In these cases the following relationship appears to give a better estimate.

$$\Delta H_{\text{tot}} = [(\Delta H_1)^2 + (\Delta H_2)^2]^{\frac{1}{2}} \quad (51)$$

The thermally sensitive Δb values are still assumed to sum. A calculated hardness curve based on the use of this expression for an Fe-7.5Cr-20Ni-3.6Si-.2Ti alloy is shown in Figure 94 together with the measured data.

It should be emphasized that these techniques are simply suggested empirical procedures to extract estimated alloy rankings in the absence of other data. It should be used only as an indication of which alloys are likely to exhibit properties of interest. It does appear that the proposed techniques give estimated values which agree with experiment within the limits set by engineering practice. To minimize the errors of estimation points beyond the range of this particular data set of single additions should be avoided.

Y-141419

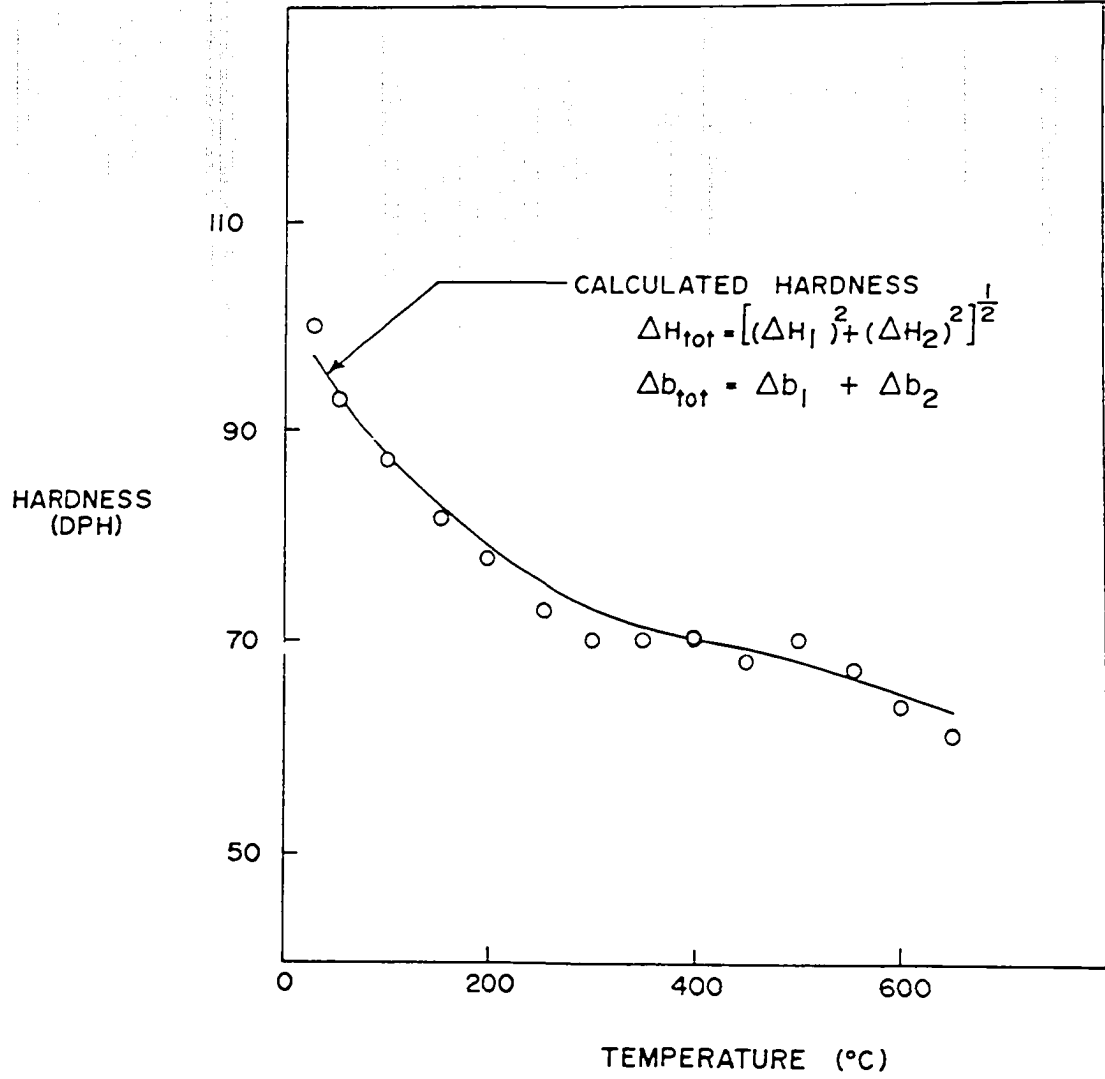


Figure 94. Calculated hot hardness and experimental data for an Fe-7.5 Cr-20 Ni-3.6 Si-0.2 Ti alloy.

CONCLUSIONS

The influence of various solute elements on the strength and swelling behavior of an Fe-7.5 Cr-20 Ni alloy was investigated using hot hardness and 4 MeV Ni ion bombardment. The principal experimental observations were as follows:

1. It was found that on an atom percent basis, the elements may be arranged in order of decreasing effectiveness in reducing peak temperature swelling as follows: Ti, C, Nb, Si, and Mo.

2. Additions of Si, Ti, or Nb truncated the high temperature swelling of the ternary alloy.

3. Mo, W, and C do not have a strong effect on the temperature dependence of swelling.

4. Small additions of Al enhanced swelling and produced an apparent lower peak swelling temperature. Large Al additions produced a fine precipitate structure and showed no swelling at all temperatures investigated.

5. Double additions of various elements also resulted in lower swelling alloys. All double additions involving Si showed no swelling. The nearly identical results for 4 vastly different Si + Ti alloys indicated that the amounts added were in excess of that required for low swelling. The one Mo + Ti alloy investigated showed no swelling. This result indicates that silicon is not necessary for a low swelling stainless steel.

6. For the molybdenum series the peak swelling decreased for increasing solute concentration at low solute concentrations. At the molybdenum concentration of 4.34 atom percent the peak swelling began to increase.

7. A good correlation was found between hot hardness and the ultimate tensile strength of the Fe-7.5 Cr-20 Ni alloy.

8. On an atom percent basis Nb and Ti were most effective in conferring solid solution strengthening and silicon the least effective.

The experimental observations have led to the following interpretations.

1. The swelling results may be interpreted in terms of the effect of point defect trapping on void growth rates. It is suggested that the observed changes in peak temperature are the result of small changes in the free vacancy formation energy.

2. The enhancement in swelling observed in the case of aluminum additions may be interpreted as the result of a small change in the vacancy migration energy.

3. Hot hardness measurements below 650°C can be fit with a function of the form

$$H = H_0 + \frac{b}{T}$$

where H is the hardness, T is the temperature, and H_0 and b are constants for a given alloy.

REFERENCES

1. Appleby, W. K., E. E. Bloom, J. A. Flinn, and F. A. Garner. 1977. Swelling in neutron-irradiation 300-series stainless steels. In the Proceedings of the International Conference on Radiation Effects in Breeder Reactor Structural Materials, Scottsdale, Arizona, June 19-23.
2. Laidler, J. J., and J. J. Holmes. 1977. U.S. programs on reference and advanced cladding/duct materials. In the Proceedings of the International Conference on Radiation Effects in Breeder Reactor Structural Materials, Scottsdale, Arizona, June 19-23.
3. Johnston, W. G., T. Lauritzen, J. H. Rosolowski, and A. M. Turkalo. 1976. The effect of metallurgical variables on void swelling. Page 227 in N. L. Petersen and S. D. Harkness, eds. Radiation damage in metals. American Society for Metals, Metals Park, Ohio.
4. Moteff, J., R. K. Bhargava, and W. L. McCullough. 1975. Correlation of the hot-hardness with the tensile strength of 304 stainless steel to temperatures of 1200°C. Met. Trans. A, 6A:1101.
5. Cawthorne, C., and E. J. Fulton. 1967. Voids in irradiated stainless steels. Nature 216:576.
6. Bement, A. L. 1973. Void formation in irradiated austenitic stainless steels. Advan. Nucl. Sci. Technol. 7:1.
7. Norris, D. I. R. 1972. Voids in irradiated metals. Radiat. Eff. 14:1, 15:1.
8. Bullough, R., and R. S. Nelson. 1974. Voids in irradiated metals. Phys. in Technol. 5(1):29.
9. Corbett, J. W., and L. C. Ianniello, eds. 1972. Radiation-induced voids in metals. Proceedings of an International Conference (Conf. 710601), Albany, N.Y., June 9-11, 1971.
10. Pugh, S. F., M. H. Loretto, and D. I. R. Norris, eds. 1971. Voids formed by irradiation of reactor materials. Proceedings of the British Nuclear Energy Society European Conference, Reading University, England, March 24-25.
11. Robinson, M. T., and F. W. Young, Jr., eds. 1975. Fundamental aspects of radiation damage in metals. 2 vols. Proceedings of an International Conference (Conf. 751006), Gatlinburg, Tennessee, October 6-10.

12. Watson, J. S., and F. W. Wiffen, eds. 1975. Radiation effects and tritium technology for fusion reactors. 4 vols. Proceedings of an International Conference (Conf. 750989), Gatlinburg, Tennessee, October 1-3.
13. International Atomic Energy Agency. 1969. Radiation damage in reactor materials. 2 vols. Proceedings of a Symposium, Vienna, Austria, June 2-9.
14. American Society for Testing and Materials. 1966. Effects of radiation on structural metals. A Symposium (STP 426), Atlantic City, N.J., June 26-July 1.
15. American Society for Testing and Materials. 1968. Irradiation effects in structural alloys for thermal and fast reactors. A Symposium (STP 457), San Francisco, California, June 23-28.
16. American Society for Testing and Materials. 1972. Effects of radiation on substructure and mechanical properties of metals and alloys. A Symposium (STP 529), Los Angeles, California, June 25-30.
17. American Society for Testing and Materials. 1976. Irradiation effects on the microstructure and properties of metals. A Symposium (STP 611), St. Louis, Missouri, May 4-6.
18. American Society for Testing and Materials. 1974. Properties of reactor structural alloys after neutron or particle irradiation. A Symposium (STP 570), Gatlinburg, Tennessee, June 11-13.
19. Peterson, N. L., and S. D. Harkness, eds. 1975. Radiation damage in metals. American Society for Metals, Metals Park, Ohio.
20. Olander, D. R. 1976. Fundamental aspects of nuclear reactor fuel elements. Technical Information Center Office of Public Affairs Energy Research and Development Administration (TID-26711-PI).
21. Mazey, D. J., J. A. Hudson, and R. S. Nelson. 1971. Void formation in nickel during 20 meV C^{++} irradiation at 525°C. J. Nucl. Mater. 41:257.
22. Beeler, J. R., and M. F. Beeler. 1975. Collision cascades in iron for energies up to 5 meV. Page 28 in M. T. Robinson and F. W. Young, eds. Fundamental aspects of radiation damage in metals. Proceedings of an International Conference (Conf. 751006), Gatlinburg, Tennessee, October 6-10.

23. Baluffi, R. W., and D. N. Seidman. 1972. Void formation in quenched or irradiated metals. Page 563 in J. W. Corbett and L. C. Ianniello, eds. Radiation-induced voids in metals. Proceedings of an International Conference (Conf. 710601), Albany, N.Y., June 9-11, 1971.
24. Doran, D. G., and J. O. Schiffgens. 1976. Cascade annealing— an overview. Page 3 in Correlation of neutron and charged particle damage. Proceedings of a workshop (Conf. 760673), Oak Ridge National Laboratory, Oak Ridge, Tennessee, June 8-10.
25. Beeler, J. R., Jr. 1966. Displacement spikes in cubic metals: I. α -iron, copper, and tungsten. Phys. Rev. 150:470.
26. Eyre, B. L. 1976. Irradiation damage structures generated in metals and alloys during irradiation at elevated temperatures. Page 729 in M. T. Robinson and F. W. Young, Jr., eds. Fundamental aspects of radiation damage in metals. Proceedings of an International Conference (Conf. 75-1006-PZ), Gatlinburg, Tennessee, October 6-10.
27. DePino, A., Jr. 1967. Helium production by (n, α) reactions in stainless steel. Nucl. Applications 3:620.
28. Bloom, E. E., K. Farrell, J. O. Stiegler, and M. H. Yoo. 1974. Void nucleation as inferred from reactor data. Page 330 in R. S. Nelson, ed. The physics of irradiation produced voids. Proceedings of a Consultants Symposium (AERE-R7954), Harwell, Didcot, Oxfordshire, England, September 9-11.
29. Mazey, D. J., and R. S. Nelson. 1975. The influence of pre-injected helium on void swelling in ion-irradiated stainless steels. Page I-240 in J. S. Watson and F. W. Wiffen, eds. Radiation effects and tritium technology for fusion reactors. 4 vols. Proceedings of an International Conference (Conf. 750989), Gatlinburg, Tennessee, October 1-3.
30. Makin, M. J., and G. P. Walters. 1973. The simulation of fast reactor void swelling in the Harwell HVM. Page 180 in J. E. Harris and E. C. Sykes, eds. Physical metallurgy of reactor fuel elements. Proceedings of an International Conference, Berkeley, U.K., September 2-7.
31. Levy, V., N. Azam, L. LeNaour, G. Didout, and J. Delaplace. 1977. Effect of structure and alloying elements on void formation in austenitic steels and nickel alloys. In Proceedings of the International Conference on Radiation Effects in Breeder Reactor Structural Materials, Scottsdale, Arizona, June 19-23.

32. Mansur, L. K., M. H. Yoo, and W. A. Coghlan. 1977. The effects of impurities on void nucleation and growth. A paper presented at the American Nuclear Society Winter Meeting, San Francisco, California.
33. Brimhall, J. L., H. E. Kissinger, and G. L. Kulcinski. 1972. The effect of temperature on void formation in irradiated pure and impure metals. Page 558 in J. W. Corbett and L. C. Ianniello, eds. Radiation-induced voids in metals. Proceedings of an International Conference (Conf. 710601), Albany, N.Y., June 9-11, 1971.
34. Christian, J. W. 1965. The theory of transformations in metals and alloys. Pergamon Press, Oxford, England. 973 pp.
35. Katz, J. L., and H. Wiedersich. 1971. Nucleation of voids in materials supersaturated with vacancies and interstitials. J. Chem. Phys. 55:1414.
36. Russell, K. C. 1971. Nucleation of voids in irradiated metals. Acta Met. 19:753.
37. Wiedersich, H., and J. L. Katz. 1976. The nucleation of voids and other irradiation-produced defect aggregates. Page 21 in Correlation of neutron and charged particle damage. Proceedings of a Workshop (Conf. 760673), Oak Ridge National Laboratory, Oak Ridge, Tennessee, June 8-10.
38. Mansur, L. K., and W. G. Wolfer. 1977. A study of the effect of void surface coatings on radiation-induced swelling. ORNL/TM-5670. (Oak Ridge National Laboratory, Oak Ridge, Tennessee.)
39. Weinberg, A. M., and E. P. Wigner. 1959. The physical theory of neutron chain reactors. University of Chicago Press, Chicago, Illinois. 800 pp.
40. Wolfer, W. G., L. K. Mansur, and J. A. Sprague. 1977. Theory of swelling and irradiation creep. In the Proceedings of the International Conference on Radiation Effects in Breeder Reactor Structural Materials, Scottsdale, Arizona, June 19-23.
41. Farrell, K., J. Bentley, and D. N. Braski. 1977. Direct observation of radiation-induced coated cavities. Scripta Met. 2:243.
42. Wolfer, W. G., and M. Ashkin. 1976. Diffusion of vacancies and interstitials to edge dislocations. J. App. Phys. 47(3):791.
43. Bullough, R., and R. D. Newman. 1970. The kinetics of migration of point defects to dislocations. Rep. Prog. Phys. 33:101.

44. Norris, D. I. R. 1971. The simulation of fast reactor irradiation effects in the high voltage electron microscope. Page 247 in S. F. Pugh, M. H. Loretto, and D. I. R. Norris, eds. Voids formed by irradiation of reactor materials. Proceedings of the British Nuclear Energy Society European Conference, Reading University, England, March 24-25.
45. Carpenter, R. W., and J. C. Ogle. 1975. The effect of solute content and precipitate distribution on fast neutron damage in aluminum-copper alloys. Page 1203 in M. T. Robinson and F. W. Young, eds. Fundamental aspects of radiation damage in metals. 2 vols. Proceedings of an International Conference (Conf. 751006), Gatlinburg, Tennessee, October 6-10.
46. Bullough, R., and R. C. Perrin. 1972. Theory of void formation and growth in irradiated materials. Page 769 in J. W. Corbett and L. C. Ianniello, eds. Radiation-induced voids in metals. Proceedings of an International Conference (Conf. 710601), Albany, N.Y., June 9-11, 1971.
47. Brailsford, A. D., and R. Bullough. 1972. The rate theory of swelling due to void growth in irradiated metals. J. Nucl. Mater. 44:121.
48. Wiedersich, H. 1972. On the theory of void formation during irradiation. Rad. Eff. 12:111.
49. Harkness, S. D., and C. Y. Li. 1971. A study of void formation in fast neutron-irradiated metals. Met. Trans. 2:1457.
50. Mansur, L. K. 1976. Void growth kinetics: an assessment of the theory. Page 61 in Correlation of neutron and charged particle damage. Proceedings of a workshop (Conf. 760675), Oak Ridge National Laboratory, Oak Ridge, Tennessee, June 8-10.
51. Cottrill, R. M. J., M. Doyama, J. J. Jackson, and M. Meshii, eds. 1975. Lattice defects in quenched metals. Proceedings of an International Conference, Argonne National Laboratory, June 15-17, 1964, Academic Press, New York. 807 pp.
52. Johnson, R. A., and N. Q. Lam. 1976. Solute segregation in metals under irradiation. Phys. Rev. B13:4364.
53. Smidt, F. A., and J. A. Sprague. 1973. Suppression of void nucleation by a vacancy trapping mechanism. Scripta Met. 7:495.
54. Straalsund, J. L. 1974. The effect of cluster formation on the "temperature shift" for accelerator simulation of neutron irradiation. J. Nucl. Mater. 51:302.

55. Bullough, R., B. L. Eyre, and K. Krishan. 1975. Cascade damage effects on the swelling of irradiated materials. (AERE-R7952), Harwell, Oxfordshire, England.
56. Yoo, M. H., and W. H. Butler. 1976. Steady-state diffusion of point defects in the interaction force field. Phys. Stat. Sol. B, B:77.
57. Baluffi, R. W. 1975. Voids, dislocation loops and grain boundaries as sinks for point defects. Page 852 in M. T. Robinson and F. W. Young, eds. Fundamental aspects of radiation damage in metals. 2 vols. Proceedings of an International Conference (Conf. 751006), Gatlinburg, Tennessee, October 6-10.
58. Wolfer, W. G. 1975. Segregation of point defects by internal stress fields. Page 812 in M. T. Robinson and F. W. Young, eds. Fundamental aspects of radiation damage in metals. 2 vols. Proceedings of an International Conference (Conf. 751006), Gatlinburg, Tennessee, October 6-10.
59. Brailsford, A. D., R. Bullough, and M. R. Hayns. 1976. Point defect sink strengths and void swelling. J. Nucl. Mater. 60:246.
60. Flinn, J. E., and T. A. Kenfield. 1975. Neutron swelling observations on austenitic stainless steels irradiated in EBR II. Page 253 in Correlation of neutron and charged particle damage. Proceedings of a Workshop (Conf. 760673), Oak Ridge National Laboratory, Oak Ridge, Tennessee, June 8-10.
61. Wolfer, W. G. 1975. A short review of stress effects on swelling. Page 369 in Correlation of neutron and charged particle damage. Proceedings of a Workshop (Conf. 760673), Oak Ridge National Laboratory, Oak Ridge, Tennessee, June 8-10.
62. Bullough, R., and M. R. Hayns. 1975. The swelling effects to be expected in materials under high transmutation gas generation rates. Page 230 in J. S. Watson and F. W. Wiffen, eds. Radiation effects and tritium technology for fusion reactors. 2 vols. Proceedings of an International Conference (Conf. 750989), Gatlinburg, Tennessee, October 1-3.
63. Odette, G. R., and S. C. Langley. 1975. Modeling of synergistic effects of displaced atom and transmutant damage in fission and fusion environment. Page 395 in J. S. Watson and F. W. Wiffen, eds. Radiation effects and tritium technology for fusion reactors. 2 vols. Proceedings of an International Conference (Conf. 750989), Gatlinburg, Tennessee, October 1-3.

64. Seeger, A. 1975. The stationary distribution of vacancies and interstitials in irradiated plates. *Phys. Stat. Sol. A*, 28:157.
65. Guthrie, G. L., and J. L. Straalsund. 1975. Spatial dependence of void growth rates in the irradiation of thin foils—theory and calculations. *Scripta Met.* 9:1149.
66. Yoo, M. H., and L. K. Mansur. 1976. Distributions of point defects in bounded media under irradiation. *J. Nucl. Mater.* 62:282.
67. Brailsford, A. D. 1975. An effect of solute segregation on void growth in irradiated dilute alloys. *J. Nucl. Mater.* 56:7.
68. Okamoto, P. R., and H. Wiedersich. 1974. Segregation of alloying elements to free surfaces during irradiation. *J. Nucl. Mater.* 53:336.
69. Nolfi, F. V., Jr. 1976. Elastic interactions between "voids" induced by solute segregation. *J. Appl. Phys.* 47(1):24.
70. Yoo, M. H. 1977. Dislocation loop growth and void swelling in bounded media by charged particle damage. ORNL/TM-5789 (Oak Ridge National Laboratory, Oak Ridge, Tennessee.)
71. Ghoniem, N., and G. Kulcinski. 1976. Fully dynamic rate theory (FDRT) simulation of radiation induced swelling of metals. UWFDM-180, University of Wisconsin, Madison, Wisconsin.
72. Weiner, R. A., and A. Boltax. 1977. Microstructural modeling of irradiation creep and swelling. *J. Nucl. Mater.* 66:1.
73. Nelson, R. S., and D. J. Mazey. 1969. Void formation in stainless steel during charged-particle irradiation at elevated temperatures. Vol. 2, page 157 in International Atomic Energy Agency. Radiation damage in reactor materials. Proceedings of a symposium, Vienna, Austria, June 2-9.
74. Garr, K. R., and A. G. Pard. 1976. Swelling and tensile property changes in neutron-irradiated type 316 stainless steel. Page 72 in American Society for Testing and Materials. Irradiation effects on the microstructure and properties of metals. A symposium (STP 611), St. Louis, Missouri, May 4-6.
75. Walter, G. P. 1971. Temperature dependence of void swelling in 18/8/Ti steel. Page 223 in S. F. Pugh, M. H. Loretto, and D. I. R. Norris, eds. Voids formed by irradiation of reactor materials. Proceedings of the British Nuclear Energy Society European Conference, Reading University, England, March 24-25.

76. Bloom, E. E., J. O. Stiegler, A. F. Rowcliffe, and J. M. Leitnaker. 1976. Austenitic stainless steels with improved resistance to radiation-induced swelling. *Scripta Met.* 10:303.
77. Johnston, W. G., J. H. Rosolowski, A. M. Turkalo, and T. Lauritzen. 1974. An experimental survey of swelling in commercial Fe-Cr-Ni alloys bombarded with 5 MeV Ni ions. *J. Nucl. Mater.* 54:24.
78. Bates, J. F., and W. G. Johnston. 1977. Effects of alloy composition on void swelling. A paper presented at the International Conference on Radiation Effects in Breeder Reactor Structural Materials, Scottsdale, Arizona, June 19-23.
79. Garner, F. A., R. W. Powell, S. Diamond, T. Lauritzen, A. F. Rowcliffe, J. A. Sprague, and D. Keefer. 1977. Simulation of high fluence swelling behavior in technological materials. A paper presented at the International Conference on Radiation Effects in Breeder Reactor Structural Materials, Scottsdale, Arizona, June 19-23.
80. Manning, I., and G. P. Mueller. 1974. Depth distribution of energy deposition by ion bombardment. *Computer Phys. Comm.* 7:85.
81. Robinson, M. T. 1977. The status of defect production theory. Page 1 in *Correlation of neutron and charged particle damage. Proceedings of a workshop (Conf. 760673)*, Oak Ridge National Laboratory, Oak Ridge, Tennessee, June 8-10.
82. Marwick, A. D. 1975. The primary recoil spectrum in the simulation of fast-reactor radiation damage by charged-particle bombardment. *J. Nucl. Mater.* 55:259.
83. Garner, F. A., and G. L. Guthrie. 1976. The influence of displacement gradients on the interpretation of charged particle simulation experiments. Page 491 in J. S. Watson and F. W. Wiffen, eds. *Radiation effects and tritium technology for fusion reactors. Proceedings of an International Conference (Conf. 750989)*, Gatlinburg, Tennessee, October 1-3.
84. Johnston, W. G., W. G. Morris, and A. M. Turkalo. 1977. Excess sub-surface void swelling produced by Ni ion bombardment. A paper presented at the International Conference on Radiation Effects in Breeder Reactor Structural Materials, Scottsdale, Arizona, June 19-23.
85. Brailsford, A. D., and L. K. Mansur. 1977. Effect of implanted interstitials on swelling during self-ion bombardment. A paper presented at the American Nuclear Society special session, *Simulation of radiation damage effects: Theory and practice*. New York, June 12-17.

86. Johnston, W. G., T. Lauritzen, J. H. Rosolowski, and A. M. Turkaio. 1976. Void swelling in fast reactor materials—a metallurgical problem. *J. of Met.* 28(6):19.
87. Bloom, E. E., and J. O. Stiegler. 1970. A comparison of irradiation-induced swelling and void formation in two austenitic stainless steels. *J. Nucl. Mater.* 35:244-94.
88. Lauritzen, T., A. Withop, and V. E. Wolff. 1969. Swelling of austenitic stainless steels under fast neutron irradiation at elevated temperatures. *Nuc. Eng. and Design* 9:265.
89. Leitnaker, J. M., E. E. Bloom, and J. O. Stiegler. 1973. The effect of minor constituents on swelling in stainless steel. *J. Nucl. Mater.* 49:57.
90. Bates, J. F. 1974. Irradiation-induced swelling variations resulting from compositional modifications of type 316 stainless steel. Page 369 in *American Society for Testing and Materials. Properties of reactor structural alloys after neutron or particle bombardment. Proceedings of a symposium (STP 570), Gatlinburg, Tennessee, June 11-13.*
91. Ellis, J. A., Jr., W. K. Appleby, and T. Lauritzen. 1976. Swelling simulation studies of type 316 stainless steel. Page 195 in *American Society for Testing and Materials. Irradiation effects on the microstructure and properties of metals. Proceedings of a symposium (STP 611), St. Louis, Missouri, May 4-6.*
92. Guthrie, G. L., B. Mastel, H. E. Kissinger, and E. R. Bradley. 1970. Absence of voids in neutron irradiated sputtered nickel. *J. Nucl. Mater.* 37:343.
93. Peckner, D., ed. 1964. *The strengthening of metals.* Reinhold Publishing Company, New York. 250 pp.
94. Collings, E. W., and H. L. Gegel, eds. 1973. *Physics of solid solution strengthening. Proceedings of a symposium, McCormick Place, Chicago, Illinois, October 2.*
95. Kelly, A., and R. B. Nicholson, eds. 1971. *Strengthening methods in crystals.* Halsted Press Division, John Wiley & Sons, Inc., New York. 627 pp.
96. Hirsch, P. B., ed. 1975. *The physics of metals. 2 defects.* Cambridge University Press, Cambridge, England. 302 pp.
97. Mott, N. F., and F. R. N. Nabarro. 1940. An attempt to estimate the degree of precipitate hardening with a simple model. *Proceedings of the Physical Society* 52:86.

98. Nabarro, F. R. N. 1977. The theory of solution hardening. *Phil. Mag.* 35(3):613.
99. Fleischer, R. L., and W. R. Hibbard. 1963. Solution hardening. Page 262 in N. P. Allen, ed. The relation between the structure and mechanical properties of metals. Proceedings of a Conference, National Physical Laboratory, Teddington, Middlesex, England, January 7-9.
100. Fleischer, R. L. 1960. Effects of non-uniformities on the hardness of crystals. *Acta Met.* 8:598.
101. Eshelby, J. D. 1951. Forces on an elastic singularity. *Phil. Trans. Roy. Soc. A*, 244:87.
102. Friedel, J. 1956. *Les Dislocations*. Gauthier-Villars, Paris. 491 pp.
103. Fleischer, R. L. 1963. Substitutional solution hardening. *Acta Met.* 11:203.
104. Saxl, I. 1964. Elastic interactions of point defects with dislocations. *Czech. J. Phys. B*, 14:381.
105. Labusch, R. 1970. A statistical theory of solid solution hardening. *Phys. Stat. Sol.* 41:659.
106. Friedel, J. 1963. On the elastic limit of crystals. Page 605 in G. Thomas and J. Washburn, eds. *Electron microscopy and strength of crystals*. Proceedings of an International Conference, University of California, Berkeley, July 5-8.
107. Koppenaar, T. J., and D. Kuhlmann-Wilsdorf. 1964. The effect of prestressing on the strength of neutron-irradiated copper single crystals. *Appl. Phys. Lett.* 4:59.
108. Ashby, M. F. 1972. A first report on deformation-mechanism maps. *Acta Met.* 20:887.
109. Tabor, D. 1951. *The hardness of metals*. Oxford University Press, Amen House, London, England. 171 pp.
110. Shaw, M. C., and G. J. DeSalvo. 1970. On plastic flow beneath a blunt axisymmetric indenter. *Trans. ASME* 92:481.
111. Westbrook, J. H. 1952. Temperature dependence of the hardness of pure metals. *Trans. ASM* 45:221.

112. Geach, G. A. 1974. Hardness and temperature. Intern. Met. Rev. 19:255.
113. George, R. A., S. Dinda, and A. S. Kasper. 1976. Estimating yield strength from hardness data. Metals Progress 109:30.
114. Underwood, E. E. 1957. Creep properties from short time tests. Mater. Methods 15:129.
115. Atkins, A. G., and D. Tabor. 1966. The plastic deformation of crossed cylinders and wedges. J. Inst. Metl. 94:369.
116. Bens, F. B. 1946. Hardness testing of metals and alloys at elevated temperatures. Trans. ASM 38:506.
117. Garofalo, F., P. R. Malenock, and G. V. Smith. 1952. Hardness of various steels at elevated temperatures. Trans. ASM 45:377.
118. Tabor, D. 1951. The hardness and strength of metals. J. Inst. Met. 79:1.
119. Hill, M. J., and D. J. Rowcliffe. 1974. Deformation of silicon at low temperatures. J. Mater. Sci. 9:1569.
120. Packan, N., and W. Coghlan. 1977. Injecting irradiation samples with He using a Cm^{244} source. To be submitted to Nucl. Sci. Tech.
121. Shabason, L., and W. J. Choyke. 1976. Helium depth profiles in thin metal foils. Nucl. Inst. Meth. 138:533.
122. Lewis, M. B., F. K. McGowan, C. H. Johnson, and M. J. Saltmarsh. 1975. The Oak Ridge CN Van de Graff as a facility for heavy ion radiation damage studies. Page 15 in D. Kramer, ed. Experimental methods for charged-particle irradiations. Proceedings of a symposium (Conf. 750947), Gatlinburg, Tennessee, September 30.
123. Johnston, W. G., J. H. Rosolowski, A. M. Turkalo, and T. Lauritzen. 1973. A direct measurement of gross swelling in nickel-ion-bombarded stainless steel. J. Nucl. Mater. 46:273.
124. Doyama, M., and J. S. Koehler. 1976. The relation between the formation energy of a vacancy and the nearest neighbor interactions in pure metals and liquid metals. Acta Met. 24:871.
125. Allan, G., and M. Lannoo. 1976. Vacancies in transition metals. J. Phys. Chem. Sol. 37:699.

126. Seeger, A., D. Schumacher, W. Schilling, and J. Diehl, eds. 1970. Vacancies and interstitials in metals. Proceedings of the International Conference held at Jülich, Germany, September 23-28, 1968.
127. American Society for Metals. 1973. Metal handbook, Vol. 8. Metals Park, Ohio.

ACKNOWLEDGMENTS

This research was carried out in the Metals and Ceramics Division of the Oak Ridge National Laboratory, operated by Union Carbide Corporation for the Department of Energy. Financial support during the course of this study was provided by a fellowship from Oak Ridge Associated Universities.

The author wishes to thank his major professor Dr. D. M. Roberts for his guidance and understanding during this graduate program. Appreciation is also expressed to Dr. J. O. Stiegler, Dr. E. E. Bloom, Dr. M. S. Wechsler, Dr. A. F. Rowcliffe, and Dr. L. K. Mansur for countless helpful discussions and useful suggestions throughout the course of this investigation. The author also thanks Dr. E. Lee for performing microscopy of the alloys. Several other individuals in the Radiation Effects group and Metals and Ceramics Division of Oak Ridge National Laboratory have made contributions during various phases of this study.